DISPERSION OF OFFSHORE DISCHARGED PRODUCED WATER IN THE MARINE ENVIRONMENT: HYDRODYNAMIC MODELING AND EXPERIMENTAL STUDY

HAIBO NIU


CENTRE FOR NFLD. STUDIES
MEMORIAL UNIVERSITY
OF NEWFOUNDLAND

DISPERSION OF OFFSHORE DISCHARGED PRODUCED WATER IN THE MARINE ENVIRONMENT: HYDRODYNAMIC MODELING AND EXPERIMENTAL STUDY

by

© **Haibo Niu**

A Thesis submitted to the School of Graduate Studies
in partial fulfillment of the requirements for the
Degree of Doctor of Philosophy

Faculty of Engineering & Applied Science
Memorial University of Newfoundland

January, 2008

St. John's **Newfoundland** **Canada**

ABSTRACT

This study has two major components: hydrodynamic modeling and experimental study of the dispersion of produced water in a marine environment. The general objective was to develop a hydrodynamic model that predicts the concentration of produced water and conduct experiments to validate the model. This consisted of seven more specific objectives: (1) developing a steady state model that predicts the near field, intermediate field, and far field mixing process; (2) integrating the wave effects into the steady state model; (3) conducting uncertainty analysis and expanding the model to probabilistic format; (4) conducting laboratory experiments and validating the model; (5) applying the model to a case study dealing with the discharge from an offshore oil platform; (6) coupling the steady state model with a non-steady state model to study the far field time-dependent dispersion; (7) collecting field data using an Autonomous Underwater Vehicle.

For the objective (1) and (2), a steady state model named PROMISE (PROduced water Mixing In Steady-state Environment) was developed in this study. The model has four major hydrodynamic modules: (1) a Lagrangian based integral type near field model that employs a new entrainment formulation based on extensive laboratory experiments was employed; (2) a wave effects model that considers the effects of both ocean surface waves and internal waves. A new wave effect formulation based on previous experimental and analytical studies was developed; (3) upstream intrusion and downstream control module; and (4) a buoyant spreading and turbulent diffusion model. Unlike previous approaches which treat the buoyant spreading and turbulent

dispersion separately, a unified approach that considers both effects simultaneously was used.

By analysis of the uncertainties associated with modeling parameters, statistical distributions for these parameters were derived. Together with the known uncertainties of the ambient and discharge conditions, the PROMISE model was used in a probabilistic analysis using the Monte Carlo simulation technique.

To validate the formulation of the PROMISE model, laboratory experimental data from various sources have been collected. The model has been executed under different conditions to compare with these data. While most of the previous experiments were conducted at small scales, relatively large scale laboratory experiments were conducted in this study to further validate the model.

To test the performance of the model, a hypothetical study has been performed. Two scenarios were tested: one with the effects of waves and the other without. By integrating the hydrodynamic model with a food chain model, a simulation which studies the distribution of Phenol among the food chain components, especially fish, was performed.

To study the dispersion of produced water under a non-steady state environment, the PROMISE was coupled with a three-dimensional non-steady state model, MIKE 3. While most previous coupling was only one-way coupling, a two-way coupling was adopted in this study.

To collect field data to validate the hydrodynamic model and test the potential of using an Autonomous Underwater Vehicle (AUV) to map the produced water outfall, two field experiments using the *MUN EXPLORER* AUV were conducted. A submerged freshwater outfall with Rhodamine WT dye was discharged into the

Holyrood Bay and the AUV equipped with a fluorometer was used to measure the dye concentration and the extent of the dispersed plume. The results have shown that the AUV can be effectively used to map the outfall.

ACKNOWLEDGEMENT

First and foremost, I would like to express my sincere thanks to Dr. Tahir Husain, Dr. Brian Veitch, and Dr. Neil Bose for their excellent supervision and guidance during the course of my research. Without their support this thesis would not have been possible. I am very grateful to Dr. Kelly Hawboldt for her continuous guidance and help.

I also gratefully acknowledge the Faculty of Engineering and Applied Science, Memorial University of Newfoundland (MUN), and the PRAC/NSERC Project for financial support. An expression of thanks is also extended to Judith Bobbit at the Oceans Limited for the supply of experimental instruments.

Personal thanks are extended to Jim Gosse, Craig Michel, Tom Pike, and Matthew Curtis for their help during the laboratory experiments, and to Sara Adams, Moqin He, and Jihad Shanaa for their help during the field experiments. I also would like to express my thanks to Andrew Cook for his help on processing current meter data.

The DHI Software is thanked for the providing of the MIKE 3 software system (Evaluation Version). The model coupling studies could not have been undertaken without their support.

Last but by no means least, I would like to offer my deepest appreciation to my wife Liping Wang, my mother Jinzhi Xue, my father Zhijun Niu and my elder sister Hongxia Niu for their love and encouragement.

This thesis is dedicated to the memory of my grandfather, Enrong Niu (1919-2005).

TABLE OF CONTENTS

LIST OF TABLES

LIST OF FIGURES

NOMENCLATURE

a	wave amplitude
A	area
B	port source buoyancy flux
B_0	initial buoyant flux
b	buoyant jet width
$b_{gaussian}$	Gaussian plume width
b_{top}	top-hat plume width
b_v	far field plume thickness
$b_{v(outflow)}$, b_{v0}	plume thickness at the end of the control volume
C	concentration of the jet
C_0	source initial concentration
C_a	ambient concentration
C_c	jet centerline concentration
C_D	drag coefficient
$C_{gaussian}$	Gaussian profiles of concentration
C_p	absorpted concentration on phytoplankton
C_{disol}	dissolved concentration
C_{phyto}	phytoplankton concentration in water column
co_n	experimental constants, n = 1,2,3…..n
C_m	maximum excess concentration
C_n	experimental constants, n = 1,2,3…..n
C_t	top-hat velocity
C_w	experimental constants
C_z	concentration in zooplankton
C_{total}	total concentration
D	port diameter

E	entrainment rate
E_f	ratio of maximum centerline concentration to average concentration
E_t	bulk entrainment due to turbulent diffusion
E_b	bulk entrainment due to buoyant spreading
$EL(P_i, t)$	element at position P_i and time t
F	fetch
F_b	buoyant spreading force
F_D	ambient drag force
F_i	buoyant force acting on a plume element
F_L	local Froude number
F_r	densimetric Froude number
Δf	surface element of the plume element ΔV_{vol}
g	acceleration of gravity
g'	reduced gravity
g_i	acceleration of gravitation in x_i direction
h	intermediate field plume thickness
h_B	frontal plume height
h_k	k^{th} plume element thickness
h_{water}	water depth
H	wave height
K_H, K_M	eddy diffusivities for scalar and momentum, respectively
K	velocity ratio, U_j/U_a
K_x, K_y, K_z	turbulent diffusivity in x, y, and z directions
k	kinetic energy
k_n	experimental constants, n = 1,2,3…..n
K_p	equilibrium partitioning coefficient
k_w	wave number
L	far field plume width
L_Q	discharge length scale, $Q/M^{1/2}$

L_a	length scale, $L_a = u_a/[(-g/\rho_a)(d\rho_a/dz)]^{1/2}$
L_b	buoyancy length scale
L_b'	plume/stratification length scale
L_M	jet/plume length scale
L_D	plume width at the downstream end
L_m'	jet/stratification length scale
L_m	jet/crossflow length scale
L_s	upstream intrusion length
L_I	upstream intrusion near field length scale
L_N	length scale representing the relative importance of momentum flux versus stability effects of buoyancy force
L_0	Initial plume width at the beginning of turbulent diffusion region
L_w	wave length
M	momentum flux (L^4/T^2)
M_0	initial momentum flux (L^4/T^2)
M_k	mass of k^{th} jet element
ΔM_k	increase of mass for k^{th} element
Δm	change of mass
N	a random quantity
P	pressure
Q	volume flux
Q_0	initial volume flux
q	upstream plume speed
r	radial distance
R_e	Reynolds number
R_i	Richardson number
Rj	integration limit
R_n	regression coefficients, $n = 1,2,3\ldots n$
S	dilution

S_{ave}	average dilution at downstream end
S_{min}	minimum dilution at downstream end
S_{inflow}	dilution at the beginning of the control volume
$S_{outflow}$	dilution at the end of the control volume
S_{sur}	surface dilution
S_{wave}	dilution with the effect of wave
$S_{No\ Wave}$	dilution without the effect of wave
S_i	initial dilution
s_y	standard deviation of cross-plume distribution function
SA_a	ambient salinities
SA_j	initial jet salinities
S_{Source}	volumetric source term
t	time
T_w	wave period
T_k	temperature of k^{th} jet element
T_a	ambient temperature
U	jet velocity
U_i	instantaneous velocity component in the direction of x_i
U_j	initial discharge jet velocity
U_c	centerline jet velocity
U_{ent}	rate of entrainment
$U_{gaussian}$	Gaussian profiles of velocity
U_m	maximum excess velocity
U_t	top-hat velocity
u_a, U_a	ambient velocity
u_t	effective propagation speed of plume boundary
u_i	velocities of a plume element along its trajectory
u_{max}	wave induced velocity
u_*	shear velocity

U_{wind}	wind speed
ν	kinematic viscosity
ν_t	turbulent eddy viscosity
u,v,w	velocity vectors in, x, y, z direction respectively
u_b	propagation speed of plume boundary due to buoyant spreading
u_t	propagation speed of plume boundary due to turbulent diffusion
u_c	jet centerline velocity
u_{up}, v_{up}	upstream plume internal velocity
V_k	jet local velocity of k^{th} element
v_{lat}	lateral velocity
w_e	entrainment velocity
w_{ew}	wind-induced entrainment
w_{ei}	interfacial entrainment
w_{ef}	frontal entrainment
x_D	downstream distance from impingement center to the end of the control volume
Z	depth of water above discharge port
Z_B	Length scale measures the distance required for buoyancy induced momentum to be on the order of the wave induced momentum
Z_e	equilibrium height-of-rise
Z_m	maximum height-of-rise
Z_M	Length scale measures the distance required for the jet momentum to be on the order of the wave induced momentum
ρ	local density
ρ_a	density of ambient fluid
ρ_j	density of jet
ρ_0	initial density of jet
ρ_{ref}	reference density
ρ_{up}	upstream plume density
ρ'	turbulent fluctuation of density

ϕ	vertical angle of jet with respect to horizontal plane
θ	horizontal angle with respect to x-axis
θ_1	plume discharge angle relative to the direction of wave propagation
θ_{front}	frontal angle
θ_{imp}	impingement angle
σ	standard deviation of plume width
σ_w	wave freqency
ξ	horizontal displacement of a fluid particle for linear wave
ζ	diffusivity
ε_D	stratification parameter
α_1	entrainment coefficient for buoyant spreading
α_2	constants for estimation of u_b
α_s, α_{shear}	shear entrainment coefficient
α_{vortex}	vortex entrainment coefficient
ψ	function
φ_k	separation angle
λ	dispersion ratio for the scalar quantities
λ_g	ratio of concentration to velocity
λ_i	interfacial friction coefficient
δ_{ij}	Kronecker delta
Γ	turbulent diffusivity of mass
β	constant range from 0.15 to 0.25

1. INTRODUCTION

1.1 BACKGROUND OF STUDY

The exploration and extraction of offshore oil and gas from beneath the ocean floor requires the disposal of produced water in the marine environment. Produced water is the aqueous fraction extracted along with oil and gas from geological formations. The produced water consists of formation water (water naturally present in the reservoir), flood water (seawater previously injected into the formation to maintain reservoir pressure), and condensed water (in the case of gas production).

The water and oil is usually separated on the platform. After separation, the oil and gas are sent to shore by pipeline or transported to shore by tanker, and the produced water is either discharged to the sea, or re-injected into the reservoir after receiving additional treatment. The quantity of produced water varies from site to site depending upon the reservoir characteristics. In 2003, it was estimated that 667 million metric tons of produced water were discharged world wide (Neff *et al.*, 2007). The discharge of produced water to offshore waters of North America was about 21.1 million tons, and to offshore waters of Europe was about 358-419 million tons (Neff *et al.*, 2007). Produced water discharge in Atlantic Canada is currently limited as the offshore oil and gas resources are in the early stages of development with only five discoveries having been put into production to date. These five fields are: Cohasset, Sable Island, Hibernia, Terra Nova and White Rose.

The composition of produced water depends on the nature of the formation from which it is withdrawn and the procedures used to treat it. The composition includes a

variety of naturally occurring (e.g., salinity, heavy metals) and production chemicals (e.g., BTEX, PAHs). Some of the constituents of discharged produced water may cause toxic effects and impact the marine ecosystem structure and function. The transport mechanisms and pathways for the individual chemicals are different, however, their fates are determined by the following mechanisms: dilution, volatilization, chemical reaction, adsorption, and biodegradation. These mechanisms are shown in Figure 1.

The present research will only focus on the physical mechanisms that is the dilution and dispersion process, following discharge. The chemical and biological mechanisms (for example, the degradation, bioaccumulation, and biomagnifications etc.) are beyond the scope of this study.

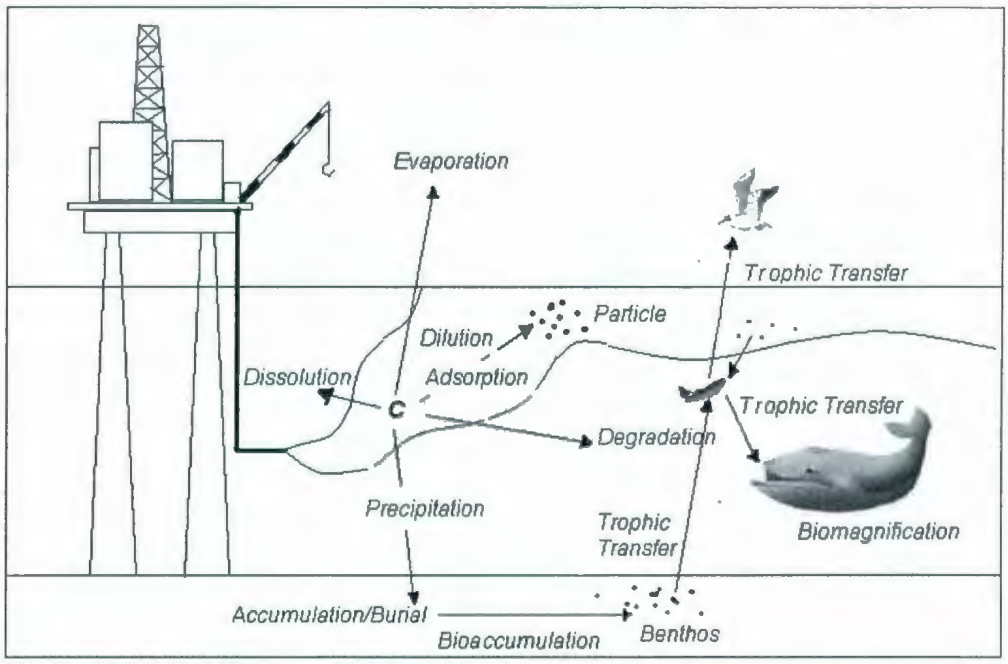

Figure 1. Environmental fates of chemical (C) from produced water in seawater (modified from Neff, 2002).

1.2 THE MIXING PROCESSES

Once discharged, the produced water plume will descend or ascend depending on its density relative to the ambient seawater, and it will bend in the direction of the ambient current until it encounters the seafloor or reaches the water surface. In the case of a stratified environment, the plume will usually be trapped at a neutrally buoyant level before it encounters the seafloor or reaches the water surface. This phase, named the near field, ends within minutes and within a few meters from the discharge source and the corresponding dilution is in the range of 100 to 1,000.

After the plume reaches the boundary (surface/seabed), it spreads as a thin layer and the mixing is dominated by two mechanisms: buoyant spreading and oceanic turbulent diffusion. Buoyant spreading is a self-driven dispersion process because the horizontal transverse spreading and vertical collapse of the plume are due to the residual buoyancy contained in the plume. Buoyant spreading is particularly important for a plume that is poorly diluted during the initial mixing process. The far field mixing process starts from the turbulent diffusion region. The turbulent diffusion is a passive dispersion process resulting from oceanic turbulence or eddies. Both buoyant spreading and turbulent diffusion could be important over a distance from the discharge point, but the buoyancy effect decreases while the turbulence effect increases as a plume travels down stream.

The length and time scales for the mixing process is illustrated in Figure 2.

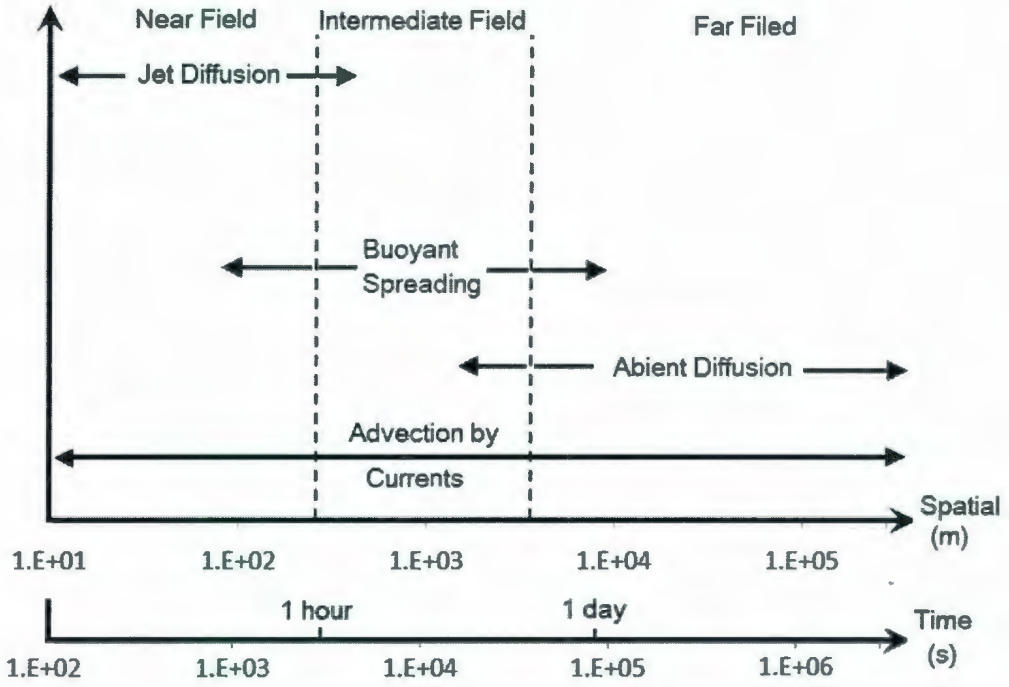

Figure 2. Physical processes and length and time scales of discharged outfalls in marine environments (after Jirka et al., 1975).

In order to give operators and regulatory agencies the ability of assessing the fate of produced under a variety of ocean conditions, mathematical modeling of the dispersion processes of produced water in a marine environment is an important tool.

1.3 DISPERSION MODELS

Over the past few decades, a number of computer models have been developed to describe the dispersion of discharges (e.g., drilling muds and produced waters) in the vicinity of offshore platforms. A considerable number of environmental discharge models which were developed for sewage outfall or power plant surface discharge applications can also be used to estimate the dilution of produced water. In this section, a brief summary of these models will be presented.

The OOC model was originally developed by the Offshore Operators Committee (Brandsma et al., 1980, 1992) to simulate the dispersion of drilling muds. OOC model simulates the behavior of discharges from a single, submerged circular port oriented in any direction. Effluents are assumed to consist of a water-miscible fluid phase that can contain particles that are heavier or lighter than ambient water. The receiving water is described by water depth, temperature, salinity, and current velocity. The model outputs consist of predictions of the trajectory and the shape of the discharge plume, the concentration of the soluble and insoluble discharge components in the water column, and the accumulation of solids on the seabed. The OOC model treats plumes as comprising three distinct flow regimes: convective descent, wherein material transport is dominated by the initial discharge momentum, entrainment, and drag forces; dynamic collapse, where the plume seeks its equilibrium level or reaches the surface or seabed; and passive diffusion, in which the plume has lost any dynamic character of its own and diffusive phenomenon and advection are the primary transport mechanisms. These processes are described in OOC by a Lagrangian approach. Applications of OOC model can be found from Terrens & Tait (1993) and Brandsma & Smith (1996).

The PROVANN (Reed et al., 1996) model is a three dimensional model which is able to simulate the spreading of produced water in three dimensions for a time varying wind input. The produced waters are spread due to horizontal and vertical diffusion and advected away due to residual currents, tidal currents, and wind induced Ekman currents. PROVANN system has four components: a near field release model, a far field transport model, a biological exposure model, and a bioaccumulation and biomagnification model. The near field model of PROVANN is based on the integral

model of Brandsma et al. (1980, 1992) and the far field model uses a particle tracking approach.

The pollution risk offshore technical evaluation system, PROTEUS (Sabeur & Tyler, 2001), has been developed and is widely used within the European oil industry to support environmental risk assessments of discharged produced water. The PROTEUS is built with a set of modules, each executing specific internal tasks and providing information dynamically to other modules in the same system. Besides a physical dispersion model which is similar to that of the PROVANN, it also includes a geochemistry model for the prediction of contaminant behaviour between dissolved and solid particulate phases, and a biological model which simulates the process of chemical uptake by marine species.

Berry & Wells (2005) studied the produced water from the Baud platform off the east coast of Canada using the CORMIX (Doneker & Jirka, 1990) model to predict the dilution. They integrated a fugacity model to estimate the partitioning of PAH and BTEX among water column, suspended particles, sediments, and fish. The CORMIX is a general environmental discharge model developed by Cornell University under the support of U.S. EPA. The methodology of CORMIX for near field buoyant jet mixing processes is based on asymptotic analysis to classify near field flow patterns and the use of asymptotic solutions. In the far field, CORMIX uses a buoyant spreading model. In transitions between the near and far field, CORMIX uses a control volume model to connect the near field and far field. CORMIX does not consider the wave effect on near field mixing but it does consider the wind induced mixing in far field.

Hodgins (1993) carried out dilution modeling for the Hibernia produced water discharges using PLUMES (Baumgartner et al., 1994) for the initial mixing phase and integrated a steady state transport-diffusion for the far field dilution. In a later study (Hodgins & Hodgins, 2000), the PLUMES model was used to study the near field mixing of produced water discharged from the White Rose site off the east coast of Canada. Once the plume reached the surface, a particle tracking based model was used to simulate the far field dispersion. This approach is similar to that of the PROVANN and PROTEUS.

Smith et al. (1996) have used the TRK model (Riddle, 1993) to predict the produced water discharge from the Clyde platform in the UK sector of the North Sea. TRK is a plume type model which uses a particle tracking technique with a random walk component to simulate the dispersion. This method provides detailed information about the plume by tracking many thousands of particles simultaneously, but the model can be computationally intensive. Like CORMIX, TRK considers the wind induced additional mixing in far field spreading. One of the main drawbacks of TRK is its constant diffusion coefficient.

Although they were only used for sewage discharges and have not been used for produced water discharges before, the OMZA (Huang & Fergen, 1996) and VISJET (Lee & Chu, 2003) may also be used to analyze the mixing process of produced water. For the near field buoyant jet mixing process, OMZA uses a three-rank jet classification concept and an all-regime prediction method to predict behaviors. For the far field plume mixing process, OMZA uses a model that includes both buoyant spreading and turbulent diffusion to predict far field dilution. For the transition between the near field and far field, OMZA uses a modified control volume model to

connect the near field and far field. VISJET is a general interactive computer modeling system that predicts the impact of an effluent discharge into the water environment. The model is based on the Lagragian model JETLAG, and it provides 3D flow visualization of the predicted path and mixing of an arbitrarily inclined buoyant plume in moving receiving water which may be density-stratified. It has been validated against a number of laboratory and field measurements. The VISJET model only describes the near field mixing and lacks a far field regime.

1.4 PROBLEMS ASSOCIATED WITH EXISTING APPROACHES

There are several limitations of these existing models. For those models specifically developed for produced water discharges (e.g., OOC, PROTEUS, PROVANN) and some general environmental discharge models (e.g., PLUMES), none of them considered the boundary (for example, the sea surface) interaction process, which provides a transition between the buoyant jet mixing in the near field and buoyant spreading in the far field. Although the CORMIX and OZMA included the boundary interaction, they did not consider the effects of ocean surface waves on initial mixing and they are not suitable for long term prediction because these models did not consider the diurnal changes in current strength and direction, diurnal and seasonal changes in density stratification of ambient seawater, and the changes of discharge rate. Without the consideration of these parameters, the re-entrainment of pollutants and change of plume direction cannot be modeled.

The PROTEUS and PROVANN have a particle tracking algorithm which enables their application in long term time dependent analysis. However, they employed

separate near and far field models and ignored the interaction between them. For example, near field models implicitly assume that the plume mixes with clean ambient water and ignore the return of pollution from far field to near field. Therefore, research on the development and testing of a better approach for optimal coupling of the near and far field models becomes necessary.

Another problem with existing models is that they (except the OZMA model) did not provide uncertainty analysis. A probabilistic based approach has been proposed by Mukhtasor (2001) to deal with the inherent uncertainty in the mixing processes between the produced water and the ambient sea water. The model used by Mukhtasor (2001) and the OZMA are only applicable for uniform ambient conditions and can only be used for positively discharged jets. There is a need to expand the Mukhtasor's model and the OZMA model to more discharge conditions.

1.5 OBJECTIVE AND OUTLINE OF RESEARCH

This study has two major components: numerical modeling and experimental study. These two components have the following more specific objectives:

1. Develop a probabilistic based steady state model which is applicable for stratified environment with the consideration of boundary interaction and wave effects;
2. Validate the model using laboratory experimental data;
3. Couple the steady state model with non-steady state model to study the far field long term dispersion;

4. Conduct field experiments using an Autonomous Underwater Vehicle (AUV) to validate the model.

This thesis consists of eight chapters. This chapter describes the background and objectives of the study. The physical nature of the mixing process is presented in Chapter 2. Chapter 3 proposes a steady state mixing model in both deterministic and probabilistic formats. The near field model is validated in Chapter 4 with existing laboratory data. A relatively large scale experiment on vertically discharged buoyant jets is also described in Chapter 4. In Chapter 5, a hypothetical case study using the proposed model is presented. Chapter 6 study the coupling of steady state model with non-steady state model. The field experiments using an AUV are described in Chapter 7. Conclusions and recommendations are presented in the Chapter 8.

2. FUNDAMENTALS OF MATHEMATICAL MODELING

2.1 BUOYANT JETS

Discharges of liquid effluents into ambient waters are classified as pure jet, pure plume, and buoyant jet depending on the source momentum (M) and buoyancy (B). A pure jet is one that exhibits momentum flux but no buoyancy flux. A pure plume experiences only buoyancy flux. Most discharges have both momentum and buoyancy and are termed buoyant jets. Initially, a buoyant jet is dominated mostly by the source momentum and geometry and it behaves like a jet. After some distance, the buoyancy becomes dominate and it behaves like a plume. An illustration of pure jet, buoyant jet and pure plume is given in Figure 3.

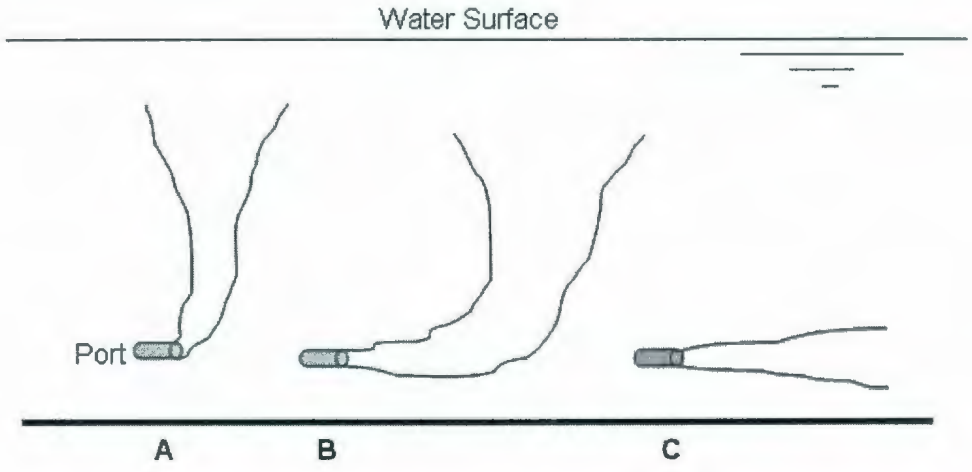

Figure 3. Discharges into the environment A) pure plume; B) buoyant jet; C) pure jet (modified from Tsanis and Valeo 1994).

For a round buoyant jet the initial volume flux, Q, momentum flux, M, and buoyancy flux, B, are

$$Q = U_j A = \frac{\pi D^2}{4} U_j \tag{1}$$

$$M = Q \cdot U_j = \frac{\pi D^2}{4} U_j^2 \tag{2}$$

$$B = Q\left(\frac{\rho_a - \rho_j}{\rho_a}\right) g = Qg' \tag{3}$$

where A is the port area, D is the port diameter, U_j is the discharge velocity, ρ_a is the density of ambient water, ρ_j is the density of the jet, g is the acceleration of gravity, and g' is the reduced gravity defined as $g(\rho_a - \rho_j)/\rho_a$.

The discharge of a round buoyant jet with a vertical angle ϕ with respect to the horizontal plane and a horizontal angle θ with respect to the x-axis is illustrated in Figure 4. The initial jet momentum and buoyancy induced momentum produce a shear flow; fluid is entrained into the jet by shear entrainment. In the presence of ambient current u_a, the vortex flow of the jet produces additional entrainment (forced entrainment). The relative importance of inertial force, buoyancy force and ambient current is characterized by two non-dimensional parameters: the velocity ratio K and densimetric Froude number F_r (as shown in Equations 4 and 5).

$$K = U_j / u_a \tag{4}$$

$$F_r = U_j \Big/ \sqrt{g \frac{(\rho_a - \rho_0)}{\rho_a} D} \tag{5}$$

where ρ_0 is the initial density of the jet.

As the ambient fluid is entrained into the buoyant jet, the initial concentration of the pollutant C_0 is affected (in most cases, reduced) by the entrained ambient fluid. Therefore, a dilution, S, of the pollutant is achieved and it is defined as

$$S = \frac{C_0 - C_a}{C - C_a} \tag{6}$$

where C_a is the pollutant concentration in ambient fluid, and C is the pollutant concentration of the jet. In case of zero ambient concentration, Equation (6) becomes

$$S = \frac{C_0}{C} \tag{7}$$

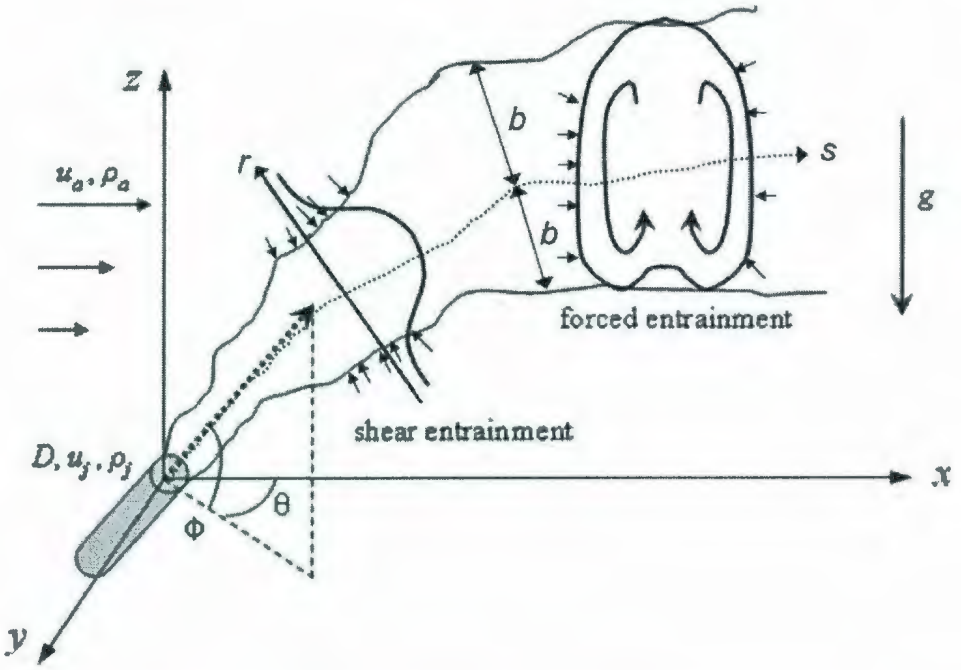

Figure 4. An arbitrary turbulent round jet discharged into a current.

2.2 MATHEMATICAL DESCRIPTION OF THE MIXING PROCESSES

2.2.1 Initial Mixing

Mathematical modeling of the initial mixing of buoyant jets fall into three main categories: integral type, length scale type, and turbulence type. The integral model category can be further subdivided into two sub-categories: Eulerian model and Lagrangian model. An Eulerian model determines the amount of ambient fluid entrained to the jet and hence the dilution ratio by solving a set of ordinary differential Equations. The Equations dictate the rate of change of various parameters with respect to the centerline trajectory *s*, of the buoyant jet. A Lagrangian model follows the jet element throughout its course with respect to time. Changes of various parameters are determined in adjacent elements at each time increment.

2.2.1.1 Eulerian formulation

The following assumptions as stated by Tsanis and Valeo (1994) need to be made for the mathematical modeling of buoyant jets:

- flow is steady and incompressible;
- pressure is hydrostatic;
- plume is fully turbulent and axisymmetric;
- turbulent diffusion dominates and is significant only in the radial direction;
- velocity and concentration are distributed about the centerline;
- density differences between the jet and the ambient are small compared to the density of the fluid.

For the discharge in Figure 4 with a initial volume flux Q_0, momentum flux M_0, buoyancy flux B_0, and mass flux QC_0, the following bulk variables for total volume flux Q, momentum flux M, buoyancy flux B, and pollutant mass flux QC are obtained through cross-sectional integration (Jirka 2004)

$$Q = 2\pi \int_0^{Rj} Urdr = \pi b^2 (U_c + 2u_a \cos\phi \cos\theta) \tag{8}$$

$$M = 2\pi \int_0^{Rj} U^2 rdr = \pi \frac{b^2}{2} (U_c + 2u_a \cos\phi \cos\theta)^2 \tag{9}$$

$$B = 2\pi \int_0^{Rj} Ug' rdr = \pi \frac{b^2}{2} (U_c + 2u_a \cos\phi \cos\theta) g_c' \tag{10}$$

$$QC = 2\pi \int_0^{Rj} C \cdot Urdr = \pi b^2 (U_c \frac{\lambda^2}{1+\lambda^2} + \lambda^2 u_a \cos\phi \cos\theta) C_c \tag{11}$$

where r is radial distance in local cylindrical coordinate system, Rj is a integration limit ($Rj \rightarrow \infty$), U is the jet velocity and subscript c denotes centerline values, b is the jet width and λ describes a dispersion ratio for the scalar quantities.

For a jet element of length ds centered on the trajectory, the conservation principles for volume, momentum, and mass lead to the following Equations (Jirka, 2004)

voulume change $$\frac{dQ}{ds} = E \tag{12}$$

x-momemtum change $$\frac{d}{ds}(M \cos\phi \cos\theta) = Eu_a + F_D \sqrt{1 - \cos^2\phi \cos^2\theta} \tag{13}$$

y-momemtum change $$\frac{d}{ds}(M \cos\phi \sin\theta) = -F_D \frac{\cos^2\phi \sin\phi \sin\theta}{\sqrt{1 - \cos^2\phi \cos^2\theta}} \tag{14}$$

z-momemtum change $$\frac{d}{ds}(M\sin\theta)=\pi\lambda^2 b^2 g'_c-F_D\frac{\sin\phi\cos\phi\cos\theta}{\sqrt{1-\cos^2\phi\cos^2\theta}} \quad (15)$$

buoyancy change $$\frac{dB}{ds}=Q\frac{d\rho_a}{dz}g\sin\phi \quad (16)$$

pollutant mass flux change $$\frac{dQC}{ds}=0 \quad (17)$$

jet trajectory $$\frac{dx}{ds}=\cos\phi\cos\theta,\ \frac{dy}{ds}=\cos\phi\sin\theta,\ \frac{dz}{ds}=\sin\phi \quad (18)$$

where E is the entrainment rate and F_D is the ambient drag force acting on the jet element. The turbulence closure of the above formulations is obtained by specification of E and F_D. The total entrainment E is the sum of shear entrainment and vortex entrainment (as shown in Figure 5)

$$E=2\pi bU_c\left(\alpha_1+\alpha_2\frac{\sin\phi}{F_L^{\ 2}}+\alpha_3\frac{u_a\cos\phi\cos\theta}{U_c+u_a}\right)+ 2\pi bu_a\sqrt{1-\cos^2\phi\cos^2\theta}\,\alpha_4\left|\cos\phi\cos\theta\right| \quad (19)$$

where U_c is the jet centerline velocity, α_1 to α_4 are entrainment coefficients, F_L is the local Froude number defined as $F_L=U_c/\sqrt{g'_c b}$. The jet drag force is defined as (Jirka, 2004)

$$F_D=C_D\left(2\sqrt{2}b\right)\left(\frac{u_a^2(1-\cos^2\phi\cos^2\theta)}{2}\right) \quad (20)$$

where C_D is a drag coefficient.

The Equations (12) to (20) can be solved using a fourth-order Runge-Kutta method with specified initial conditions.

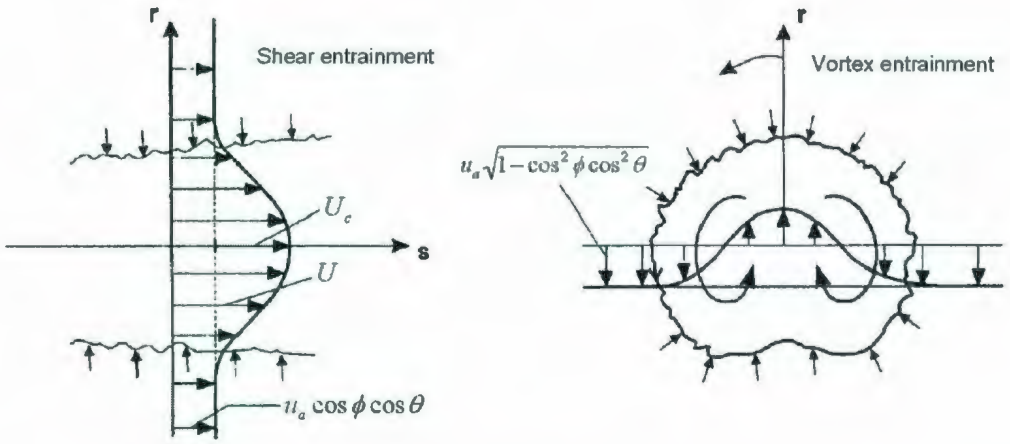

Figure 5. Illustration of the two entrainment mechanisms (modified from Jirka, 2004)

2.2.1.2 Lagrangian formulation

In the Lagrangian framework, the unknown jet properties (e.g., trajectory, radius, etc.) are analyzed by tracing a sequential series of jet elements (Figure 6). Each jet element can be treated as a section of a bent cone and the change of element properties is examined at discrete time steps Δt.

The entrainment of the ambient fluids into the jet element is determined at each time step. Based on the increase in element mass, the momentum, energy, and tracer mass conservation Equations can be solved in their integral form to give the velocity, density, and concentration at the next time step (Lee & Chu, 2003).

At the k^{th} step consider a jet element located at (x_k, y_k, z_k) with horizontal velocity (u_k, v_k), and vertical velocity w_k. The local velocity of the jet is $V_k = \sqrt{u_k^2 + v_k^2 + w_k^2}$. The thickness of the jet over length h_k is defined as proportional to the magnitude of the local velocity V_k, $h_k \propto V_k$. The angle of the jet relative to the horizontal plane is

denoted by ϕ_k, and angle of the jet relative to the x-axis is denoted by θ_k. The temperature, salinity and density are denoted by T_k, S_k, ρ_k. The mass of the jet element is given by $M_k = \rho_k \pi b_k^2 h_k$.

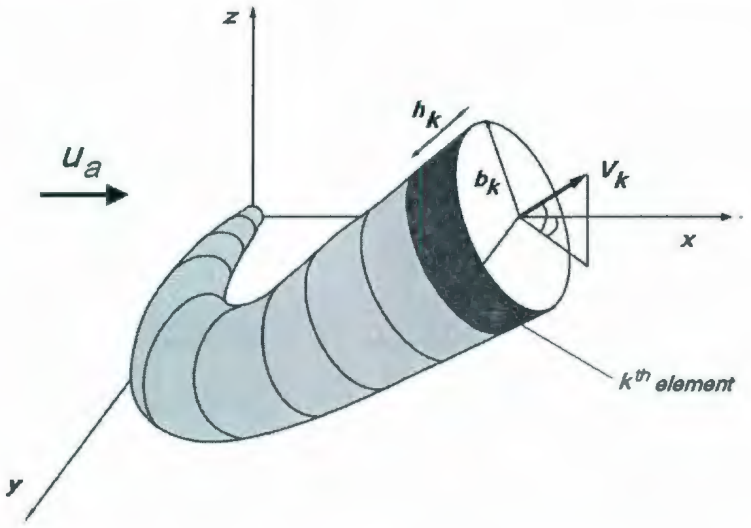

Figure 6. Schematic diagram of jet trajectory traced out by Lagrangian plume elements (modified from Lee & Chu, 2003).

Given the increase in mass, ΔM_k, due to entrainment of ambient fluids, the properties of the jet element at the next step k+1 are obtained by applying the conservation Equations to the discrete element (Lee & Chu, 2003).

- Mass

$$M_{k+1} = M_k + \Delta M_k \tag{21}$$

$$M_{k+1} = \rho_{k+1} \pi b_{k+1}^2 h_{k+1} \tag{22}$$

- Salinity, Temperature, Density and Concentration

$$S_{k+1} = \frac{M_k S_k + \Delta M_k S_a}{M_{k+1}} \tag{23}$$

$$T_{k+1} = \frac{M_k T_k + \Delta M_k T_a}{M_{k+1}} \tag{24}$$

$$\rho_{k+1} = \rho(S_{k+1}, T_{k+1}) \tag{25}$$

$$C_{k+1} = \frac{M_k C_k + \Delta M_k C_a}{M_{k+1}} \tag{26}$$

- Horizontal momentum

$$u_{k+1} = \frac{M_k u_k + \Delta M_k U_a}{M_{k+1}} \tag{27}$$

$$v_{k+1} = \frac{M_k v_k}{M_{k+1}} \tag{28}$$

- Vertical momentum

$$w_{k+1} = \frac{M_k w_k + M_{k+1}\left(\frac{\Delta\rho}{\rho}\right)_{k+1} g\Delta t}{M_{k+1}} \tag{29}$$

$$HVEL_{k+1} = \left(u_{k+1}^2 + v_{k+1}^2\right)^{1/2} \tag{30}$$

$$V_{k+1} = \left(u_{k+1}^2 + v_{k+1}^2 + w_{k+1}^2\right)^{1/2} \tag{31}$$

- Thickness/radius

$$h_{k+1} = \frac{V_{k+1}}{V_k} h_k \tag{32}$$

$$b_{k+1} = \left(\frac{M_{k+1}}{\rho_{k+1} \pi h_{k+1}}\right)^{1/2} \tag{33}$$

- Jet orientation

$$\sin\phi_{k+1} = \left(\frac{w}{V}\right)_{k+1} \tag{34}$$

$$\cos\phi_{k+1} = \left(\frac{HVEL}{V}\right)_{k+1} \tag{35}$$

$$\sin\theta_{k+1} = \left(\frac{V}{HVEL}\right)_{k+1} \tag{36}$$

$$\cos\theta_{k+1} = \left(\frac{u}{HVEL}\right)_{k+1} \tag{37}$$

- Location

$$x_{k+1} = x_k + u_{k+1}\Delta t \tag{38}$$

$$y_{k+1} = y_k + v_{k+1}\Delta t \tag{39}$$

$$z_{k+1} = z_k + w_{k+1}\Delta t \tag{40}$$

$$\Delta s_{k+1} = V_{k+1}\Delta t \tag{41}$$

- Initial Condition

$$(u, v, w)_0 = (V_0\cos\phi_0\cos\theta_0, V_0\cos\phi_0\sin\theta_0, V_0\sin\phi_0) \tag{42}$$

$$(b, h)_0 = (0.5D, 0.5D) \tag{43}$$

$$(S, T, \rho, C)_0 = (S_0, T_0, \rho_0, C_0) \tag{44}$$

$$(\Delta t)_0 = 0.1\times\frac{h_0}{V_0} \tag{45}$$

The closure of above Equations is obtained by specifying the amount of ambient fluid entrained at each step ΔM which is computed as a function of two components: the shear entrainment due to the relative velocity between the jet element and the

ambient velocity in the direction of the jet axis, ΔM_s, and the vortex (forced) entrainment due to the ambient crossflow, ΔM_v.

The shear entrainment, ΔM_s, at the time step k is defined as

$$\Delta M_s = 2\pi\alpha_s b_k h_k \Delta U \Delta t \tag{46}$$

where V_k is the jet velocity, ΔU is the relative jet velocity in the direction of the jet axis, b_k, h_k are are radius and thickness of the jet element, F_L is the local jet densimetric Froude number and α_s is the shear entrainment coefficient defined as

$$\alpha_s = \sqrt{2}\left(0.057 + 0.554\frac{\sin\phi_k}{F_L^2}\right)\left(\frac{2V_k}{\Delta U + V_k}\right) \tag{47}$$

The vortex entrainment can be modeled using the Projected Area Entrainment (PAE) hypothesis

$$\begin{aligned}\Delta M_v = \rho_a U_a [&2b_k h_k \sqrt{1-\cos^2\phi_k \cos^2\theta_k} \\ &+ \pi b_k \Delta b_k \cos\phi_k \cos\theta_k \\ &+ \frac{\pi b_k^2}{2}\Delta(\cos\phi_k \cos\theta_k)]\Delta t\end{aligned} \tag{48}$$

The total entrainment is a function of shear entrainment and vortex entrainment and it is given as

$$\Delta M = \Delta M_s \frac{\pi - \varphi_k}{\pi} + \Delta M_v \sin\varphi_k \tag{49}$$

where φ_k is a separation angle which delineates the relative importance of shear and vortex entrainment.

2.2.1.3 Length Scale formulation

Length scales describe the relative importance of discharge momentum flux, buoyancy flux, ambient crossflow and density stratification in controlling flow behavior (Jirka and Akar, 1991). Length scale models are extensions of dimensional analysis and use semi-empirical Equations derived from experiments. These empirical Equations relate a dilution achieved and the height of rise of the plume or jet to a function of one or a number of length scales.

Considering a buoyant jet discharge into a stratified environment with crossflow, any dependent variable ψ, such as a minimum dilution or center line velocity, can be characterized as a function of several jet and ambient flow variables

$$\psi = f(Q, M, B, U_a, \varepsilon_D, z) \tag{50}$$

Where ε_D is the stratification parameter and Z is the depth of water above discharge.

Through dimensional analysis, Wright (1977a) obtained seven length scales and they are listed in Table 1.

Table 1. Definition of length scales associated with buoyant jets in a stratified crossflow.

Jet length Scales	Crossflow Length Scales	Stratification lengscales
$L_Q = Q/M^{1/2}$	$L_m = M^{1/2}/U_a$	$L_m' = (M/\varepsilon_D)^{1/4}$
$L_M = M^{3/4}/B^{1/2}$	$L_b = B/U_a^3$	$L_b' = B^{1/4}/\varepsilon_D^{3/8}$
		$L_a = U_a/\varepsilon_D^{1/2}$

Discharge length scale $L_Q = Q/M^{1/2}$ relates volume flux to momentum flux. For a round jet, $L_Q = \sqrt{(\pi/4)}D$ is proportional to the diameter of the orifice. For distances

less than L_Q, the source geometry will have a significant effect on the flow behavior and for distances greater than L_Q, the jet momentum or buoyancy will control the flow behavior.

The presence of a crossflow U_a will deflect the jet. The jet/crossflow length scale $L_m = M^{1/2}/U_a$ is the distance to the position where the jet becomes strongly deflected by the ambient flow.

Similarly, the plume/crossflow length scale $L_b = B/U_a^3$ is the distance to the position where the plume becomes strongly deflected by the ambient flow. For distances less than L_b, the initial plume buoyancy will dominate and for distances greater than L_b, the ambient velocity will have a strong influence on the plume behavior.

Jet/plume length scale $L_M = M^{3/4}/B^{1/2}$ is the distance at which the transition from jet behavior to plume behavior takes place in a stagnant uniform environment.

Jet/stratification length scale $L_m' = (M/\varepsilon_D)^{1/4}$ is the distance at which the jet becomes strongly affected by the stratification, in other words, the height of water at which the flow becomes trapped.

Similar to the jet/stratification length scale L_m', the Plume/Stratification length scale $L_b' = B^{1/4}/\varepsilon_D^{3/8}$ is the distance at which the plume becomes strongly affected by the stratification.

L_a is a length scale that relates the ambient density stratification and crossflow velocity.

Among the seven length scales given above, there are only five independent length scales. Any other two length scales can be formed from an algebraic reasoning.

The Equation (50) can be rewritten using of length scales. One possible relationship is

$$\psi^* = f(\frac{Z}{L_b}, \frac{L_Q}{L_b}, \frac{L_m}{L_b}, \frac{L_b'}{L_b}) \tag{51}$$

where ψ^* is a dimensionless form of ψ. The reasoning results of Equation (51) by Wright (1977a, 1984) are summarized in Table 2 and Table 3. The constants C_1 to C_8 and k_1 to k_{12} need to be determined experimentally.

Table 2. Trajectory and dilution relations (Wright, 1977a).

Flow Regime	Trajectory relation	Dilution relation
Momentum-dominated near field	$Z/l_m = C_1 (x/l_m)^{1/2}$	$SQU_a/M = C_5 (Z/l_m)$
Momentum-dominated far field	$Z/l_m = C_2 (x/l_m)^{1/3}$	$SQU_a/M = C_6 (Z/l_m)^2$
Buoyancy-dominated near field	$Z/l_b = C_3 (x/l_b)^{3/4}$	$g'B/U_a^5 = C_7 (Z/l_m)^{-5/3}$
Buoyancy-dominated near field	$Z/l_b = C_4 (x/l_b)^{2/3}$	$g'B/U_a^5 = C_8 (Z/l_m)^{-2}$

Table 3. Height-of-rise and dilution relations for buoyant jets in stratified crossflow (Wright, 1984).

	Height of rise relation		Dilution relation
	maximum	equilibrium	
Momentum-dominated near field	$Z_m/l_m = k_1(l_a/l_m)^{1/2}$	$Z_e/l_m = k_2(l_a/l_m)^{1/2}$	$SQ/U_a l_m^2 = k_9 (Z_m/l_m)$
Momentum-dominated far field	$Z_m/l_m = k_3(l_a/l_m)^{1/3}$	$Z_e/l_m = k_4(l_a/l_m)^{1/3}$	$SQ/U_a l_m^2 = k_{10}(Z_m/l_m)^2$
Buoyancy-dominated near field	$Z_m/l_b = k_5(l_a/l_b)^{3/4}$	$Z_e/l_m = k_6(l_a/l_b)^{3/4}$	$SQ/U_a l_b^2 = k_{11}(Z_m/l_b)^{5/3}$
Buoyancy-dominated near field	$Z_m/l_b = k_7(l_a/l_b)^{2/3}$	$Z_e/l_m = k_8(l_a/l_b)^{2/3}$	$SQ/U_a l_b^2 = k_{12}(Z_m/l_b)^2$

As shown in Table 2 and Table 3, asymptotic approach must be used in the length scale model formulation. Unlike the integral approach, there is no uniform length scale model solution for various flow behaviors. As indicated by Tsanis and Valeo

(1994), length scale models have over taken integral models in popularity as they are unsophisticated.

2.2.1.4 Turbulence formulation

Generally, three methods can be used to simulate the fluid flow problems numerically: Direct Numerical Simulation (DNS), Large Eddy Simulation (LES), and Reynolds Averaged Navier-Stokes Simulation (RANS).

The direct numerical simulation solves the Equation of motion for a fluid resolving all scales of motion. As smallest scales are typically bounded by molecular length scales and largest scales are bounded by the physical size of the problem, the DNS requires a vast amount of computation to resolve all scales of motion, therefore, it is limited to very simple geometries with low velocities and small physical dimensions.

The large eddy simulation assumes that the small scales of motion are similar across a wide range of flows, and thus only resolves the large scales of the flow which depend on the geometry and flow conditions.

The Reynolds averaged Navier-Stokes simulation further simplifies the Equation of motion by time-averaging over a time period which is much longer than the typical turbulent fluctuations (Yuan, 1997). Although the time-averaging process in RANS filters all the short time scales, it introduces additional variables into the system of Equations. These variables cannot be explicitly computed from known quantities and must be modeled. The RANS approach is summarized below.

Turbulent flows must simultaneously satisfy conservation of mass and momentum. Thus, the incompressible continuity and Navier-Stokes Equations can be solved for the instantaneous turbulent flow field. The continuity (mass conservation) Equation is (Rodi, 1980)

$$\frac{\partial U_i}{\partial x_i} = 0 \tag{52}$$

The Navier-Stokes (momentum conservation) Equation is

$$\frac{\partial U_i}{\partial t} + U_j \frac{\partial U_i}{\partial x_j} = -\frac{1}{\rho_{ref}} \frac{\partial P}{\partial x_i} + \nu \frac{\partial^2 U_i}{\partial x_j \partial x_j} + g_i \frac{\rho - \rho_{ref}}{\rho_{ref}} \tag{53}$$

The concentration conservation is

$$\frac{\partial C}{\partial t} + U_i \frac{\partial C}{\partial x_j} = \varsigma \frac{\partial^2 U_i}{\partial x_j \partial x_j} + S_{source} \tag{54}$$

where U_i is the instantaneous velocity component in the direction x_i, P is the instantaneous pressure, and C is the instantaneous concentration, S_{source} is a volumetric source term, ν and ς are the molecular (kinematic) viscosity and diffusivity respectively, g_i is the gravitational acceleration in the direction of x_i, ρ_{ref} is the reference density and ρ is the local density.

The instantaneous values of U_i, P and C can be separated into mean and fluctuating quantities

$$U_i = \overline{U_i} + u_i, \; P = \overline{P} + p, \; C = \overline{C} + c \tag{55}$$

where the mean quantities (overbar) are defined as

$$\overline{U_i} = \frac{1}{t_2 - t_1}\int_{t_1}^{t_2} U_i dt,\ \overline{P} = \frac{1}{t_2 - t_1}\int_{t_1}^{t_2} P dt,\ \overline{C} = \frac{1}{t_2 - t_1}\int_{t_1}^{t_2} C dt \tag{56}$$

By introducing Equation (55) and (56) into (52) to (54), the following mean flow Equations are obtained

Continuity: $$\frac{\partial \overline{U_i}}{\partial x_i} = 0 \tag{57}$$

Momentum: $$\frac{\partial \overline{U_i}}{\partial t} + \overline{U_j}\frac{\partial \overline{U_i}}{\partial x_j} = -\frac{1}{\rho_{ref}}\frac{\partial \overline{P}}{\partial x_i} + \frac{\partial}{\partial x_j}\left(\nu \frac{\partial \overline{U_i}}{\partial x_j} - \overline{u_i u_j}\right) + g_i \frac{\rho - \rho_{ref}}{\rho_{ref}} \tag{58}$$

Concentration: $$\frac{\partial \overline{C}}{\partial t} + \overline{U_i}\frac{\partial \overline{C}}{\partial x_j} = \frac{\partial^2}{\partial x_j}\left(\varsigma \frac{\partial \overline{C}}{\partial x_i} - \overline{u_i c}\right) + S_{source} \tag{59}$$

Both Equations (52) to (54) and (57) to (59) are exact Equations but (57) to (59) are not closed due to the introduction of unknown correlation between fluctuating velocities, $\overline{u_i u_j}$, and between velocity and concentration fluctuations $\overline{u_i c}$. Equations (57) to (59) can be solved for the mean values of velocity, pressure, and concentration only when the turbulence correlations $\overline{u_i u_j}$ and $\overline{u_i c}$ can be determined.

As described earlier, the nonlinear terms $\overline{u_i u_j}$ and $\overline{u_i c}$ cannot be explicitly computed and must be modeled. The development of models to determine these nonlinear terms has been a subject over the past 60 years. The oldest method for turbulent modeling is the eddy viscosity concept and eddy-diffusivity concept (Rodi, 1980). The eddy viscosity concept assumes that turbulent stresses are proportional to the mean velocity gradient as

$$-\overline{u_i u_j} = \nu_t \left(\frac{\partial U_i}{\partial x_j} + \frac{\partial U_j}{\partial x_i} \right) - \frac{2}{3} k \delta_{ij} \tag{60}$$

where ν_t is the turbulent or eddy viscosity which, in contrast to the molecular viscosity ν, is not a fluid property but depends on the state of the turbulence, δ_{ij} is the Kronecker delta, k is the kinetic energy of the fluctuating motion. Similar to the momentum transport $\overline{u_i u_j}$, the mass transport is described by

$$-\overline{u_i c} = \Gamma \frac{\partial C}{\partial x_i} \tag{61}$$

where Γ is the turbulent diffusivity of mass.

To model the turbulence, several models were developed which do not make the use of the above turbulent viscosity/diffusivity concept but employ different transport Equations for the turbulent momentum and mass fluxes. According to the number of transport Equations used for turbulence quantities, the turbulence model can be classified as: zero Equation, one Equation, and two Equations model. For buoyant jet problems, the two Equations $k - \varepsilon$ model is widely used (Rodi, 1980).

2.2.2 Intermediate Mixing

The formulations described in section 2.2.1 assume that the discharge is in "infinitely" deep water, which means the plume behavior is not affected by the boundaries such as water surface, seabed, or pycnocline (a layer across which there is a rapid change of water density with depth). However, the majority of the environmental applications involve discharges into ambient water of finite depths in which a bounding surface or bottom serves to re-direct the impinging buoyant jet,

discharges into a stratified environment in which the pycnocline serves to re-direct the impinging buoyant jet.

2.2.2.1 Discharge into Stagnant Environment

For a round buoyant jet discharged into a uniform stagnant environment (as shown in Figure 7), Wright et al. (1991) and Ulasir and Wright (2003) studied the surface effects by dividing the plume into four sub-zones: 1) submerged jet zone, 2) surface impingement region, 3) inter hydraulic jump zone (highlighted area in Figure 7), and 4) far field buoyant spreading zone.

Dimensional analysis yields the following expression for the dilution

$$\frac{SL_Q}{h} = f\left(\frac{L_M}{h_{water}}\right) \tag{62}$$

where the S is the dilution, and h_{water} is the total water depth. For the submerged region, the empirical expression of Equation (62) is given by Kotsovinos (1978) as

$$\frac{SL_Q}{Z} = C_9\left(1 + C_{10}\left(\frac{Z}{L_M}\right)^2\right)^{1/3} \tag{63}$$

where $C_9 \approx 0.29$ and $C_{10} \approx 0.16$ are experimentally determined constants, Z is the water depth above discharge. For the surface impinging region, a similar formula (as shown in Equation 64) was derived by Wright et al. (1991) to describe the surface dilution

$$\frac{SL_Q}{h} = 0.77\left(\frac{h_{water}}{L_M}\right)^{2/3} \tag{64}$$

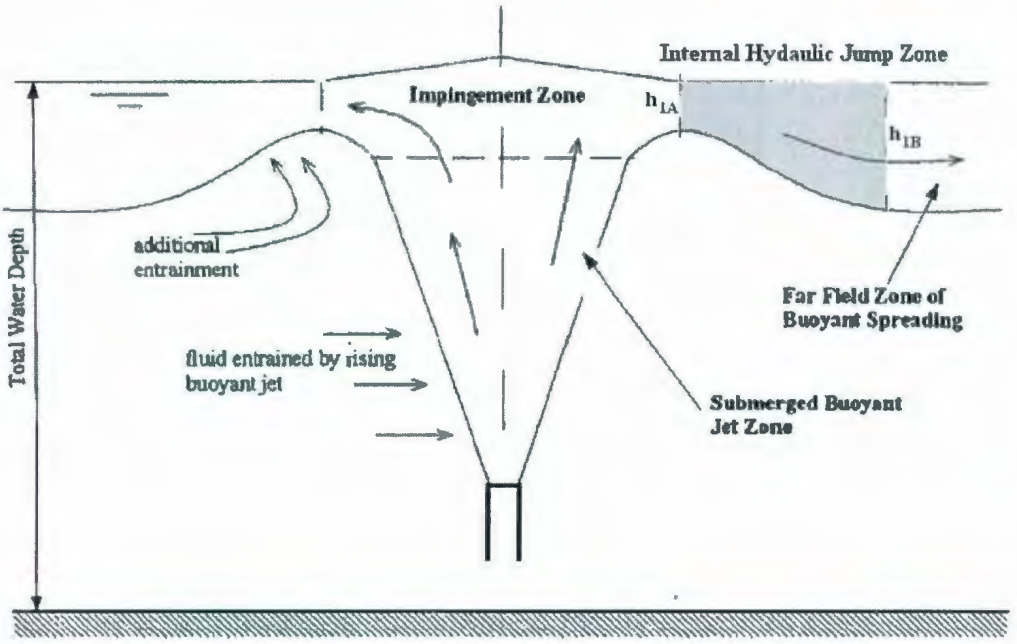

Figure 7. Definition sketch of submerged round buoyant jet impinging on a free surface (Modified from Ulasir and Wright, 2003).

The most significant effect of boundaries on the dilution is the additional entrainment that occurs in the internal hydraulic jump zone. The internal hydraulic jump is the jump-like flow transition at the interfaces of two moving fluids of different densities. Figure 8 gives a schematic description of the internal hydraulic jump. The internal hydraulic jump zone starts from section A, which is the end of the impingement zone, and extends all the way to section B, at which point the buoyancy force stabilizes the flow and confines it to the vicinity of the bounding surface. The terms h_1, h_2, v_1, and v_2 refer to local layer thickness and velocity terms in the respective layers at an arbitrary radial distance from the vertical buoyant jet axis.

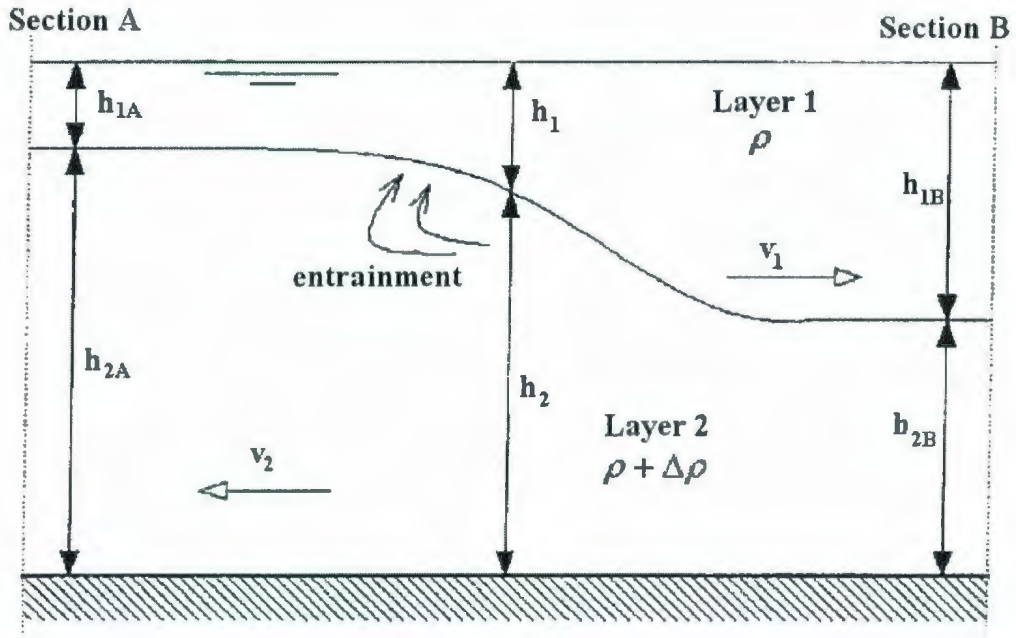

Figure 8. Schematic description of the internal hydraulic jump zone.

The stability of the flow can be determined by a composite Froude number, $F_{r1}^2 + F_{r2}^2$, for the two layers. If the composite Froude number is greater than or equal to one, no wave can propagate upstream (Ulasir and Wright, 2003). Empirical relations based on the experiments by Wright et al. (1991) can be used to describe the dilution at the end of the internal hydraulic jump zone

$$\frac{S_{avg} L_Q}{h_{water}} \approx 0.7 \tag{65}$$

and

$$\frac{S_{\min} L_Q}{h_{water}} \approx 0.5 \tag{66}$$

where S_{ave} is the average dilution, and S_{min} is the minimum dilution.

It was concluded by Wright et al. (1991) and Ulasir and Wright (2003) that the dilution may be increased up to 5-fold in the presence of a free boundary. The last zone, buoyant surface spreading is considered as a far field mixing mechanism and will be discussed in section 2.2.3.

2.2.2.2 Discharge into a Flowing Environment

The interaction of a submerged buoyant discharge with boundaries in the presence of a current is illustrated in Figure 9. After the flow impinges on the boundary at an angle θ_{imp}, the plume is redirected and spreads horizontally.

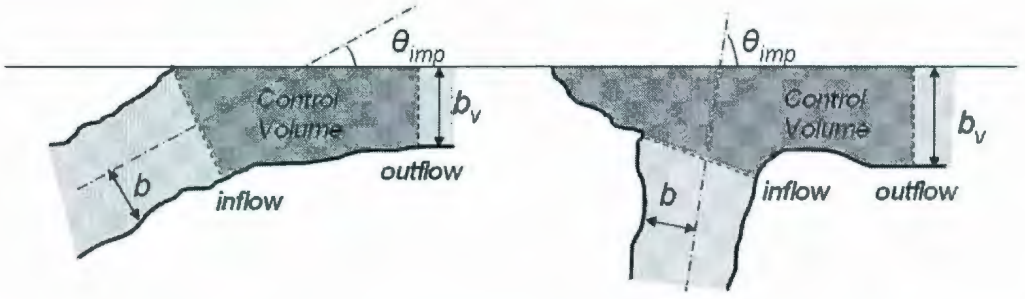

Figure 9. Flow interaction with boundary, near horizontal (left), and near vertical (right).

The control volume concept of Doneker & Jirka (1990) can be used for intermediate mixing. For cross flow dominated cases that are relatively weakly buoyant, the flow is strongly deflected, the flow will impinge on the surface near horizontally with an impingement angle θ_{imp}<45° (Figure 9, left). It was suggested by Doneker & Jirka (1990) that the flow will change from the assumed Gaussian distribution (round jet) at the beginning of the control volume (inflow) to a top-hat distribution (rectangular plume) at the end of the control volume (outflow). The

dilution at the outflow section is about 1.5 to 2.0 times that at the inflow section. By assuming a cross-section aspect ratio for the outflow section of 2:1, the following Equation are obtained

$$S_{outflow} = (1.5 \sim 2.0) S_{inflow} \tag{67}$$

$$b_{v(outflow)} = \sqrt{\frac{S_{outflow} L_m L_b}{2}} \tag{68}$$

where $S_{outflow}$ is the dilution at the end of control volume (outflow section), S_{inflow} is the dilution at the beginning of the control volume (inflow section), $b_{v(outflow)}$ is the plume thickness at the end of the control volume. The plume width at the outflow section is two times $b_{v(outflow)}$.

If the discharge has strong buoyancy or the crossflow is weak, the plume will impinge on the surface near vertically with an impingement angle θ_{imp}>45° (Figure 9, right). In this case, the flow spreads some distance upstream against the current and laterally across the current. The schematic diagram of an upstream intrusion is illustrated in Figure 10.

The plume spreading is determined by the interplay between two forces acting along the boundary: the buoyant spreading force F_b, and the ambient drag force F_D. The buoyant spreading force is defined as

$$F_b = \frac{\rho_{up}}{2} g' h_B^2 \tag{69}$$

where ρ_{up} is the upstream plume density, and the drag force is defined as

$$F_D = 0.5 C_D \rho_a (U_a \sin\theta_{front})^2 h_B \tag{70}$$

where the C_D is a drag coefficient, θ_{front} is a front angle, h_B is the frontal plume height defined as

$$h_B = \frac{C_D}{g'} U_a^2 \tag{71}$$

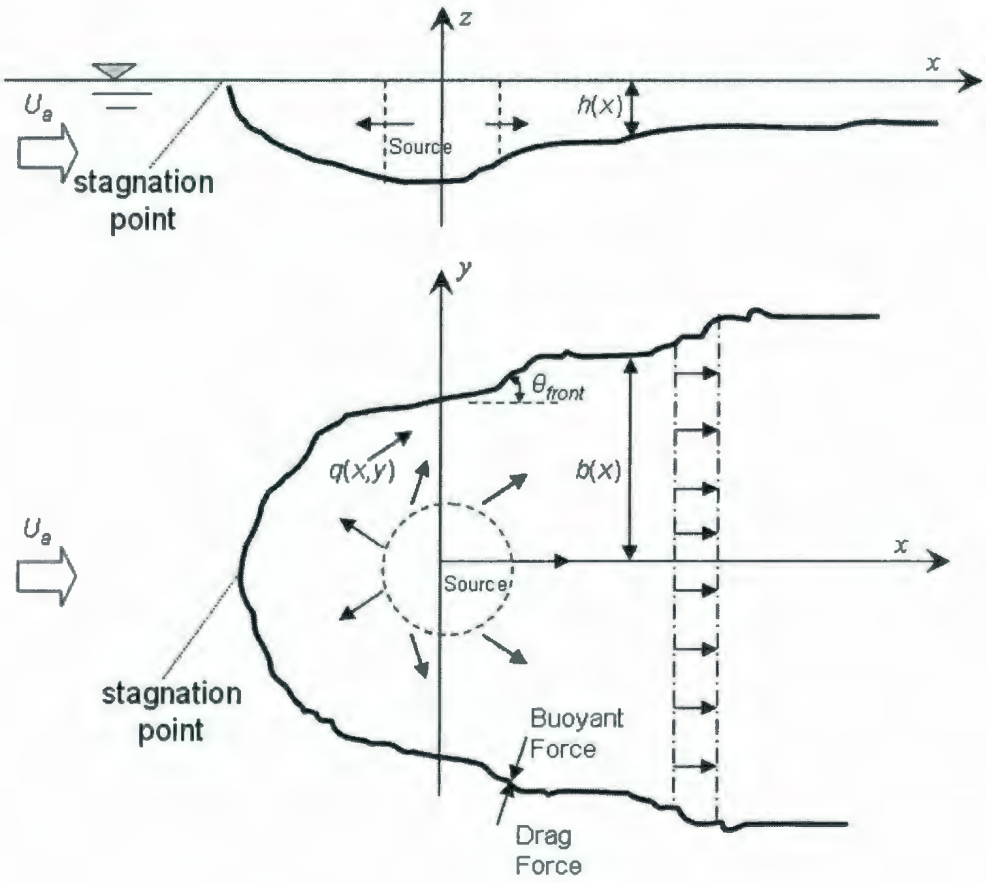

Figure 10. Schematic diagram of upstream intrusion.

Jones et al. (1983) presented a numerical description of the upstream intrusion flow field

$$\frac{\partial(u_{up}h)}{\partial x}+\frac{\partial(v_{up}h)}{\partial y}=w_e \tag{72}$$

$$\frac{\partial(u_{up}{}^2h)}{\partial x}+\frac{\partial(u_{up}v_{up}h)}{\partial y}=-g'h\frac{\partial h}{\partial x}+w_eU_a \tag{73}$$

$$\frac{\partial(u_{up}v_{up}h)}{\partial x}+\frac{\partial(v_{up}{}^2h)}{\partial y}=-g'h\frac{\partial h}{\partial y}+w_eU_a \tag{74}$$

$$\frac{\partial(u_{up}g'h)}{\partial x}+\frac{\partial(v_{up}g'h)}{\partial y}=0 \tag{75}$$

$$\frac{q^2}{2}+g'h=g'h_s \tag{76}$$

where u_{up}, v_{up}, and h are the upstream intrusion plume internal velocities and height respectively, w_e is the entrainment velocity, q is the plume speed $q=\sqrt{u_{up}^2+v_{up}^2}$, h_s is the height at the stagnation point.

The upstream distances L_s can be predicted by Jones et al. (1983) as

$$L_s=1.9L_I \qquad \text{(for weakly near field } \frac{L_I}{L_N}\le 3.3\text{)} \tag{77}$$

$$L_s=4.2L_I\left(L_I/L_N\right)^{-3/2} \qquad \text{(for weakly near field } \frac{L_I}{L_N}>3.3\text{)} \tag{78}$$

where the L_I is an intrusion length scale defined as

$$L_I = Qg'/2\pi C_D U_a^3 \qquad \text{(for surface case)} \qquad (79)$$

$$L_I = Q\sqrt{\varepsilon_D g}/2\pi(3/2C_D)^{1/2}U_a^2 \qquad \text{(for internal case)} \qquad (80)$$

C_D is a drag coefficient, L_N is a length scale representing the turbulent mixing action of the horizontal momentum flux versus stability effect of buoyancy force

$$L_N = M_N^{3/4}/B_N^{1/2} \qquad \text{(for surface case)} \qquad (81)$$

$$L_N = M_N^{1/4}/(\varepsilon_D g)^{1/2} \qquad \text{(for internal case)} \qquad (82)$$

The downstream distance from the impingement center to the end of the control volume, x_D is assumed approximately equal to the distance of the upstream intrusion $x_D \approx L_s$. The plume width at the downstream end L_D=2.6L_s. The parabolic shape of the plume as fitted by Jones et al. (1983) is

$$L(x) = L_D\left(\frac{x+L_s}{x_D+L_s}\right)^{1/2} \qquad (83)$$

2.2.3 Far Field Mixing

The far field mixing of a buoyant jet is largely governed by two mixing mechanisms: buoyant spreading and turbulent diffusion (as shown in Figure 11). Buoyant spreading is a self driven process due to the residual buoyancy contained in the plume while the turbulent diffusion is a passive dispersion process resulting from oceanic eddies. Both buoyant spreading and turbulent diffusion could be important for a distance from an outfall. Buoyancy effects decrease while turbulence effects increase as plume travels.

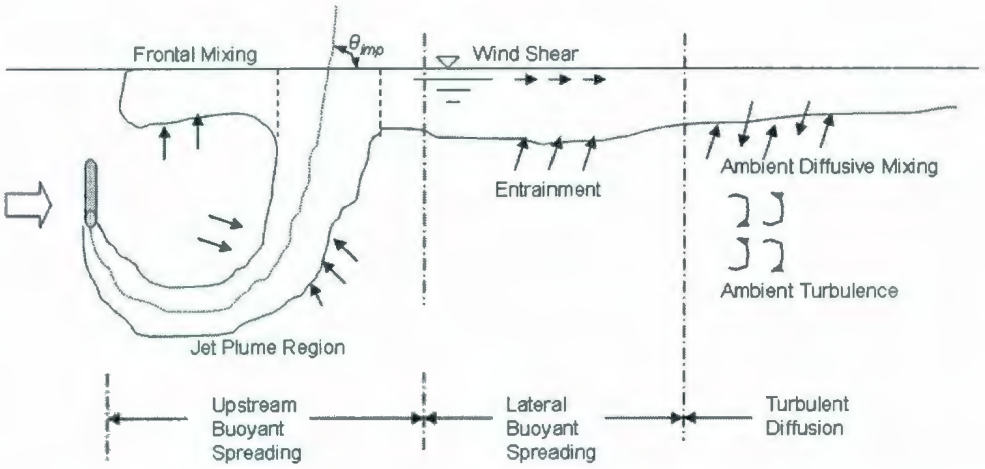

Figure 11. Submerged buoyant jet discharged from a single port into flowing unstratified receiving water.

2.2.3.1 Buoyant Spreading

Through the literature search, very limited research can be found on the subject of buoyant spreading. The study of Akar and Jirka (1994) is summarized below. By assuming that the flow is affected by wind-induced entrainment, interfacial shear entrainment and frontal entrainment, the following conservation Equations were derived

Continuity:
$$U_a \frac{\partial h}{\partial x} + \frac{\partial (v_{lat} h)}{\partial y} = w_{ew} + w_{ei} + w_{ef} \tag{84}$$

Lateral Momentum:
$$v_{lat} \frac{\partial v_{lat}}{\partial y} = -g' \frac{\partial h}{\partial y} + \lambda_i \frac{v_{lat}^2}{h} \tag{85}$$

Buoyancy:
$$U_a \frac{\partial (g' h)}{\partial x} + \frac{\partial (g' v_{lat} h)}{\partial y} = -k_{bl} g' \tag{86}$$

where x is the downstream coordinate, y is the lateral coordinate, v_{lat} is the lateral velocity, h is the plume height, λ_i is the interfacial friction coefficient with values

ranging from 0.002 to 0.005, w_{ew} is the wind-induced entrainment, w_{ei} is the interfacial shear entrainment, and w_{ef} is the frontal entrainment.

The partial differential Equations (84) to (86) can be laterally integrated to get the following ordinary differential Equations

$$\frac{dh}{dx} = \underbrace{\left(\frac{co_1 u_*^3}{U_a}\right)\frac{1}{g'h}}_{\text{wind}} + \underbrace{\left(\frac{co_2 U_a^4}{6}\right)\frac{1}{(g'h)^2}\left(\frac{db}{dx}\right)^5}_{\text{interfacial shear}} + \underbrace{(\beta-1)\frac{h}{b}\frac{db}{dx}}_{\text{frontal}} \tag{87}$$

$$\frac{db}{dx} = \left(\frac{3g'h^2}{3C_D U_a^2 h + 2\lambda_1 U_a^2 b}\right)^{1/2} \tag{88}$$

$$\frac{dg'}{dx} = -\frac{k_{bl}}{U_a}\frac{g'}{h} - \frac{g'}{h}\frac{dh}{dx} - \frac{g'}{b}\frac{db}{dx} \tag{89}$$

where co_1 and co_2 are empirical parameters with values of 0.234 and 0.0015 respectively, β is a constant with a range of 0.15 to 0.25.

In case of the plume interaction with the seabed instead of the surface, similar governing Equations as (84) to (86) can be derived, except for the absence of wind-induced entrainment, and surface heat loss. Furthermore, an additional term which represents the bottom friction needs to be added to the right-hand side of Equation (85).

If the ambient is stratified rather than uniform, the plume will be trapped in a neutral density level before it reaches the surface or bottom. In this case, the lateral momentum Equation becomes

$$\text{Lateral momentum:} \qquad v_{lat}\frac{\partial v_{lat}}{\partial y} = -\frac{1}{2}\varepsilon_D \frac{\partial h^2}{\partial y} + \lambda_i \frac{v_{lat}^2}{h} \tag{90}$$

The wind entrainment and heat loss do not play a role in internal spreading. The partial differential Equations can be integrated to get the following ordinary differential Equations for the internal spreading:

$$\frac{dh}{dx} = \underbrace{\left(\frac{co_2 U_a^4}{6\varepsilon_D^2 h^4}\right)\left(\frac{db}{dx}\right)^5}_{\text{interfacial shear}} + \underbrace{(\beta - 1)\frac{h}{b}\frac{db}{dx}}_{\text{frontal}} \tag{91}$$

$$\frac{db}{dx} = \left(\frac{2\varepsilon_D h^3}{3C_D U_a^2 h + 2\lambda_i U_a^2 b}\right)^{1/2} \tag{92}$$

The above Equations, (87) to (89) and (91), (92), were solved by Arka and Jirka (1994) with a fifth-order Runge-Kutta method with given initial conditions for h, b, and g'.

As the plume travels downstream, the residual buoyancy gradually diminishes and at some point the mixing process becomes dominated by the ambient turbulence. This point is determined by the comparison of local Richardson number R_i (Equation 93) with a critical value R_{ic}. The K_H and K_M are eddy diffusivities for scalar (heat) and momentum, respectively. Once the condition $R_i < R_{ic}$ is attained, the plume is dominated by ambient turbulent diffusion controlled by the horizontal and vertical eddy diffusion coefficients K_y and K_z, respectively.

$$R_i = -\frac{gK_H(d\rho/dz)}{\rho K_M(du/dz)^2} \tag{93}$$

2.2.3.2 Turbulent Diffusion

After all residual buoyancy contained in the plume diminishes, the turbulent diffusion process dominates, which involves both an advective component (transport process) and a diffusion component (mixing process). The advection is the bulk

transport of a plume element of diluted effluent by the mean component of the current. The diffusion is the spreading of the plume element as a consequence of the mixing process.

The governing Equation for a three dimensional time-dependent advection-diffusion of a pollutant in a turbulent dominated flow field can be written as

$$\frac{\partial C}{\partial t}+\underbrace{u\frac{\partial C}{\partial x}+v\frac{\partial C}{\partial y}+w\frac{\partial C}{\partial z}}_{advection}=\underbrace{\frac{\partial}{\partial x}\left(K_x\frac{\partial C}{\partial x}\right)+\frac{\partial}{\partial y}\left(K_y\frac{\partial C}{\partial y}\right)+\frac{\partial}{\partial z}\left(K_z\frac{\partial C}{\partial z}\right)}_{diffusion}+\underbrace{S_{source}}_{source} \qquad (94)$$

where u, v, and w are velocity vectors in the x, y, and z direction respectively, K_x, K_y, and K_z are the corresponding eddy diffusivities. The Equation (94) is composed of three terms: (1) the second to fourth terms on the left hand side represent the advection from water transport; (2) the first three terms on the right hand side represent the diffusion from turbulent flow; and (3) the fourth term S_{source} is the source term which serves as an interface between far field and near field computation.

The analytical solution to Equation (94) currently does not exist. Numerical methods, such as finite difference or finite element methods should therefore be used. Because these methods are complicated, only the simplified steady state conditions of the Equation (94) will be discussed in this section.

Consider a steady continuous line source, as shown in Figure 12, of length L_0 kept perpendicular to the current U_a, the advection-diffusion Equation of a non-conservative tracer becomes

$$\underbrace{u\frac{\partial C}{\partial x}}_{advection}=\underbrace{\frac{\partial}{\partial x}\left(K_x\frac{\partial C}{\partial x}\right)+\frac{\partial}{\partial y}\left(K_y\frac{\partial C}{\partial y}\right)+\frac{\partial}{\partial z}\left(K_z\frac{\partial C}{\partial z}\right)}_{diffusion} \qquad (95)$$

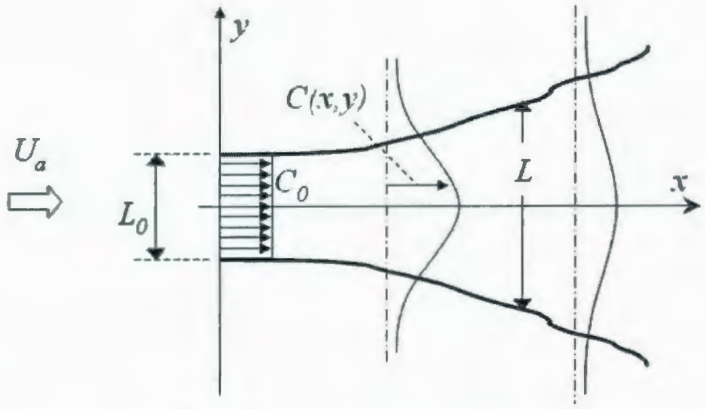

Figure 12. Schematic diagram of a steady turbulent diffusion plume.

Compared to the lateral direction, the concentration gradients in the x-direction are very small and thus the diffusion in the flow direction is negligible (K_x~0). Due to the width and depth scales of the ocean, the vertical diffusion is negligible compared with horizontal diffusion (K_y>>K_z). The lateral diffusivity K_y is assumed to be a function of plume width L, which, with the preceding assumptions, is only a function of downstream x and not of y. This implies that

$$\underbrace{u\frac{\partial C}{\partial x}}_{advection} = \underbrace{\frac{\partial}{\partial y}\left(K_y\frac{\partial C}{\partial y}\right)}_{diffusion} \tag{96}$$

The Equation (96) can be integrated to get the following solution (Csanady, 1973)

$$C(x,y) = \frac{C_0}{2}\left[erf\left(\frac{L_0 - y}{\sqrt{2}\sigma_y}\right) + erf\left(\frac{L_0 + y}{\sqrt{2}\sigma_y}\right)\right] \tag{97}$$

where the C_0 is the initial concentration at the begging of turbulent diffusion. $C(x, y)$ is the concentration at location (x, y), and σ_y is the standard deviation of the cross plume distribution function, i.e.

$$\sigma^2(x) = \frac{1}{C_0 L} \int_{-\infty}^{\infty} C(x,y) y^2 dy \tag{98}$$

The σ_y can be related with plume width by

$$\sigma = \frac{L}{2\sqrt{3}} \tag{99}$$

Generally, three types of relations can be used to relate the lateral eddy diffusivity to the scale or the width L of the plume, they are:

Fickian Diffusion: K_y = Constant (100)

Shear Diffusion: $K_y \propto L$ (101)

Inertial Sub-range Diffusion: $K_y \propto L^{4/3}$ (102)

2.3 REVIEW OF AVAILABLE MODELS

2.3.1 Summary of Important Factors that Affect the Mixing Behaviors

There are many factors that affect the mixing behavior of a buoyant jet in a marine environment. These factors can be generally grouped into two main categories: discharge parameters and ambient parameters.

Discharge parameters includes: flowrate, density of produced water, port size, discharge angle (port orientation), and depth of discharge.

The flowrate together with the port size will determine the effluent velocity. This effluent velocity is important for the near field behavior, which determines if the

discharge is jet-like or plume-like. The near field trajectory is strongly affected by this discharge velocity.

The discharge density, or more specifically the density difference between discharge and the ambient, will determine the buoyancy force of the effluent. If the buoyancy force is in the same direction as the discharge, it forms a positively buoyant jet, otherwise a negatively buoyant jet (Note: the definition of a negative buoyant jet in this study is somewhat different from other studies in which the negative means a dense jet).

It can be seen from the integral formulation, the buoyant jet behavior is affected by its discharge angle. For the same discharge conditions and ambient conditions, different dilutions and trajectories can be achieved. Actually, some studies have suggested using a 60° discharge degree, which forms an inclined jet to maximize the dilution.

The depth of discharge is important as it determines the near field mixing length. Take the example of a freshwater jet discharge upward into a uniform ocean at a depth of 50 m. It will achieve a higher dilution ratio at the surface than a discharge at 30 m depth. However, when the discharge is close to a boundary, the seabed for example, unstable mixing may occur due to the phenomenon of Coanda attachment.

The ambient parameter includes the following: ambient density profile, current speed and direction profile, surface wave and internal waves, and boundaries such as the surface and seabed.

Depending on the density at the discharge point, the discharged jet may rise or descend until it reaches the terminal level. In a uniform ambient environment, the

terminal levels are the sea surface or seabed, while in a stratified environment, the terminal level is a level of neutral buoyancy.

Although only very limited studies have been conducted, both the surface and internal waves are believed to enhance the mixing and thus result in higher near field dilution ratios. Moreover, the far field dispersion is affected by the mixing coefficients, and the vertical mixing coefficient is affected by the significant wave height and period.

The boundaries, such as sea surface and seabed will redirect the jet horizontally as the jet reaches them. Additional mixing behaviors such as internal hydraulic jump and up-stream intrusions have been observed.

To model the mixing behavior of buoyant jet accurately, it is important to consider these factors. In the following section, the existing models that can be used to model the produced water discharges will be reviewed.

2.3.2 General Environmental Discharge Models

(1) CORMIX

CORMIX is a USEPA-supported mixing zone model and decision support system for environmental impact assessment of regulatory mixing zones resulting from continuous point source discharges. The system emphasizes the role of boundary interaction to predict steady-state mixing behavior and plume geometry.

The current version of CORMIX includes three submodels—CORMIX1 for submerged single-port discharges, CORMIX2 for submerged multi-port discharges, and CORMIX3 for surface discharges. CORMIX also has a D-CORMIX submodel

which extends the CORMIX expert system to water quality prediction from continuous dredge disposal sources.

CORMIX contains a rule-based flow classification scheme developed to classify a given discharge and environment interaction into one of the several flow classes with distinct hydrodynamic features. The classification scheme places major emphasis on the near field behavior of the discharge and uses the length scale concept as a measure of the influence of each potential mixing process. Flow behavior in the far field, after boundary interactions, is largely controlled by ambient conditions. Once a flow has been classified, integral, length scale, and passive diffusion simulation modeling methods are utilized to predict the flow process details (CORMIX, 2007).

The near field of CORMIX is an Eulerian formulation as shown in section 2.2.1.1. In the intermediate field, it adopts the approach developed by Jones et al. (1983). CORMIX also considers the buoyant spreading and considers the wind-induced entrainment. In the turbulent diffusion region, it assums a top-hat profile and considers only the change of concentration along x- (downstream) and z-direction (vertical). The CORMIX is the most advanced steady-state model to date. The data required to run CORMIX model is summarized in Table 4.

The major advantage of CORMIX is its ease of use. The CORMIX system is characterized by a user-friendly interface and a variety of output options including graphical display. The user interface (Figure 13) allows the CORMIX system to be efficiently used by relatively inexperienced users, with the built-in decision support capability providing ample warnings if further detailed analysis or interpretation is required.

Table 4. Data requirements for CORMIX model.

		Data Requirement
Ambient data		• Water body depth (meters) • Water body depth at discharge (meters) • Ambient flow rate if steady (cubic meters/second) • Water body width if bounded (meters) • Tidal period (hours) • Maximum tidal velocity (meters/second) • Manning's *n* or Darcy-Weisback *f* • Wind speed (meters/second) • Density of water body (fresh or marine water) • Units of density • Stratification data: pycnocline height (meters) • Density/temp at surface • Density/temp at bottom
Discharge Data	Single Port	• Location of nearest bank • Distance to nearest bank (meters) • Vertical angle (degrees) • Horizontal angle (degrees) • Port diameter (meters) • Port height (meters) • Port area (square meters)
	Multi-Port	• Nearest bank orientation • Distance to endpoints • Diffuser length • Total number of openings • Port diameter • Port height • Concentration ratio • Diffuser arrangement type • Alignment angle • Horizontal angle • Vertical angle • Relative orientation
	Surface	• Discharge location • Discharge configuration • Horizontal angle • Distance form bank • Depth at discharge • Bottom slope • Discharge width and channel depth if rectangular • Discharge diameter and bottom invert pie if circular
Effluent Characteristics		• Flow rate (cubic meters/second) • Effluent velocity (meters/second) • Effluent temperature (°C) • Heat loss coefficient in cases of heated discharge • Effluent concentration and units • Decay rate coefficient in case of nonconservative substances
Mixing zone data		• Value of water quality standard • Toxicity of pollutant • CMC and CCC for toxic pollutants • Distance, width, or area of mixing zone in case specified.

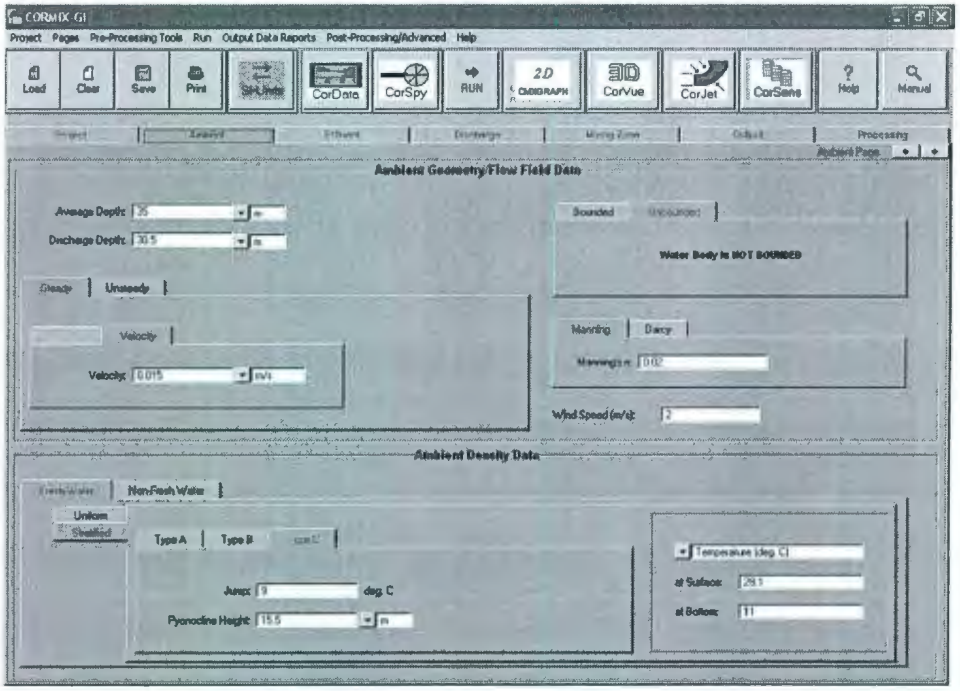

Figure 13. User graphic interface of CORMIX model.

There are several limitations of CORMIX in predicting produced water outfall: 1) it is a steady state model and can not account for spatial and temporal changes of the flow field. For example, the ambient flow could include tidal, wind- and wave-driven components having significant horizontal and vertical variations, Current magnitudes and direction could also change significantly over the course of a few hours due to tidal phase, sea breeze effects, and incident wave direction changes in contrast to CORMIX's assumption of steady current; 2) it does not consider the wave effects on initial dilution; 3) the top-hat assumption of far field concentration profile can not provide the details of concentration along the lateral direction; 4) the vertical diffusion coefficient is not energy dependent; 5) the limitation of some input parameters makes it inapplicable for vertical downward discharge, which is the case for many produced water discharges.

(2) Visual Plumes

Visual Plumes (VP), is a Windows-based computer application that supersedes the DOS Plumes (Baumgartner et al., 1994) mixing zone modeling system (Figure 14). VP simulates single and merging submerged plumes in arbitrarily stratified ambient flow and buoyant surface discharges. Among its new features are graphics, time-series input files, user specified units, a conservative tidal background-pollutant build-up capability, a sensitivity analysis capability, and a multi-stressor pathogen decay model that predicts coliform mortality based on temperature, salinity, solar insolation, and water column light absorption.

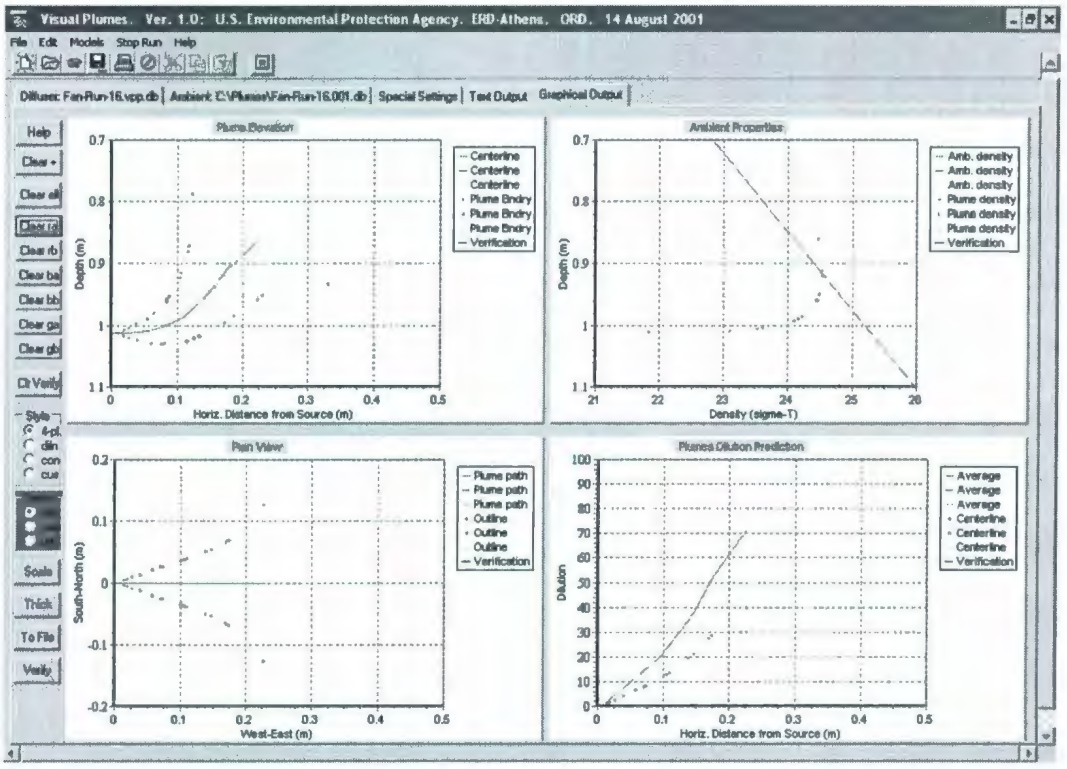

Figure 14. User graphic interface of Visual Plumes model.

There are presently five recommended models in VP: DKHW, NRFIELD/FRFIELD, UM3, PDSW, and DOS Plumes. DKHW is a three dimensional

Eulerian based model for positive buoyant jets. NRFIELD is a length scale model for multi-port discharges. FRFIELD is a simple analytical solution of a steady state turbulent diffusion Equation. UM3 is an acronym for the three dimensional Lagrangian type Updated Merge (UM) model, which is appropriate for both single- and multi-port submerged discharges. The formulation of UM3 is similar to the one described in section 2.2.1.2. PDSW is an acronym for the PDS model for windows. PDSW is a three-dimensional plume model that applies to discharges to water bodies from tributary channels, such as cooling towing discharge canals. The data required to run Visual Plumes model is summarized in Table 5.

Table 5. Data requirements for Visual Plumes model.

	Data Requirement
Ambient data	• Water body depth • Far field distance • Far field increment • Current speed • Density • Salinity • Temperature • Ambient concentration • Farfield dispersion coefficient • Average current speed in the farfield
Discharge Data	• Total diffuser flow • Number of ports in the diffuser • Spacing between ports • Port depth • Port diameter • Port elevation • Vertical angle • Contraction coefficient cell • Horizontal diffuser angle
Effluent Characteristics	• Effluent density • Pollutant concentration • Effluent salinity • Effluent temperature • First-order decay coefficient

Compared to CORMIX, the advantage of visual Plumes is its ability to conduct simple time series analysis. Visual Plumes permits the input of time series discharge

and tidal current information. By assuming a simple 1-dimensional re-entrainment, Visual Plume considers the effects of background concentration on dilution.

There major limitations of Visual Plumes are: 1) although it enables the temporal change of current field, it can not handle the spatial variation of currents; 2) it does not consider the wave effects on initial dilution; 3) VP does not have an intermediate mixing module, the upstream intrusion and effects of boundary is not included; 4) the far field dispersion does not consider the vertical mixing; 5) the far field solution is too simple to provide the details of concentration along lateral direction.

(3) VISJET

VISJET is a general interactive computer modeling system developed by the University of Hong Kong. Based on a Lagrangian model JETLAG, VISJET can be used to study the impact of either a single or a group of inclined buoyant jets in three-dimensional space.

The Lagrangian model JETLAG (Lee and Cheung, 1990) predicts the mixing of buoyant jets with three-dimensional trajectories. The unknown jet trajectory is viewed as a series of non-interfering "plume-elements" which increase in mass as a result of shear-induced entrainment and vortex-entrainment while rising by buoyant acceleration. The model tracks the evolution of the *average* properties of a plume element at each step by conservation of horizontal and vertical momentum, conservation of mass accounting for entrainment, and conservation of tracer mass/heat. The detailed formulation of JETLAG has already been described in section 2.2.1.2. The advantage of the JETLAG model is its capability of giving predictions under the whole range of jet orientation, ambient current and stratification conditions. There is

no limitation on discharge angles. The data required for the VISJET model is summarized in Table 6.

Table 6. Data Requirements for VISJET model.

		Data Requirement
Ambient data		• Water body depth (meters) • Water body depth at discharge (meters) • Ambient flow rate if steady (cubic meters/second) • Density of water body (fresh or marine water) • Units of density
Discharge Data	Single Port	• Vertical angle (degrees) • Horizontal angle (degrees) • Port diameter (meters) • Port height (meters) • Port area (square meters)
	Multi-Port	• Diffuser length • Total number of openings • Port diameter • Port height • Concentration ratio • Diffuser arrangement type • Alignment angle • Horizontal angle • Vertical angle • Relative orientation
Effluent Characteristics		• Flow rate (cubic meters/second) • Effluent velocity (meters/second) • Effluent temperature (°C) • Effluent concentration and units

The enhanced user graphic interface (Figure 15) of VISJET demonstrates clearly the evolution and interaction of multiple buoyant jets discharged at different angles to the ambient current.

VISJET has been used to predict the dilution of a number of sewage outfalls and no literature has shown the application of VISJET to a produced water outfall. Although VISJET is a powerful tool for near field analysis, the model does not have an intermediate field and far field module. Furthermore, the near field mixing did not include the effects of surface waves.

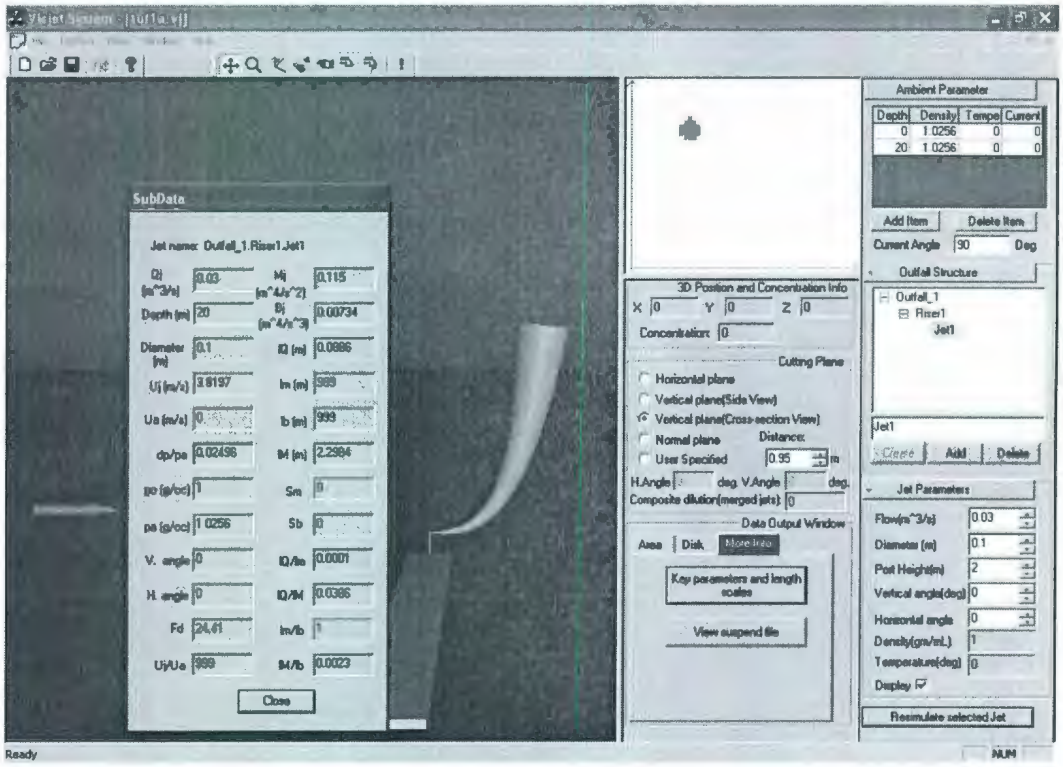

Figure 15. User graphic interface of VISJET model.

2.3.3 Produced Water Discharge Models

(1) PROTEUS

The pollution risk offshore technical evaluation system, PROTEUS (Sabeur & Tyler, 2001), was developed by BMY Marine Information Systems Ltd., UK under the Managing Impacts on the Marine Environment (MIME) program.

The PROTEUS is built with a set of modules, each executing specific internal tasks and providing information dynamically to other modules in the same system. Besides a physical dispersion model, it also includes a geochemistry model for the prediction of contaminant behaviour between dissolved and solid particulate phase,

and a biological model which simulates the process of chemical uptake by marine species.

PROTEUS represents the dissolved and solid material in typical offshore discharges as an ensemble of fundamental particles, which are governed by specific laws of transport within the marine environment pathways. Particles are released with known initial conditions then advected and dispersed by ambient hydrodynamic turbulence. The numerical update of the position, momentum and chemical content of particles of the same class leads to the computation of the overall concentrations and rate of spreading of the discharged materials in the offshore receiving waters. The user graphic interface of PROTEUS is shown in Figure 16.

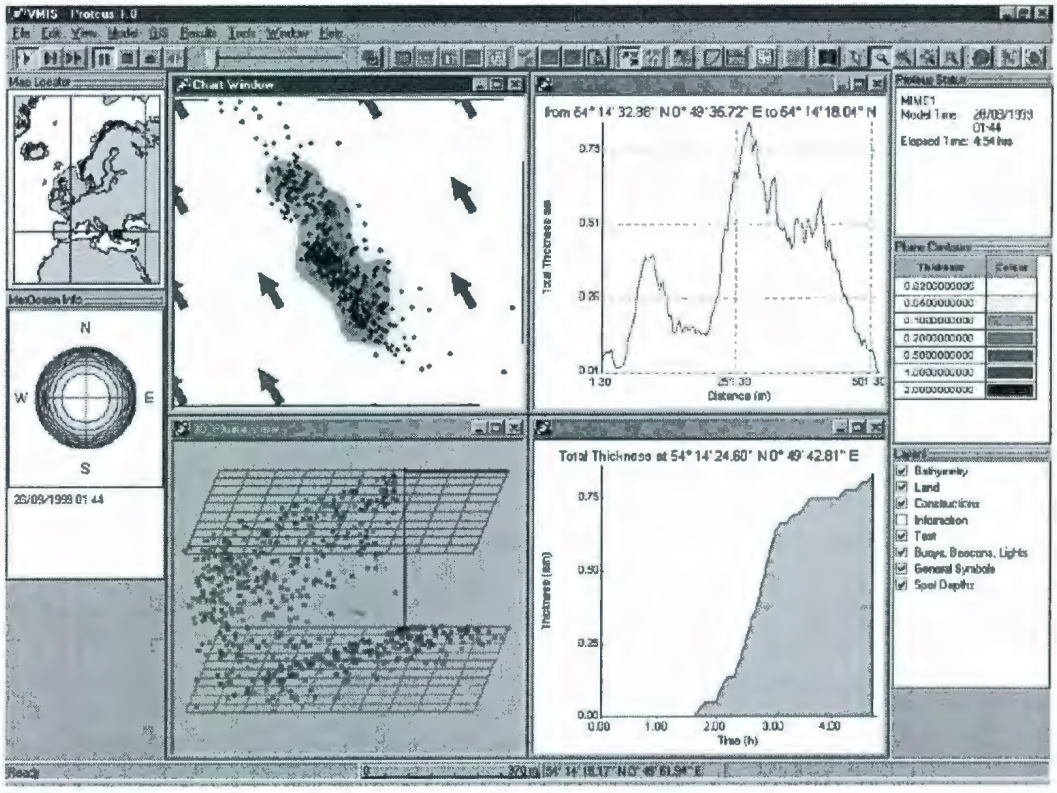

Figure 16. User graphic interface of PROTEUS model.

As PROTEUS was developed by a consultant company, very limited information is available in the literature about the model formulation. According to Sabeur et al. (2000), PROTEUS adopted a random walk particle based approach. The advantage of this approach is its ability to consider the re-entrainment of the returning pollutant into the near field plume. However, the intermediate field mixing and interactions of plume with boundaries were not included which are more important than the re-entrainment. Furthermore, the effects of surface wave on the mixing were also neglected.

(2) DREAM (PROVANN)

PROVANN (Reed et al., 1996) model is a three dimensional model which is able to simulate the spreading of produced water in three dimensions for a time varying wind input. The produced waters are spread due to horizontal and vertical diffusion and advected away due to residual currents, tidal currents, and wind induced Ekman currents.

PROVANN system has four components: a near field release model, a far field transport model, a biological exposure model, and a bioaccumulation and biomagnification model. The near field model of PROVANN is based on the integral model of Brandsma et al. (1980, 1992) and the far field model uses a particle tracking approach.

The PROVANN model has now been incorporated into the Dose-related Risk and Effects Assessment Model (DREAM) model which is a software tool designed to support rational management of environmental risks associated with operational discharges of complex mixtures (Reed et al., 2001). The current version of DREAM can account for the physical-chemical processes such as:

- Vertical and horizontal dilution and transport;
- Dissolution from droplet form;
- Volatilization from the dissolved or surface phase;
- Particulate adsorption/desorption and settling;
- Degradation;
- Sedimentation to seafloor.

Although DREAM (PROVANN) is the most advanced model than other models because of its integration of many transport and biological processes, its most basic physical model need to be improved. DREAM uses separate near field and far models rather a dynamic coupled model. The important intermediate field mixing is not considered and the wave effect is not included. For the far field mixing, the important buoyant spreading is also neglected.

(3) OOC

The OOC model was developed by the Offshore Operators Committee (Brandsma et al., 1980, 1992). It simulates the behavior of discharges from a single, submerged circular port oriented in any direction. Effluents are assumed to consist of a water-miscible fluid phase that can contain particles that are heavier or lighter than ambient water. The receiving water is described by water depth, temperature, salinity, and current velocity. The model outputs consist of predictions of the trajectory and the shape of the discharge plume, the concentration of the soluble and insoluble discharge components in the water column, and the accumulation of solids on the seabed.

The OOC model treats plumes as comprising three distinct flow regimes: convective descent, wherein material transport is dominated by the initial discharge

momentum, entrainment, and drag forces; dynamic collapse, where the plume seeks its equilibrium level or reaches the surface or seabed; and passive diffusion, in which the plume has lost any dynamic character of its own and diffusive phenomenon and advection are the primary transport mechanisms. These processes are described in OOC by a Lagrangian approach. The wave effect was not considered.

The OOC model has been validated extensively against field and laboratory data. Smith et al. (2001) have compared the OOC model with the field tests of Smith et al. (1994). In Smith et al.'s (1994) tests, produced water was discharged from a 15 cm diameter pipe at 80° below horizontal at an azimuth of 105°. The mouth of the pipe was 3 m below the sea surface. Nedwed et al. (2001) compared the OOC model with several laboratory scale experiments including: a heated water plume in unstratified and two-layer stratified flow (Viollet, 1979), a cold nitrogen jet into uniform density crossflow (Dunn et al., 1982), dense plume collapsing on bottom (Cavola, 1982), a high Froude number jet in uniform crossflow (Fan, 1967), and reversing jets in crossflow (Chu, 1975). Most experiments were conducted at scales of 15:1 to 20:1 except the Cavola (1982) which was conducted at a scale of 6:1 by considering the prototype pipe diameter to be 15 cm. The result of the validation increases confidence in the use of the OOC model predictions as an alternative to the difficult and expensive process of performing field measurements.

Terrens & Tait (1993) used the OOC model to predict the fate of produced water discharged from platform Halibut to Bass Straight off southeastern Australia. The discharge rate used for simulation was 14 million L/d and the median current speed was 26 cm/s. The predicted dilution was 30-fold within 10 m of the discharge and 1800-fold 1000 m down-current of the discharge.

Brandsma & Smith (1996) modeled the mixing of produced water under typical Gulf of Mexico and North Sea conditions. The discharge rates for Gulf of Mexico conditions were 115,740 L/d and 3,975,000 L/d. The predicted dilutions ranged from 300- to 2300-fold depending on the discharge rate and ambient current speed.

Compared with PROTEUS and DREAM, OOC only considers the physical transport process and OOC can not be used in non-steady state simulations. Like the other models reviewed above, OOC also neglected the wave effects on initial dilution.

A summary of the advantage and limitations of above models is shown in Table 7.

2.4 SUMMARY

In this Chapter, the fundamentals of the transport processes of produced water, or more generally, a buoyant jet, in a marine environment has been described. There are four important regions that need to be considered: initial mixing region, intermediate/boundary interaction region, which includes the upstream intrusion and downstream control process, buoyant spreading, and turbulent diffusion.

These mixing processes are affected by both discharge and receiving environmental parameters such as: rate of discharge, density (or temperature/salinity) of discharge, port orientation and size, depth of discharge, water depth, ambient density profile, current speed and direction, surface wave and internal waves.

A number of models can be used to predict the dispersion of produced water in the marine environment, such as the CORMIX, Visual Plumes, VISJET, PROTEUS, DREAM/PROVANN, and OOC models. The problem associate with the produced water transport models, such as PROTEUS , DREAM/PROVANN , and OOC, is that they all lack a intermediate transport module which is very important as it affect the

Table 7. Advantages and Limitations of Existing Models.

Model	Advantages	Limitations
CORMIX	• Provides flow classification; • Considers boundary interaction; • Considers wind effects on surface mixing; • Good approximation of near field behaviors.	• Cannot account for variability of current speed and direction; • No wave effect; • Use constant vertical diffusion; • No uncertainty analysis.
Visual PLUME	• Good approximation of near field behaviors.	• Cannot account for variability of current speed and direction; • No wave effect; • Far field model too simple; no buoyant spreading effect; • No uncertainty analysis.
VISJET	• Provides visualization of jet/plume behavior; • Good approximation of near field behaviors.	• Cannot account for variability of current speed and direction; • No wave effect; • No far field model; • No uncertainty analysis.
PROTEUS	• Can account for variability of current speed and direction; • Can simulate particles	• Near field behavior can not be predicted; • Not buoyant spreading; • No wave effect; • No uncertainty analysis.
PROVANN	• Can account for variability of current speed and direction; • Can simulate various transport process, such as evaporation, degradation etc.	• Not buoyant spreading; • No wave effect; • No uncertainty analysis.
OOC	• Good approximation of near field behaviors.	• Cannot account for variability of current speed and direction; • Not buoyant spreading; • No wave effect; • No uncertainty analysis.

accuracy of the far field mixing. To date, CORMIX is the only model that considered the intermediate mixing process. However, CORMIX neglected the effects of surface wave and internal wave on initial mixing and it can not be used to simulate the non-steady state mixing. It needs to be coupled with a time-dependent far field dispersion model. Also, the CORMIX output for far field is one-dimensional, which needs to be improved to three dimensional and give more accurate prediction. Moreover, the

produced water transport models, such as PROTEUS and DREAM/PROVANN considered more advanced multi-media transport process but the CORMIX does not have this capability.

In conclusion, to effectively model the fate of produced water, the following modeling work is needed:

- Develop a steady state model which considered all the mixing processes. This model should have all the capability of CORMIX but take into consideration waves effects, and have more accurate prediction in far field;
- This model should be able to predict the multi-media transport process;
- Coupling this model with a non-steady state far field model to predict the dispersion process of produced water in a non-steady environment.

3. STEADY STATE APPROACH: THE PROMISE MODEL

In this chapter, a composite steady state model, PROMISE (PROduced-water Mixing In Steady-state Environment), is proposed. Generally, Plume dispersion modeling can either be deterministic or probabilistic. Deterministic models treat the problem in a purely deterministic sense. The variables are not considered as random variables, nor are the model simulations repeated multiple times within a Monte Carlo loop. On the other hand, probabilistic models do accommodate random variables in some sense.

In section 3.1, the deterministic form of the PROMISE model, which includes five sub-models, will be described. The probabilistic form of the model using Monte Carlo simulation will be explained in section 3.2.

3.1 DETERMINISTIC BASED APPROACH

The proposed model has five sub-components: 1) PROMISE1 - a near field model which simulates the initial mixing behavior before boundary interaction occurs; 2) PROMISE2 - a wave effect model which accounts for the effects of both internal and surface waves; 3) PROMISE3 - a boundary interaction model which may include an upstream intrusion and a downstream control model depending on the impinging angle; 4) PROMISE4 - a far field dispersion model which models the buoyant spreading and turbulent diffusion process; 5) PROMISE5 - a multimedia fate model which simulates the steady state pollutant concentration in multimedia environments.

3.1.1 PROMISE1 – Near Field Mixing

As described in Chapter 2, three types of approaches can be used to simulate the near field behavior of a buoyant jet. The turbulence models are very complicated to use. Although the turbulence models can simulate various types of discharges, they need significant amount of computation time. For example, if 1 hour is needed for a single simulation, a 1000 times Monte Carlo simulation for a probabilistic based analysis requires 1000 hours (41 days). Therefore, this approach is unrealistic for the present work. On the other hand, the length scales are very simple but they are only applicable for certain flow conditions and cannot be used as a general model. Different from the turbulence models and length scale models, the integral type models are easy to use and can be used for a wide range of flow conditions. Therefore, it is adopted in this study to model the near field mixing.

3.1.1.1 Lagrangian Formulation

Integral formulations have been adopted by a number of authors (e.g., Lee and Cheung, 1990; Jirka, 2004). Most of the previous approaches have used specified shapes (for example, round) for the source of the buoyant fluid. In this study, the Lagrangian formulation of Tate (2002) is modified to model the initial mixing behaviors of buoyant jets. The advantage of this approach is that the specification of the buoyant jet shape is not needed.

Consider a arbitrarily shaped buoyant jet element of volume $\Delta\tau$ and surface area Δf moving along its trajectory with a velocity $u_i=(u_x, u_y, u_z)$ through the ambient fluid (as shown in Figure 17) with velocity $U_i=(U_x, U_y, U_z)$. Let $EL(P_i, t)$ denote the element at position P_i and time t. After time Δt, the element has moved to a new position $EL(P_i+\Delta P_i, t+\Delta t)$. During the movement, the element maps out a volume

ΔV_{vol} of length ΔP_i. As a result of this movement, ambient water is entrained into the plume element. The mass, momentum, and buoyancy are conserved and the Equations are derived in a Lagrangian framework.

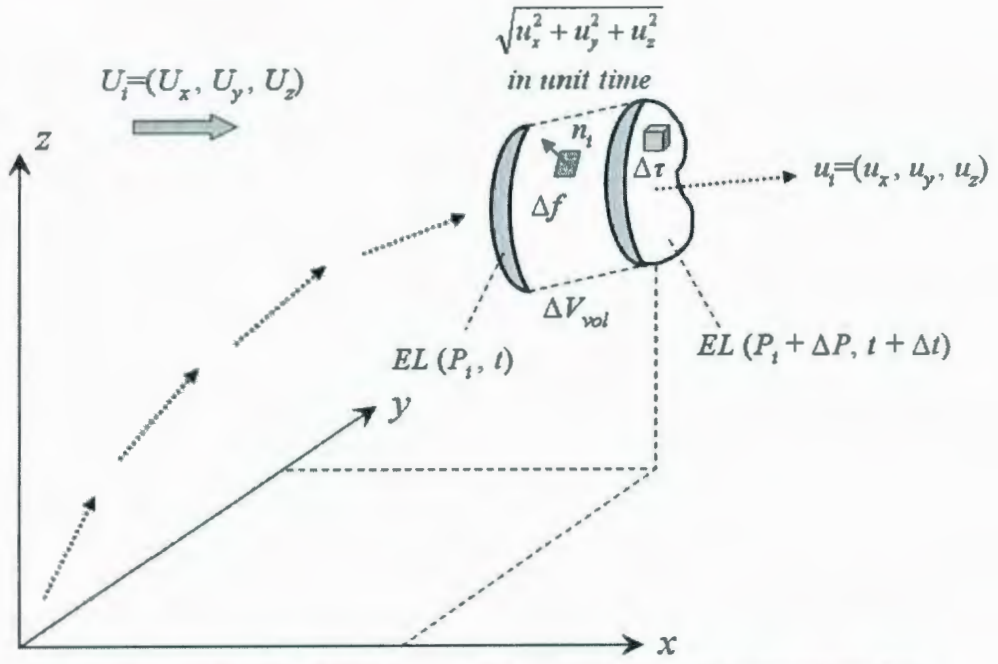

Figure 17. An arbitrary shape buoyant jet element moving within an ambient fluid.

Conservation of Mass

Consider a surface element Δf of the plume element ΔV_{vol}, the mass of ambient fluid flowing out is

$$-(\rho_a+\rho')v_i n_i \Delta f \Delta t \tag{103}$$

where $(\rho_a+\rho')$ is the density of the fluid crossing the surface, ρ' is the turbulent fluctuation of density, v_i is the cross velocity, and n_i is a unit outward normal vector.

The change of mass, Δm, can be obtained by summing over all surface elements, that is

$$\Delta m = \sum -(\rho_a + \rho')v_i n_i \Delta f \Delta t \tag{104}$$

The summing also eliminates the ρ' as it becomes zero. Therefore, the Equation (104) becomes

$$\Delta m = \sum -\rho_a v_i n_i \Delta f \Delta t \tag{105}$$

Now consider a unit volume element at position P_i and time t, the mass is

$$m(P_i, t) = \sum \rho(P_i, t)\Delta\tau \tag{106}$$

Similarly, the volume element at position $P_i + \Delta P_i$ and time $t+\Delta t$ is

$$m(P_i + \Delta P_i, t + \Delta t) = \sum \rho(P_i + \Delta P_i, t + \Delta t)\Delta\tau \tag{107}$$

The change of mass for this volume element is obtained by subtracting Equation (106) from Equation (107)

$$\Delta m = \sum [\rho(P_i + \Delta P_i, t + \Delta t) - \rho(P_i, t)]\Delta\tau \tag{108}$$

From Equation (105) and Equation (108), Equation (109) can be derived by dividing both sides by Δt

$$\int \frac{\partial \rho}{\partial t} d\tau = \int -\rho_a v_i n_i df \tag{109}$$

By introducing an entrainment assumption, the Equation (109) becomes

$$\int \frac{\partial \rho}{\partial t} d\tau = \int -\rho_a (-\alpha U_{ent} n_i) n_i df \tag{110}$$

where U_{ent} is the rate of entrainment, and α is an entrainment coefficient.

As the Equation (110) must hold for all volume and area elements, it can be rewritten as

$$\frac{\partial \rho V_{vol}}{\partial t} = \rho_a \alpha U_{ent} A \tag{111}$$

where $V_{vol} = \int d\tau$ is the total volume and $A = \int df$ is the total surface area.

Conservation of Momentum

Consider a volume element at position P_i and time t moving with velocity u_i, its momentum can be expressed as

$$\rho(P_i,t)\cdot\Delta\tau\cdot u_i(P_i,t) \tag{112}$$

The momentum of ambient fluid of volume $\Delta\tau_a$ is

$$\rho_a(P_i,t)\cdot\Delta\tau_a\cdot U_i(P_i,t) \tag{113}$$

The total momentum is the difference of the above two momentums. By summing over all volume elements, the total momentum M_i is

$$M_i(P_i,t)=\sum\left[\rho(P_i,t)\cdot\Delta\tau\cdot u_i(P_i,t)-\rho_a(P_i,t)\cdot\Delta\tau_a\cdot U_i(P_i,t)\right] \tag{114}$$

A similar expression can be obtained for the total momentum at position $P_i+\Delta P_i$ and time $t+\Delta t$

$$M_i(P_i+\Delta P_i,t+\Delta t)=\sum\begin{bmatrix}\rho(P_i+\Delta P_i,t+\Delta t)\cdot\Delta\tau\cdot u_i(P_i+\Delta P_i,t+\Delta t)\\-\rho_a(P_i+\Delta P_i,t+\Delta t)\cdot\Delta\tau_a\cdot U_i(P_i+\Delta P_i,t+\Delta t)\end{bmatrix} \tag{115}$$

and the change of momentum between time t and $t+\Delta t$ is obtained by subtracting Equation (114) from (115). The rate of change of momentum is then obtained by dividing Δt

$$\begin{aligned}\frac{\partial M_i}{\partial t}&=\int\frac{\partial(\rho u_i)}{\partial t}d\tau-\int\frac{\partial(\rho_a U_i)}{\partial t}d\tau_a\\&=\frac{\partial(\rho V_{vol}u_i)}{\partial t}-U_i\frac{\partial(\rho_a V_{vol-a})}{\partial t}\end{aligned} \tag{116}$$

where $V_{vol-a}=\int d\tau_a$ is the total volume of ambient fluid. As the mass entrained into the buoyant jet equals the change in mass of the ambient fluid, the Equation (116) can be rewritten as

$$\frac{\partial M_i}{\partial t} = \frac{\partial(\rho V_{vol} u_i)}{\partial t} - U_i \frac{\partial(\rho V_{vol})}{\partial t} \tag{117}$$

The buoyancy force acting on the plume element is

$$F_i = \sum \rho G i \Delta\tau = \int \rho G_i d\tau = G_i \rho V_{vol} \tag{118}$$

where G_i is zero in the horizontal direction and has a value of g' in the vertical direction. This buoyancy force is equivalent to the rate of change of momentum, hence

$$F_i = G_i \rho V_{vol} = \frac{\partial M_i}{\partial t} = \frac{\partial(\rho V_{vol} u_i)}{\partial t} - U_i \frac{\partial(\rho V_{vol})}{\partial t} \tag{119}$$

The element velocity u_i has horizontal components u_x, u_y, and a vertical component u_z. The ambient velocity U_i has horizontal components U_x, U_y, and a vertical component U_z. Replace the u_i and U_i in Equation (119) with their horizontal and vertical components, the momentum conservation Equation becomes

x component: $$\frac{\partial(\rho V_{vol} u_x)}{\partial t} = U_x \frac{\partial(\rho V_{vol})}{\partial t} \tag{120}$$

y component: $$\frac{\partial(\rho V_{vol} u_y)}{\partial t} = U_y \frac{\partial(\rho V_{vol})}{\partial t} \tag{121}$$

z component: $$\frac{\partial(\rho V_{vol} u_z)}{\partial t} = U_z \frac{\partial(\rho V_{vol})}{\partial t} + \rho g' V_{vol} \tag{122}$$

Conservation of Buoyancy

The change of buoyancy is related to the change of energy. The conservation of buoyancy is the energy added to the system less the work done by the system. In time Δt, the buoyancy added to the buoyant jet element is

$$-g\left[(\rho_a + \rho') - \rho_{ref}\right] u_i n_i \Delta f \Delta t \tag{123}$$

By summing over all surface elements and converting the surface integral to a volume integral using Green's theorem, Equation (123) becomes

$$\text{Buoyancy Added} = -g\Delta t\left[u_x\frac{\partial \rho_a}{\partial x}+u_y\frac{\partial \rho_a}{\partial y}+u_z\frac{\partial \rho_a}{\partial z}\right]\int d\tau \tag{124}$$

The work done by the system in time Δt is via the change of buoyancy in that time, hence

$$\text{Work} = -g\int\{[\rho(P_i+\Delta P_i,t+\Delta t)-\rho_a(P_i+\Delta P_i,t+\Delta t)]-[\rho(P_i,t)-\rho_a(P_i,t)]\}d\tau \tag{125}$$

For conservation of energy, energy added is equivalent to work done, hence

$$g\int\frac{\partial(\rho-\rho_a)}{\partial t}d\tau = -gu_i\frac{\partial \rho_a}{\partial x_i}\int d\tau \tag{126}$$

Summing over all elements, Equation (126) becomes

$$\frac{\partial[(\rho-\rho_a)V_{vol}]}{\partial t} = -gu_iV_{vol}\frac{\partial \rho_a}{\partial x_i} \tag{127}$$

or

$$\frac{\partial[(g'V_{vol}]}{\partial t} = -u_iV_{vol}\varepsilon_D \tag{128}$$

where $g' = -g(\rho-\rho_a)/\rho_a$ and $\varepsilon_D = (-g/\rho_a)(d\rho_a/dz)$. As the change is only in vertical direction, u_i is replaced by u_z and Equation (128) becomes

$$\frac{\partial[(g'V_{vol}]}{\partial t} = -u_zV_{vol}\varepsilon_D \tag{129}$$

3.1.1.2 System Closure-Entrainment Formulation

The conservation Equations derived above are summarized in Table 8.

It can be seen from the above Equations that there are six unknown parameters: u_x and u_y are the horizontal jet velocities; u_z is the vertical jet velocity; A is the surface area, V_{vol} is the volume and g' is the buoyancy modified gravity. It is impossible to

solve the above parameters using only five Equations and therefore the sixth Equation (a closure Equation) must be provided to close the system.

Table 8. Governing Equations of the Lagrangian formulation

Parameter	Equation	No.
Mass	$\frac{\partial \rho V_{vol}}{\partial t} = \rho_a \alpha U_{ent} A$	(111)
x-momentum	$\frac{\partial (\rho V_{vol} u_x)}{\partial t} = U_x \frac{\partial (\rho V_{vol})}{\partial t}$	(120)
y-momentum	$\frac{\partial (\rho V_{vol} u_y)}{\partial t} = U_y \frac{\partial (\rho V_{vol})}{\partial t}$	(121)
z-momentum	$\frac{\partial (\rho V_{vol} u_z)}{\partial t} = U_z \frac{\partial (\rho V_{vol})}{\partial t} + \rho g' V_{vol}$	(122)
Buoyancy	$\frac{\partial [(g' V_{vol}]}{\partial t} = -u_z V_{vol} \varepsilon_D$	(129)

Closure of the governing Equation is often achieved by introducing an entrainment function. The entrainment is traditionally regarded as a constant ratio between the entrainment velocity and the mean vertical velocity of the fluid. Through the search of reported entrainment coefficients, α, from the literature, 141 values for different types of discharges were collected from various sources. The descriptive statistics of these entrainment coefficients is listed in Table 9 and plotted in Figures 18 and 19.

Table 9. Descriptive statistics of the entrainment coefficient.

Parameters	Value	Parameters	Value
Number of Data	141	25 Percentile (Q1)	0.0800
Mean	0.2176	50 Percentile (Median)	0.1400
Standard Error	0.0158	75 Percentile (Q3)	0.3200
Standard Deviation	0.1871	Interquartile Range (IQR)	0.2400
Variance	0.0350	Minimum	0.0400
Coefficient of Variance	86.01	Maximum	0.9300

It can be seen from the histogram in Figure 18 that the data are not normally distributed. 90 percent of the data lie between 0.05 and 0.705 with a mean value of 0.2176. Figure 19 also shows the maximum value 0.9300 is an outlier. The best fit of the data using @RISK software has shown the data is log-normally distributed.

Due to the high degree of variability in the entrainment coefficient, it is necessary to use more complex entrainment functions to satisfactorily close the system of Equations and accurately reproduce the results of laboratory and field experiments.

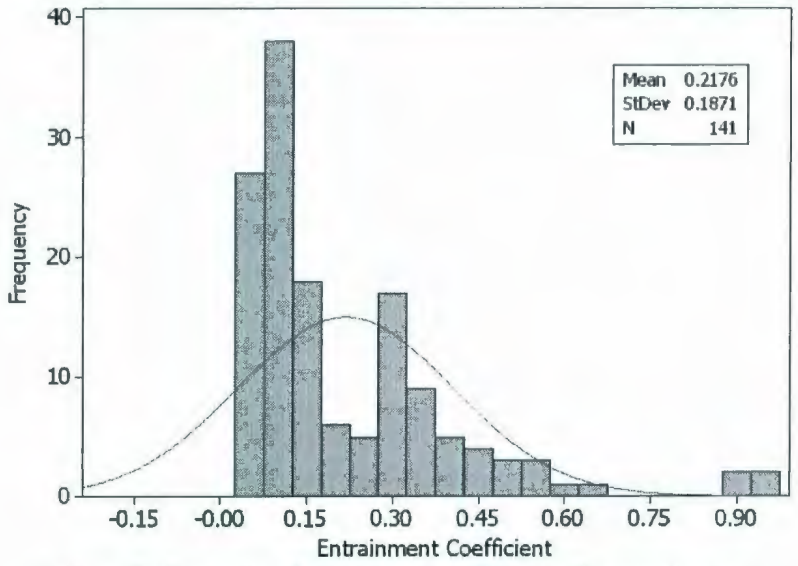

Figure 18. Histogram of entrainment coefficient with normal curve.

Two entrainment functions have been described in Chapter 2 (Equation 19 and Equations 46 to 49). They have been used by the CORMIX and VISJET models and provide good agreement with laboratory and field data over a wide range of environmental conditions. With the same shear entrainment formulation as Lee & Cheung (1990), Tate (2002) proposed a different formulation for vortex entrainment as

$$\alpha_{vortex} = 0.34\left(F_L K\right)^{0.125} \tag{130}$$

Together with the above entrainment formulation, the governing Equations in Table 8 can be solved by Runge-Kutta method.

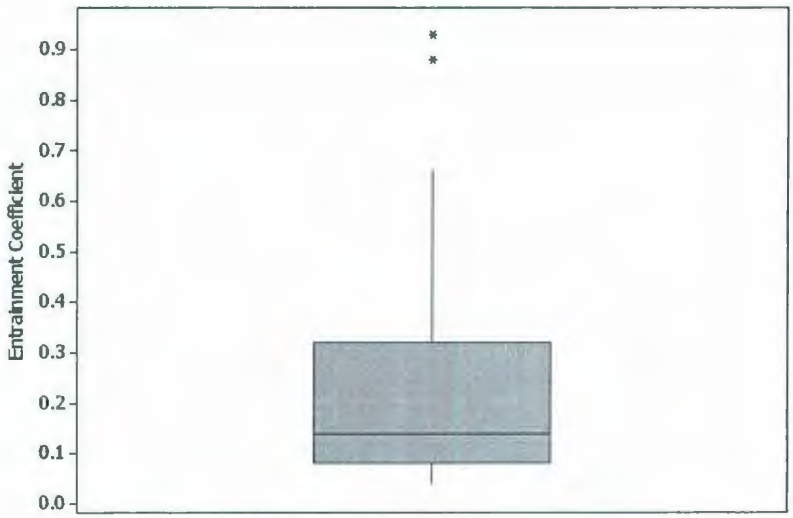

Figure 19. Box plot of entrainment coefficient.

3.1.1.3 Modification to Tate (2002) Model

Two modifications are necessary for the Tate (2002) formulation. First, the formulation was developed based on a Top-hat profile assumption. Therefore, all the model calculations and predictions are expressed in terms of the average properties of the plume element. For example, the concentration predicted is the same for the centerline and the plume boundary. In practice, the concentration is either a Gaussian in the near field or a Kidney-shape in the far field, in which the centerline concentration is much higher than the boundary concentration (Lee and Chu, 2003). The model must be modified to predict the centerline concentration as well as average concentration. Second, the entrainment formulation needs to be refined as the previous formulation (Equation 130) was based on limited data points. The Equation was

developed based on 5 data sets of vertical positive buoyant jets (Fan, 1967) in cross-flowing and 9 data sets of horizontal buoyant jets (Davidson, 1989) in co-flowing environments. There is a need to refine the Equation (130) with more data sets and various discharge conditions, for example, high Froude number conditions, horizontal buoyant jets in cross-flowing conditions, and negative buoyant jets.

Relating Average Value to Centerline Value

Consider a jet with 2-dimensional trajectory, the Gaussian and top-hat profiles are illustrated in Figure 21. The general Gaussian profiles of velocity, $U_{gaussain}$, and concentration, $C_{gaussain}$, can be represented by

$$U_{gaussain} = U_a + U_m e^{-(r/b_{gaussian})^2} \tag{131}$$

$$C_{gaussain} = C_m e^{-(r/\lambda_g b_{gaussian})^2} \tag{132}$$

where U_m and C_m are the maximum excess velocity and concentration respectively, $b_{gaussian}$ is the width, λ_g is the ratio of concentration to velocity. The top-hat profile for the velocity and concentration are

$$U_{top-hat} = \begin{cases} U_t & b < b_{top} \\ U_a & b > b_{top} \end{cases} \tag{133}$$

$$C_{top-hat} = \begin{cases} C_t & b < b_{top} \\ C_a & b > b_{top} \end{cases} \tag{134}$$

where U_t and C_t are the top-hat velocity and concentration respectively, and b_{top} is the width.

By integrating the respective profiles, the volume, momentum, and mass flux are obtained and listed in Table 10.

In the near field, the ambient velocity is generally very small compared with buoyancy and momentum generated velocity, therefore the following relationship can be derived by taking λ_g as 1.2 (Holley and Jirka, 1985)

$$U_t = 0.5U_m \tag{135}$$

$$b_{top} = \sqrt{2}b_{gassuain} \tag{136}$$

$$C_t = \frac{1}{1.7}C_m \tag{137}$$

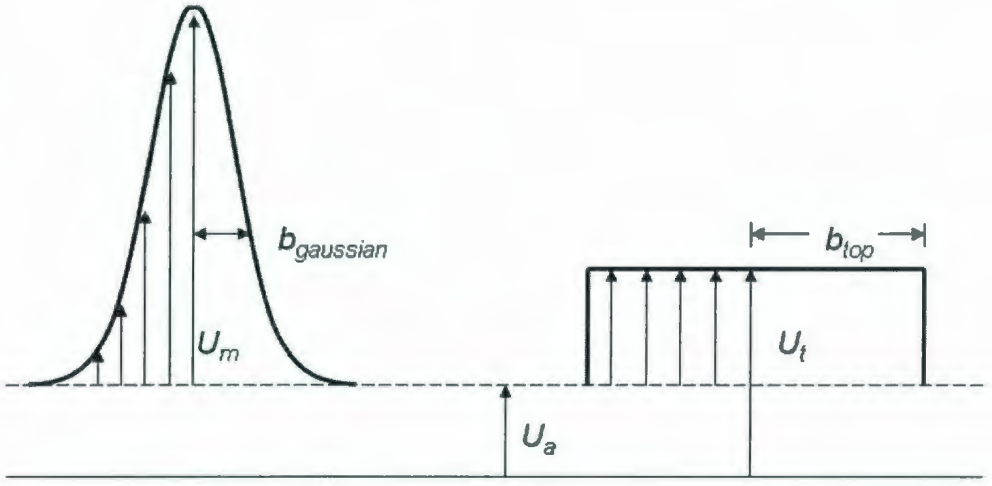

Figure 20. Gaussian (left) and Top-hat (right) profiles.

Table 10. Flux Equations for Top-hat and Gaussian profiles.

Flux	Top-hat	Gaussian
Volume	$Q_t = \pi b_{top}^2 U_t$	$Q_g = \pi b_a^2 U_a + \pi b_{gaussian}^2 U_m$
Momentum	$M_t = \pi b_{top}^2 U_t^2$ (138)	$M_g = \pi b_a^2 U_a^2 + 2\pi b_a^2 U_a U_m + \frac{\pi}{2} b_{gaussian}^2 U_m^2$ (139)
Mass	$C_t = \pi b_{top}^2 U_t C_t$	$C_g = \pi \lambda_g^2 b_{gaussian}^2 U_a C_m (1 - e^{-(ba/\lambda_g b)^2}) + \pi \frac{\lambda^2}{1+\lambda_g^2} b_{gaussian}^2 U_m C_m$

In the far field, the excess velocity is very small, by taking the same λ_g as suggested by Holley & Jirka (1985), the relationship becomes

$$U_t - U_a = 0.5U_m \tag{140}$$

$$b_{top} = \sqrt{2}b_{gaussian} \tag{141}$$

$$C_t = \frac{1}{1.85}C_m \tag{142}$$

In the region between near field and far field, the factors fall between these limits. Equation (142) is based on the assumption that the far field profile is also Gaussian. Based on the several experimental measurements (for example, Cheung, 1991), the far field profile is generally a kidney shape rather than a Gaussian shape. Therefore, the coefficient 1.85 must be calibrated with experimental measurements. Cheung (1991) has suggested a value of 2.3 based on the data reported by Fan (1967) and Ayoub (1971).

The model uses a factor of 1.7 to relate the centerline dilution with the average dilution in the near field. The factor increased gradually to 2.3 in the far field. For the intermediate field, the factor is determined by a linear interpolation based on the relative magnitude of shear entrainment α_{Shear} and vortex entrainment α_{Vortex} as shown in Equation (143)

$$Factor = \begin{cases} E_f = 1.7 & \alpha_{\text{Shear}}/\alpha_{\text{Vortex}} > 5 \\ 1.7 < E_f < 2.3 & 0.2 < \alpha_{\text{Shear}}/\alpha_{\text{Vortex}} < 5 \\ E_f = 2.3 & \alpha_{\text{Shear}}/\alpha_{\text{Vortex}} < 0.2 \end{cases} \tag{143}$$

Refining the Entrainment Coefficient

The total entrainment can be obtained from a maximum hypothesis, or alternatively an additive hypothesis. The maximum hypothesis uses the maximum

value of shear and vortex entrainment, while the additive hypothesis uses the sum of these two entrainments. Although Lee and Chu (2003) pointed out the maximum hypothesis in general gives better results, it may give unreasonable prediction for a weak current. Therefore, the additive hypothesis is adopted in this study.

Tate (2002) adopted the same shear entrainment function (Equation 47) developed by Lee and Cheung (1990) but used a different vortex entrainment function (Equation 130) from Lee and Cheung's function (Equation 48). The advantage of Tate's (2002) function is that it was based on experimental data while Lee and Cheung's function is purely theoretical and several iterations are required to get convergence. Tate's (2002) function was derived based only on two types of flow conditions: vertical jets in cross-flowing, and horizontal jets in co-flowing conditions. As there are many other flowing conditions for buoyant jets problems, such as horizontal jet in a cross-flowing environment in which the trajectory becomes 3-D rather than 2D, discharges in a stratified environment, and inclined jets, it is important to refine the entrainment Equation (130) with extended data sets from various types of discharge conditions.

For practical reasons, the laboratory observations used to derive the entrainment function differ from those of full scale field discharges. Because of this, the length scales used in the laboratory must be the same as those of the full scale discharges. For study of buoyant jet problems, two important length scales are the densimetric Froude number F_r and velocity ratio K. For produced water problems, the Froude number could range from zero to infinity (for neutrally-buoyant effluent), but most discharges have a Froude number range from 0.4 to 80. Similarly, most discharges

have a velocity ratio range from 0.1 to 80 although it may vary from zero to infinity theoretically (Nedwed et al., 2001).

Table 11. Summary of data used to derive the entrainment coefficient.

Source	Buoyancy	Orientation	Current	Density	*Fr*	*K*
Fan (1967)	Positive	Vertical	CrossFlow	Uniform	10	4
Fan (1967)	Positive	Vertical	CrossFlow	Uniform	10	8
Fan (1967)	Positive	Vertical	CrossFlow	Uniform	20	4
Fan (1967)	Positive	Vertical	CrossFlow	Uniform	20	8
Fan (1967)	Positive	Vertical	CrossFlow	Uniform	20	12
Fan (1967)	Positive	Vertical	CrossFlow	Uniform	20	16
Fan (1967)	Positive	Vertical	CrossFlow	Uniform	40	8
Fan (1967)	Positive	Vertical	CrossFlow	Uniform	40	16
Fan (1967)	Positive	Vertical	CrossFlow	Uniform	80	16
Davidson (1989)	N/A	Horizontal	CoFlow	Uniform	1.66	1
Davidson (1989)	N/A	Horizontal	CoFlow	Uniform	3.2	5
Davidson (1989)	N/A	Horizontal	CoFlow	Uniform	3.31	2
Davidson (1989)	N/A	Horizontal	CoFlow	Uniform	33.1	20
Davidson (1989)	N/A	Horizontal	CoFlow	Uniform	6.4	10
Davidson (1989)	N/A	Horizontal	CoFlow	Uniform	5.6	8.33
Davidson (1989)	N/A	Horizontal	CoFlow	Uniform	14.0	20
Davidson (1989)	N/A	Horizontal	CoFlow	Uniform	8.3	5
Davidson (1989)	N/A	Horizontal	CoFlow	Uniform	1.66	10
Cheung (1991)	Positive	Vertical	CrossFlow	Uniform	4	4
Cheung (1991)	Positive	Vertical	CrossFlow	Uniform	8	4
Cheung (1991)	Positive	Vertical	CrossFlow	Uniform	16	6
Cheung (1991)	N/A	Horizontal	CrossFlow	Uniform	16	6
Cheung (1991)	N/A	Horizontal	CrossFlow	Uniform	16	4
Anderson et al. (1973)	Negative	Vertical	Crossflow	Uniform	10.9	5.5
Anderson et al. (1973)	Negative	Vertical	Crossflow	Uniform	40.7	10.2
Tian (2002)	Positive	Vertical	Crossflow	Stratified	7.6	5.6

To refine Tate's (2002) Equation, extensive data sets as shown in Table 11 have been used. It includes: vertical buoyant jets in crossflow (Fan, 1967; Cheung, 1991), horizontal buoyant jets in crossflow (Cheung, 1991), negative buoyant jets in crossflow (Anderson, 1973), and vertical buoyant jets in stratified crossflow (Tian,

2002). The range of Froude number and velocity ratio is shown in Figure 21 and the maximum Froude number has been extended from 33.1 to 80 in this study.

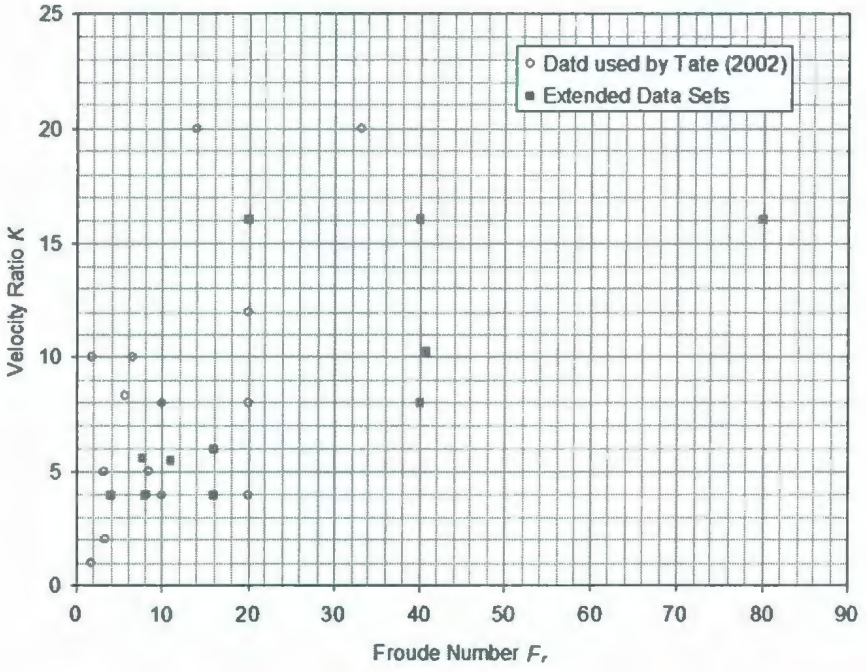

Figure 21. Froude number F_r and velocity ratio used for deriving entrainment function.

It is assumed that the vortex entrainment is a function of local densimetric Froude number and the velocity ratio and follows a power law relationship

$$\alpha_{vortex} = k_{20}\left(F_L K\right)^{k_{21}} \tag{144}$$

where F_L is the local densimetric Froude number, k_{20} and k_{21} are empirical coefficients. For a given set of experiments in Table 11, different α_{vortex} values were used to match the predictions with observations in a least square sense. This was a trial-and-error process and the resulting α_{vortex} is plotted in Figure 22.

A power law curve was fitted to the data by regression analysis, which yielded a k_{20} value of 0.355 and k_{21} value of 0.119 (Figure 22). The regression results are shown

in Figure 23 and Figure 24. It can be seen that the residuals are evenly and normally distributed and the regression is acceptable. Although the new mean values of k_{20} and k_{21} do not differ from Tate's value significantly, the uncertainty level was increased. The new 95% confidence intervals for k_{20} and k_{21} are [0.297, 0.412] and [0.081, 0.158] respectively while their previous values were [0.290, 0.383] and [0.089, 0.172]. The regression coefficient R^2 also decreased from 0.89 to 0.62 which means the data are more scattered.

The results from a test case are compared with the predictions from CORMIX and VISJET models. As shown in Figure 25, although all three models can predict the dilution reasonably, there exists a degree of uncertainty. The prediction by PROMISE1 lies between the prediction by CORMIX and VISJET.

A more detailed validation study of PROMISE1 against a wide range of experimental data is presented in Chapter 4.

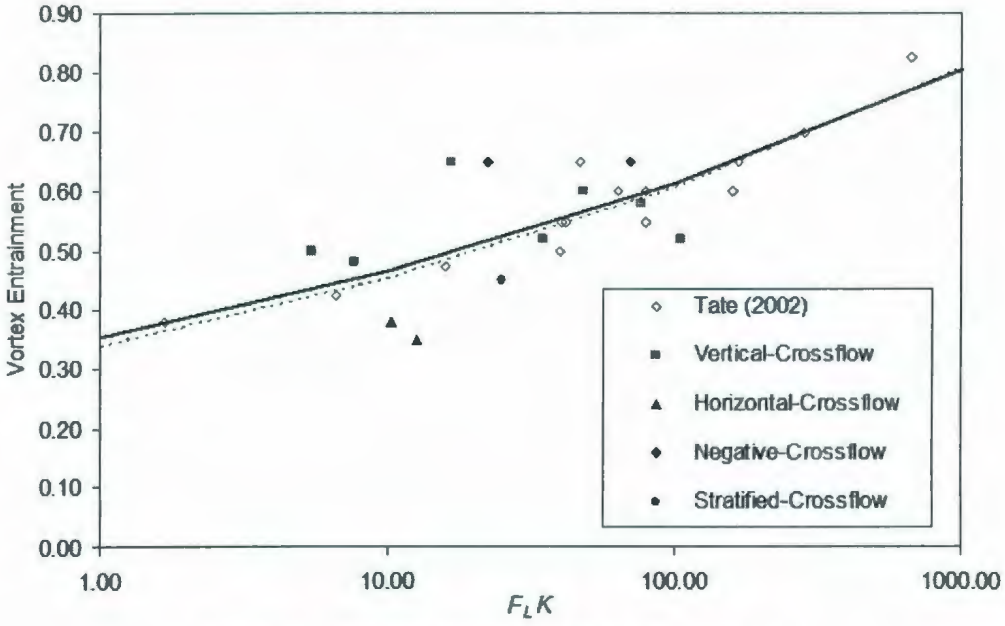

Figure 22. The vortex entrainment as a function of $F_L K$.

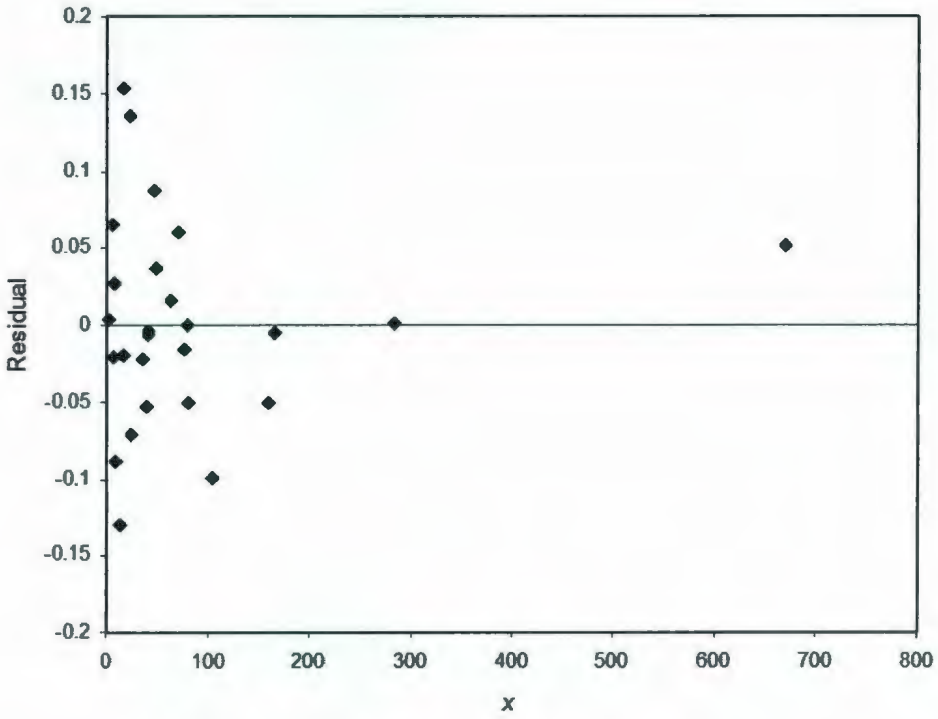

Figure 23. Residual plot for the entrainment coefficients.

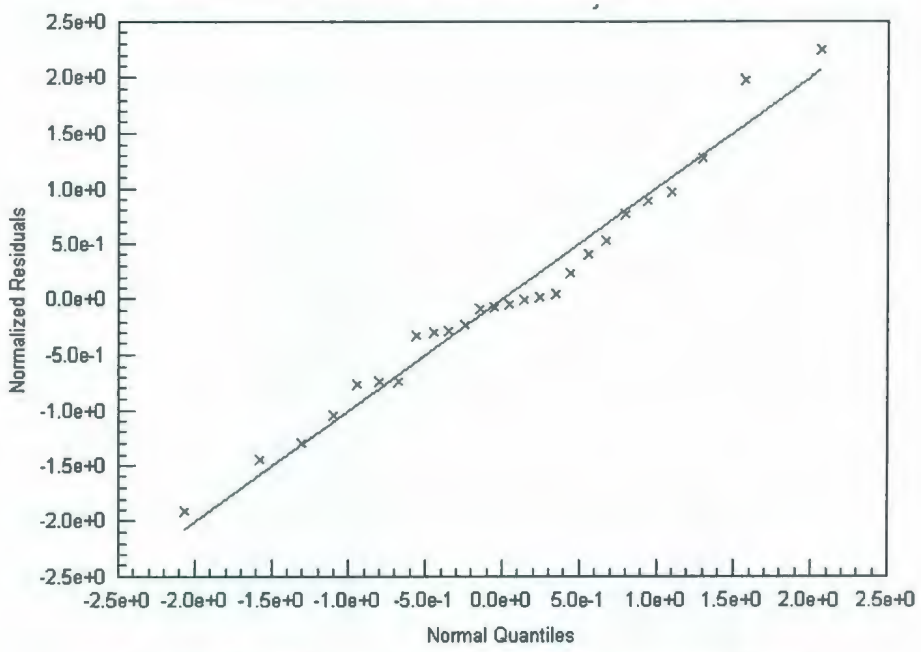

Figure 24. Residual normality plot for the entrainment coefficients.

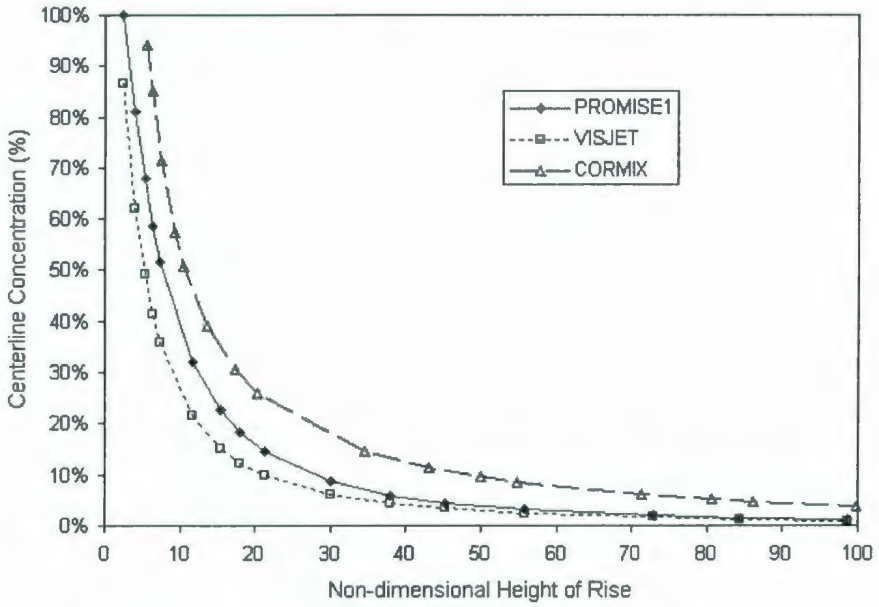

Figure 25. Comparison of PROMISE with CORMIX and VISJET.

3.1.2 PROMISE2 – Wave Effects on Initial Mixing

The PROMISE2 studies the effects of waves on initial mixing, which includes both the effects of surface waves and internal waves.

3.1.2.1 Effects of Surface Waves

The effects of ocean surface waves on the initial mixing process have long been a concern. The earliest study of the influences of waves on the initial dilution can be traced back to Shuto and Ti (1974). A vertical buoyant jet was discharged into a 7.4 m long, 0.75 m high, and 0.5 m wide wave tank. It is found by Shuto and Ti (1974) that the time-averaged surface dilution with the influence of waves is higher than that without the influence of waves. The dilution is inversely proportional to the square of the ratio of water depth to the port diameter and is proportional to the ratio of the discharge velocity to a characteristic horizontal velocity of the ambient.

Ger (1979) studied a horizontally discharged buoyant jet from circular ports. It was observed by Ger (1979) that the axial dilution varies linearly with the horizontal distance, and the rate of change of dilution is highly dependent on the wave characteristics.

Sharp (1986) studied a vertically discharged buoyant jet into waves qualitatively. The jet was discharged via a 12.7 mm diameter pipe into a 58.2 m long, 4.6 m wide and 3.0 m deep wave tank. Both deep and shallow water waves were generated. It is suggested by Sharp (1986) that in the area close to the port the jet was not significantly disturbed by the deep water waves but was enormously affected by shallow water waves.

Chin (1987) studied the influence of intermediate water surface waves on the initial mixing process. A dimensional analysis was used to characterize the wave effects. It was found that for a wave with a period of 5 s and amplitude of 30cm, the dilution was increased by a factor of 2. As the length scale formulation by Chin (1987) is only based on limited conditions, Chin (1988) developed a Lagrangian model which enables the study on wave effects for a wider range of source and ambient conditions.

Chyan and Hwung (1993) studied the vertical buoyant jets in a wave environment using Laser Induced Fluorescence (LIF) measurements. It was concluded by Chyan and Hwung (1993) that the vertical jet is more sensitive to the wave action than the horizontal jet parallel to the propagating wave. However, a horizontal jet orthogonal to the propagating wave may be more efficient in the enhancement of initial dilution.

While the concentration and velocity profile for a buoyant jet are normally Gaussian in an environment without waves, the study by Koole and Swan (1994) noted the occurrence of "flat-topped", and in particular, "bi-peaked" velocity and

concentration profiles for buoyant jets in a wave environment. This phenomena was also observed by Sharp (1986) and Chyan and Hwung (1993). This non-Gaussian profile makes it difficult to simulate the wave effect using most integral models. As suggested by Koole and Swan (1994), a three-fold increase in the radial entrainment coefficient may be used for two dimensional cases, but it is unlikely that one universal entrainment will be applicable to three dimensional cases. For this reason, a length scale approach rather than an integral approach will be employed in this research to account for the effects of surface waves on initial dilution.

3.1.2.2 Length Scale Formulation

The surface dilution, S, of a submerged buoyant jet in an unstratified environment may be written in the functional form

$$S = f(D, U_j, U_a, g', Z, \theta_1, \phi, \theta, a, T_p) \tag{145}$$

where θ is the horizontal angle with respect to the current direction (x-axis), ϕ is the vertical angle with respect to horizontal plane, θ_1 is the angle relative to the direction of wave propagation, Z is the water level above discharge, U_j is the discharge velocity, U_a is the ambient velocity, g' is the effective gravity, D is the port diameter, a is the wave amplitude, and T_p is the wave period.

The Equation (145) may be alternatively formulated using the discharge fluxes, M, B, and Q as

$$S = f(M, B, Q, U_a, Z, \theta_1, \phi, \theta, ag, T_p) \tag{146}$$

where g is the acceleration due to gravity. The dominant mechanisms affecting the dilution of the effluent may be more easily identified using length scales. In the previous chapter, two length scales, L_Q and L_M have been introduced. To study the wave effects, Chin (1987) derived two additional length scales, they are

$$Z_M = \frac{M^{1/2}}{u_{\max}} \tag{147}$$

$$Z_B = \frac{B}{u^3_{\max}} \tag{148}$$

where Z_M is a length scale that measures the distance required for the jet momentum to be on the order of the wave-induced momentum, and Z_B measures the distance required for buoyancy induced momentum to be on the order of the wave-induced momentum. The wave induced velocity $u_{\max}$ is defined as

$$u_{\max} = \frac{agk_w}{\sigma_w \cosh k_w h_{water}} \tag{149}$$

where σ_w is the wave frequency, and k_w is the wave number, h_{water} is the water depth.

Nondimensionalizing Equation (146) using the Buckingham Pi Theorem and utilizing the four length scales defined above yields

$$S = f(\frac{Z}{L_M}, \frac{L_M}{L_Q}, \frac{Z_M}{L_Q}, \frac{h_{water}}{L_w}, \frac{U_a}{u_{\max}}, F_r, \theta_1, \phi, \theta) \tag{150}$$

where L_w is the wave length. The Z_B is excluded from Equation (150) because it is not an independent length scale. The ratio h_{water}/L_w measure the shape of wave induced velocity profile, and $U_a/u_{\max}$ measure the relative importance of ambient velocity and wave induced velocity.

For a given discharge with known discharge angles, the Equation (150) can be simplified as

$$S = f(\frac{Z}{L_M}, \frac{L_M}{L_Q}, \frac{Z_M}{L_Q}, \frac{h_{water}}{L_w}, \frac{U_a}{u_{\max}}, F_r) \tag{151}$$

To date, no experiment has been performed in flowing environments to derive empirical relations based on Equation (151), therefore, it is assumed in this study that

the effects of waves on initial dilution are the same in flowing and stagnant environments. The term U_a/u_{max} is vanished.

As indicated by Hwung et al. (1994), in most practical conditions, $H >> L_M >> L_Q$. By neglecting the effects of Z/L_M, L_M/L_Q, U_a, and F_r, Chin (1987) derived the following Equation.

$$\frac{S_{wave}}{S_{nowave}} = 1 + C_w \frac{L_Q}{Z_M} \tag{152}$$

where C_w is an empirical coefficient. The h_{water}/L_w is excluded from Equation (152) as it is not independent of Z_M/L_Q. The same Equation has been used by Hwung et al. (1994) and Chyan et al. (2002).

In this study, a new formulation is proposed to consider the effects of Z_{water}/L_M, and Fr. Based on the numerical simulation of Hwang et al. (1996) and the experimental data of Chin (1987), two new Equations are proposed.

For deep water discharges, with Z_{water}/L_M greater than 9.03, a power law relationship can be used (Equation 153) and the relationship is shown in Figure 26. The regression has an R^2 of 0.95.

$$\frac{S_{wave}}{S_{nowave}} = 1 + \left(0.4574 F_r^{0.8818}\right) \frac{L_Q}{Z_M} \tag{153}$$

For shallow waters with Z_{water}/L_M less than 4.51, a power law relationship can be used (Equation 154) and the relationship is shown in Figure 27. The regression has an R^2 of 0.99.

$$\frac{S_{wave}}{S_{nowave}} = 1 + \left(0.3807 F_r^{0.6351}\right) \frac{L_Q}{Z_M} \tag{154}$$

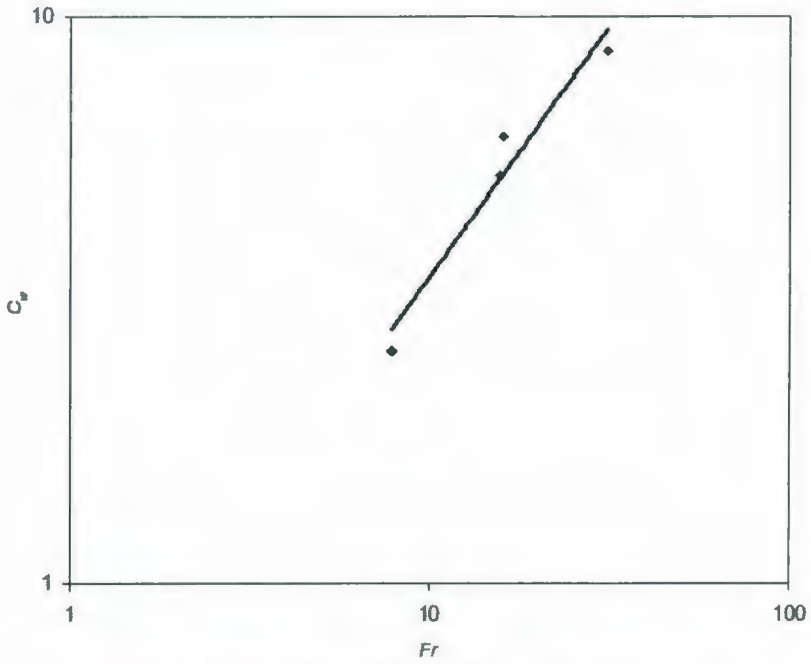

Figure 26. Relationship between F_r and C_w (deep water case).

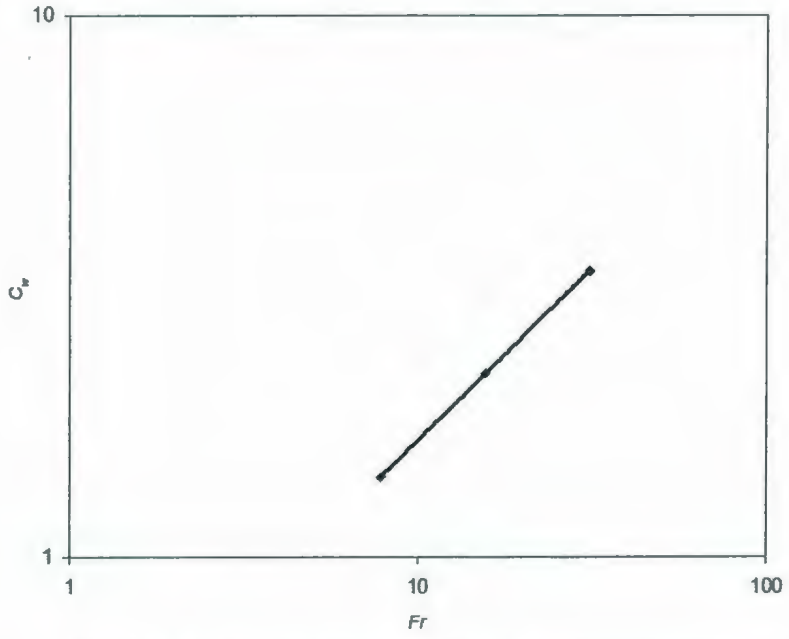

Figure 27. Relationship between F_r and C_w (shallow water case).

To validate the proposed Equations, experimental data of Chin (1987) and Hwang et al. (1996) were used. Their data has a Z_{water}/L_M value of 9 and therefore only Equation (153) was used. The comparison is shown in Figure 28. It can be seen from Figure 28 that the new Equation agrees with experimental data well. It should be mentioned that the new Equations were developed based on limited data sources; further validation against more extensive experimental data is suggested.

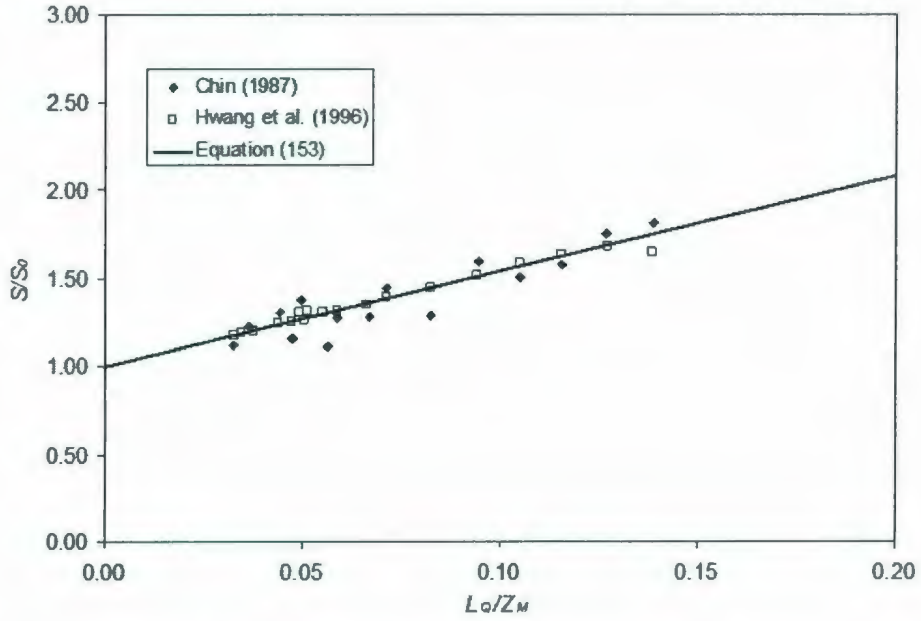

Figure 28. Validation of Equation (153) against experimental data.

3.1.2.3 Calculation of Waves

In this study, Equations (155) and (156) will be used to compute the wave height (H) and wave period (T_w) as functions of wind speed (U_{wind}), water depth h_{water}, and fetch F, and gravitational acceleration g. These Equations are taken from the U.S. Army Corps of Engineers Shore Protection Manual (1984).

$$\frac{gH}{U_{wind}^2} = 0.283 \tanh\left[0.530\left(\frac{gh_{water}}{U_{wind}^2}\right)^{3/4}\right] \tanh\left\{\frac{0.00565\left(\frac{gF}{U_{wind}^2}\right)^{1/2}}{\tanh\left[0.530\left(\frac{gh_{water}}{U_{wind}^2}\right)^{3/4}\right]}\right\} \quad (155)$$

$$\frac{gT_w}{U_{wind}^2} = 7.54 \tanh\left[0.833\left(\frac{gh_{water}}{U_{wind}^2}\right)^{3/8}\right] \tanh\left\{\frac{0.0379\left(\frac{gF}{U_{wind}^2}\right)^{1/3}}{\tanh\left[0.833\left(\frac{gh_{water}}{U_{wind}^2}\right)^{3/8}\right]}\right\} \quad (156)$$

3.1.2.4 Effects of Internal Waves

Vertical motions along density contours have been recorded since the early days of oceanography (Figure 29). They were often treated as noise and filtered out of the record but latterly they have been recognized as internal waves.

These internal waves propagate along the density interfaces in the water column and they can reach amplitudes of more than 100m. Therefore, they may have significant impacts on the marine environment, and for example, the impacts on the initial dilution of a produced water outfall. It has been described in the previous chapter that the rise and dilution of buoyant jets are affected by various parameters, such as density stratification. The terminal rise height and dilution are affected by the location and magnitude of stratification. The passage of an internal wave may have a significant effect on the location of the stratification in the water column, as a result, it may significantly affect the rise and dilution of buoyant jets.

The internal wave effect model used in this study is an adoption of work by Tate (2002). In contrast to previous approaches, which assumed that the buoyancy frequency is only a function of water depth, Tate (2002) proposed an Equation that

assumed the buoyancy frequency is a function of both water depth and time. The new formulation enables the incorporating of internal wave effects by varying the boundary conditions defining the stratification at each time step. The details of the formulation are referred to in Tate (2002).

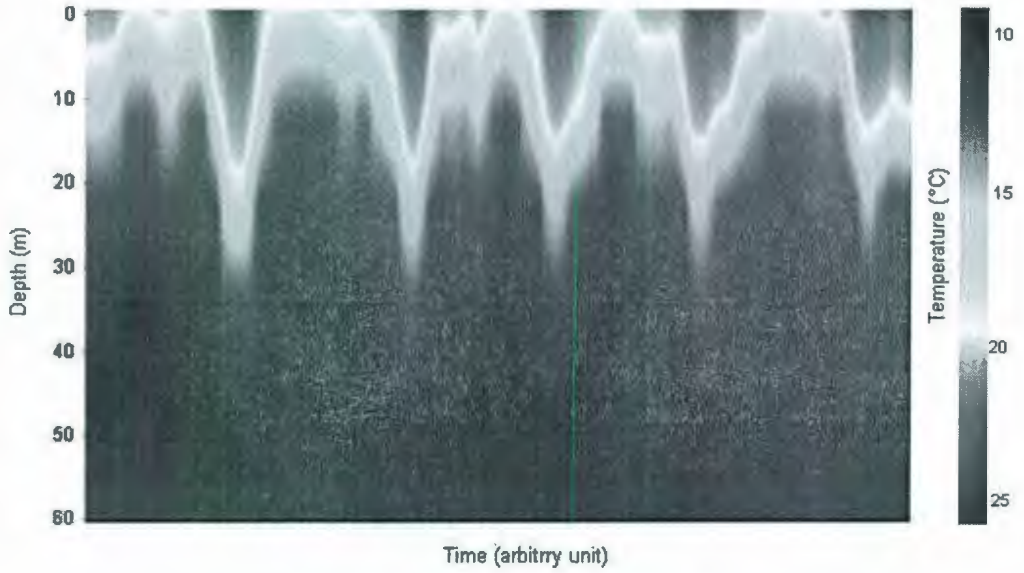

Figure 29. Vertical temperature profile.

3.1.2.5 Modeling the Effects of Waves on Initial Dilution

It can be seen from the analysis above, both surface waves and internal waves may have significant effects on the initial dilution. However, the overall effects of these two mechanisms on the initial dilution are still unknown. Similar to the case of shear entrainment and vortex entrainment, two hypotheses may be used to model the overall effects. They are the maximum hypothesis and the additive hypothesis. To prevent the over estimation of wave effects, a maximum hypothesis is adopted by PROMISE2.

3.1.3 PROMISE3 – Upstream Intrusion and Downstream Control

After the plume reaches the surface or an internal density jump layer, impingement may take place (as shown in Figure 30). The plume will be deflected horizontally and spread downstream. Depending on the impingement angle, the plume may spread upstream (named upstream intrusion). Most existing models except the CORMIX model do not include this intermediate mixing behavior.

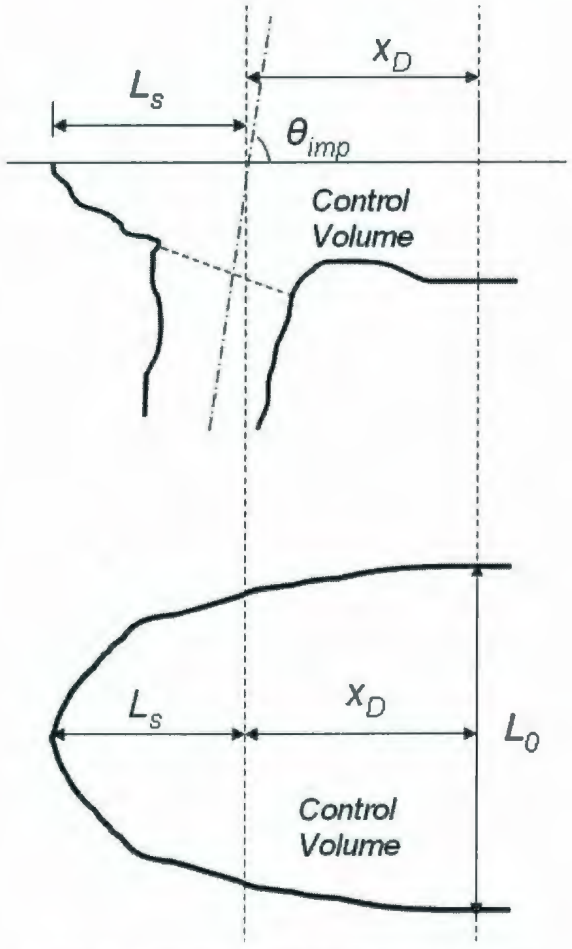

Figure 30. Upstream intrusion and control volume.

Mukhtasor (2001) adopted the formulation of Huang et al. (1996) to analyse the intermediate field mixing behaviors of produced water. A formulation similar to those used by Mukhtasor (2001) and Huang et al. (1996) will be used by PROMISE3. However, by taking advantage of its integral type initial mixing model (PROMISE1), PROMISE3 uses a more accurate impingement angle θ_{imp} to calculate the upstream intrusion length L_s and downstream plume width L_0. The formulations for the upstream intrusion and downstream control are summarized below.

For a weakly deflected plume (θ_{imp}>45°), the plume width at the downstream end of the control volume is estimated as (Doneker and Jirka 1990, Huang 1996, Mukhtasor 2001):

$$L_0 = 5.2L_s \tag{157}$$

The upstream intrusion length L_s can be estimated by (Doneker and Jirka, 1990; Huang et al., 1996; Mukhtasor 2001):

$$L_s = 2.12H^{3/2}(1-\cos\theta_{imp})^{3/2}L_b^{-1/3} \qquad \text{for } L_s/Z \le 6.11(1-\cos\theta_{imp}) \tag{158}$$

$$L_s = 0.38L_b \qquad \text{for } L_s/Z > 6.11(1-\cos\theta_{imp}) \tag{159}$$

The length scale formulation of Huang et al. (1996) and Mukhtasor (2001) cannot provide the impingement angle accurately and they estimated the angle using $\theta_{imp} = \tan^{-1}(Z/x_b)$. On the contrary, the integral formulation of PROMISE1 enables the detailed outputs of 3D plume trajectory and the impingement angle, which enables PROMISE3 to give a more accurate estimation of upstream intrusion length L_s and downstream plume width L_0.

For a relatively strongly deflected plume, the plume width L_0 at the downstream end of the control volume and the upstream intrusion length are estimated by

$$L_0 = 2\sqrt{\frac{S_{ave}Q}{2U_a}} \tag{160}$$

$$L_s = \frac{1}{\sin\theta_{imp}}\sqrt{\frac{S_{ave}Q}{\pi U_a}} \tag{161}$$

where S_{ave} is the average dilution at the end of control volume. The S_{ave} is about 4 times the initial dilution for a weakly deflected jet and about 1.75 times the initial dilution for a strongly deflected jet. The Equation (160) is based on an equivalent cross-section aspect ratio for the outflow section of 2:1. In other words, the width L_0 is two time the thickness b_{v0}.

3.1.4 PROMISE4 – Buoyant Spreading and Turbulent Mixing

The buoyant spreading and turbulent diffusion have been described in Chapter 2. Most of the existing models only consider the turbulent diffusion and do not have a buoyant spreading model. Mukhtasor (2001) adopted a buoyant spreading model from CORMIX bur did not take account of turbulent diffusion. CORMIX is the only model that considered both buoyant spreading and turbulent diffusion.

The disadvantage of CORMIX is that the buoyant spreading and turbulent diffusion models used are separate and the transition point between these two mechanisms needs to be determined by a Richardson number.

In this study, a new buoyant spreading/turbulent diffusion approach will be used to model the buoyant spreading and turbulent diffusion process. This study uses a unified model rather than separate buoyant spreading and turbulent diffusion models. If the vertical turbulent diffusion is unimportant, this model will cover the whole modeling domain. The advantage of this approach is that both mechanisms are

considered at the same time where the previous approach only considers the dominant mechanism in certain regions. If the vertical turbulent diffusion needs to be considered, a two stage approach is used. In the first stage, the previous study only considered buoyant spreading and neglected both horizontal and vertical turbulent diffusion. This study will also neglect the vertical turbulent diffusion in this stage because it is very small when compared with horizontal diffusion and buoyant spreading. However, unlike the previous approach, the horizontal turbulent diffusion is considered in this stage rather than neglected. After a certain distance where the buoyant spreading becomes less important, the vertical turbulent diffusion is then considered as it becomes comparable to the horizontal diffusion. Unlike CORMIX, where a constant vertical mixing was used, this study uses an energy dependent vertical mixing coefficient. The formulations of PROMISE4 are described below.

3.1.4.1 Unified Buoyant Spreading and Turbulent Diffusion Model

A. Huang and Fergen's (1997) Formulation

The unified buoyant spreading/turbulent diffusion model is a modification of a model proposed by Huang and Fergen (1997). The original Huang and Fergen's (1997) model is only applicable for surface spreading. By modification of modeling coefficients, the model has been expanded for the cases of internal layer buoyant spreading.

By assuming that the mixing is governed by buoyant spreading and horizontal turbulent diffusion, the mixing behavior of a plume can be described by Equation (162) as (Huang and Fergen, 1997)

$$\frac{U_a}{2}\frac{d(Lb_v)}{dx} = E_b + E_t \tag{162}$$

where E_b is the bulk entrainment per unit width of the plume boundary due to buoyant spreading, and E_t is the effective entrainment due to turbulent diffusion. E_b can be estimated by (Britter and Simpson, 1978)

$$E_b = \alpha_1 u_b b_v \tag{163}$$

where α_1 is the entrainment coefficient for buoyant spreading. A value of 0.6 can be used for α_1 based on the laboratory experiments of Britter and Simpson (1978) and the field experiments of Luketina and Imberger (1986). The u_b is the propagation speed of the plume boundary and can be estimated by the formulation of Benjamin (1967)

$$u_b = \alpha_2 \sqrt{g' b_v} \tag{164}$$

For a surface spreading case, the α_2 is suggested by Luketina and Imberger (1986) as 0.57. Similiarly, the E_t can be estimated by (Huang and Fergen, 1997)

$$E_t = u_t b_v \tag{165}$$

where the u_t is effective propagation speed of the plume boundary due to horizontal turbulent diffusion. The u_t can be related to lateral diffusivity K_y and plume width L as (Huang and Fergen, 1997)

$$u_t = 6\frac{K_y}{L} \tag{166}$$

The plume width L is assumed to be $2\sqrt{3}\sigma$. Where the σ is the standard deviation of the concentration distribution across the plume width.

By combination of Equations (162) to (166), the continuity Equation becomes (Huang and Fergen 1997)

$$\frac{U_a}{2}\frac{d(Lb_v)}{dx} = \alpha_1\alpha_2\sqrt{\frac{B}{U_a L}} + 6\frac{K_y}{L}b_v \tag{167}$$

At the plume boundary which is also a streamline, this yields (Huang 1998)

$$\frac{U_a}{2}\frac{dL}{dx} = u_b + u_t \tag{168}$$

By rearranging Equation (168), Huang and Fergen (1997) derived the following governing Equations for the surface spreading case:

$$\frac{dL}{dx} = \frac{2}{U_a}\left[\alpha_2\sqrt{\frac{B}{U_a L}} + 6\frac{K_y}{L}\right] \tag{169}$$

$$\frac{db_v}{dx} = \frac{2}{U_a}\alpha_2(\alpha_1 - 1)\sqrt{\frac{B}{U_a L}}\frac{b_v}{L} \tag{170}$$

The initial conditions are $L=L_0$, and $b_v=b_{v0}$. The L_0 is the plume width at the downstream end of the control volume and b_{v0} is the plume thickness at the downstream end of the control volume. The b_{v0} can be estimated by Doneker and Jirka (1990) as

Strongly deflected plume: $$b_{v0} = \left(\frac{S_{ave}L_m L_Q}{2}\right)^{1/2} \tag{171}$$

Weakly deflected plume: $$b_{v0} = \left(\frac{S_{ave}L_m L_Q}{L_0}\right) \tag{172}$$

B. Modifications

In Huang and Fergen's (1997) formulation, a constant α_2 value of 0.57 was used. Although Doneker and Jirka (1990) suggested that the α_2 for a surface buoyant spreading case is dependent on the relative depth of the plume to the water depth, they used a constant value of 0.70 in the CORMIX model.

In this study, a variable α_2 rather than a constant α_2 will be used with Equations (169) and (170). The formulation of α_2 is based on the Equation suggested by Jirka and Arita (1987)

$$\alpha_2 = \sqrt{\frac{(1-b_v/H)(2-b_v/H)}{(1+b_v/H)}} \tag{173}$$

where the $0 \le b_v/H \le 1$ and this gives α_2 values in a range from 0.70 to 1.41.

The above formulations were only applicable for surface spreading of plumes in unstratified cases. The majority of discharges, especially for produced waters, are in stratified environments. The above Equations must be modified to consider the stratification effects.

To modify the above Equation, formulation of u_b for stratified cases by Doneker and Jirka (1990) are used

$$u_b = \alpha_3 \sqrt{\varepsilon_D b_v^2} \tag{174}$$

where the $\alpha_3 = \sqrt{1/2C_D}$ is a constant for the stratified case. C_D is a drag coefficient. By substituting Equations (166) and (174) into Equation (162), the continuity Equation for the stratified case becomes

$$\frac{U_a}{2}\frac{d(Lb_v)}{dx} = \alpha_1\alpha_2\left(\sqrt{\varepsilon_D b_v^2} + 6\frac{K_y}{L}\right)b_v \tag{175}$$

Similar to Equation (169) and (170), the governing Equations for stratified cases are

$$\frac{dL}{dx} = \frac{2}{U_a}\left[\alpha_3\sqrt{\varepsilon_D b_v^2} + 6\frac{K_y}{L}\right] \tag{176}$$

$$\frac{db_v}{dx} = \frac{2}{U_a}\alpha_3(\alpha_1 - 1)\sqrt{\varepsilon_D}\frac{b_v^2}{L} \tag{177}$$

The above ordinary differential Equations can be solved using a fourth-order Runge-Kutta method.

The solution of the above unified buoyant spreading and turbulent diffusion (BS+TD) model was compared with the buoyant spreading (BS) only and turbulent diffusion (TD) only formulations of the CORMIX model. Five test cases with different R_{bt} ratios ranging from 0.1 to 200 were conducted. The R_{bt} is the ratio of E_b to E_t which stands for the relative importance of buoyant spreading and turbulent diffusion. For small R_{bt} values, the buoyant spreading is very weak and the turbulent diffusion dominates, while for large R_{bt} values, the buoyant spreading dominates and turbulent diffusion is weak. The results are shown in Figures 31 to 35.

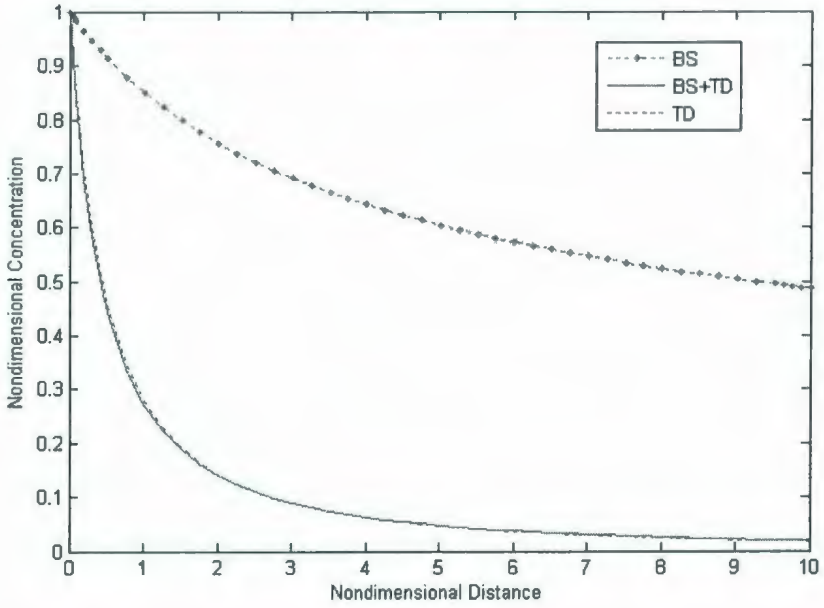

Figure 31. Nondimensional concentration versus nondimensional distance (very weak BS, initial R_{bt}=0.1).

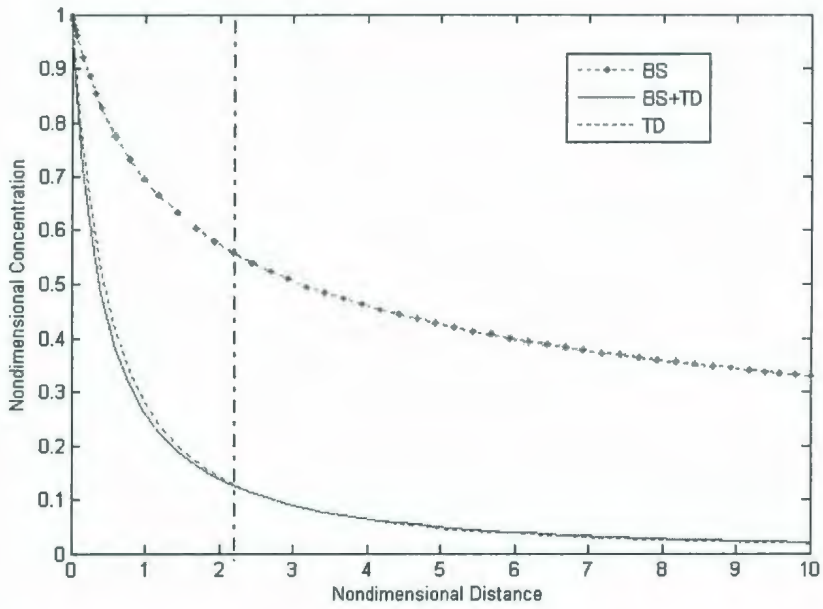

Figure 32. Nondimensional concentration versus nondimensional distance (weak BS, Initial R_{bi}=0.3).

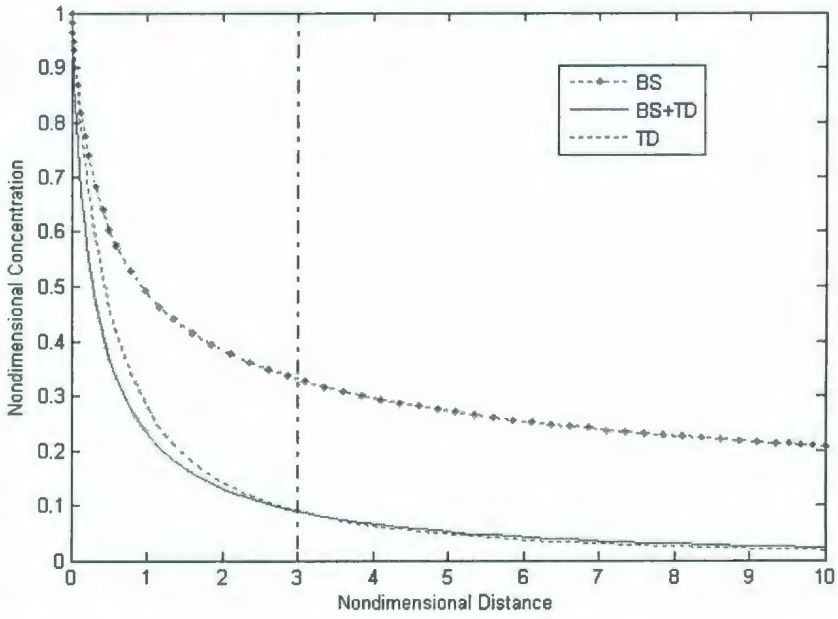

Figure 33. Nondimensional concentration versus nondimensional distance (same BS and TD, Initial R_{bi}=1).

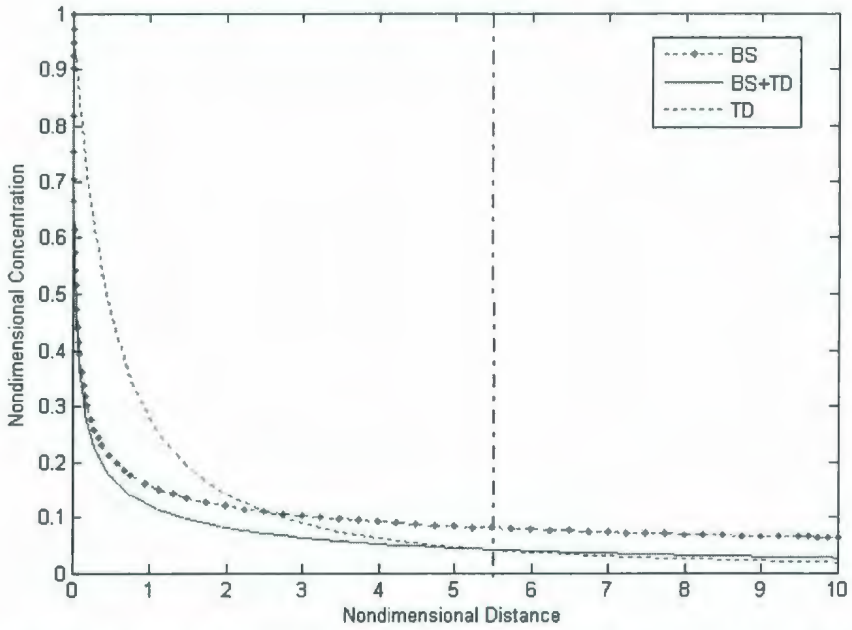

Figure 34. Nondimensional concentration versus nondimensional distance (strong BS, Initial R_{bi}=20).

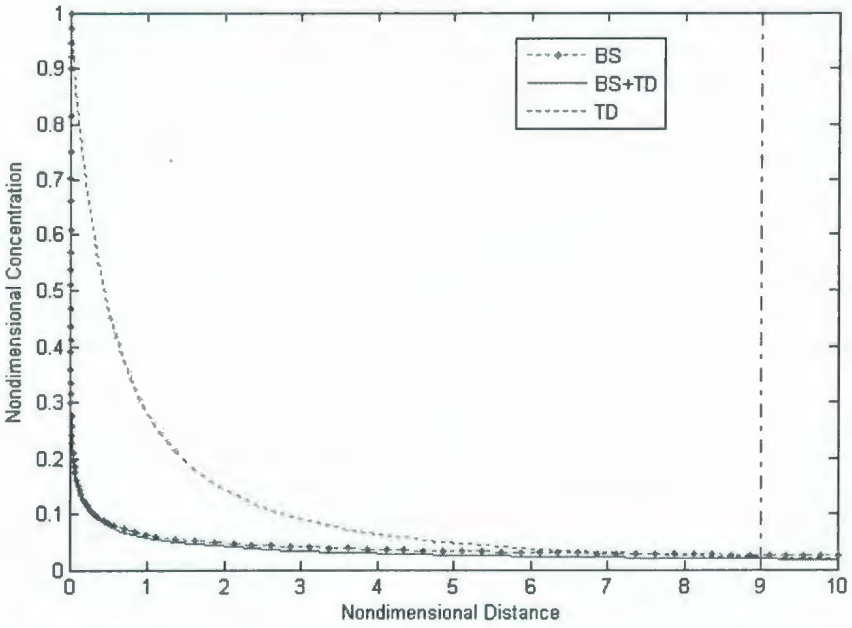

Figure 35. Nondimensional concentration versus nondimensional distance (very strong BS, Initial R_{bi}=200).

For the very weak buoyant spreading case (Figure 31), for example E_b is only 1/10 E_t, the unified solution and the turbulent diffusion model overlap together. This implies that the buoyant spreading has almost no effects on the dilution in this case. If a buoyant spreading formulation is used in this case, it will underestimate the dilution and result in a high concentration.

For the weak buoyant spreading case (Figure 32), for example E_b is 3/10 E_t, the unified solution and the turbulent diffusion model are separated at the beginning. This implies that the buoyant spreading has started to affect the dilution. The unified solution is very close to the turbulent diffusion solution because this is a turbulent diffusion dominated case. The unified model predicted the lowest concentration because it considered both the buoyant spreading and turbulent diffusion. However, when the plume moves downstream, the unified model and turbulent diffusion only model start to overlap again at a nondimensional distance of 2.2. The reason is that additional ambient fluids have been entrained into the plume as it moves downstream and the buoyancy gradually diminished. At a nondimensional distance of 2.2, the buoyancy has completely diminished and only the turbulent diffusion effect is present and therefore the two solutions overlap together again. If a buoyant spreading formulation is used in this case, it will underestimate the dilution and result in a high concentration.

For the case that the initial E_b and E_t are of the same order (Figure 33), $R_{bt}=E_b/E_t=1$, the unified solution and the turbulent diffusion model are separated further at the beginning due to the increased effects of buoyant spreading. The unified model predicted the lowest concentration because it considered both the buoyant spreading and turbulent diffusion. As the plume moves downstream, the buoyancy

effects diminish and it becomes completely diminished at a nondimensional distance of 3.0. From this point forward, only the turbulent diffusion is in effect and the unified solution and turbulent diffusion solution overlap again.

For the case of strong buoyant spreading (Figure 34), for example E_b is 20 E_t, the unified solution (BS+TS) is close to the buoyant spreading (BS) solution at the beginning because this is a buoyant spreading dominated case. The unified model predicted the lowest concentration because it considered both the buoyant spreading and turbulent diffusion. When the plume moves downstream, the buoyancy effects gradually diminish, the buoyant spreading (BS) solution then becomes separated from the unified (BS+TD) solution. The turbulent diffusion (TD) solution becomes close to the unified (BS+TS) solution because it gradually becomes the dominant mixing mechanism. At a nondimensional distance of 5.5, the turbulent diffusion (TD) solution and the unified (BS+TD) solution overlap together.

For a very strong buoyant spreading case (Figure 35), for example E_b is 200 E_t, the trend of mixing is similar to the R_{bt}=20 case. However, it can be seen from Figure 35 that it takes a long distance for the buoyant spreading (BS) to separate from the unified (BS+TD) solution because the strong buoyancy in this case needs a longer time to diminish. It also takes a longer time and distance for the turbulent diffusion to become dominant.

The nondimensional plume width and thickness of the unified model for various R_{bt} values are shown in Figures 36 and 37. It can be seen from Figure 36 that the plume width increased rapidly for the very strong initial buoyancy case. If the initial buoyancy is very weak, the plume width increased slowly by the ambient turbulent diffusion.

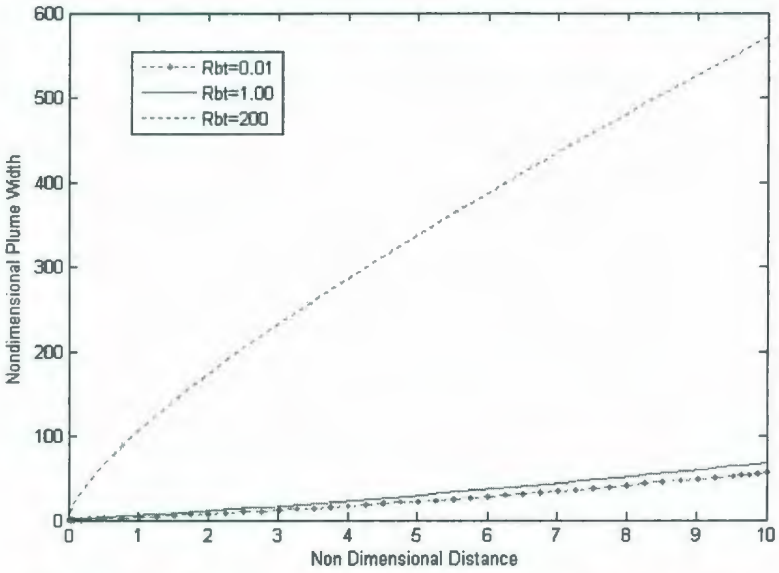

Figure 36. Nondimensional plume width versus nondimensional distance.

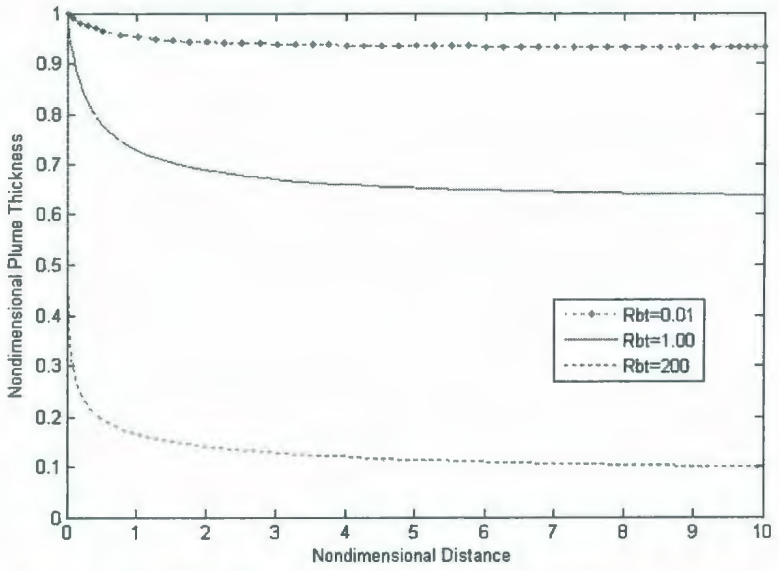

Figure 37. Nondimensional plume thickness versus nondimensional distance.

Similarly, it can be seen from Figure 37 that if the plume has strong initial buoyancy, the buoyancy will drive the plume to spread into a very thin layer. If the initial buoyancy is very weak, it does not have many effects on changing the plume

thickness. It should be noted that the vertical turbulent diffusion was not considered in this unified model, therefore the plume thickness for this weak buoyancy case did not change. If the vertical turbulent diffusion is considered, the plume thickness will increase. This turbulent diffusion will be considered by PROMISE4 after the overlap points.

3.1.4.2 Vertical Turbulent Diffusion

When the plume travels farther downstream and the buoyancy effect diminishes, the buoyant spreading becomes less important. At this point, it may be necessary to consider the vertical turbulent mixing because although it is still small compared with horizontal turbulent mixing, it is of a comparable order.

The above formulations did not consider the vertical mixing and the formulation by Doneker and Jirka (1990) will be used:

$$L = 2L_1\left[1+\frac{\pi}{3}K_{y1}\frac{(x-x_1)}{\left(U_a\frac{L_1}{2}\right)^2}\right]^{3/2} \tag{178}$$

$$b_v = \left[\pi K_z\frac{(x-x_1)}{U_a}+b^2{}_{v1}\right]^{1/2} \tag{179}$$

where x_1 is the distance from discharge to the end of unified model zone, K_{yl} is the initial horizontal turbulent diffusion coefficient at x_1, and K_z is the vertical turbulent diffusion coefficient, b_{vl} and L_1 is the plume thickness and width at the end of unified buoyant spreading/turbulent diffusion model. The K_{yl} has been suggested by Doneker and Jirka (1991) as

$$K_{yl} = 0.0015 L_l^{4/3} \tag{180}$$

and the K_z has been suggested as

$$K_z = 0.2 u_* h_{water} \tag{181}$$

where u_* is a shear velocity.

In this study, the vertical turbulent diffusion coefficient (Equation 181) will be replaced with different formulations. For a stratified case, the K_Z is estimated using the empirical relation based on the field measurements (Figure 38). The regression gives an empirical relation as

$$K_z = \frac{0.0129}{\varepsilon_D^{0.897}} \tag{182}$$

For the unstratified case, the density gradient in the surface layer is often zero. The vertical transport is governed primarily by the vertical turbulence created by wind and wave, therefore, the Equation proposed by Golubeva (1963) is used:

$$K_z = \frac{H}{T_w} \tag{183}$$

where the H is the wave height and T_w is the wave period.

For the east coast of Canada, the most frequently occurring waves are less than 3 m and have periods around 10 s (TDC, 1991). The Equation (182) gives a K_z less than 180 cm^2/s.

The advantage of using this formulation is that it enables the analysis of wave effects on far field mixing.

While the plume width and thickness can be calculated by Equations (169), (170), (176), (177), (178), and (179), PROMISE4 uses the formulation by Huang *et al.* (1996) to calculate the concentration field

$$C(x,y) = 1.832\frac{C_0}{S_{ave}}\frac{b_{v0}}{b_v(x)}\frac{1}{2}\left[erf\left(\frac{0.273L_0 + y}{\sqrt{2}\sigma(x)}\right) + \left[erf\left(\frac{0.273L_0 - y}{\sqrt{2}\sigma(x)}\right)\right]\right] \quad (184)$$

where $C(x, y)$ is the concentration at location (x, y), L_0 is the plume width at the end of the control volume, b_{v0} is the plume thickness at the end of the control volume, $b_v(x)$ is the plume thickness at location x, S_{ave} is the dilution at the end of the control volume, and $\sigma(x)$ is the standard deviation of plume concentration at location x.

The advantage of this formulation over the CORMIX model and the Visual Plumes model is that it considers the variation of concentration along the y-axis.

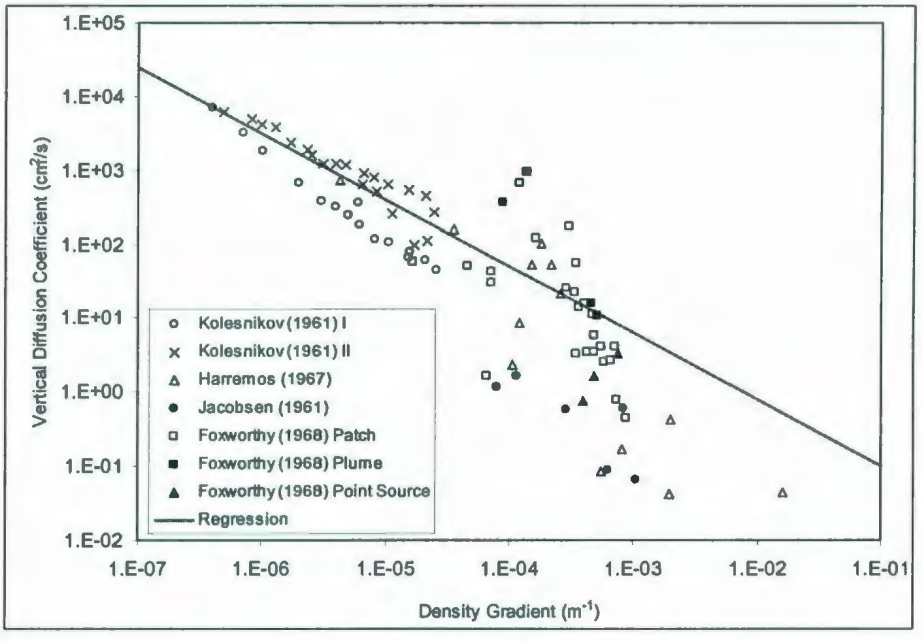

Figure 38. Correlation of K_Z with density gradient.

3.1.5 PROMISE5 – Food Chain Model

Although the major objective of this study is the development of hydrodynamic model, a simple food chain model (Reed et al., 1996) is integrated with the hydrodynamic model to study the biological effects.

The food chain model has four components: Bacteria/Phytoplankton, Zooplankton (Calanus copepods), Krill, and Pelagic Fish. The concentration of pollutant in Bacteria/Phytoplankton is estimated by assuming equilibrium partitioning kinetics:

$$\frac{C_p}{C_{disol}} = K_p C_{phyto} \tag{185}$$

where C_p is the absorpted concentration on phytoplankton, C_{disol} is the dissolved concentration. K_p is the equilibrium partitioning coefficient, and C_{phyto} is the concentration of plankton in the water column.

The concentration of pollutants in the Zooplankton (Calanus copepods), Krill, and Pelagic Fish are assumed to be a combination of adsorption across gill membranes and ingestion of lower trophic organisms. The concentration on the phytoplankton can be calculated from

$$C_p = K_p C_{phyto} C_{total} / (1 + K_p C_{phyto}) \tag{186}$$

where total concentration of a substance averaged over a given volume of water, C_{total} is

$$C_{total} = C_d + C_p + C_z + C_k + C_f \tag{187}$$

where C_z is the concentration in zooplankton, and C_k is the concentration in Krill and C_f is the concentration in fish. The concentration on zooplankton is give as

$$C_p = (K_z C_d + K_{grazingz-p} C_p) / K_{z-dep} \quad (188)$$

The concentration on Krill is give as

$$C_p = (K_k C_d + K_{grazingk-z} C_z) / K_{k-dep} \quad (189)$$

The dynamic Equation for bioaccumulation and depuration for Fish is given as

$$C_p = \left[\frac{(-K_f C_d + K_{grazingf-k} C_k)}{K_{f-dep}} + C_{f0} \right] \exp(-K_{f-dep}) + \frac{K_f C_d + K_{grazingf-k} C_k}{K_{f-dep}} \quad (190)$$

where the C_{f0} is the internal concentration in the fish at the beginning of the exposure. The $K_{grazing-}$ and K_{-dep} are the grazing and depuration parameters.

3.2 PROBABILISTIC BASED APPROACH

For computation of exposure concentration using dispersion models, two approaches can be used: deterministic based approach and probabilistic based approach.

The deterministic approach calculates a single value exposure concentration by considering the combination of a number of single value parameters. The advantage of the deterministic based approach is its simplicity. However, the results derived from this approach may be insufficient in many cases because the uncertainty and variability associated with the model parameters are not considered.

Unlike the deterministic based approach, a probabilistic approach considers parameter variability, which is often described in terms of time series or probability distributions. This approach is often implemented using a Monte Carlo simulation method and the result is a probabilistic description of concentrations. Several applications of probabilistic based assessment of effluent discharges into rivers have

been reported (Bumgardner et al., 1993; Donigian and Waggy, 1974). Huang *et al.* (1996) used this approach to model a sewage ocean outfall. More recently, this approach was adopted by Mukhtasor (2001) to model the dispersion of produced water in the marine environment.

In the following sections, the uncertainties associated with the previously described PROMISE formulations will be examined. By taking into consideration these uncertainties, the PROMISE model can provide the exposure concentration in a probabilistic form.

3.2.1 Uncertainties Associated with Vortex Entrainment Formulation

Uncertainties associated with PROMISE1 are related to the uncertainties of the vortex entrainment coefficient, α_{vortex}. In Equation (144), single values of k_{20} and k_{21} were used for the deterministic based approach. In the probabilistic based approach, the uncertainties of the vortex entrainment coefficient α_{vortex} were taken into account by using the 95% confidence interval of the regression coefficients k_{20} and k_{21}. The probabilistic formulation of α_{vortex} is

$$\alpha_{vortex} = [0.3548 \pm 0.0577](F_L K)^{[0.1196 \pm 0.0387]} \quad (191)$$

It can be seen from Figure 39 and Equation (191) that a deterministic based approach gives a single value vortex entrainment of 0.51 but the probabilistic based approach provides a number of possible values range from 0.38 to 0.66 (1000 simulations). The mean value of the probabilistic based approach is 0.51 with a 95% confidence interval of [0.41, 0.61].

Based on the entrainment coefficients generated in Figure 38, the probabilistic based PROMISE model has been executed 1000 times for a test case. The results are shown in Figure 40 and Table 12.

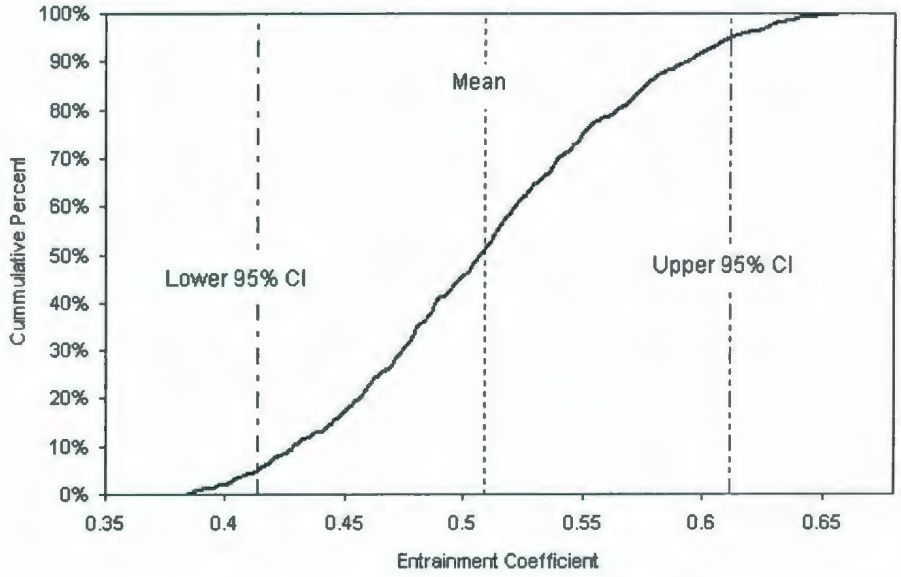

Figure 39. Uncertainties of the vortex entrainment coefficient.

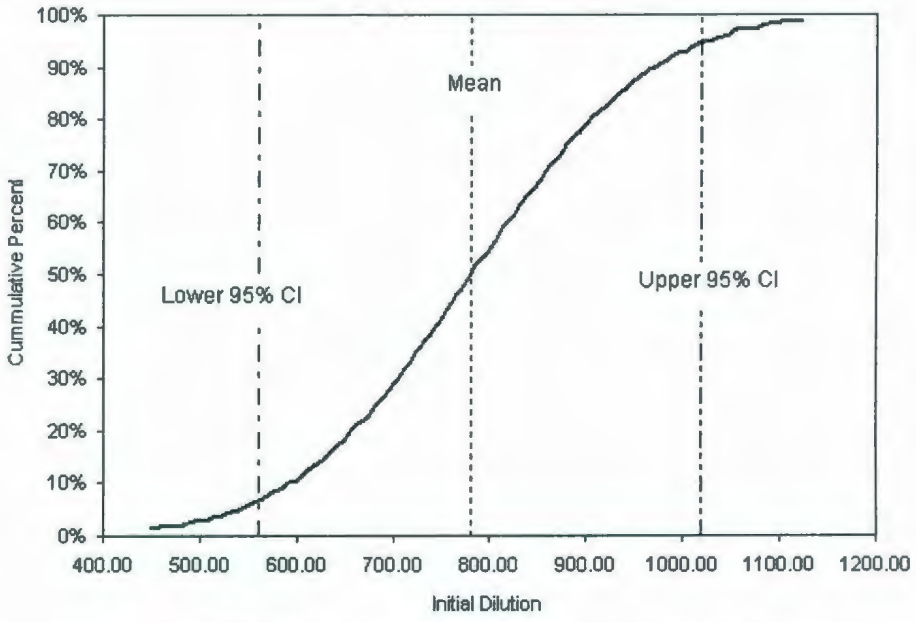

Figure 40. Probabilistic outputs of the initial dilution for a test case.

Table 12. Statistics of the initial dilution predicted by the probabilistic based PROMISE1 for a test case.

Mean	780.9	Median	776.4
Standard Deviation	146.8	Standard error	10.4
Minimum	538.5	25 Percentile	651.8
Maximum	1041.6	75 Percentile	907.3
95% Lower CI	561.3	95% Upper CI	1018.7

3.2.2 Uncertainties Associated with Wave Effects Model

In the deterministic based approach, Equation (153) was used to study the effects of surface waves on the initial dilution. Compared with previous formulations, although the Equation (153) considered the effects of densimetric Froude number, it did not consider many other factors, such as discharge angle, and angle between the propagating wave and currents. Based on the experimental study of Hwung et al. (1994) and Chyan et al. (2002), these discharge angles can significantly affect the initial dilution.

The existing experimental data is still inadequate to derive an empirical relation that considers all these effects, therefore the original Chin's (1987) formulation (Equation 152) rather than the new formulation (Equation 153) is used in the probabilistic based model.

The uncertainty of Equation (152) is associated with the experimental coefficient C_w. For a horizontally discharged jet in co-wave environment, Chin (1987) gave a value of 6.15 for the L_Q/Z_M values in the range from 0.03 to 0.15. For horizontal discharges in the same L_Q/Z_M range, Hwung et al. (1994) got a value of 4.21 for co-wave, 4.16 for opposing-wave, and 5.55 for orthogonal discharge. For the same L_Q/Z_M range, Hwang et al. (1996) suggested the C_w range from 1.4 to 8.66. Chyan et al.

(2002) studied the inclined jet (0° to 180° relative to horizontal plan) in a wave environment. The L_Q/Z_M ranged from 0.01 to 0.03. It was found that the C_w ranges from 2.9 to 14.5.

Based on these experimental results, the probabilistic based analysis used two sets of C_w values for different ranges, see Table 13. The C_w for L_Q/Z_M values lies between 0.03 and 0.05 was interpolated. The results from a probabilistic based analysis of Equation (152) are given in Figure 41.

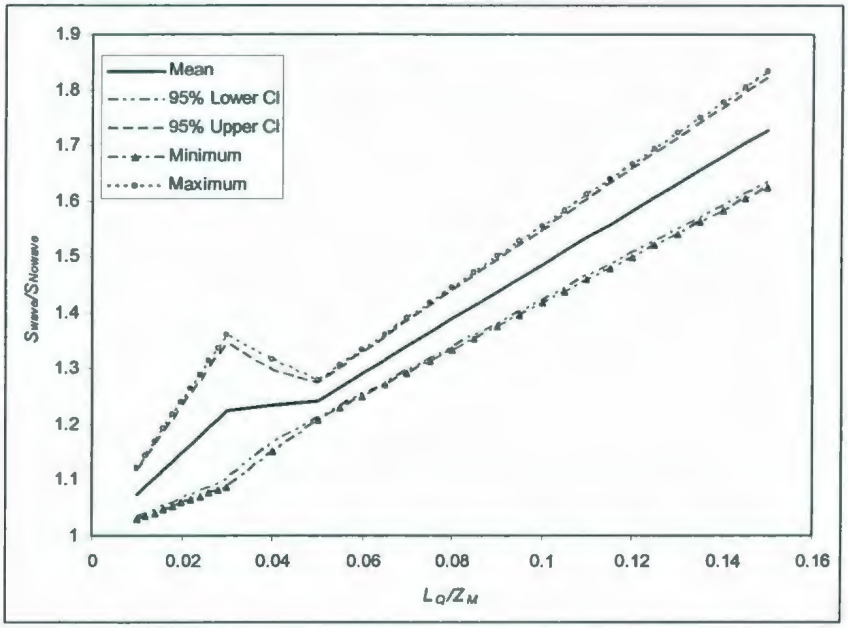

Figure 41. Probabilistic outputs of the wave effects on initial dilution.

Table 13. Uncertainty associated with experimental coefficient C_w.

L_Q/Z_M	0.01 – 0.03	0.03-0.05	0.05 – 0.15
Minimum	2.9	Interpolation	1.4
Maximum	14.5	interpolation	6.15
Distribution	Uniform	Uniform	Uniform

3.2.3 Uncertainty Associated with Downstream Control Model

For the upstream intrusion and downstream control model, uncertainties are related with the constants that estimate the downstream dilution S_{ave}. As described previously, a factor of 1.75 was used to estimate the downstream dilution for strongly deflected case. Doneker and Jirka (1990) have suggested a value in the range from 1.5 to 2 can be used. As the result of this uncertainty, the plume width and thickness at the end of the control volume have uncertainties and this will further affect the prediction of buoyant spreading and turbulent diffusion behaviors.

In the probabilistic based analysis, a triangular distribution is assumed to estimate the downstream end dilution and the related plume thickness and width. The triangular distribution has a minimum value of 1.5 and a maximum value of 2.0. The most likely value is 1.75. Therefore, the Equations for the strongly deflected case are

$$S_{ave} = Triangular[1,5,1.75,2.0]S_i \tag{192}$$

$$L_0 = 2b_{v0} = \sqrt{\frac{Triangular[1,5,1.75,2.0]S_i Q}{2U_a}} \tag{193}$$

Based on the above Equations, the probabilistic output of the plume width (Equation 160) at the downstream end of the control volume for the strongly deflected case is shown in Figure 42.

Similar to the strongly deflected case, a coefficient of 4.0 has been used in the deterministic based approach. As suggested by Huang et al. (1996) and Wright et al. (1991), the constant for the weakly deflected case ranges from 3.0 to 5.0. A triangular distribution with a minimum value of 3.0 and a maximum value of 5.0 is therefore assumed. The most likely value is 4.0. Therefore, the Equations for the weakly deflected case are

$$S_{ave} = Triangular\,[3,4,5]S_i \tag{194}$$

$$b_{v0} = \sqrt{\frac{Triangular\,[3,4,5]S_i L_m L_Q}{5.2L_s}} \tag{195}$$

Based on the above Equations, the probabilistic output of the plume width (Equation 160) at the downstream end of the control volume for the weakly deflected case is shown in Figure 43.

3.2.4 Uncertainty Associated with Buoyant Spreading and Turbulent Mixing

The uncertainty associated with the buoyant spreading and turbulent diffusion model are associated with the uncertainties of the entrainment coefficients α_1, the horizontal diffusion coefficient K_y and the vertical diffusion coefficient K_z (Equations 169,170, 176, 177, and 182).

For the entrainment α_1, a constant value of 0.6 was used in the deterministic based approach. Based on two field experiments conducted in the Koombana Bay in Australia, Luketina and Imberger (1987) derived a value of 0.58 for the September 22, 1984 test and a value of 0.75 for the September 24, 1984 test. These values are in good agreement with the study by Britter and Simpson (1978) in which they derived a value of 0.75 from laboratory experiments. A triangular distribution for α_1 with a minimum value of 0.58, a maximum value of 0.75 and a most likely value of 0.73 is then assumed in the probabilistic based approach. The effect of this coefficient on the downstream concentration is shown in Figure 44. The minimum and maximum values are shown.

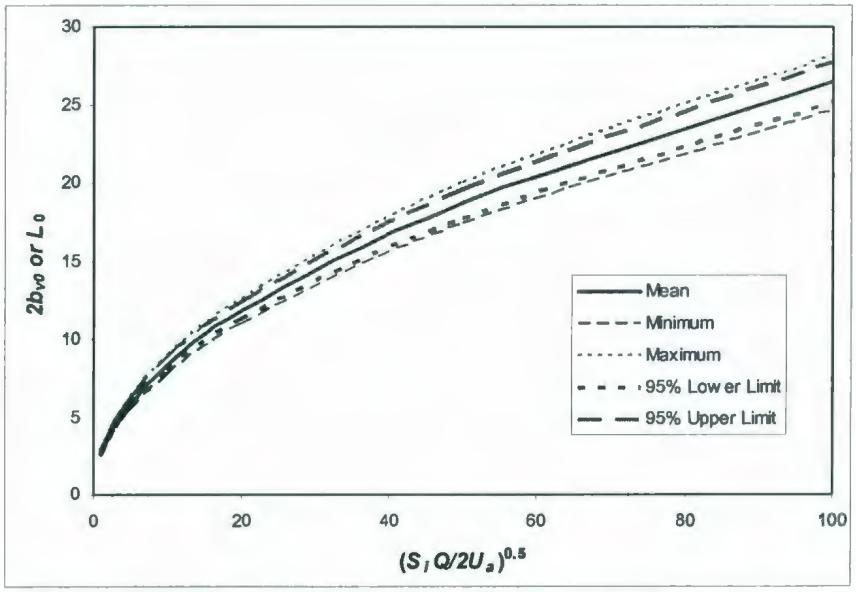

Figure 42. Plume thicknesses and widths at the downstream end of control volume for various initial conditions (strongly deflected cases).

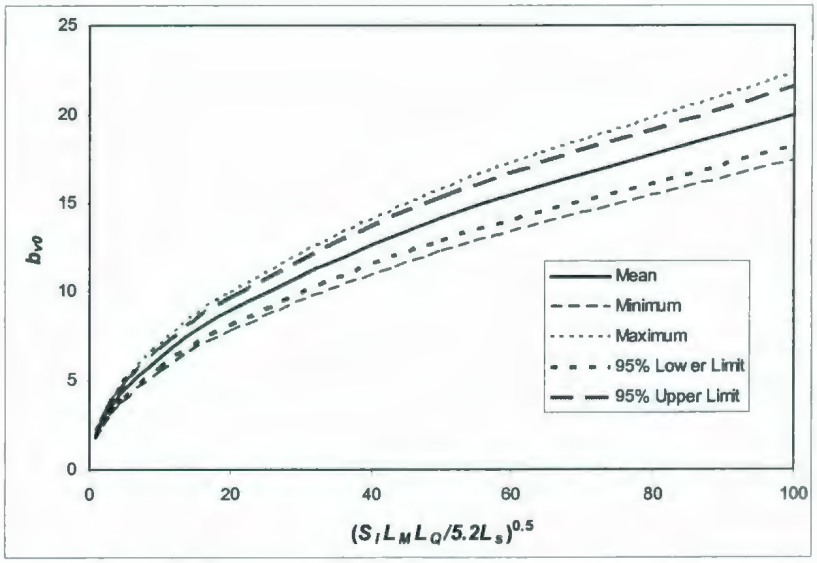

Figure 43. Plume thicknesses at the downstream end of control volume for various initial conditions (weakly deflected cases).

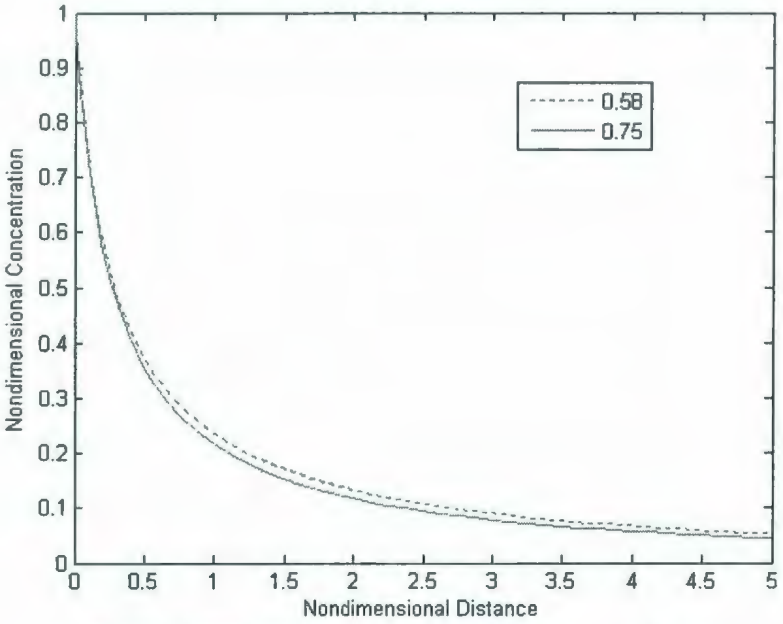

Figure 44. The effects of α_1 on the far field concentration.

In the deterministic based approach, a 4/3 power law relationship was used for the horizontal dispersion,

$$K_y = \text{constant}(\sigma_y)^{4/3} \tag{196}$$

where the horizontal diffusion coefficient K_y is in [cm^2/s], and the standard deviation of the horizontal plume σ_y is in [cm]. A constant value of 0.043 $cm^{2/3}/s$ was used in the deterministic based approach (Doneker and Jirka, 1990). Based on the extensive data from Orlob (1959), the following Equation is used for the probabilistic based analysis

$$K_y = \text{Triangular}[0.00015, 0.001, 0.009] L^{4/3} \tag{197}$$

A Triangular distribution with a minimum value of 0.00015, maximum value of 0.009, and most likely value of 0.001 $feet^{2/3}/s$ is assumed for the horizontal dispersion coefficient.

Monte Carlo simulation was used to generate K_y for a wide range of plume width, the simulated results are compared with the experimental measurements in Figure 45.

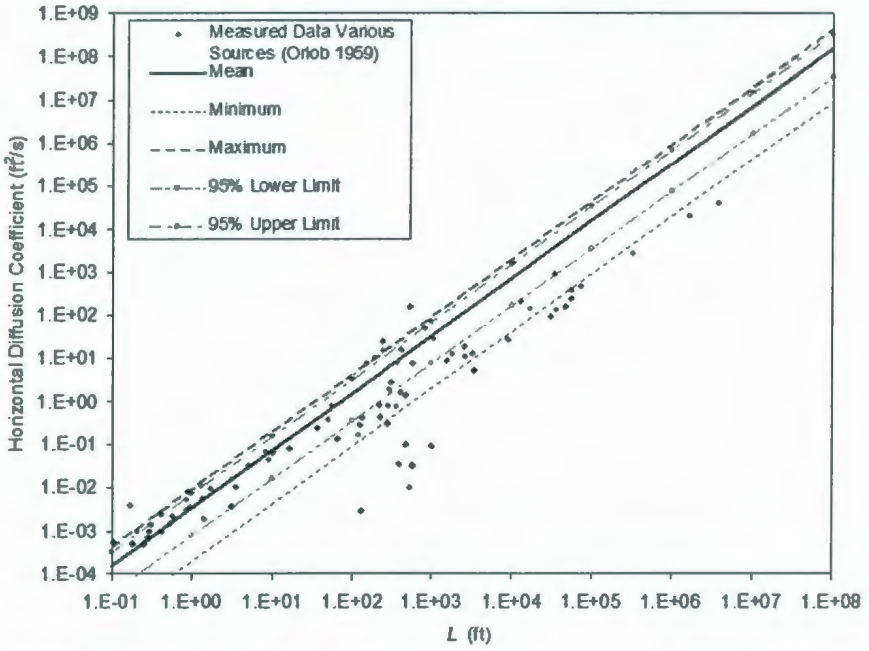

Figure 45. Comparison of simulated and measured horizontal diffusion coefficients.

The Equation (182) was used in the deterministic based approach to calculate the vertical diffusion coefficient in the stratified case. In the probabilistic based approach, the 95% percent confident limits are used, as shown in Equation (198).

$$K_z = \frac{Triangular(0.001, 0.0129, 0.0289)}{\varepsilon_D^{0.897 \pm 0.088}} \tag{198}$$

The constants in Equation (198) are assumed to be triangularly distributed. The Monte Carlo simulation results for this vertical diffusion coefficient are given in Figure 46. This agrees with the measurements well.

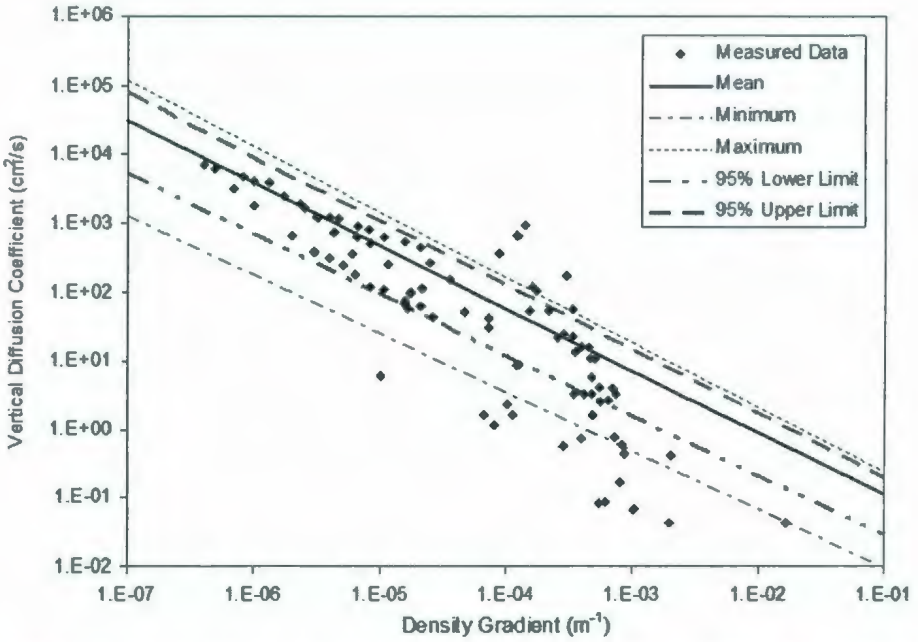

Figure 46. Comparison of simulated and measured vertical diffusion coefficients in stratified case.

3.3 SUMMARY OF THE ADVANTAGES

In this chapter, the formulations of a steady state model, the PROMISE, have been described. Unlike the non-steady state models, such as PROTEUS and DREAM (PROVANN), the PROMISE cannot be used for time dependent analysis. However, the model is capable of providing a more accurate near field analysis than those non-steady state models. Compared with other steady state model, the PROMISE also has a number of advantages. These advantages are summarized in Table 14. For a given criteria, a rank range from 1 to 5 was given to the selected models based on their degree of advantage for that criteria. For example, a rank of 5 indicate the model uses the best available approach. Similarly, a rank of 1 means that the model does not account for that effect.

It can be seen from Table 14 that PROMISE has many advantages compared to other models except for the criteria 5 and 9.

While the Visual Plumes and VISJET only considered the variation of current speeds with depth, PROMISE and CORMIX also considered the variation of current direction with depth. The Mukhtasor (2001) can only take a single current value. The PROMISE and CORMIX have the same rank for these criteria.

Table 14. Comparison of PROMISE with other steady state models.

		PROMISE		CORMIX		Visual PLUMES		VISJET		Mukhtasor (2001)	
No.			Rank		Rank		Rank		Rank		Rank
1	*Variation of* U_a direction with depths	yes	**5**	no	**5**	no	1	no	1	no	1
2	Surface wave effects	yes	**5**	no	1	no	1	no	1	no	1
3	Internal wave effects	yes	**5**	no	1	no	1	no	1	no	1
4	Unified Buoyant spreading and Turbulent diffusion	yes	**5**	no	4	no	2	no	1	no	3
5	Wind effects on buoyant spreading	no	4	yes	**5**	no	1	no	1	no	3
6	Vertical mixing module	yes	**5**	yes	4	no	1	no	1	no	1
7	Wave effects on vertical mixing	yes	**5**	no	4	no	1	no	1	no	1
8	Lateral variation of far field concentration	yes	**5**	no	3	no	1	no	1	yes	4
9	Upstream Intrusion	yes	4	yes	**5**	no	1	no	1	no	3
10	Ecological effects (food chain model)	yes	**5**	no	1	no	1	no	1	no	1
11	Probabilistic analysis	yes	**5**	no	1	no	1	no	1	yes	4

Note: Rank ranges from 1 to 5. Rank 5 is the best among others.

Although it is still in simple form, PROMISE considered the surface waves effects on initial dilution. This effect is not considered by any other models. PROMISE also considered the effects of ocean internal waves on initial dilution. Therefore, PROMISE is ranked 5 for criteria 2 and 3.

PROMISE has a unified buoyant spreading (BS) and turbulent diffusion (TD) model. Other models have either a separated BS/TD model or no BS/TD model.

For criteria 5, the CORMIX is more advanced than PROMISE as it included the wind effects on the buoyant spreading process.

The PROMISE has a sea state dependent vertical mixing module and variable vertical mixing coefficients while the CORMIX only has a constant vertical mixing coefficient. Therefore, PROMISE is more advanced.

CORMIX only predict the average dilution, which is only dependent on the downstream distance x. The PROMISE also considered the variation of concentration along the y-axis.

For criteria 9, PROMISE is less advanced than CORMIX. The reason is that a finite difference algorithm is used by CORMIX and that enables CORMIX to give a more detailed description of the upstream intrusion region. On the contrary, PROMISE only used length scale formulations for this module. Therefore, CORMIX has a higher rank than PROMISE in this criteria.

All other steady state models are for general environmental discharges. They do not have an ecosystem model which is very important for the produced water discharges.

Except the model by Mukhtasor (2001), all other models can only be used in a deterministic way. PROMISE can provide probabilistic analyses as well.

4. VALIDATION OF PROMISE1 MODEL AGAINST LABORATORY EXPERIMENTS

Discharge models must be validated by comparing their prediction with experimental data. The validation improves user confidence in model predictions. For buoyant jet models the validation process generally involves the comparison with plume trajectory, downstream concentration, and plume width for various discharge and ambient conditions.

In the first part of this chapter, a wide variety of laboratory experiments will be reviewed and the selected data will be compared with PROMISE1 in section 4.2. A relatively large scale experiment was also conducted for further validation of PROMISE1. The results are describes in section 4.3 and 4.4.

4.1 REVIEW OF LABORATORY EXPERIMENTAL STUDIES

Buoyant jet behavior has been studied extensively and large numbers of laboratory experiments which including both single and multi-port discharges, have been conducted over the past few decades. In this study, only those experiments applicable to produced waters will be reviewed. Generally, produced waters are discharged into the ocean from a submerged single port pipe oriented either horizontally or vertically. Unlike horizontal discharges in which the buoyancy force is always in a direction perpendicular to that of the flow, a vertical buoyant jet may become a positively buoyant jet (buoyant force is in the same direction as that of the flow) or a negatively buoyant jet (buoyant force is in the direction opposite to that of the flow). In this section, three types of laboratory experiments on buoyant jets will be

reviewed, they are: vertically discharged positive buoyant jet, vertically discharged negative buoyant jet, and horizontally discharge buoyant jet.

4.1.1 Review of Experimental Techniques

The main objective of laboratory studies of buoyant jets is the measurement of tracer concentration and mapping of jet trajectory. Thus, the selection of tracer becomes an important element of experimental design.

The most commonly used tracers are temperature, salinity, and fluorescent dye. The measurement techniques are intrusive probe measurement, extracting samples and sample analysis, and non-intrusive measurement.

The temperature and salinity of a buoyant jet have two functions: generating the density difference between jet and ambient, and serving as a tracer. For this type of system, a thin probe (thermal probe or conductivity probe) or a series of probes are inserted into the plume to take measurements. The probe is connected to a recorder which stores measurements. Before measurement, the probe needs to be calibrated using solutions of known salinity or temperature. The study of Lee & Cheung (1991) used temperature as a tracer and the study of Cavola (1982) used salinity as a tracer.

The extensive use of fluorescent dyes as water tracers began in the early to mid-1960's. The outstanding characteristics of dye tracing are the low detection limit and the simplicity and accuracy in measuring dye concentration using fluorescent techniques. In an experimental setup using dye tracers, the dilution can be obtained by measuring the dye concentration using either a fluorometer or a Laser Induced Fluorescence (LIF) system, and the trajectory of a jet can be easily photographed.

Generally, a fluorometer has six components: 1) energy source, e.g., a laser sheet, or ultraviolet lamp; 2) primary filter that passes only a selected band of the source's output spectrum to match a selected band of the dye's excitation spectrum; 3) sample holder; 4) secondary filter that passes only a selected band of the dye's emission spectrum and preferably none of the light passed by the primary filter; 5) sensing device that responds to the spectral band passed by secondary filter; and 6) readout device. The intensity of fluorescent light is proportional to the amount of fluorescent substance present. The early models (e.g., Turner design 111 model) cannot do direct in-situ measurement and samples must be extracted from the plume first and then analyzed using the fluorometer offline, whereas the latest designs can do real time online measurements. Roberts & Toms (1986) studied negatively buoyant jet problems by extraction of samples using a suction pipe and analyzing the sample using a fluorometer.

All the techniques described above are point-based techniques. There are two major disadvantages to these techniques: 1) the flow field is disturbed by the probe or sample extraction pipe; and 2) measurements can only be conducted at a limited number of points. Roberts (1989) used 100 sampling probes, and this appears to be the largest number used in similar studies.

The advent of the Laser Induced Fluorescence (LIF) technique in the 1970s enabled the capture of the entire tracer concentration field in a plane in a fraction of a second. In a typical LIF experiment, a fluorescent dye is added to the flow. A laser sheet illuminates the flow and excites the fluorescent tracer. The intensity of the emitted fluorescent light is a function of the dye concentration and the intensity of the incident laser light. The relationship between the emitted light intensity and dye

concentration can be obtained by calibration. The emitted light is recorded by a CCD camera as a gray scale image and the concentration field is obtained from the image using the calibration result. The advantage of LIF is its non-intrusive nature. Some examples of laboratory studies on buoyant jet problems using the LIF technique are: Papanicolaou and List (1988), Ferrier et al. (1993), and Webster et al. (2001).

The previous studies using LIF were two-dimensional LIF. The 3D-LIF technique has been developed over the past few years. The 3D-LIF is obtained by taking a series of 2D-LIF images very quickly (e.g., 10,000,000 images/second) and constructing the 3D flow field by a visualization technique. The 3D-LIF is the most advanced technique for studying buoyant jet problems. One application example is the study by Tian (2002). In Tian's (2002) study, a 3D-LIF system was applied to single and multi-port diffusers. The near field dilution, near field length, spreading layer thickness, spreading layer level, and maximum rise height were measured.

4.1.2 Review of Laboratory Studies

One of the earliest laboratory experiments on buoyant jet problem was the study by Fan (1967). Two types of buoyant jet problems were studied: round buoyant jet discharged vertically into a stagnant environment with linear stratification and round buoyant jet discharged vertically into a uniform environment with crossflow. The experiments were performed in a laboratory tank with dimensions of 2.26 m in length, 1.07 m in width, and 0.61 m in depth. The salt water was discharged into the tank via pipes with diameters ranging from 0.223 to 0.762 cm. Conductivity measurements were carried out at several cross-sections normal to the jet axis. Photographic

observations of the trajectories were also performed. Fan (1967) used the experimental results in an integral model analysis and derived an entrainment coefficient of 0.082.

Wright (1977b) studied the vertical buoyant jet in both uniform and stratified environments. The experiments were performed in a towing tank 61 cm square in cross-section and 8.7 m in length. The depth of the towing tank was 55 cm (water level). The stratification was produced by adding salt water and freshwater at different rates into the tank. Dense effluents created by adding sodium chloride to the jet solution were discharged downward into the tank through pipes with diameters ranging from 0.2 to 1.0 cm. To determine the density profile, the salt concentration was measured using a conductivity probe which was able to adjust its position to the nearest 0.1 mm. The measurements were taken at 2.0 or 4.0 cm intervals. Some temperature profiles were also measured along with the conductivity measurements to observe any temperature effects on the density structure. To determine the trajectory and dilution, Rhodamine B Extra, was used. The samples were taken by using a set of suction pipes and analyzed using a Turner Design fluorometer. Based on large number of measurements, Wright (1977b) derived several empirical length scale relations to characterize the dilution and plume trajectory.

Ayoub (1971) studied the mixing of horizontally discharged buoyant jets in a 6.095 long, 1.525 m wide, and 0.507 m deep flow flume. Salted water was discharged from pipes of diameters ranging from 0.5 to 1cm. Conductivity measurements were conducted at various distances downstream for both co-flowing and cross-flowing cases. Photographic measurements were also obtained. Ayoub (1971) compared his experimental results with the integral model predictions and found good agreement.

Cheung (1991) studied both the vertically and horizontally discharged jets in laboratory flume. The vertical jet experiments were performed in a 10m long, 30 cm wide and 45 cm deep laboratory flume. The horizontal jet experiments were performed in a shallow water basin 11 m long, 5m wide, and 80 cm deep. Unlike previous experiments in which salt was used as the tracer, Cheung used the temperature as a tracer by discharging hot water into the cold ambient water. A thermistor probe was used to sample from twelve different positions over the cross-section. The results of Cheung's (1991) experiments were used to develop an integral model, JETLAG, which is the core computation model of the VISJET model.

Anderson et al. (1973) studied the negative buoyant jets in a 60 feet long, 2 feet wide, and 1 foot deep recirculation flume. Salt water was discharged upward from pipes of different diameters ranging from 0.7 to 0.95 cm at angles of 45°, 60°, and 90°. The salt concentrations were monitored at various downstream locations by a conductivity probe. Twenty-four sets of experiments with velocity ratios ranging from 5.3 to 20.9, and densimetric Froude numbers ranging from 5.0 to 20.7 were conducted. Anderson et al. (1973) compared their experimental results with two integral models by Fan (1967) and Abraham (1970). They found that the entrainment coefficient decreases with decreases in the initial angle of discharge.

Cavola (1982) also studied the negative buoyant jets by discharging salt water into a 12.2 m long, 0.6 m wide, and 0.9 m deep towing channel. A conductivity probe was used to measure the salt concentration at five x/D (x is the downstream distance and D is the port diameter) locations ranging from 2.5 to 30. The plume width was measured using a photographic method. The experiments were conducted under three densimetric Froude numbers from 0.5 to 1.5 and three velocity ratios from 0.5 to 1.50.

The results of Cavola's (1982) experiments have been used by Nedwed et al. (2001) to validate the OOC model.

More recently, Gaskin (1995) investigated the mixing behaviors of a single port buoyant jet using the Laser Induced Fluorescence (LIF) method. Both vertical jets and horizontal jets were studied and analyzed using a Particle Image Velocimetry (PIV) method. The advantage of this LIF/PIV method is its ability to provide detailed concentration and velocity profiles for a preset cross-section, while previous methods can only give point measurements. Gaskin's (1995) tests were performed at Froude number ranging from2.29 to 9.8 and velocity ratios from 1 to 4.39.

The LIF method used by Gaskin (1995) is a 2D LIF which means only one cross-section can be measured. Tian (2002) has developed a 3D LIF method which can give a three dimensional description of the plume field. Tian (2002) has used this method to study the mixing of both single port and multi-port discharges. However, as the main objective of Tian's (2002) study was to develop a new experimental technique rather than study the detailed buoyant jet mixing behavior, only limited cases were studied.

The more detailed experimental studies are listed in Tables 15, 16, and 17 for vertical jets, horizontal jets, and negative jets. The types of tracer, parameters measured, and analytical methods are summarized.

Table 15. Summary of investigations of vertically discharged positively buoyant jets in a crossflow.

Experiments	Type of Jet	Measurement	Analysis
Barilla (1968)	Dyed salt solutions in freshwater, towed experiments	Trajectories from photographs	
Chu & Goldberg (1974)	Dyed salt solution in freshwater	Trajectories from photographs	Integral
Fan (1967)	Dyed salt solutions in freshwater, towed experiments	Concentrations from conductivity; trajectories from concentration profiles and photographs	Dimensional analysis
Hoult & Weil (1972)	Salt solution in freshwater, towed experiments	Trajectories from photographs	Integral
Huang et al. (1998) (from Lee & Cheung, 1991)	From Lee & Cheung (1991)	From Lee & Cheung (1991)	Dimensional analysis
Lee & Cheung (1991)	Heated water into freshwater	Temperature difference from thermilinear probe	Dimensional analysis
Mukhtasor (2001) (from Lee & Cheung, 1991)	From Lee & Cheung (1991)	From Lee & Cheung (1991)	Dimensional analysis
Tian (2002)	Dyed salt water into mixed solutions (salt + ethanol)	Trajectories and concentrations from 3D-LIF	Dimensional analysis
Weil (1968)	Salt solution in freshwater	Trajectories from photographs	
Wright (1977b)	Uniform	Fluorometric	Dimensional analysis
Wright (1984)	Stratified	Fluorometric	Dimensional analysis

Table 16. Summary of laboratory investigations of horizontally discharged buoyant jets in a crossflow.

Experiments	Type of Jet	Measurement	Analysis
Ayoub (1971)	Dyed salt solutions in freshwater; crossflowing and coflowing	Trajectories from photographs; Concentrations from conductivity	Integral
Brown (1984)	Dyed salt solution in freshwater, towed experiments	Trajectories from photographs; Concentrations from conductivity	Dimensional analysis
Davidson (1989)	Coflowing	From Knudson (1988)	Integral
Gaskin (1995)	Dyed salt solutions in freshwater, towed experiments;	Concentrations from conductivity and LIF	Integral
Knudson (1988)	Coflowing		Integral
Lee (1989) (From Ayoub, 1971)	Dyed salt solutions in freshwater	Trajectories from photographs; Concentrations from conductivity	Dimensional analysis
Lee & Neville-Jones (1987)	Field tests from a series UK outfalls	Surface dilution from fluorometric method	Dimensional analysis
Proni et al. (1994)	Field tests from Florida outfalls		

Table 17. Summary of laboratory investigations of negatively buoyant jets.

Experiments	Discharge Angle (degree)	Fr	U_a/U_j	Measurement Methods	Analysis
Anderson et al. (1973)	45, 60, 90	10.3 – 46.9	0.05 – 0.19	Conductivity	Integral
Cavola (1982)	90	1.01 – 1.44	0.50 – 1.50	Conductivity	Dimensional analysis
Chu (1975)	90	1.10 – 2.30	0.08 – 0.25	Photographic	Integral
Holly & Grace (1972)	90		0.008 – 0.21	Conductivity, Temperature	Dimensional analysis
Roberts & Toms (1986)	60, 90	12.2 – 25.9	0.0 –0.07	Fluorometer	Dimensional analysis
Roberts et al. (1997)	60	18.7 – 35.7	Stagnant	LIF	Dimensional analysis
Pantokratoras (1999)	0 – 90		Stagnant	Numerical Simulation	Integral
Pantokratoras (2002)	0 – 90		Stagnant	Numerical Simulation	Integral
Pincince & List (1973)	60, 90	40.0 – 50.0	0.027 – 0.10	Conductivity	Dimensional analysis
Tong & Stolzenbach (1979)	45, 60, 90	11.7 – 22.2	0.010 – 0.108	Temperature	Dimensional analysis
Zeitoun et al. (1970)	30, 45, 60, 90				Dimensional analysis
Zhang & Baddour (1998)	90	0.37 – 36.2	Stagnant	Photographic	Dimensional analysis

4.2 VALIDATION OF MODEL AGAINST EXISTING DATA

In order to validate the performance of the near field model and improve model confidence, the predictions of PROMISE1 are compared with well-documented laboratory data of both jet trajectory and dilution over a wide range of discharge and ambient conditions.

4.2.1 Vertical Buoyant jets in Crossflow

A comprehensive set of data on a vertical buoyant jet in a crossflow was reported by Cheung (1991). Three cases were selected for comparison and the results are shown in Figures 47, 48, and 49.

The results for a vertical discharge at a densimetric Froude number of 4 and velocity ratio of 4 (V4-4) are shown in Figure 47. The predictions from the VISJET model are also given for comparison. It can be seen from Figure 47, both PROMISE 1 and VISJET can predict the dilution (bottom) and trajectory (top) well for this case. For the plume width (middle), the PROMISE1 slightly over estimated the plume width.

The results for a vertical discharge at a densimetric Froude number of 8 and velocity ratio of 4 (V8-4) are shown in Figure 48. In this case, both PROMISE1 and VISJET predicted the dilution very well. Both PROMISE1 and VISJET can predict the plume width reasonably well with slight over estimations. The VISJET predicted the trajectory better than PROMISE1 in this case.

The results for a vertical discharge at a densimetric Froude number of 16 and velocity ratio of 6 (V16-6) are shown in Figure 49. It can be seen from Figure 49, the dilution and plume width are well predicted by both models but PROMISE1 slightly underestimated the trajectory.

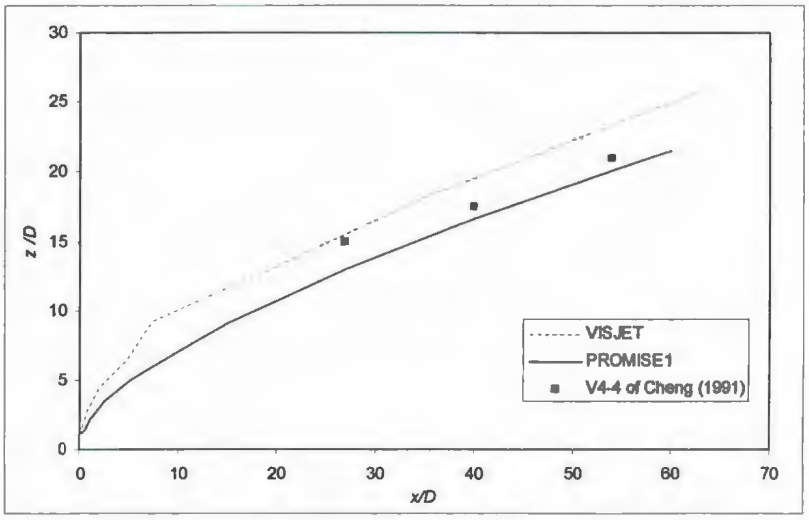

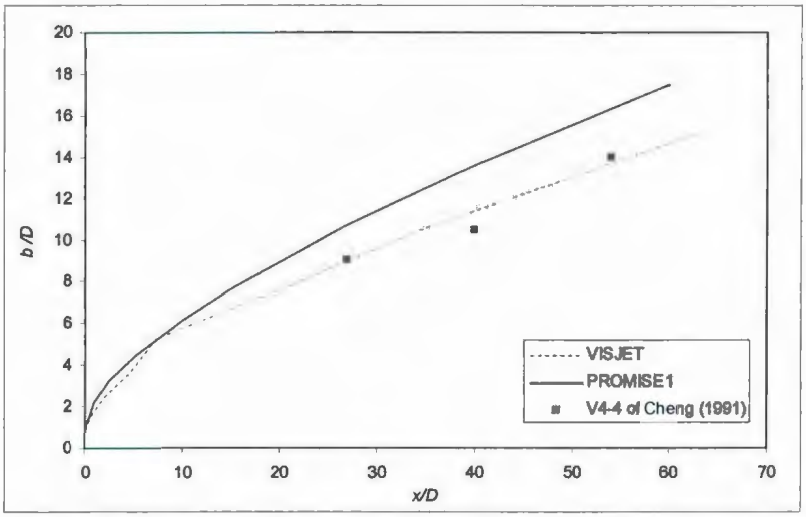

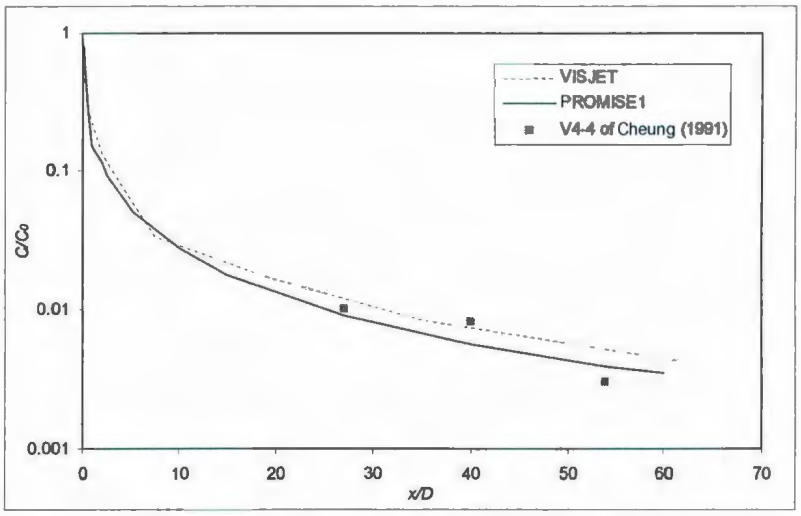

Figure 47. Vertical jets in cross flow, F_r=4, K=4.

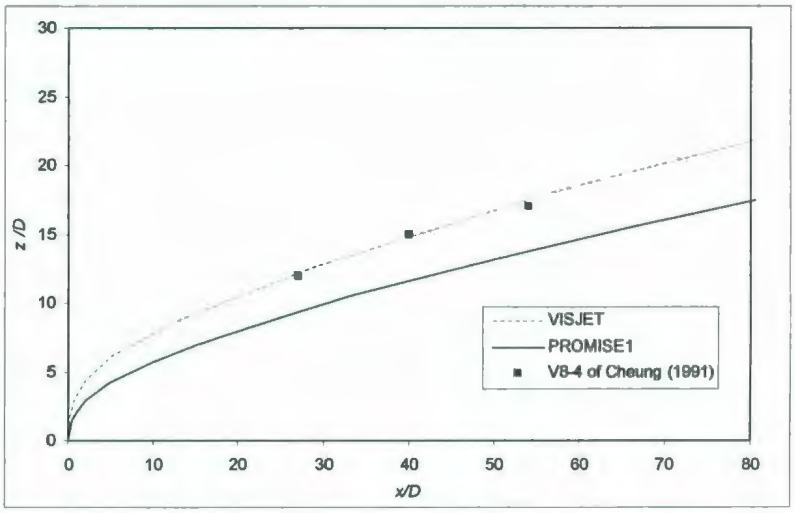

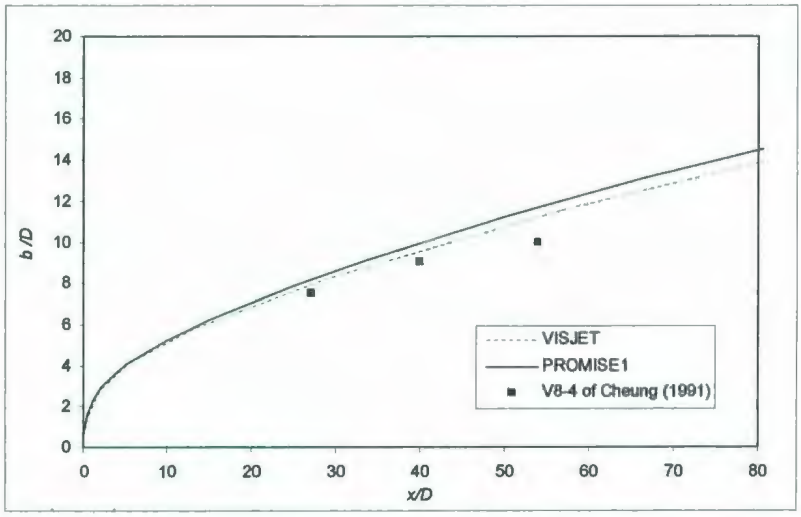

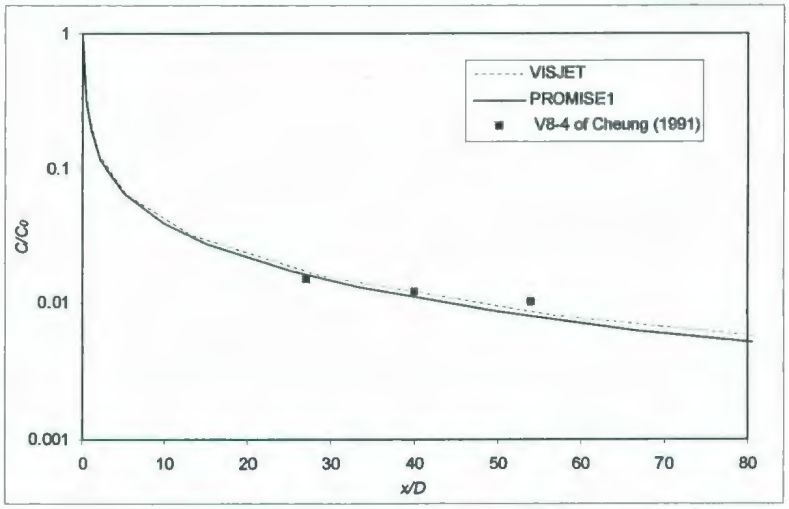

Figure 48. Vertical jets in cross flow, F_r=8, K=4.

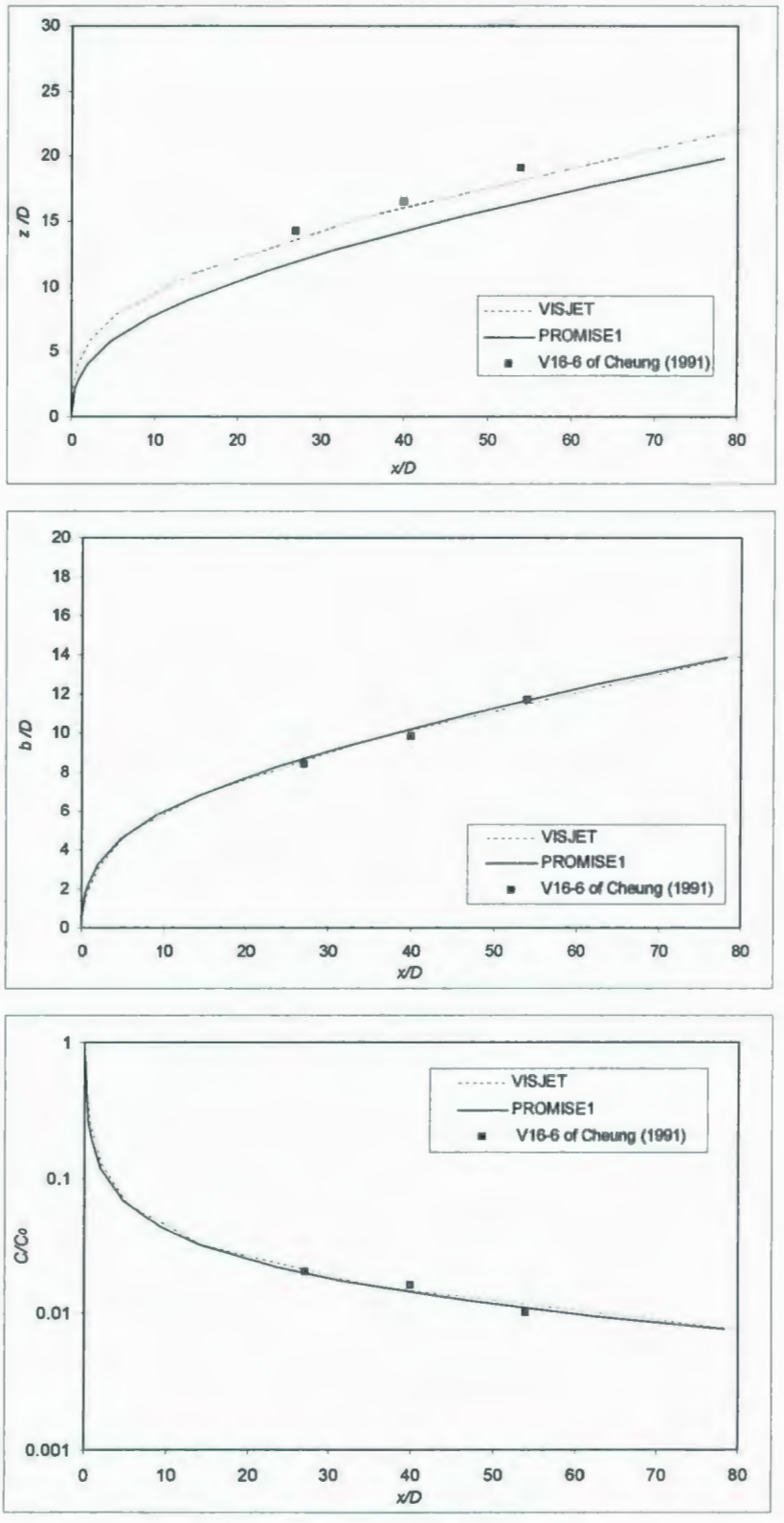

Figure 49. Vertical jets in cross flow F_r=16, K=6.

The experimental results from the more advanced 3D-LIF tests by Tian (2002) are also compared with PROMISE1. The predictions from the CORMIX, and two Visual PLUMES sub models, DKHW and UM3, are also provided. The results are shown in Figure 50. It can be seen from this case that all models underestimated the dilution and jet trajectory. The CORMIX model agrees with the experimental data better than other models in this case.

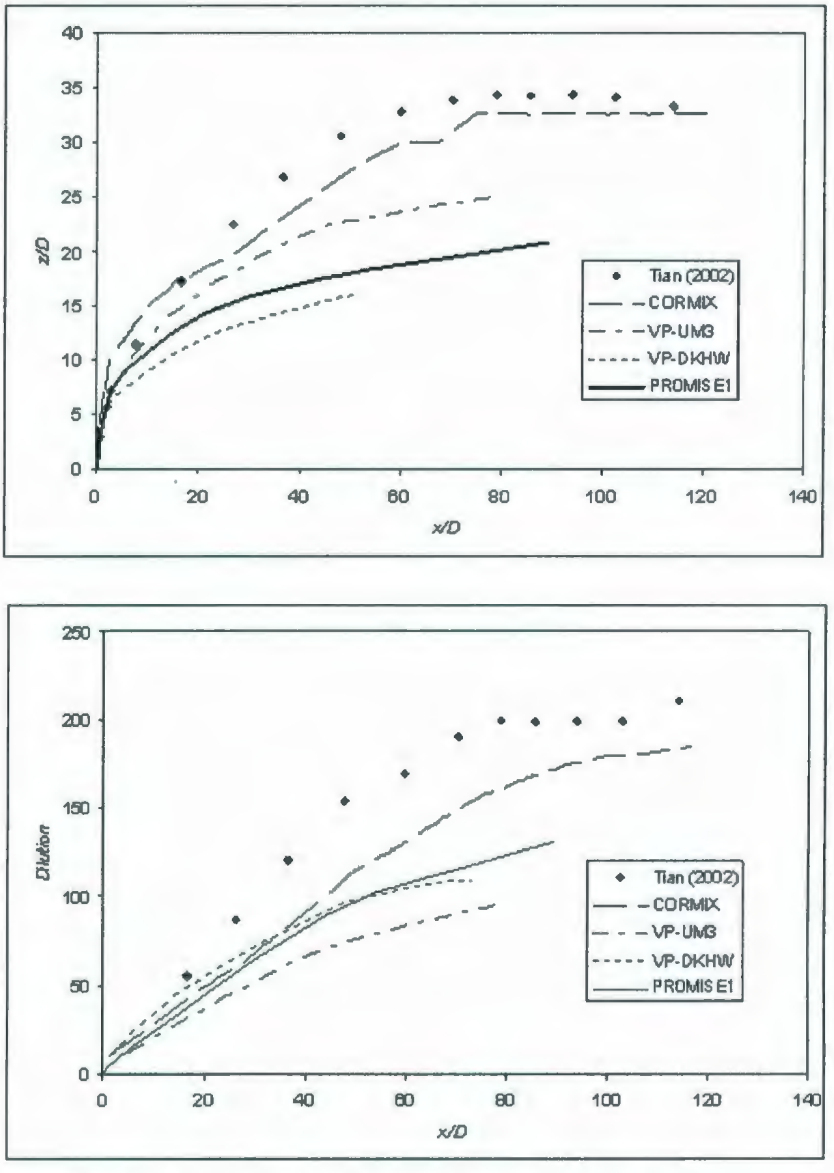

Figure 50. Comparison with the 3D-LIF experiments by Tian (2002).

4.2.2 Horizontal Buoyant Jets in Crossflow

Unlike the vertical jets whose trajectory is always two dimensional, the trajectory of the horizontal jets in a crossflow becomes three dimensional. Two cases were selected from Cheung's (1991) experiments for comparison and the results are shown in Figures 51 and 52.

It can be seen from Figure 51 that for the discharges with a densimetric Froude number of 16 and a velocity ratio of 6 (H16-6), PROMISE1 predicted the dilution and plume width very well. The prediction of PROMISE1 agrees with experimental data better than VISJET for the dilution and plume width. However, for the jet trajectory, the VISJET has better performance than the PROMISE1.

For the case of a discharge with a densimetric Froude number of 16 and a velocity ratio of 4 (H16-4), the results are shown in Figure 52. The results for this case are similar to that of H16-6. The PROMISE1 predicted the dilution and plume width better than VISJET but the VISJET predicted the trajectory better than PROMISE1.

4.2.3 Negatively Buoyant Jets in Crossflow

Two sets of experiments on negatively buoyant jets from Anderson et al. (1973) were selected to check the performance of PROMISE1. The results are shown in Figures 53 and 54.

For the discharge with a densimetric Froude number of 10.9 and a velocity ratio of 5.5, the PROMISE1 predicted the trajectory very well (Figure 53). The performance of PROMISE1 is much better than VISJET and Fan's (1967) model for this case. Same trend can be found for the plume width. For the dilution, all three

models slightly underestimated the dilution. The PROMISE1 gives the best prediction among the three models.

The results for a discharge with a high densimetric Froude number 40.7, and high velocity ratio 10.2 are shown in Figure 54. It can be seen from Figure 54 (top) that the VISJET predicted the trajectory better in regions close to the discharge ($x/D < 60$), but the PROMISE1 predicted the trajectory better in regions farther downstream ($x/D > 60$). Similar trends can also be found for the plume width and dilution. For the regions close to the discharge (x/D<20), Fan's (1967) model gives the best predictions for plume width and dilution. At distances farther from the discharge (x/D>20) PROMISE1 give the best prediction.

4.2.4 Conclusion Remarks

It can be seen from the comparison studies above that PROMISE1 can predict all three types of discharges very well. For the vertical discharges, the predictions by PROMISE1 agree with the experimental data very well. However, there is a slight underestimation of trajectory.

For horizontal jets, PROMISE1 provided better estimation for two of the three parameters than alternative models. The PROMISE1 has better performance over VISJET in dilution and plume width predictions. However, the VISJET has a better trajectory prediction than PROMISE1. The performance of PROMISE1 in trajectory prediction may be improved by further calibrate its entrainment coefficient against measured laboratory trajectory data.

For negatively discharged jets, PROMISE1 predicted all three parameters very well. The performance of PROMISE1 is better than VISJET and Fan's (1967) model.

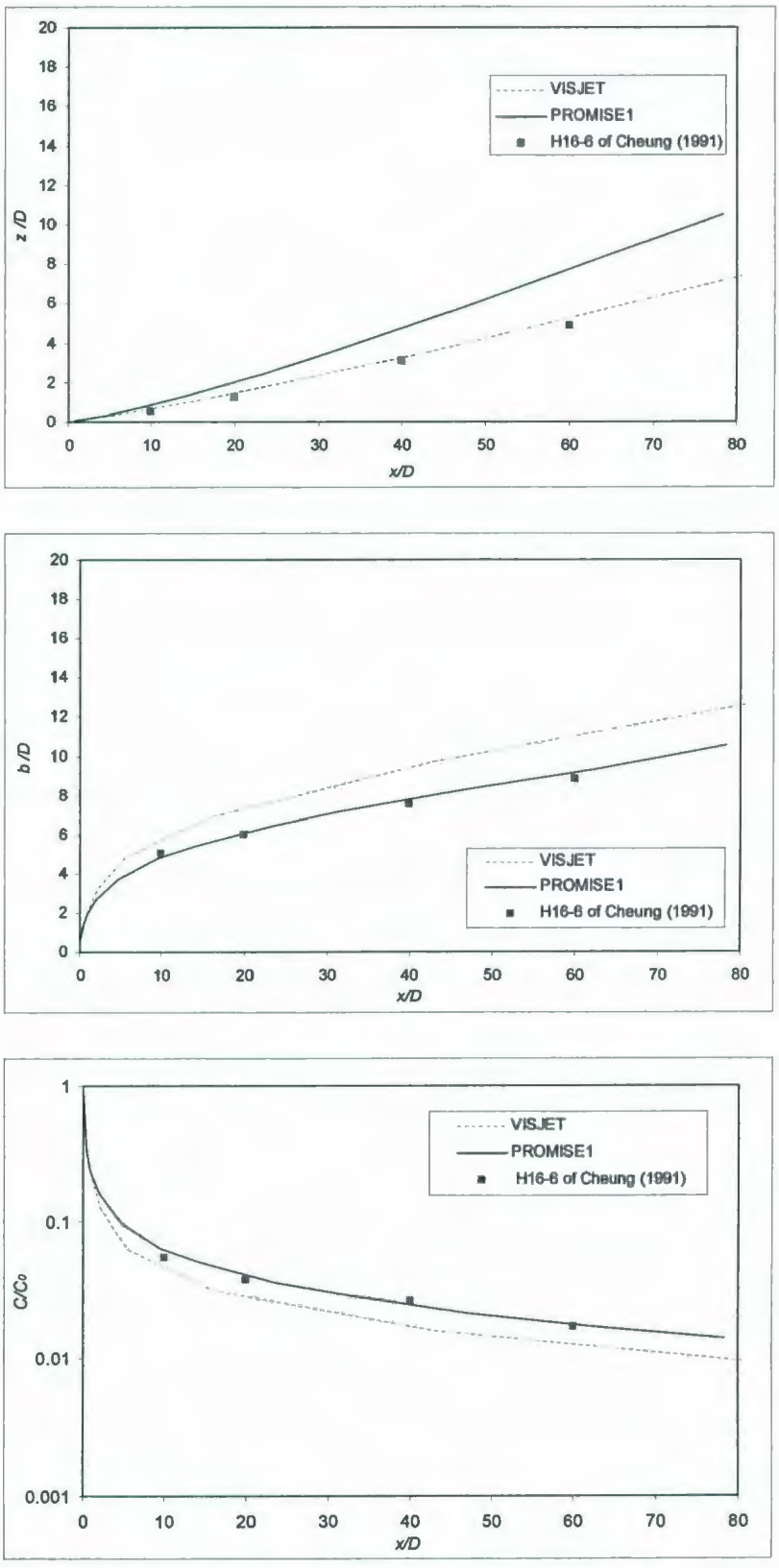

Figure 51. Horizontal jets in cross flow F_r=16, K=6.

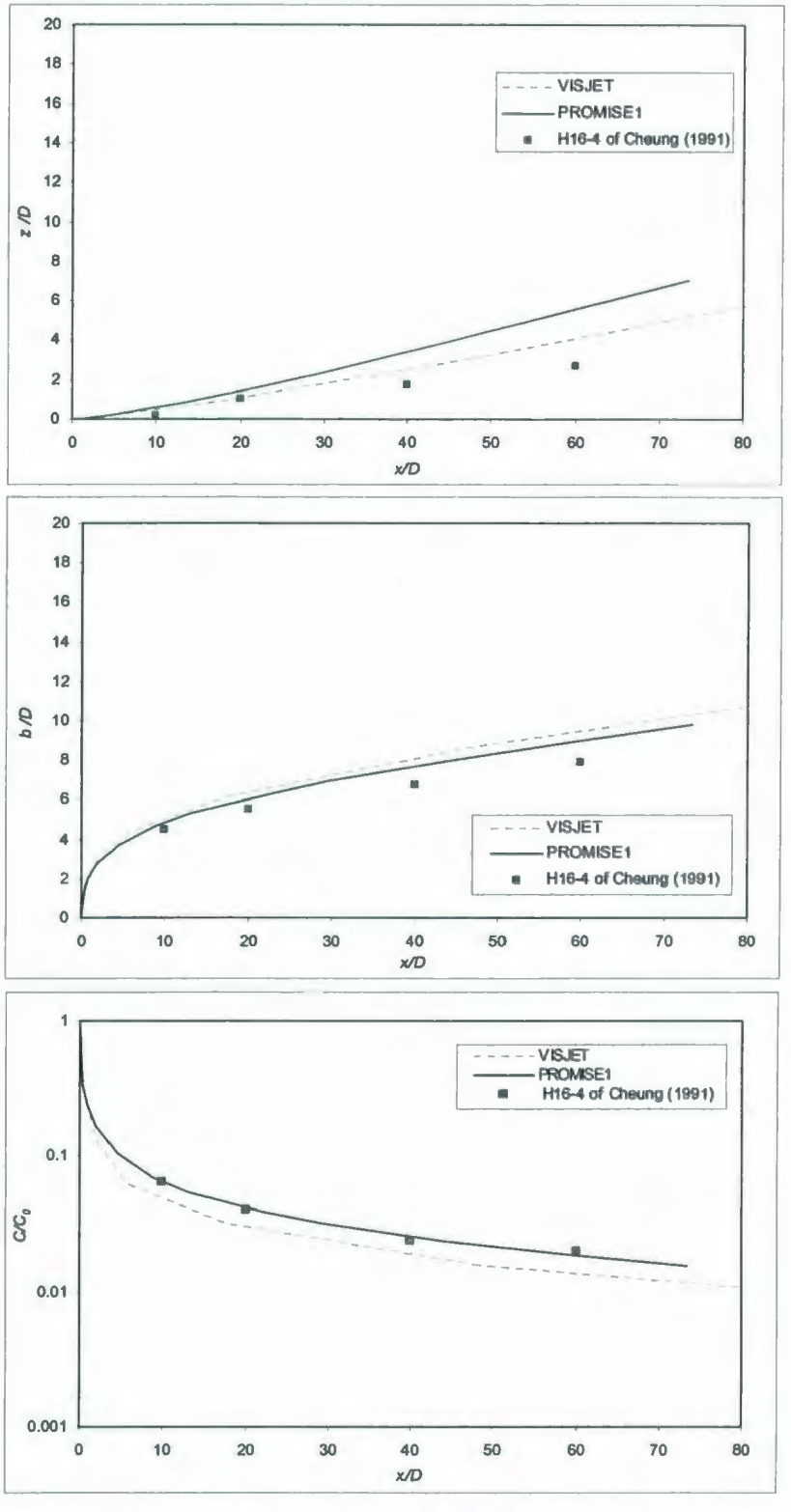

Figure 52. Horizontal jets in cross flow F_r=16, K=4.

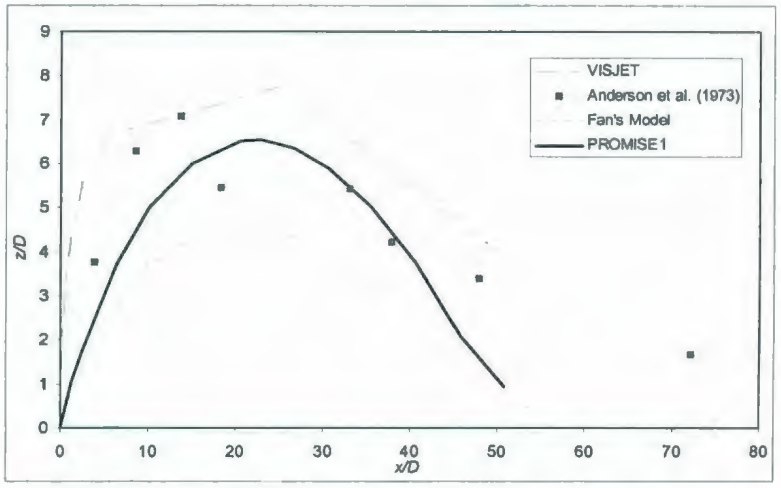

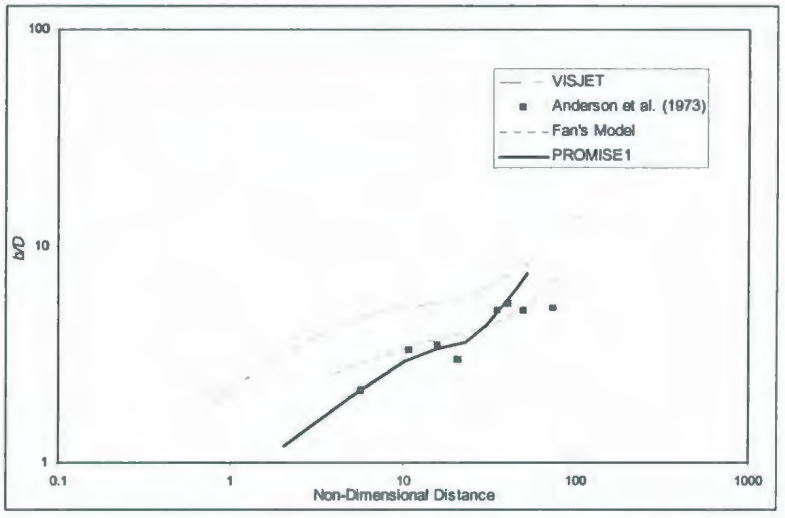

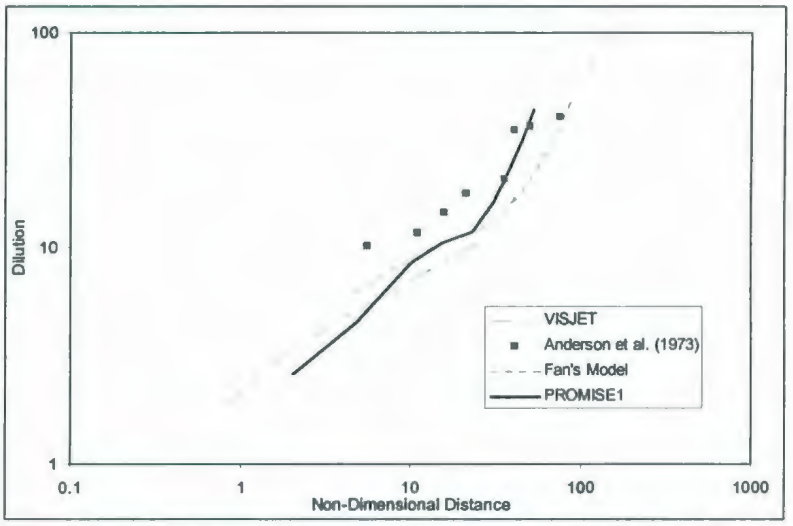

Figure 53. Negative buoyant jet in crossflow F_r=10.9, K=5.5.

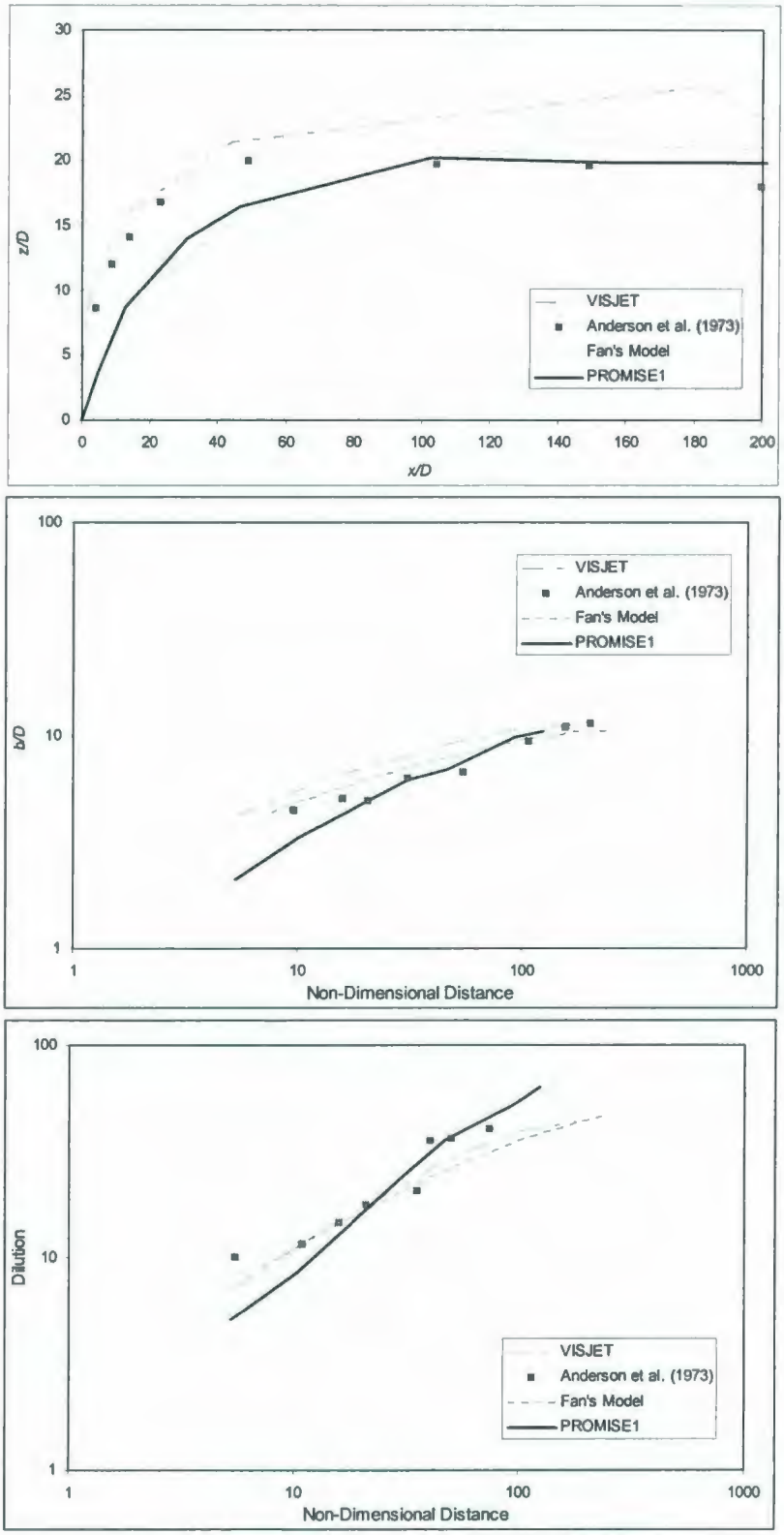

Figure 54. Negative buoyant jet in crossflow F_r=40.7, K=10.2.

4.3 LABORATORY EXPERIMENTAL STUDY

The laboratory experimental work on buoyant jets has been reviewed in section 4.1 and the experimental conditions are summarized below in Table 18.

A successful jet model must have four features. 1) The densimetric Froude number (as shown in Equation 19) of the model and prototype must be equal. The equality of Froude number means that the ratio of the jet momentum flux to jet buoyancy flux will be correct, and therefore the jet entrainment will be correctly modeled. 2) The ratio of jet velocity to current velocity must be equal in model and prototype. 3) The jet discharge angle must be identical in model and prototype. 4) The model Reynolds number (as shown in Equation 199) must be significantly large so that the model jet is fully turbulent in order that the jet mixing is similar.

$$\mathrm{Re} = \frac{U_j D}{\nu} \tag{199}$$

where the ν is the kinematic viscosity in m^2/s.

It can be seen from Table 18 that all of these studies on horizontal discharged and vertical (except the negatively) discharged jets were conducted at small scales. Considering a prototype discharge pipe of 35.6 cm in diameter (the diameter used on the FPSO for the White Rose site, east coast of Canada), the scales of these models range from 32.4:1 to 197.8:1. In order to find the effect of experimental scale and to simulate the real situations as closely as possible, large scale experiments on buoyant jet problems become important.

To further validate the PROMISE1 model, especially against large scale experiments, a set of experiments have been conducted in the Ocean Engineering Research Centre, Memorial University of Newfoundland.

Table 18. Summary of test conditions of the experiments on buoyant jets (without wave effect).

	D (cm)	W (cm)	W (D)	H (cm)	H (D)	U_j (cm/s)	U_a (cm/s)	Q(cm3/s)	Fr	K	Scale (35.6cm/D)
Fan (1967)	0.76	109	144D	50	65D	104-232	13.10-27.8	47.00-105.24	10.00-80.00	4-16	46.8
Fan (1967)	0.51	50	215D	50	98D	131-296	12.30-18.5	26.70-60.50			69.8
Ayoub (1971)	1.00	152	152D	50	50D	38-200	4.3-18.2	29.80-157.10	1.003-64.00	4.75-20	35.6
Ayoub (1971)	0.50	152	304D	50	100D	119-400	9.7-18.2	23.30-78.50	14-73	12.3-22	71.2
Holly & Grace (1972)	1.10	213	193D	61	55D					5-120	32.4
Anderson (1973)	0.80	60	76D	30	38D				10-40	10-20	44.5
Anderson (1973)	0.32			60	187D	230	6-23	18.49	50	10-37	111.3
Chu (1975)	1.01	30	30D	45	45D	23.1-100.2	5.77-8.36	18.50-80.20	1.1-2.3	4-12	35.3
Wright (1977b)	0.80	61	60D	55	55D	88.5	3.98-5.06	44.50	20	17-22	44.5
Chu & Goldberg (1974)	0.18	30	166D	45	250D	0-460	0.0-24.0			4-16	197.8
Tong & Stolzenbach (1979)	0.79	60	75D	70	88D	100-108	0.97-7.07	49.50-53.40	18.8-21.2	16.1-100	45.1
Cavola (1982)	2.50	60	24D	90	36D				0.5-1.5	0.5-1.5	14.2
Brown (1984)	0.80			100	125D	32.5-210	2.04-16.3	1.02-110.00	7.27-106	8.3-33	44.5
Roberts & Toms (1986)	1.00	75	75D	100	100D				25	13-108	35.6
Lee & Cheung (1991)	0.75	30	40D	40	53D	5.59-13.2	0.19-6.8	2.47-5.83	1.8-4.2	1.9-58	47.5
Gaskin (1995)	0.67	100	150D	90	150D	39	0.16-1.12	11.02	10	34-243	53.1
Roberts et al. (1997)	0.43	91	212D	61	142D			9.50-14.8	18.7-26.4		82.8
Zhang & Baddour (1998)	1.95	100	51D	100	51D		0		0.37-10.8		18.3
Ulasir & Wright (2003)	0.5	300	600D	45	90D		0				71.2

4.3.1 Experimental Setup and Methods

4.3.1.1 Towing Tank

The experiments were performed in a 58 m long, 4.5 m wide, and 2.2 m deep towing tank (Figure 55). This tank also has the capability to generate waves. The specifications of the towing tank are shown in Table 19.

Table 19. Specifications of the 58 meter towing tank.

Parameters	Specifications
Length	58m
Width	4.5m
Water Depth	2.2m
Tow Carriage Speed	0.05 - 5m/sec
Max. Wave Height (Regular Waves)	0.7m
Max. Sig. Wave Height (Irregular Waves)	0.2m
Range of Wavelengths	0.9m to 17m

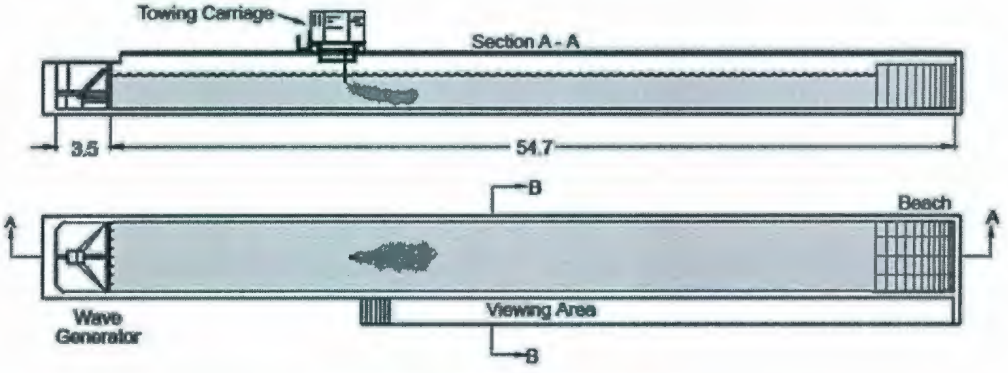

Figure 55. The 58 m towing tank.

The ambient velocity was simulated by towing the discharge pipe at a specified speed. The advantage of using a towing setup rather than a recirculation flume is that this setup can avoid the non-uniformities in ambient velocity over the jet-cross section or any effects caused by presence of non-uniform ambient turbulence.

4.3.1.2 Conductivity Measurements

For the dilution studies, the commonly used tracers are: concentration of dye, salinity, or temperature. Although the most advanced technology for this type of study is the 3D-LIF method, the cost of this system is very high. Moreover, most of the existing LIF systems can only give measurements in a limited area. This is not a problem for a small scale test as it can cover the entire plume cross-section. However, this may not provide enough coverage for a relatively large scale test. Therefore, a traditional conductivity measurement method was used.

In this study, a Micro CTD sensor was used to collect the conductivity/salinity information (Figure 56). The specifications of the Micro CTD are listed in Table 20.

Figure 56. Micro CTD for conductivity measurements.

Table 20. Specifications of the Cyclops-7 fluorometer.

Parameters	Range	Precision	Accuracy	Response	Resolution
Conductivity	0-70 mS/cm	0.005 mS/Cm	0.01 mS/cm	25 ms at 1m/s flow	0.001mS/cm
Temperature	-2 to 32 °C	0.003 °C	0.005 °C	100 ms	0.001 °C
Pressure	to 500 m			10 ms	
Salinity	0 - 40 PSU	0.005 PSU	0.01 PSU		0.001 PSU

4.3.1.3 Experimental setup

For laboratory experiments, a discharge system with a large effluent pipe has a high flow rate that discharges large volumes of source water. Three main disadvantages are associated with such a discharge system: 1) compared with a small flow rate system, the cost of the chemicals to make the density difference will be increased; 2) the designed constant water head will be altered due to the alteration of water level in the towing tank from receiving of a large volume of discharges; and 3) the plume behavior will be affected by the walls of the receiving tank if the ratio of the pipe diameter to the width of receiving tank is high. This effect is especially significant for the tests in a stagnant environment because the far field plume may be re-entrained into the near field.

Due to the above reasons, a 2.5 cm effluent pipe is considered appropriate for this study and this diameter gives an experimental scale of 14.2:1 (based on Table 18). Nedwed et al. (2001) have concluded that produced water discharges generally have densimetric Froude numbers that range in the order of magnitude from 0.1 to 10 and exit-to-cross-flow velocity ratios of 0.1 to 80. In this study, three levels of flow rates were used, the flow rates were 0.000739, 0.00059, and 0.00037 m^3/s. These flow rates corresponded to exit velocities at 1.48, 1.164, and 1.00 m/s respectively. Three levels of towing speeds were used; the towing speeds were 0.1, 0.15, and 0.2 m/s.

The ambient water was freshwater with densities ranging from 999.02 to 999.58 kg/m^3. Purified fishery salt was used to generate the density difference and the salinity was used as a tracer. The discharge densities ranged from 1022.03 to 1046.37 kg/m^3. The combination of these conditions gave a densimetric Froude number ranging from 9.81 to 17.24 and a velocity ratio ranging from 5 to 14.58.

The schematic of the source discharge system is shown in Figure 57, and the experimental procedure is described below.

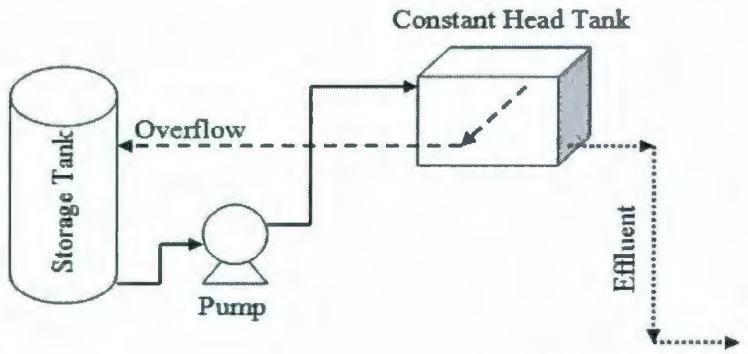

Figure 57. Schematic of the source discharge system.

4.3.1.4 Procedures

1. In this study, the salinity was selected as the concentration tracer. The salt solutions was first prepared and stored in a 140L storage tank. This volume can provide 3 to 6 minutes flow for the system depending on the flow rate.
2. In the test, the effluent valve was closed first, and then the salt solution was pumped from the storage tank into the constant head tank. The constant head was maintained by two 5 cm diameter overflow pipes mounted 30 cm above the bottom of the constant head tank. The water level inside the constant head tank was kept constantly at 30 cm. The surface of the constant head tank above the water level in the towing tank was adjusted to give the desired flow rate.
3. A discharge pipe of 2.54 cm diameters were submerged to the depth of 40 cm below water surface. The Micro CTD was positioned at predetermined downstream distance.

4. The effluent valve on the bottom of the constant head tank was opened slowly. After visual observation of the surfacing of the plume, the towing carriage was started. After the towing carriage was running for 30 seconds, and the bubbles were eliminated, the Micro CTD was submerged and moved up and down across the plume to take measurements. The Micro CTD was set to take 10 samples per second.

To reduce the bias and systematic errors, the tests were conducted in a random order. To allow for a more accurate estimate of dilution values and allow an estimate of experimental error, each test was repeated to get one replication. The detailed test configurations and sequences are listed in Tables 21, 22, and 23.

4.3.2 Experimental Results and Discussions

Although it is desired to obtain the plume trajectory, plume width as well as dilution information from the experiment, only concentration information was obtained from the experiments.

The reason for this is that a pre-calibration of the Micro CTD shows a high degree of uncertainty for the depth reading. It can be seen from Figure 58 that a bias as high as 4 cm occurred. Although this bias is acceptable compared with the 500 m measurement range, it is too high for this lab scale test. The plume width is less than 20 cm at some measurement points and this corresponds to 20% of error. Therefore, the trajectory reading and plume width are associated with a high degree of uncertainty and considered not reliable and were not used.

Table 21. Test conditions for flow rate of 0.000739 m^3/s.

No.	Q (m^3/s)	U_j (cm/s)	U_a (cm/s)	R	F_r	ρ_a (kg/m^3)	ρ_j (kg/m^3)	*Non-dimensional* Distance (D)	Experimental ID
1	0.000739	148	10	14.58	15.19	999.34	1036.34	10.0	Test 13
2					15.89	999.34	1033.13	10.0	Test 14
3					15.61	999.51	1034.55	16.5	Test 06
4					15.98	999.49	1032.90	16.5	Test 08
5					14.30	999.31	1041.03	20.0	Test 19
6					14.48	999.31	1039.99	20.0	Test 20
7	0.000739	148	15	9.72	17.24	999.34	1028.06	10.0	Test 11
8					15.37	999.34	1035.46	10.0	Test 12
9					15.11	999.51	1036.91	16.5	Test 05
10					16.76	999.49	1029.86	16.5	Test 07
11					14.25	999.31	1041.34	20.0	Test 17
12					14.51	999.31	1039.82	20.0	Test 18
13	0.000739	148	20	7.29	15.98	999.49	1032.91	10.0	Test 09
14					16.35	999.49	1031.43	10.0	Test 10
15					13.79	999.51	1044.39	16.5	Test 03
16					14.74	999.51	1038.81	16.5	Test 04
17					15.79	999.34	1033.55	20.0	Test 15
18					14.49	999.31	1039.97	20.0	Test 16

Table 22. Test conditions for flow rate of 0.00059 m^3/s.

No.	Q (m^3/s)	U_j (cm/s)	U_a (cm/s)	R	F_r	ρ_a (kg/m^3)	ρ_j (kg/m^3)	*Non-dimensional* Distance (D)	Experimental ID
19	0.00059	116.4	10	11.64	12.6	999.42	1033.67	10	Expe 15
20					---	999.42	---	10	No Data Logged
21					11.39	999.34	1041.30	16.5	Expe 11
22					11.82	999.42	1038.38	16.5	Expe 12
23					10.78	999.58	1046.37	20	Expe 05
24					11.16	999.58	1043.28	20	Expe 06
25	0.00059	116.4	15	7.76	12.83	999.42	1032.47	10	Expe 16
26					---	999.42	---	10	No Data Logged
27					11.45	999.34	1040.81	16.5	Expe 09
28					11.55	999.34	1040.09	16.5	Expe 10
29					11.32	999.58	1042.01	20	Expe 03
30					11.29	999.58	1042.29	20	Expe 04
31	0.00059	116.4	20	5.82	15.51	999.42	1022.03	10	Expe 13
32					11.68	999.42	1039.28	10	Expe 14
33					10.84	999.34	1045.59	16.5	Expe 07
34					11.28	999.34	1042.07	16.5	Expe 08
35					11.64	999.58	1039.74	20	Expe 01
36					11.06	999.58	1044.05	20	Expe 02

Table 23. Test conditions for flow rate of 0.00037 m^3/s.

No.	Q (m^3/s)	U_j (cm/s)	U_a (cm/s)	R	F_r	ρ_a (kg/m^3)	ρ_j (kg/m^3)	*Non-dimensional* Distance (D)	Experimental ID
37	0.00037	100	10	10	11.16	999.18	1031.39	10	Tria 14
38					9.92	999.18	1039.94	10	Tria 17
39					10.91	999.33	1033.08	16.5	Tria 02
40					10.80	999.33	1033.72	16.5	Tria 05
41					10.62	999.02	1034.63	20	Tria 08
42					10.18	999.02	1037.71	20	Tria 11
43	0.00037	100	15	6.67	10.33	999.18	1036.79	10	Tria 15
44					9.81	999.18	1040.86	10	Tria 18
45					10.81	999.33	1033.66	16.5	Tria 03
46					10.52	999.33	1035.61	16.5	Tria 06
47					10.26	999.02	1037.18	20	Tria 09
48					10.29	999.02	1036.92	20	Tria 12
49	0.00037	100	20	5	9.86	999.18	1040.49	10	Tria 13
50					9.93	999.18	1039.88	10	Tria 16
51					12.04	999.33	1027.03	16.5	Tria 01
52					10.75	999.33	1034.10	16.5	Tria 04
53					11.18	999.02	1031.12	20	Tria 07
54					10.07	999.02	1038.62	20	Tria 10

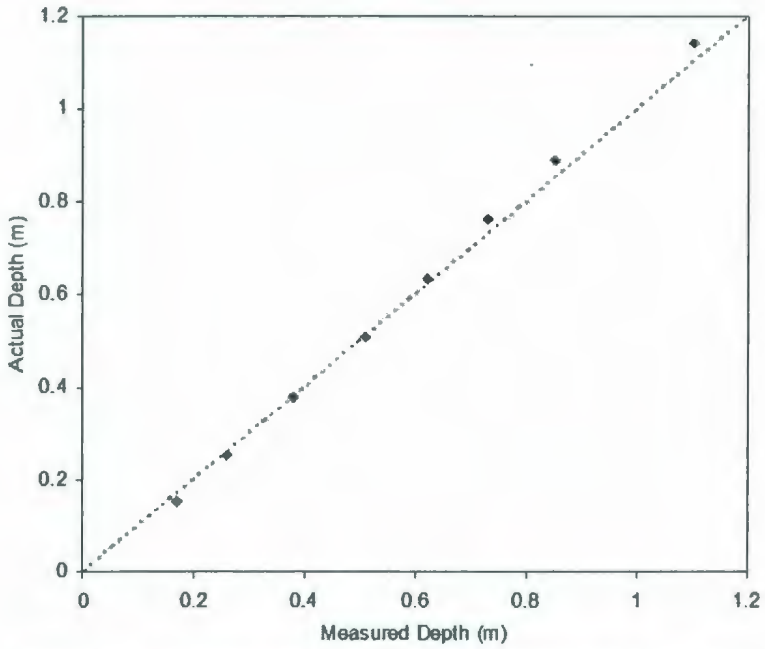

Figure 58. Calibration of the depth reading for the MicoCTD sensor.

4.3.2.1 Comparison with CORMIX Model

The experimental results were first compared with existing models. The CORMIX model was selected for comparison. The COMIX model prediction is the maximum centerline concentration. Therefore the maximum measured concentration was used. As the plume behavior is highly instantaneous, a single maximum value may not be representative, so the average of 10 maximum measured values was used as the maximum value.

The comparison examples for three test cases are shown in Figures 59, 60, and 61. It can be seen from these figures that the experimental data and CORMIX model prediction agree well.

As there are 52 experiments in total, presenting the comparisons in the form of Figures 59 to 61 is impractical. Instead, the results for three different flow rates are summarized in Figures 62 to 64.

For the case of Q=0.000739 m^3/s, it can be seen from Figure 62 that the experimental data and CORMIX model agree very well. There is a very slightly underestimation of dilution by CORMIX model. For example, when the measured dilution is about 23.5, the CORMIX predicted a dilution of about 21. The regression line showed a 15 percent underestimation.

For the case of Q=0.00059 m^3/s, it can be seen from Figure 63 that the experimental data and CORMIX model agrees very well. It can be seen from the regression line that both slight underestimation and overestimation of dilution by the CORMIX model occurred. The bias is about 15 percent.

For the case of Q=0.00037 m^3/s, a similar trend as the Q=0.00059 m3/s case is shown in Figure 64. The regression line showed that the bias is about 19 percent.

Although the individual comparison showed there is still some degree of bias, combining all three cases together in Figure 65 showed the prediction and experimental data agreed very well. The regression line shows the bias is only about 5 percent.

4.3.2.2 Calibration of Entrainment Coefficient

It can be seen from the comparison above that the experiment data and CORMIX model prediction showed good agreement. Therefore, the experiment data can be used to further calibrate the entrainment coefficients.

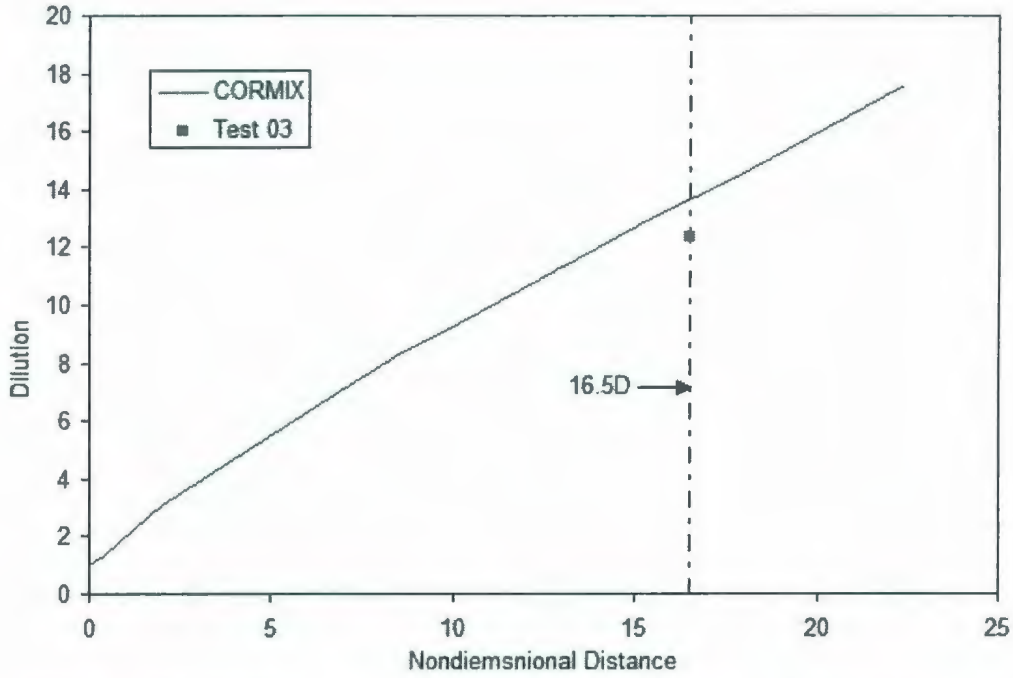

Figure 59. Comparison with CORMIX model with Test 03 (Q=0.00073, U_a=20cm/s, x=16.5D).

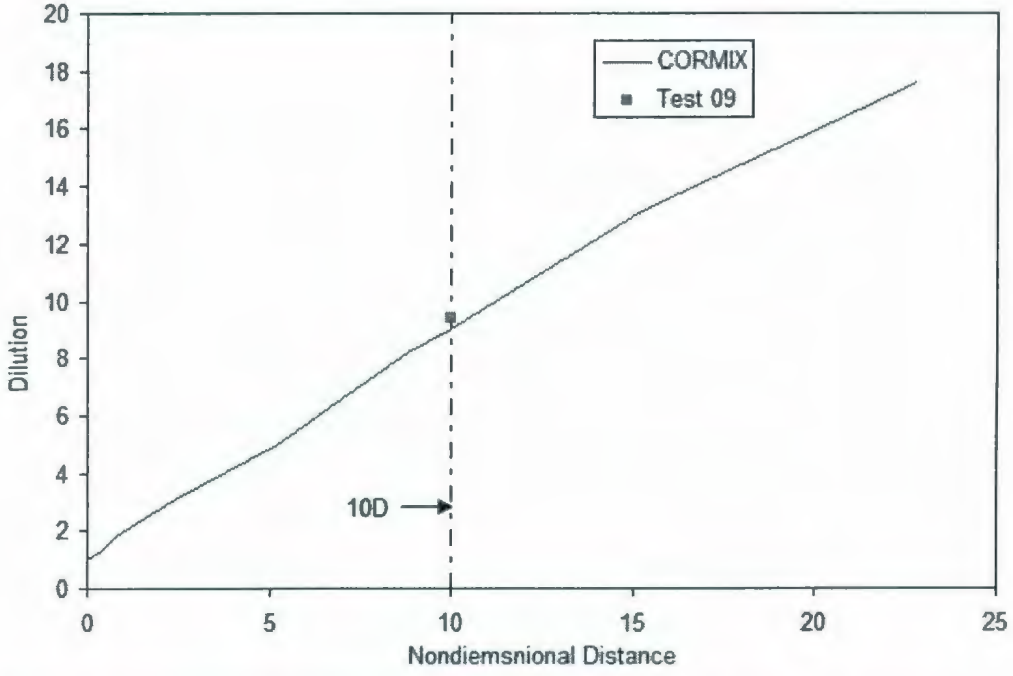

Figure 60. Comparison with CORMIX model with Test 09 (Q=0.00073, U_a=20cm/s, x=10D).

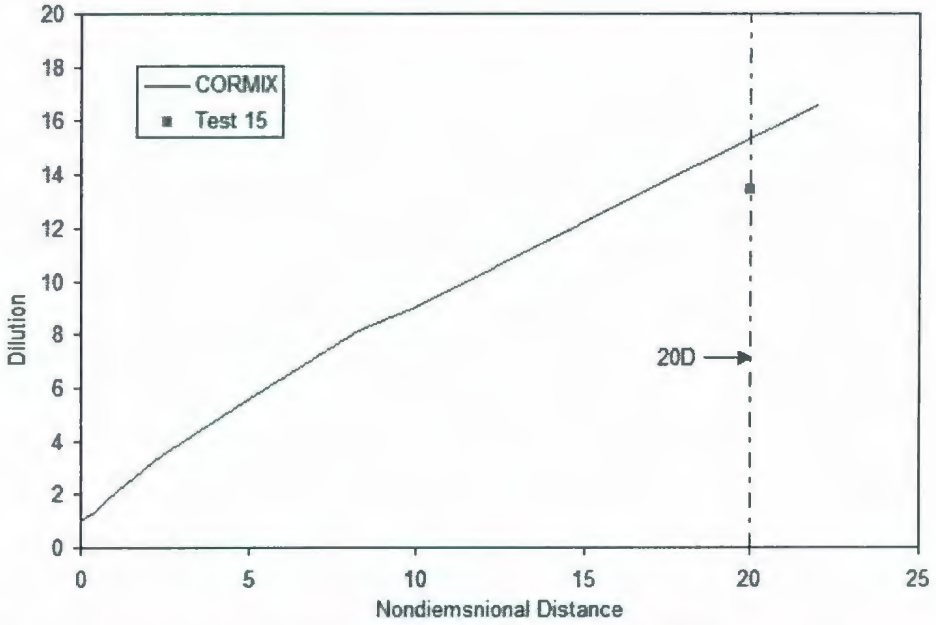

Figure 61. Comparison with CORMIX model with Test 15 (Q=0.00073, U_a=20cm/s, x=10D).

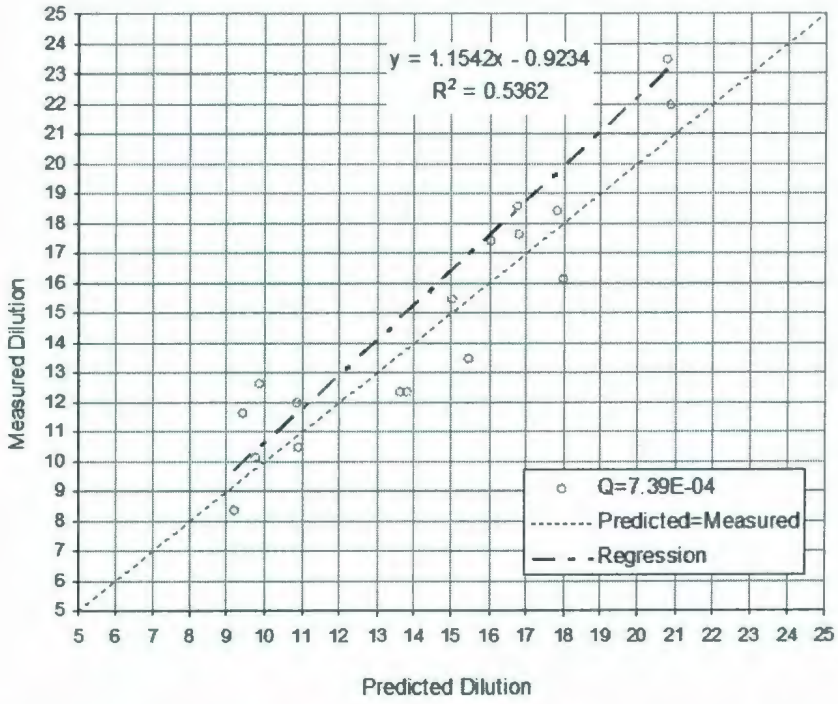

Figure 62. Comparison of CORMIX with experimental data (Q=0.000739 m^3/s).

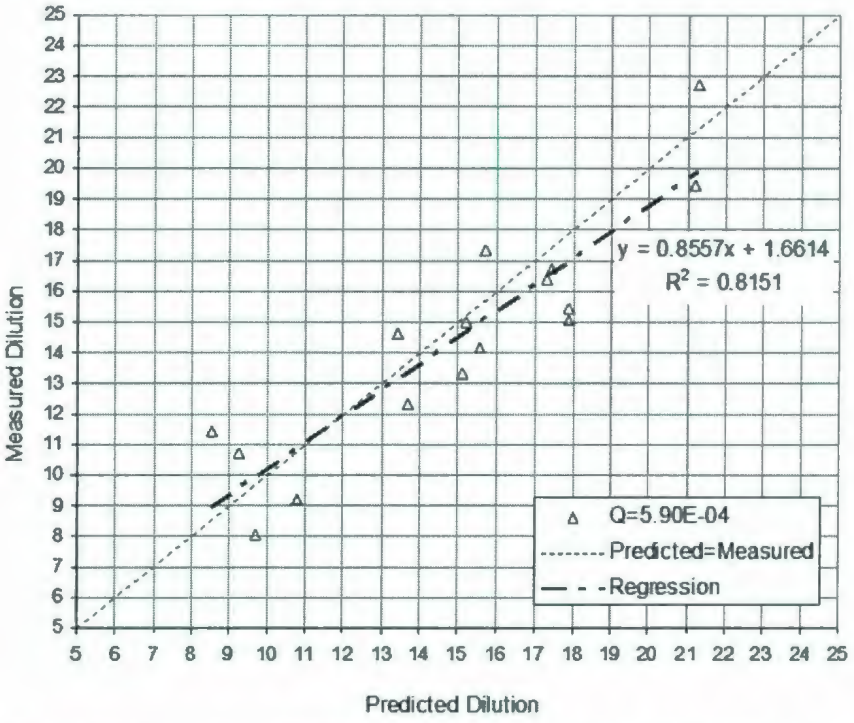

Figure 63. Comparison of CORMIX with experimental data (Q=0.00059 m^3/s).

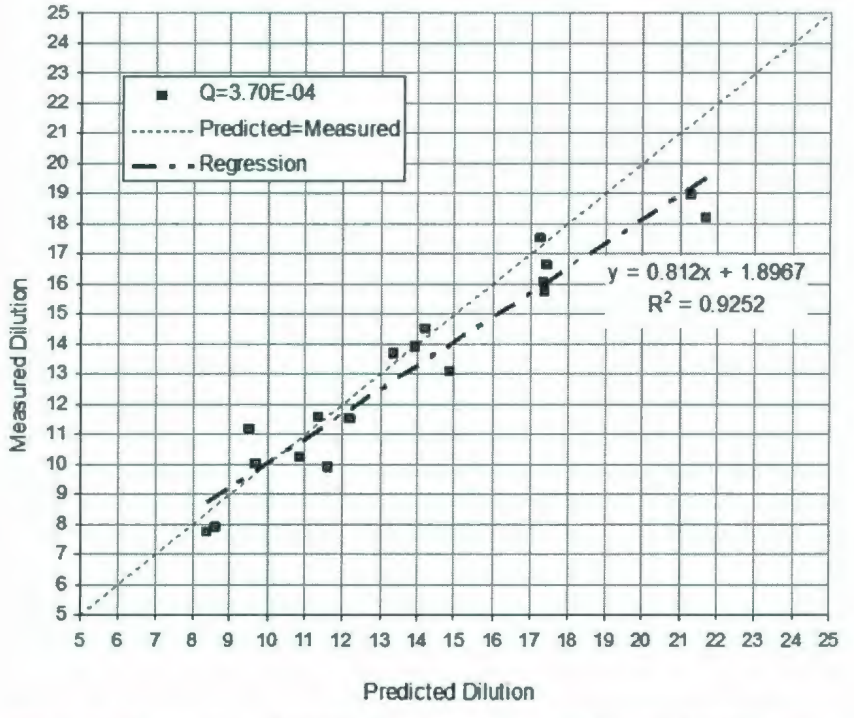

Figure 64. Comparison of CORMIX with experimental data (Q=0.00037 m^3/s).

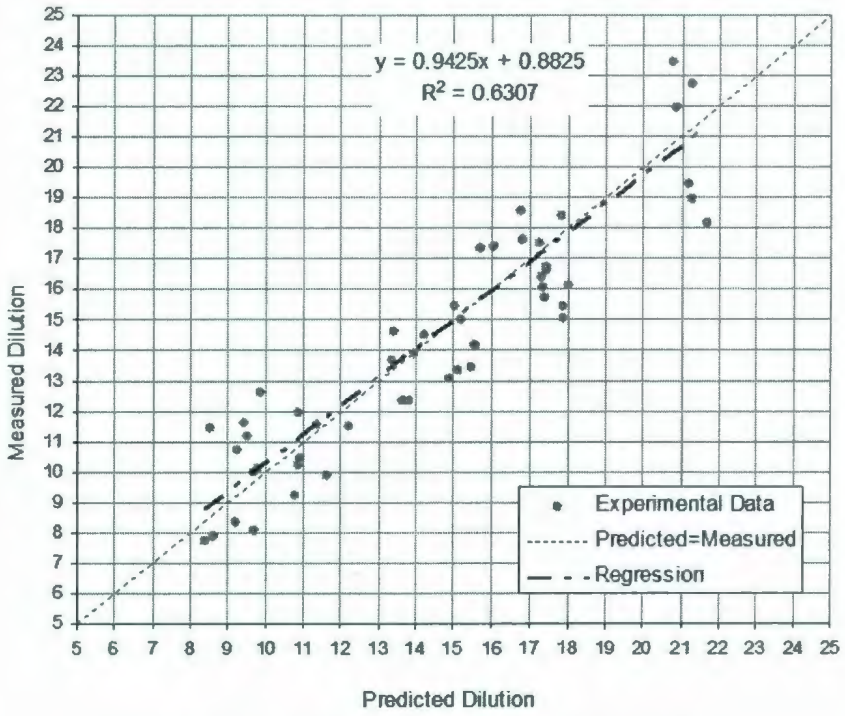

Figure 65. Comparison of CORMIX with experimental data.

The test conditions for the calibration are shown in Figure 66. The new data sets were plotted together with the data used in Chapter 3. The same trial-and-error process as used in Chapter 3 was used to match the data with the prediction of PROMISE1 in a least-square sense. The results are shown in Figure 67, Equation (200).

$$\alpha_{vortex} = [0.4047 \pm 0.0528](F_L K)^{[0.705 \pm 0.0372]} \quad \textbf{(200)}$$

In Figure 67, the Literature means the data collected from literature and used in Chapter 3. Data labeled with flowrate Q are from the present experimental work. Tate's (2002) formulation are plotted together with Equation (200). It can be seen from Figure 67 that the Equation (200) is deviated from Tate (2002) formulation in ranges where $F_L K$ is less than 10 and greater than 100. This is mainly because most of

the present data has a $F_L K$ value between 10 and 100. The mean vortex entrainment value for the new data set is about 0.49.

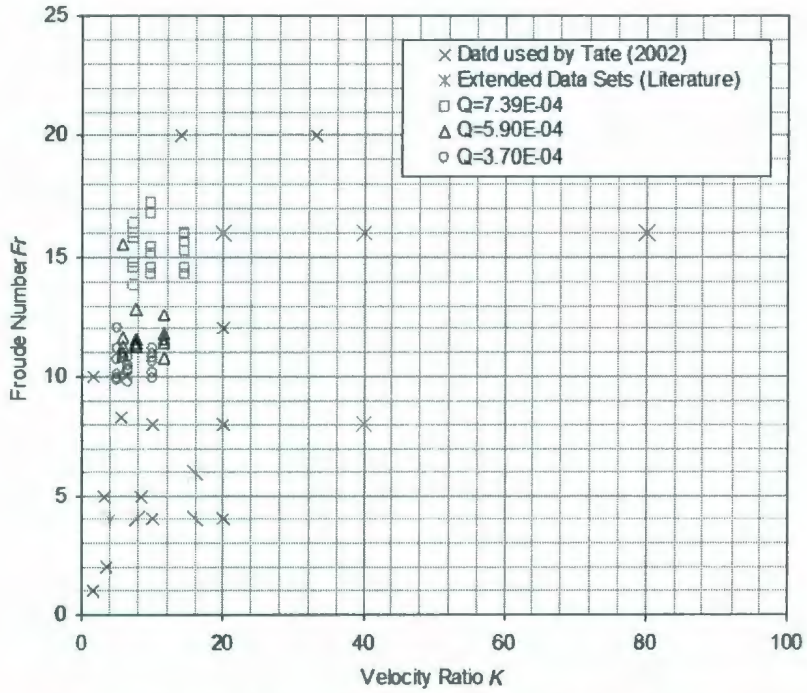

Figure 66. Experiment conditions used for the calibration of entrainment coefficients.

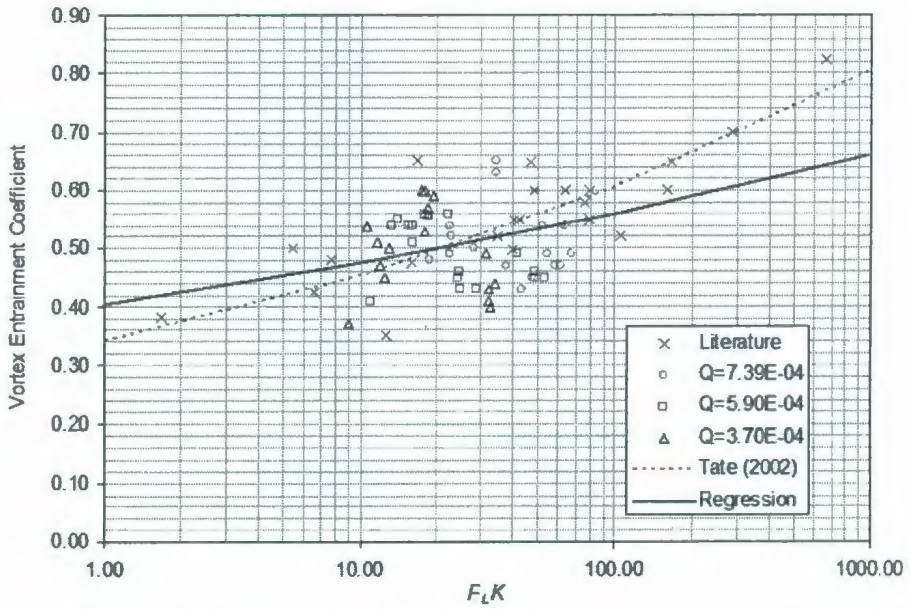

Figure 67. Vortex entrainment as a function of the product of local densimetric number and the discharge velocity ratio.

4.3.2.3 Comparison with PROMISE1 Model

Based on the calibrated entrainment formulation (Equation 200), the predictions of PROMISE1 were compared with the experimental data. The results are illustrated in Figure 68.

It can be seen from Figure 68 that the PROMISE1 can predict the dilution reasonably well. The predicted value and the measured value have a difference of about 10 percent.

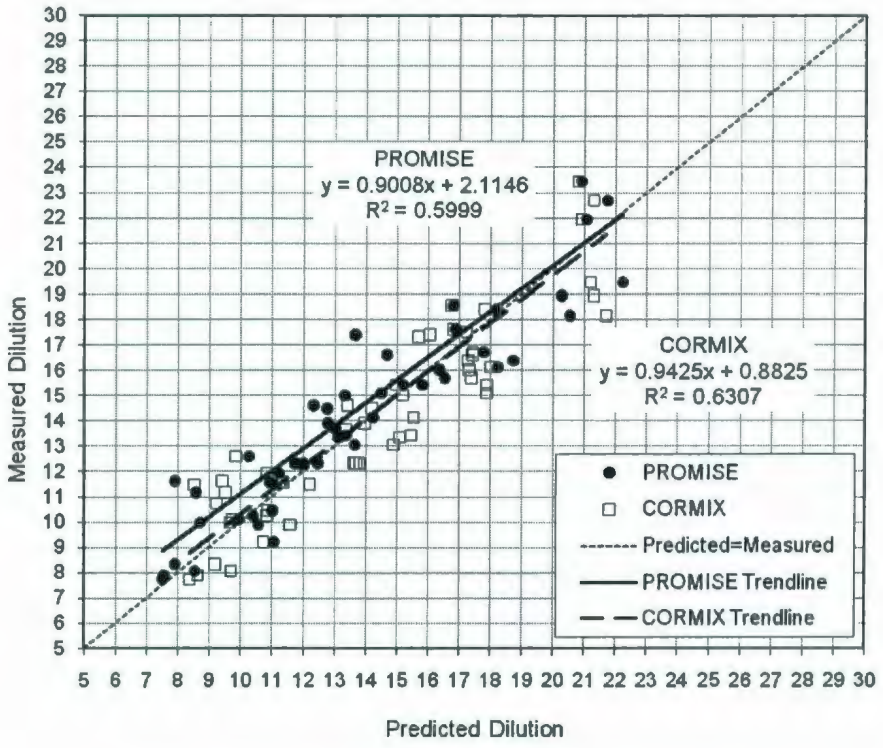

Figure 68. Comparison of experimental data with PROMISE1

4.4 SUMMARY

In this Chapter, the PROMISE1 model was first validated with reported experimental data. A well known model, VISJET, was also used for comparison. It

was found that PROMISE1 can predict the dilution very well; however its trajectory prediction is weaker than the VISJET prediction.

Large scale experiments were performed to further validate the PROMISE1 model. 56 experiments were conducted. By comparison with the CORMIX model, the measured data show good agreement. The data were then processed to calibrate the entrainment coefficient.

The predictions from the calibrated model can reproduce the measured dilution reasonably well with a difference up to 10 percent.

5. HYPOTHETICAL STUDY: APPLICATION OF PROMISE

In this Chapter, the proposed PROMISE model will be used to model the produced water discharge from a hypothetical site off the east coast of Canada. Both the deterministic and probabilistic based approaches will be used.

5.1 DESCRIPTION OF THE STUDY SITE

5.1.1 Discharge Characteristics

The hypothetical study site (48°28.86'W,46°28.53'N) is located about 350 km east-southeast of St. John's, Canada. The location of the study site is shown in Figure 69.

The temperature of the produced water is assumed to be 60 °C. This is significantly warmer than the ambient seawater which has a temperature range from 0.7 °C in winter to 9.5 °C in summer (Hodgins and Hodgins, 2000). The salinity of the produced water is assumed to be 25 ppt and this is lower than that of the receiving seawater (about 32 ppt). The density of the produced water is about 728 kg/m^3. The discharge is from an FPSO (Floating Production Storage and Offloading) vessel via a pipe of 0.325 m in diameter at a depth about 5 m below the water surface.

The maximum flow rate is estimated to be 0.35 m^3/s. Based on the measured flowrates from other sites in this area (LES, 2006), the mean flow rate is about 50% the maximum flow rate. Therefore the mean flow rate is estimated as 0.175 m^3/s. The initial pollutant concentration is assumed to be 100 (percent). In this way, the predicted concentration can be easily compared with this initial value.

Figure 69. Location of the hypothetical study site.

5.1.2 Ambient Characteristics

The water depth at this site is about 125 meters. The current information required for the modeling is available from the Bedford Institute of Oceanography, Fisheries and Oceans Canada (Hodgins & Hodgins, 2000). The currents in the vicinity of this study site are dominated by wind and tide with a weak mean flow to the south. Although located on the northeast shoulder of Grand Banks, the effects of the strong persistent Labrador currents appears to be very weak.

The detailed current information is shown in Figures 70 and 71. Based on a three-month record, the maximum surface current is 44.5 cm/s and the minimum value is 0.1 cm/s. The mean value is 13 cm/s and the median value is 12 cm/s.

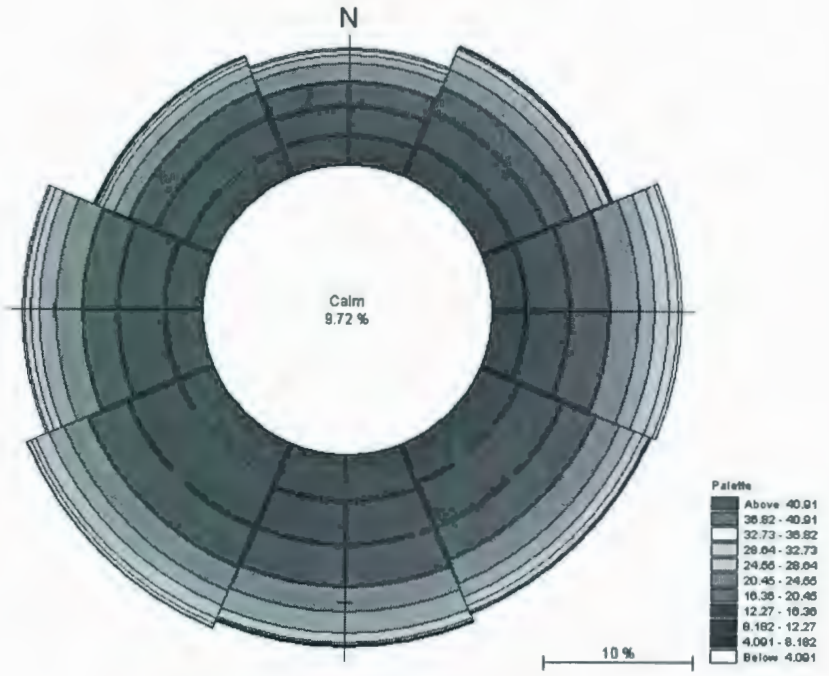

Figure 70. Rose plot of the surface currents.

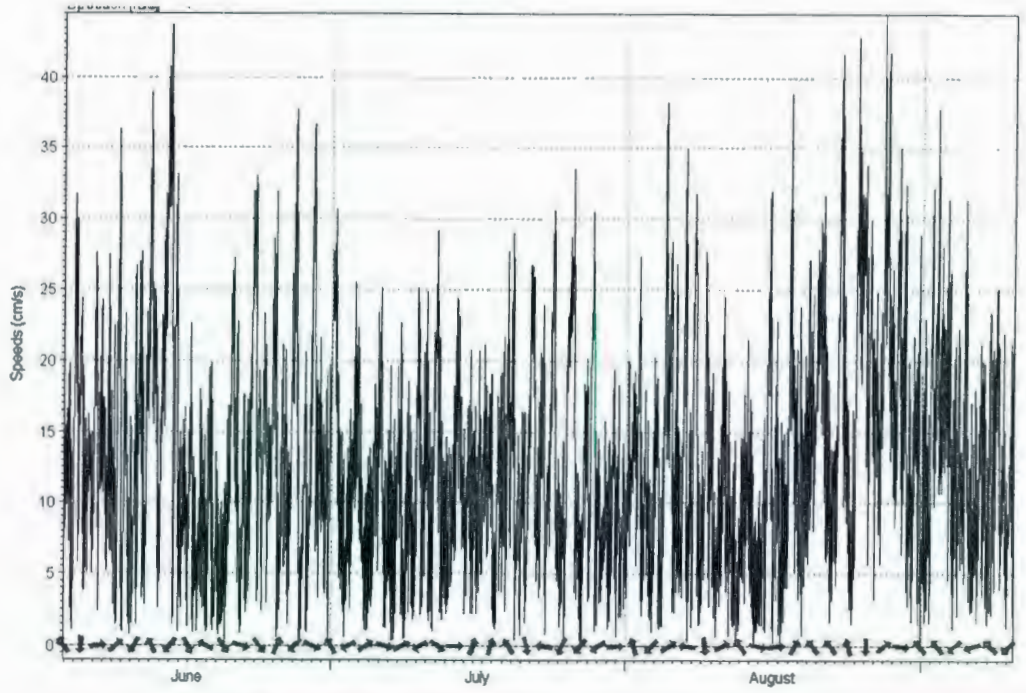

Figure 71. Time series plot of the surface currents.

For the probabilistic based approach, mathematical descriptions of the distributions for current directions and speeds are needed. Through the analysis of the data, it is found that both the current speeds and directions can be described by a BetaGeneral distribution. Four parameters are required to describe the function, they are: Coefficient 1, Coefficient 2, Minimum, and Maximum. The statistical information of the data and the fitted BetaGeneral distribution are listed in Table 24, and Figures 72 and 73.

Table 24. Statistical description of the currents speeds and directions

	Speed (Data)	Speed (BetaGeneral)	Direction (Data)	Direction (BetaGeneral)
Coefficient 1		2.14		1.19
Coefficient 2		7.60		1.23
Minimum	0.09	0.0	0.05	0
Maximum	44.53	59.8	359.88	360
5% (Left)	2.87	2.87	24.4	24.4
95% (Right)	27.3	27.3	333.4	333.4
Difference (90%)	24.44	24.44	308.9457	308.9457
Mean	13.058	13.059	177.66	177.86
Mode	8.87	8.72	105.21	168.01
Median	11.95	11.88	178.72	177.20
Standard Deviation	7.5609	7.5638	95.608	97.305
Variance	57.159	57.212	9139.56	9468.25

The density information is only available for three depths (20 m, 47 m, and 80 m) and the detailed measurements of the density profile at various depths are unavailable. For this site, because the produced water is discharged at 5 m depth and it is much lighter than ambient seawater, only the density measurement at 20 m is needed. Due to the lack of surface measurements, the seawater density is assumed to be uniform. The density data is analyzed and a triangular distribution was fitted.

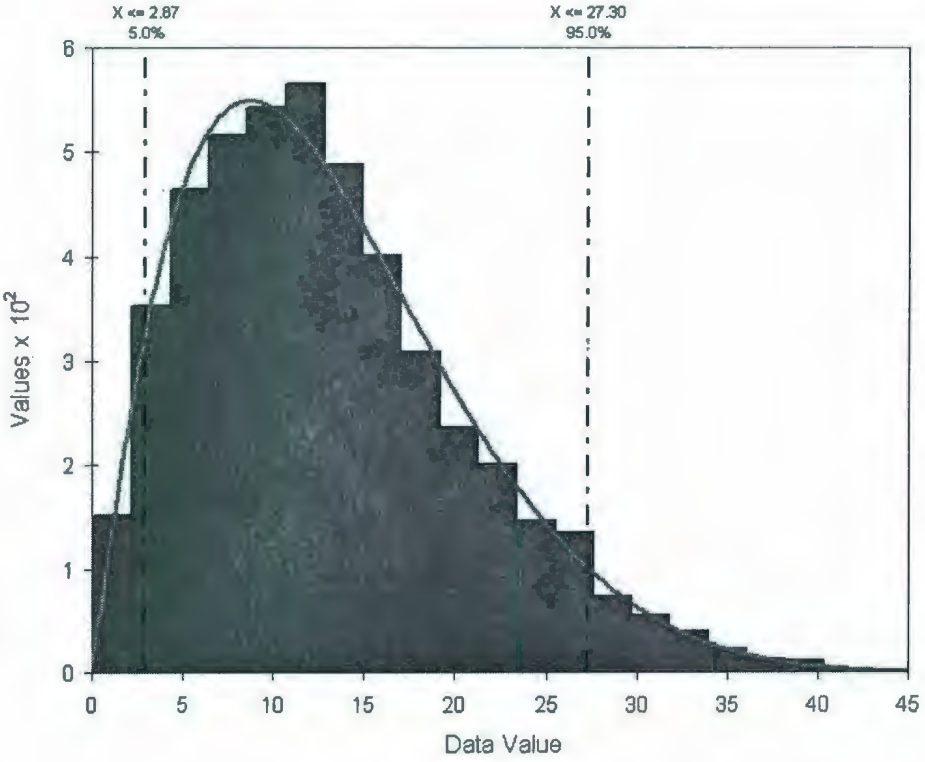

Figure 72. Fitted distribution for the current speeds.

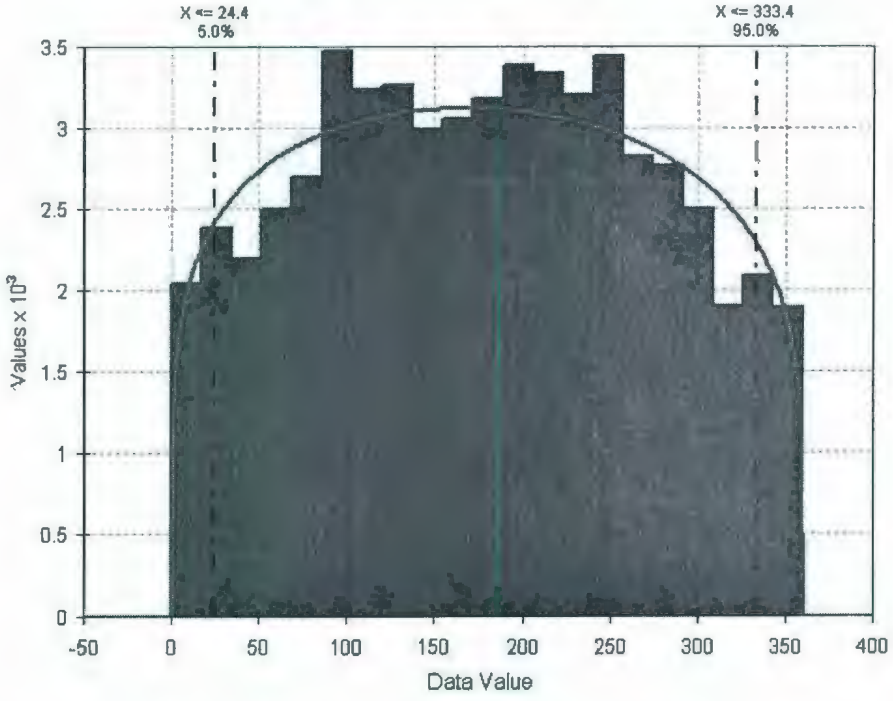

Figure 73. Fitted distribution for the current directions.

The statistical descriptions of the density are listed in Table 25. The comparison of data and fitted values are given in Figure 74. It can seen from Figure 74 the fitted value reproduces the data well.

Table 25. Statistical description of the density.

	Density (Data)	Density (Triangular)
Minimum	1023.0143	1022.9563
Most likely		1025.6361
Maximum	1026.1931	1026.1940
Mean	1024.9603	1024.9288
Mode	1025.4032	1025.6361
Median	1025.2984	1025.0392
Standard Deviation	0.7405	0.7066
Variance	0.5483	0.4993

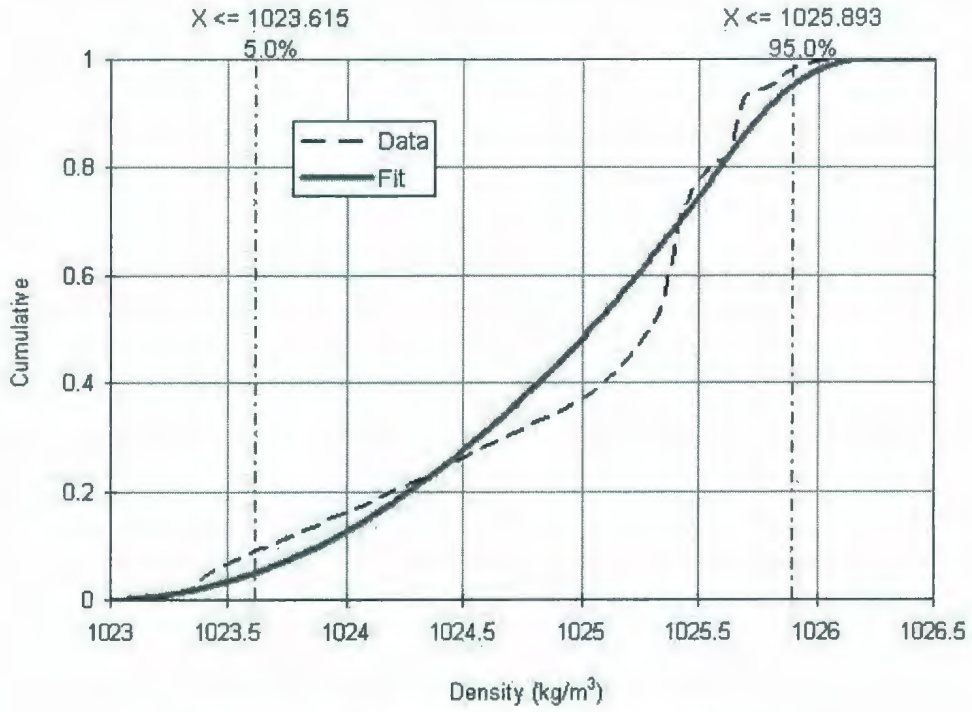

Figure 74. Fitted distribution for the ambient density.

5.1.3 Wind

Wind data is required to calculate the wave height and period. Although the real time data for this site is available, historic data is unavailable for statistical analysis. Due to this reason, wind data from a close station were used. The data were downloaded from the Environment Canada website.

The time series wind data is plotted in Figure 75 and the wind rose is plotted in Figure 76. It can be seen from Figure 75 that the maximum wind speed is about 46 km/h for and mean speed is about 17 km/h. It is shown in Figure 76 that the dominant wind directions are west and southwest.

The detailed statistics for wind speed are listed in Table 26. A Weibull distribution has been fitted to the data and the comparison is shown in Figure 77. Although the maximum number for a Weibull distribution is infinity, a trimmed maximum number of 46 was used to be consistent with data.

Table 26. Statistics for wind speed.

	Wind Speed in km/h (Data)	Wind Speed in km/h (Fitted)
Distribution		Weibull
Coefficient 1		2.9033
Coefficient 2		23.3647
Minimum	0	0
Maximum	46.00	+infinity (Trim to 46)
Mean	17.373	17.346
Mode	19.00	16.714
Median	19.00	17.105
Standard Deviation	7.74	7.79
Variance	3.31	2.74

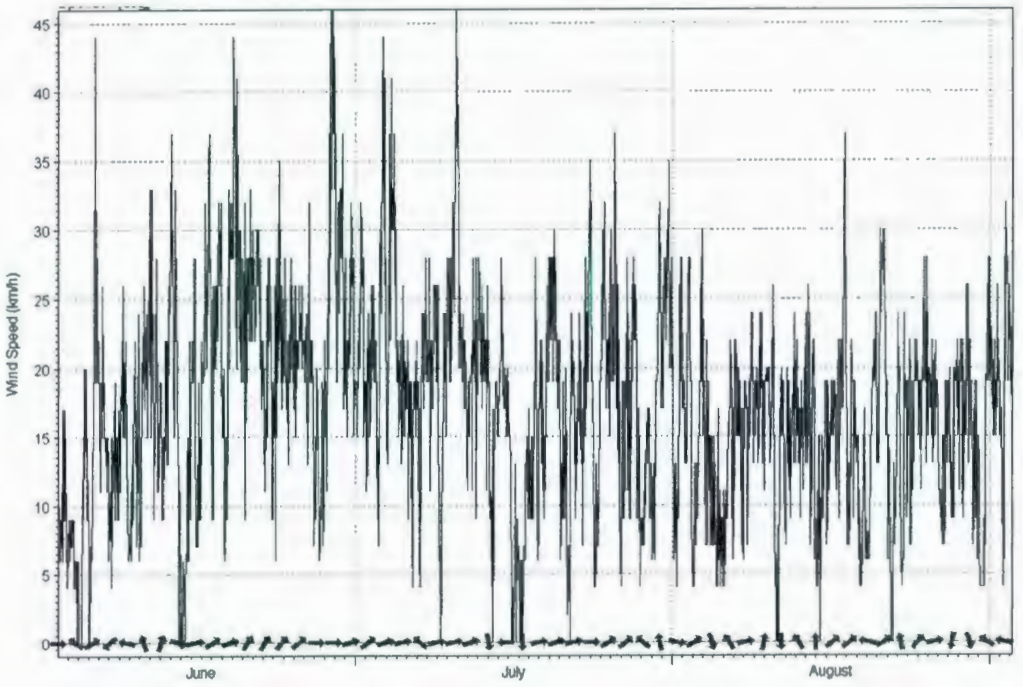

Figure 75. Wind time series plot.

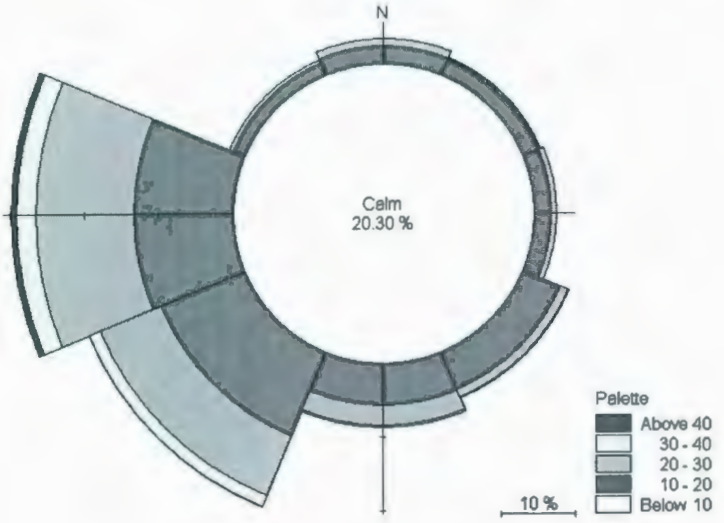

Figure 76. Rose plot of wind.

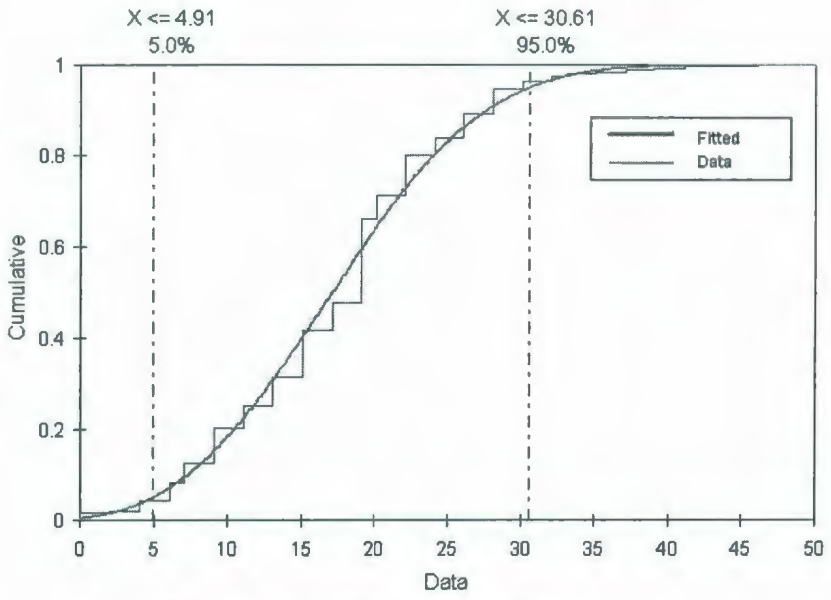

Figure 77. Fitted distribution for the wind speed.

5.2 SIMULATION PROCEDURE

5.2.1 Coordinate System

The PROMISE model is a steady state model. In a probabilistic based approach, the variation of the speeds and directions of ocean currents must be considered. Therefore, a coordinate system must be used to take consideration of this variation. A coordinate system defined by Huang et al. (1996) was used by the PROMISE. The global system is a fixed system with X in the horizontal direction to the right (East) and Y in the vertical direction to the top (North). The origin is set at the discharge point. For each simulation, a translating local coordinate system was used to account for the variation of current speeds and directions. The translating local coordinate system and the global coordinate system is related by (Huang el al., 1996):

$$x = X\cos\theta + Y\sin\theta - x_b - x_D \tag{201}$$

$$y = Y\cos\theta - X\sin\theta \tag{202}$$

where the x_b is the distance from discharge to the surface boil point (or endpoint of PROMISE1 simulation), x_D is the distance from the boil point to the downstream end of control volume, and θ is the angle between the discharge and the X-axis. The coordinate system is illustrated in Figure 78.

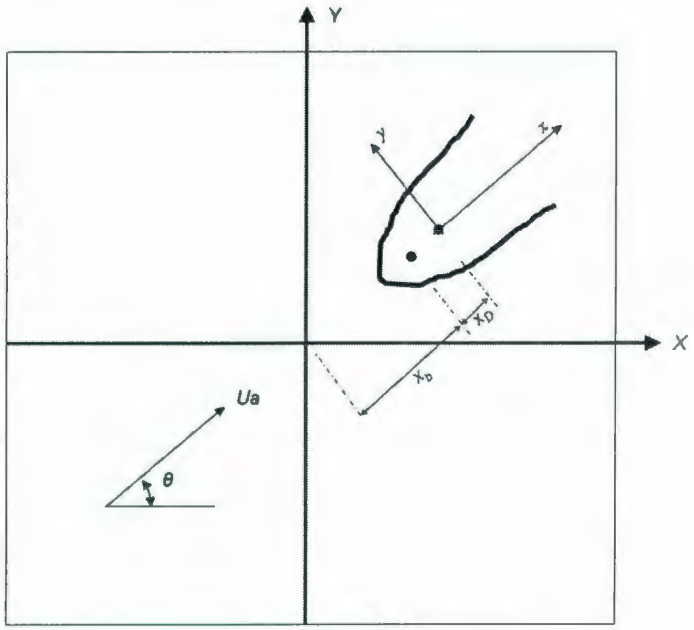

Figure 78. Coordinate system for the PROMISE model.

5.2.2 Flowchart of Simulation

The flowchart of the PROMISE simulation is shown in Figure 79. A random number for flow rate, Q, current speed, U_a, current angle, θ, and effluent density, ρ_a, will be first generated. A set of ambient density, ρ_j, at different depths will then be randomly picked from the measured data. Based on these random inputs and together with other inputs, such as depth of water, and pipe orientation, the PROMISE1 will use a randomly generated entrainment coefficient, α_v, to compute the terminal layer dilution.

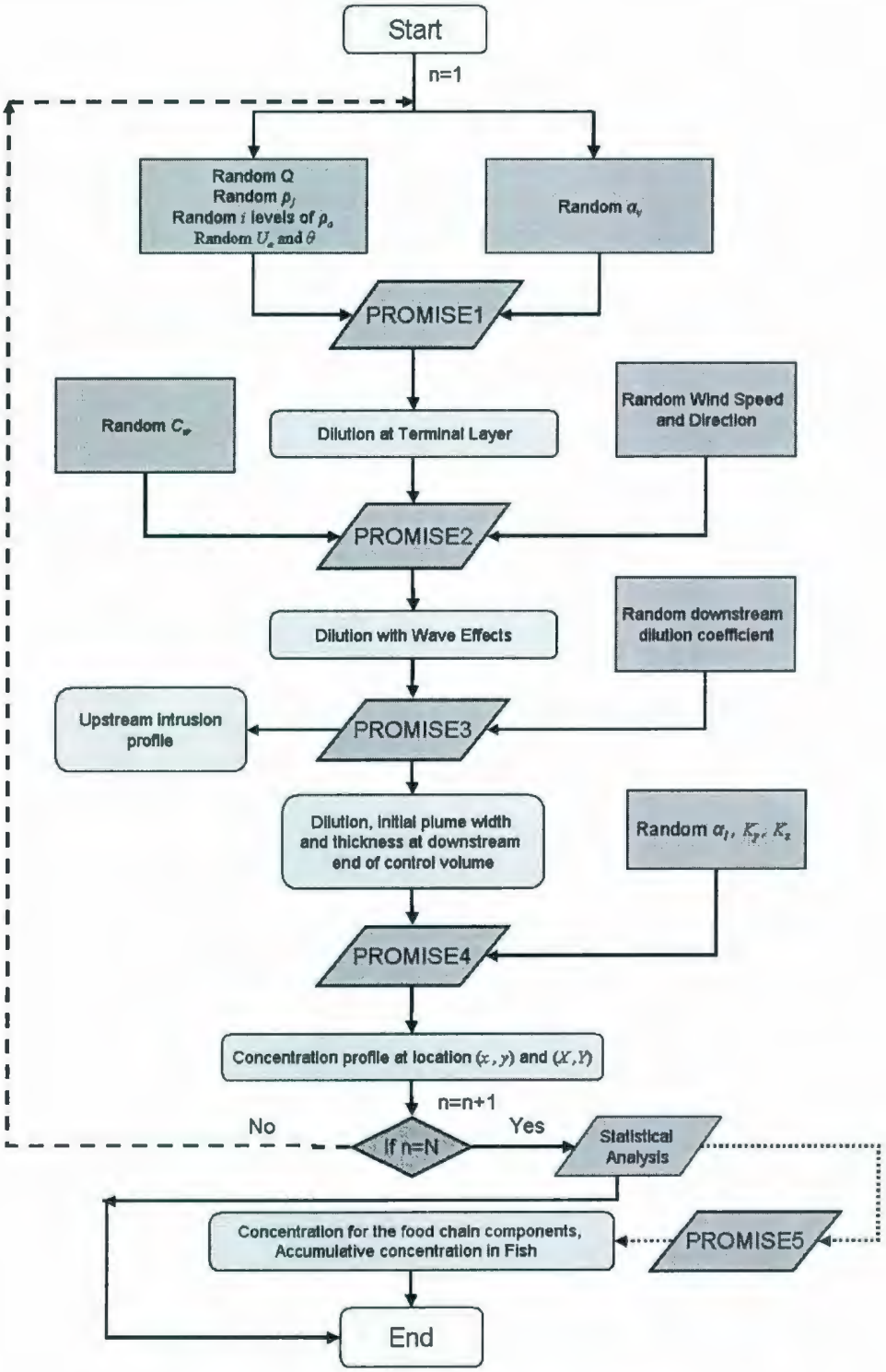

Figure 79. Flowchart of the PROMISE simulation.

A random wind speed is then used to compute the significant wave height and period. Together with the wave effect coefficient C_w, the adjusted dilution with the effects of surface waves is calculated by PROMISE2.

Based on the impingement angle calculated by PROMISE1 and the dilution from PROMISE2, PROMISE3 uses a randomly generated downstream end dilution coefficient to calculate the upstream intrusion profile and the downstream end dilution, plume width, and thickness.

Using the outputs from PROMISE3 and the random numbers of entrainment coefficient α_1, horizontal and vertical dispersion coefficients, K_y and K_z, the concentrations at location (x, y) are calculated by PROMISE4. This process will be repeated N times and the N concentration for each grid point at (x, y) will be analyzed statistically to give probabilistic based concentration profiles, for example, mean concentration, maximum concentration, and minimum concentration.

The output of PROMISE4 is the total concentration of a pollutant. If the exposure time and the partitioning coefficients of the pollutant, for example Naphthalene and C_7 Phenol, are known, the concentration among the food chain components can be calculated by PROMISE5.

5.3 SIMULATION RESULTS

5.3.1 Predicted Environmental Concentration

Based on the inputs from section 5.1, two scenarios were simulated. The first scenarios considered the effects of surface waves on dilution, while the second did not include this effect. The predicted environmental concentrations are shown in Figures 80 to 85.

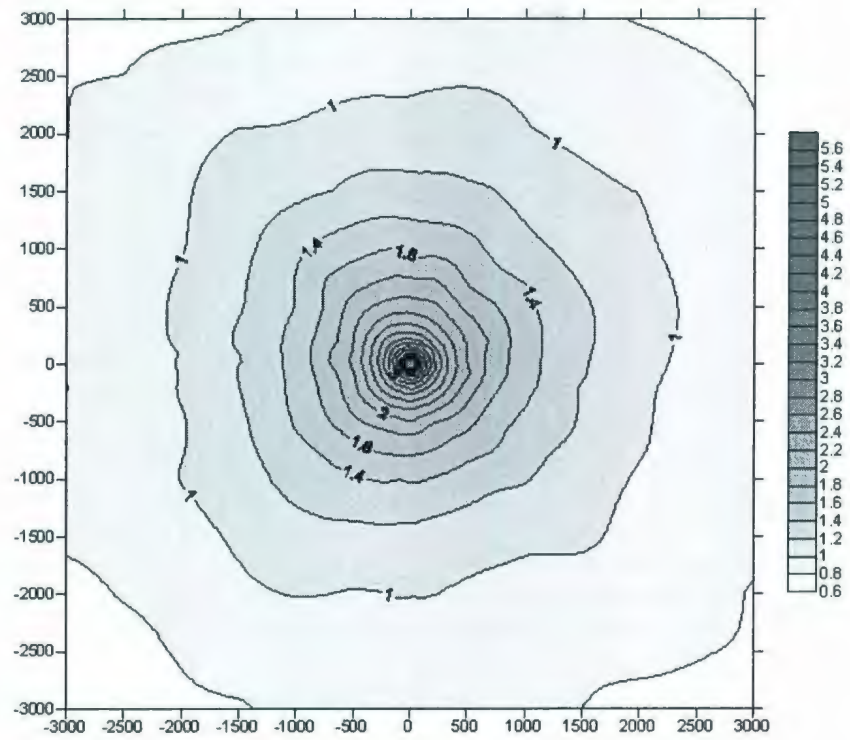

Figure 80. Mean concentration profile for Scenario 1 (with wave).

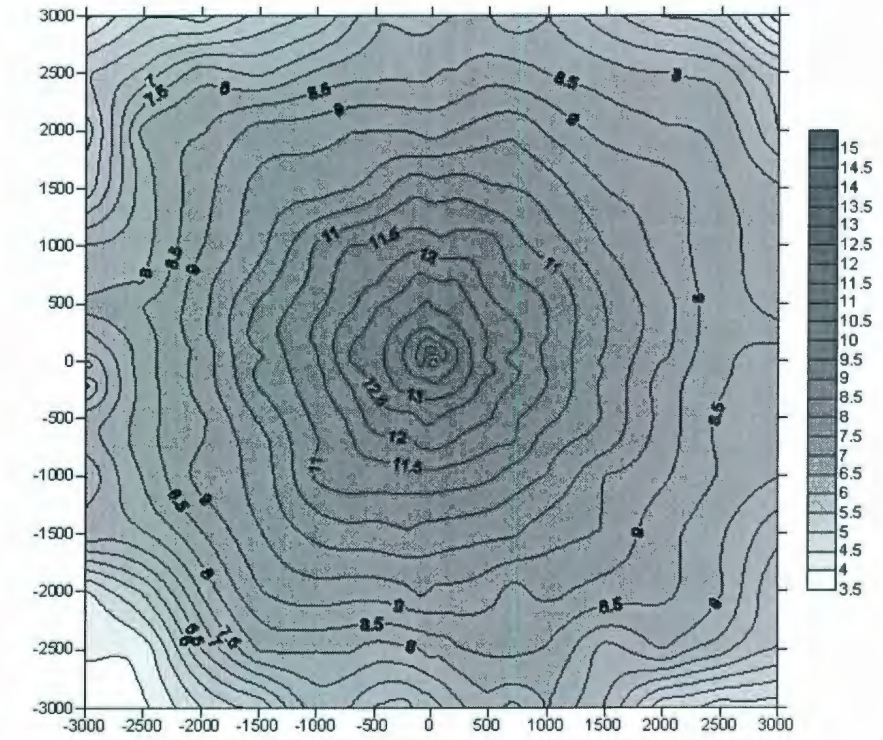

Figure 81. 95%-tile concentration profile for Scenario 1 (with wave).

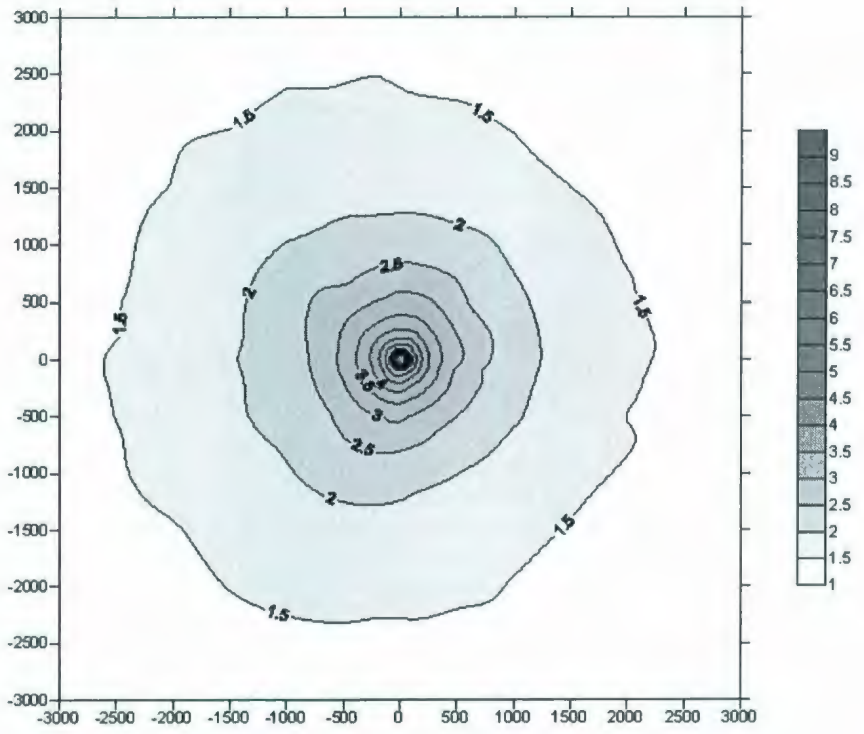

Figure 82. Mean concentration profile for Scenario 2 (without wave).

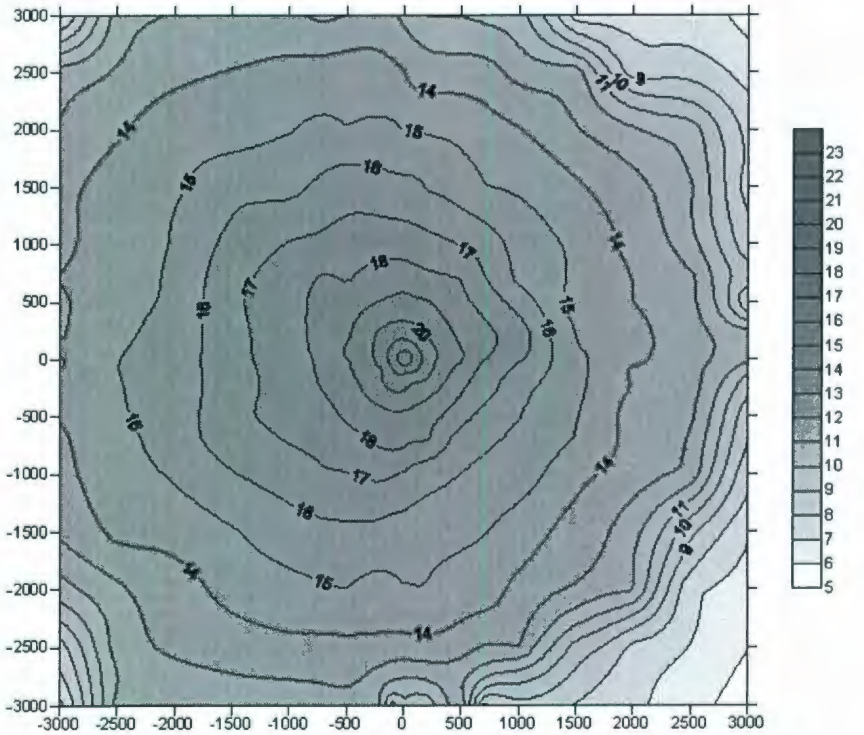

Figure 83. 95%-tile concentration profile for Scenario 2 (without wave).

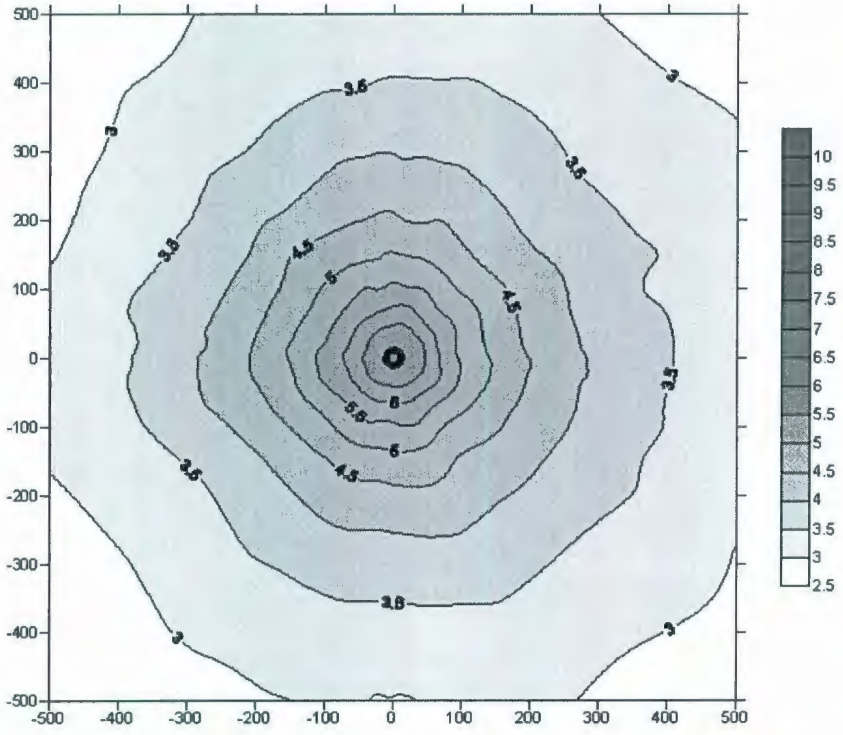

Figure 84. Mean concentration profile for Scenario 1 (with wave, 500 m grid).

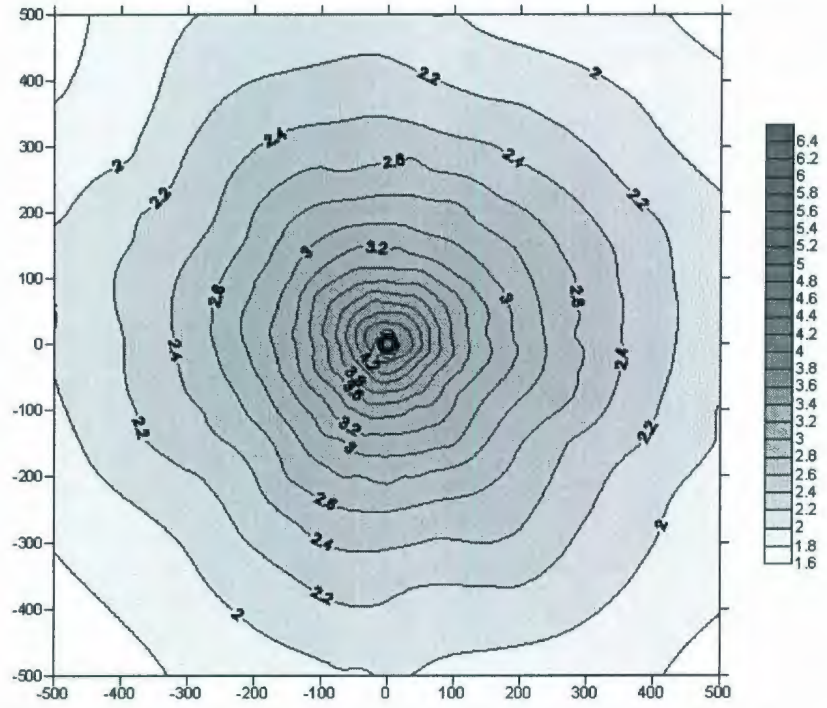

Figure 85. Mean concentration profile for Scenario 2 (without wave, 500 m grid).

The results for scenario 1 are shown in Figures 80 and 81. Figure 80 shows the predicted mean concentration, while Figure 81 shows the 95% -tile concentration for scenario 1. As shown in the figures, the 95%-tile concentration is much higher than the mean concentration. For example, at about 1500 m from the discharge, the predicted mean concentration is about only 1.2% of the initial effluent concentration, but the 95%-tile concentration is about 10.5% that of the initial concentration.

The results for the scenario 2 are presented in Figures 82 and 83. Unlike the scenario 1, the effect of surface waves was not considered in this simulation. At about 1500 m from the discharge, the predicted mean concentration is about 2% that of the initial effluent concentration (Figure 82). Similar to the scenario 1, the predicted 95%-tile concentration is about 16.5% that of the initial effluent concentration and it is much higher than the mean concentration.

By comparing Figure 80 and 82, it can be seen the wave can significantly affect the area of spreading. For example, with the effects of waves, 2% concentration is reached at about 500 m downstream. However, the same concentration can only be achieved at about 1300 m downstream without surface waves. If the regulation concentration is set as 2% of the initial concentration, the zones of impact are 196,000 m^2 for scenario 1 (with waves) and 1,767,000 m^2 (without waves). The zone of impact for scenario 2 is 9 times that of the scenario 1.

The same pattern can be found by comparing Figures 81 and 83. For example, the 13% concentration for scenario 1 is reached at 500 m downstream with the consideration of waves, but the distance required to reach the same concentration is about 2500 m for scenario 2 without the consideration of waves.

A 500 m × 500 m cell was also presented for the two scenarios to give more detailed near field information (Figures 84 and 85)

5.3.2 Accumulation of Pollutants in Fish

The above results are the predicted steady state concentration. In this section, the PROMISE5 was used to calculate the pollutant distribution among the food chain component.

It is assumed that the produced water contains 5 mg/L Phenol and the biological uptake, depuration, and predation (gazing) rate were determined as shown in Table 27 (Reed et al., 1996).

Table 27. Biological uptake, depuration, and predation (grazing) parameters (source: Reed et al., 1996).

	k_z (day^{-1})	$k_{z\text{-}dep}$ (day^{-1})	$k_{gr\,z\text{-}p}$ (day^{-1})	k_k (day^{-1})	$k_{k\text{-}dep}$ (day^{-1})	$K_{gr\,k\text{-}z}$ (day^{-1})	K_f (day^{-1})	$K_{f\text{-}dep}$ (day^{-1})	$K_{gr\,f\text{-}k}$ (day^{-1})
Phenol	7200	12	1.0	7200	12	0.5	720	1.2	0.1

A 1000 m ×1000 m area was studied and this area was divided into 50 m × 50 m cells (Figure 86). Concentration at the center of each cell was calculated and this concentration represents the mean concentration of the given cell.

Due to the lighter density of the produced water than seawater, the produced water will spread as a thin surface layer within the study area, rather than fully mixed vertically. Only those fish that stay in the surface layer will be exposed to the Phenol. In this simulation it is assumed that the fish may freely swim between the two layers, as shown in Figure 87. However, swimming among cells was not permitted. Therefore, the mean concentration that a fish is exposed to is the depth averaged concentration for that cell in which the fish lives.

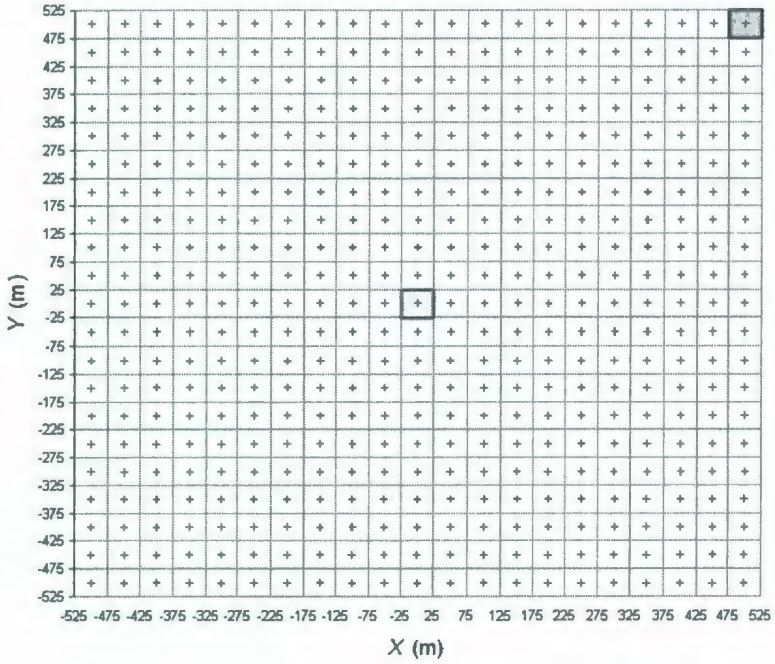

Figure 86. Computation grid for the PROMISE5 simulation.

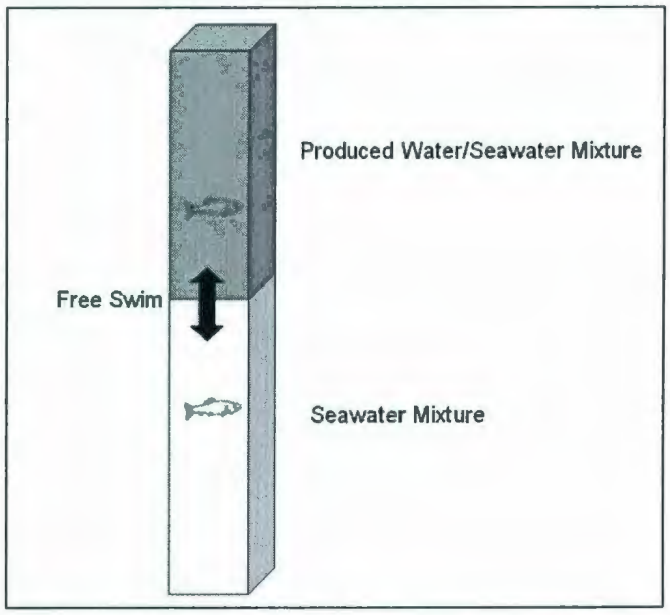

Figure 87. Schematics of the PROMISE5 computation cell.

The results of the PROMISE5 calculations are shown in Figures 88 and 89. Figure 88 shows the Phenol concentration in fish after 24 hours exposure and Figure 89 shows the concentration after 120 hours exposure.

With the increasing exposure time, the accumulated Phenol concentration in fish increases. For example, after 1 day exposure the concentration for fish living around 400 m downstream was 0.05 mg/L, but it increased to 0.07 mg/L after 5 days exposure. If the regulation concentration is 0.07 mg/L, the zone of influence after 1 day exposure was only about 31,416 m^2 (200 m in diameter) but this area increased to 125,000 m^2 (400 m in diameter) after 5 days.

The time dependent concentrations for fish in two cells are presented in Figure 90. The first cell is located in the center of the study area with a center point coordinate of (0, 0) and the second cell is at the edge of the study area with a center point coordinate of (500, 500).

For fish in both cells, the Phenol concentration continues to increase until a maximum value was reached at about 3.5 days and the concentration then keeped constant. If the discharge stopped at a certain time, for example at day 10, the concentration then started to decrease until a very low level was reached.

It should be mentioned that the above calculations were based on a simple food chain model and did not take consideration of the toxic effects of pollutants on fish. For example, the fish may die at a certain concentration level and the concentration will not keep increasing.

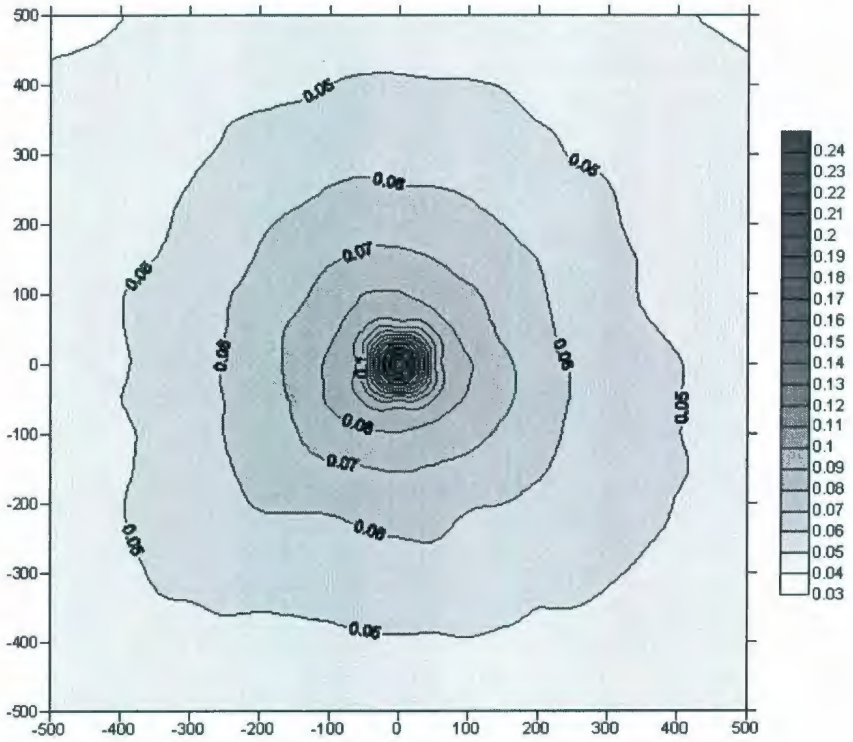

Figure 88. Concentration of Phenol in fish after 24 hours exposure.

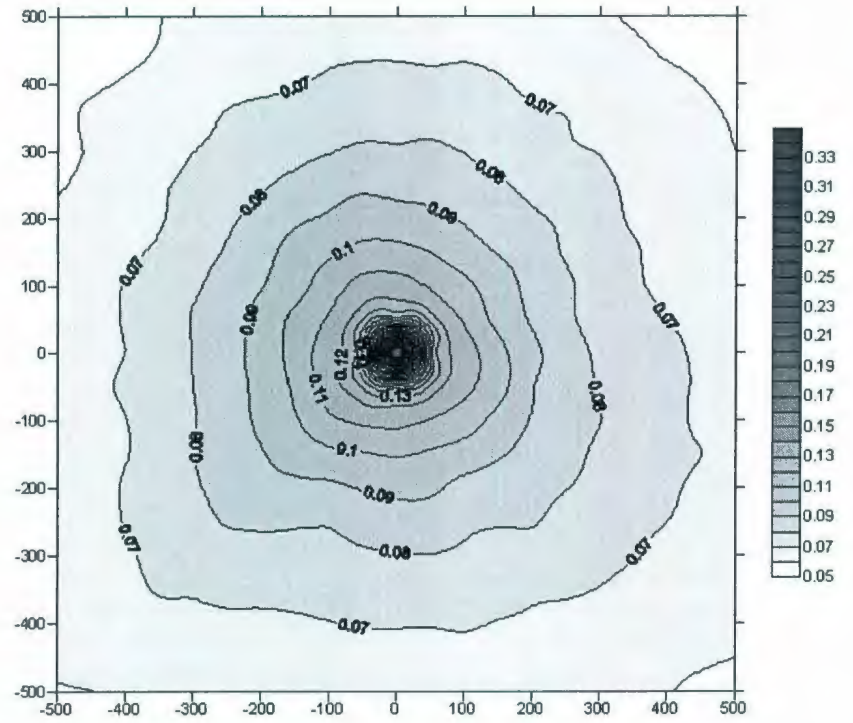

Figure 89. Concentration of Phenol in fish after 120 hours exposure.

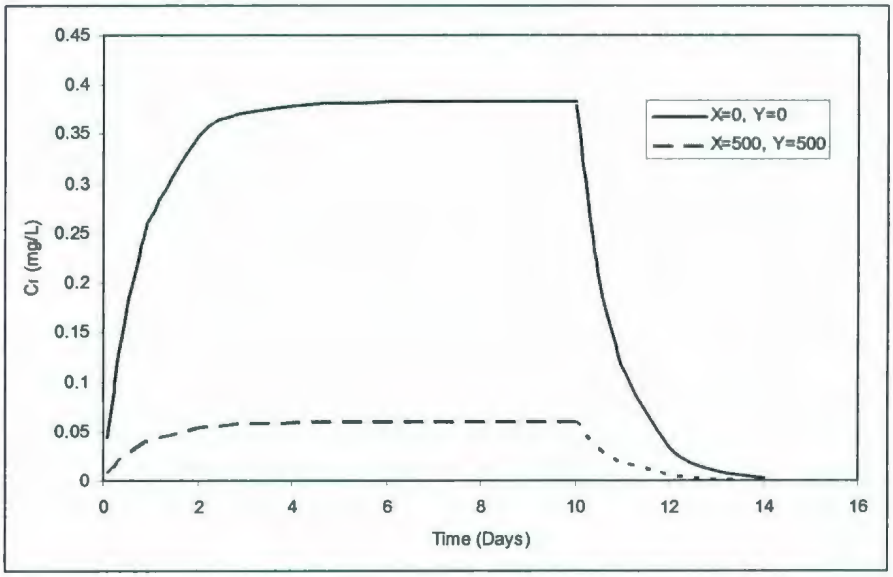

Figure 90. Time history of body burdens in fish.

5.4 SUMMARY

A hypothetical study was conducted in this Chapter to test the PROMISE model. The data collected for this study site was first analyzed and statistical information was obtained. Based on these inputs, PROMISE has been run for two scenarios: with and without the consideration of surface waves. The results have shown that the waves have significant impacts on the dilution. PROMISE5 was then used to simulate the accumulation of Phenol in fish. It was shown that the concentration continues to increase until a steady state concentration is reached. The concentration will decrease if the discharge of produced water is discontinued.

6. COUPLING PROMISE WITH NON-STEADY STATE MODELS

6.1 THE CONCEPT OF COUPLING

The physical processes and the length and time scales for discharge in a coastal environment have been illustrated in Figure 2 in Chapter 1. In the immediate vicinity of the discharge, the mixing behaviors are mainly dominated by the source momentum flux, buoyancy flux, outfall geometry, ambient velocity and stratification. These near field processes can be modeled satisfactorily by many near field models, such as CORMIX, VISJET, Visual PLUMES, and PROMISE.

The influence of the source characteristics decreases as the plume progresses away from the discharge point. In the far field region, the plume is passively transported and further diluted by ambient currents. Although some models, like CORMIX and PROMISE, include a far field module for these processes, their predictions in this region are more intended for the design goal of minimizing the possible environmental impacts, rather than as an operational or monitoring tool. This is because of the large time and length scales of far field motion are rarely steady and the changes of current speed and direction become important. To model these motions, the non-steady state models, such as DELFT3D, ECOMsi, EFDC, and MIKE21/3 should be used. While the far field models focus on the three dimensional motions of the natural water body rather than focus on the jet, plume, or waste field driven motions, they are unable to resolve the detailed near field motions, especially those depth averaged models which are sufficient for large scale flows, but not for discharge assessment.

To correctly simulate the near field and far field motions, these two types of models need to be coupled together. As stated by Bleninger and Jirka (2006), coupling models means introducing flow quantities, such as momentum or mass, from one model into the other. The flow quantities may be introduced by specifying the model boundary conditions and thus have direct effects on the whole flow, or by modifying the existing flow by adding source terms.

6.1.1 Available Coupling Approaches

Hillebrand (2003) has suggested a number of coupling approaches and these approaches can be classified as segmented coupling (or nested coupling) and overlapping coupling (or superposition coupling).

In the segmented coupling approach, the near field and far field models cover different spatial areas. They are linked by open boundary conditions (Figure 91). Because the near field models do not provide information outside the plume outlines, the boundary condition for the far field model must be constructed by the modeler. This construction process could be extremely complicated and difficult to implement, especially in a time-dependent tidal environment.

In an overlapping approach, the near field model and far field model run independently. The far field model covers the entire modeling domain. The near field flow quantities are introduced to the far field by using one or a number of grid cells (Figure 92). The results from far field predictions are then overlapped with the near field predictions by a compromise approach in which the near field model is corrected by the re-entrainment predicted by the far field model (Hillebrand, 2003).

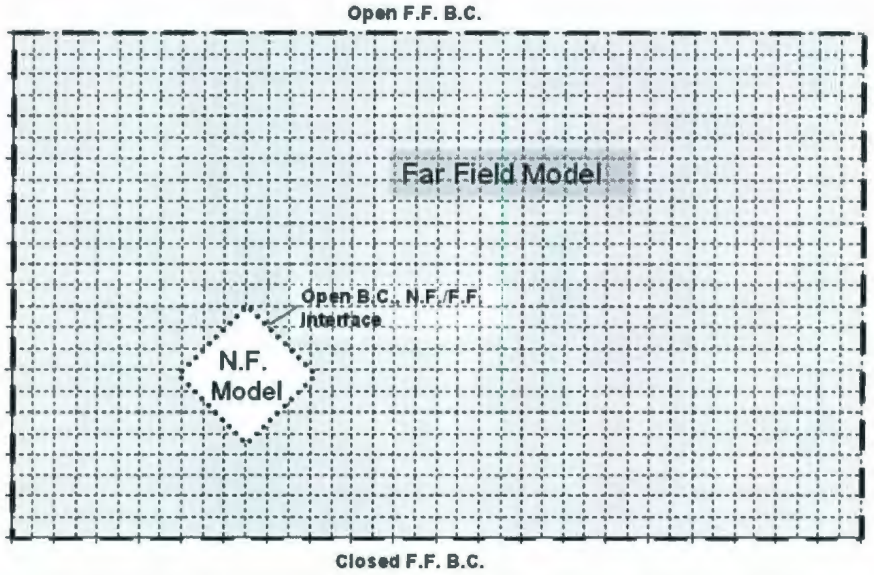

Figure 91. Schematization of segmented coupling approach (modified from Bleninger et al., 2006).

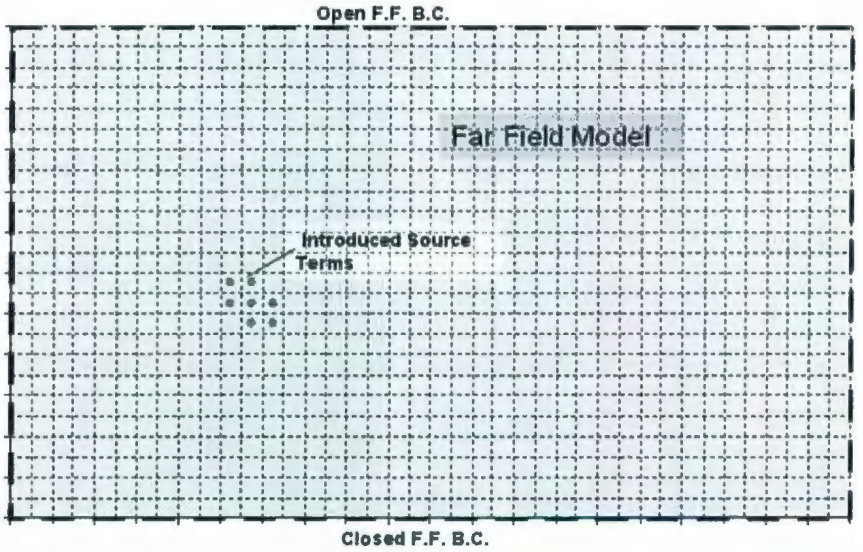

Figure 92. Schematization of overlapping coupling approach (modified from Bleninger et al., 2006).

6.1.2 Previous Coupling Studies

Zhang and Adams (1999) employed the near field model RSB (one module of the Visual Plumes model) and a 3D circulation model ECOM-si. Four methods were considered to interface the near and far field models: 1) introducing both the source

flow and pollutant load at the discharge point; 2) introducing the source flow at the discharge point and the pollutant load at the predicted trap level; 3) introducing the diluted flow and pollutant load at the predicted trap level; 4) only introducing the pollutant load at the predicted trap level. Due to the limitation of the RSB model, which cannot provide information on plume trajectories or centerline flux development, there is not much interaction between the near and far field models.

Roberts (1999) coupled the NRFIELD model with a particle tracking model. There was no circulation used and the flow field for the particle tracking routine was from the ADCP measurements. This coupling is also a one way coupling and no re-entrainment for the near field model was considered.

Li and Hodgins (2004) also coupled the RSB model with a far field circulation model. Only the centerline concentration at the plume trap depth was introduced and the dynamic effects of effluent buoyancy were neglected. The limitation of this coupling is its one way nature and re-entrainment of the far field into the near field was not considered.

While the coupling studies described above were focused on multi-port discharges, Kim et al. (2002) coupled an integral jet model with a particle tracking model to simulate the mixing of a single buoyant jet discharge. Like other coupling studies, the two models were not dynamically linked.

More recently, Choi and Lee (2005) coupled the JETLAG (VISJET) model with the EFDC model. This study is the most comprehensive coupling study to date as it is a two-way coupling. A filling box approach was used to introduce the diluted plume at the terminal level and draw the ambient back into the plume. However, the intermediate field motions (buoyant spreading) were not included.

The latest coupling study reported in the literature is from Bleninger et al. (2006). In their study, two commercial models, CORMIX and Delft 3D, were coupled together. This study considered the intermediate mixing motion by using the CORMIX prediction. However, since separate models were used, there was no dynamic interaction between the two models.

The above coupling studies are summarized in Table 28.

Table 28. Previous coupling studies.

	Near Field Model	Far Field		Near/Far Interaction	Intermediate Field
		F.F. Model	Solution		
Zhang & Adams (1999)	RSB (VP)	ECOM-si	Finite Difference, and Particle Tracking	One Way	Not Included
Roberts (1999)	NRFIELD (VP)	Not Named	Particle Tracking	One Way	Not Included
Kim et al. (2002)	Not Named	Not Named	Particle Tracking	One Way	Not Included
Choi and Lee (2005)	VISJET	EFDC	Finite Difference	Two Way	Not Included
Li and Hodgins (2004)	RSB (VP)	Not Named	Finite Difference	One Way	Not Included
Bleninger (2006)	CORMIX	Delft3D	Finite Difference	One Way	Included

*VP: Visual Plumes

6.2 COUPLING PROMISE WITH MIKE3

6.2.1 Models Used in Coupling Study

In this study, the near field model for coupling is the PROMISE model and this model has been described in Chapter 3.

There are a number of far field models available that may be coupled with PROMISE. To date, more than 30 circulation models have been developed (TAMU, 2007). Among those models, the most cited models are POM (Princeton Ocean Model - Princeton University), ECOM-si (modified version of POM - Hydroqual), Delft 3D (Delft Hydraulics), Telemac 3D (Electricité de France and Wallingford), MIKE 3 (Danish Hydraulics Institute), EFDC (Environmental Fluid Dynamics Code - TetraTech).

In this study, the DHI MIKE 3 was adopted as the far field model to couple with the PROMISE. The main reason for the selection of MIKE 3 is that this model has not been used in this type of study before. Another reason is that the MIKE3 is easier to use than other models, especially those non-commercial models. The setups of non-commercial models are generally extremely complicated and time-consuming.

MIKE3 is a professional engineering software package developed by the Danish Hydraulics Institute (DHI). MIKE3 is a general non-hydrostatic numerical modeling system for a wide range of applications in areas such as oceans, coastal regions, estuaries and lakes. MIKE3 includes several modules. The hydrodynamic module HD is the basic flow module. It simulates unsteady three-dimensional flows, taking into account density variations, bathymetry, and external forcings such as meteorology, tidal elevations, currents and other hydrographic conditions. The advection/diffusion module can be applied to a wide range of hydraulic and related phenomena. The advantage of Mike3 is its ability to use flexible mesh which is more efficient and flexible.

The first step of a MIKE 3 simulation is the setting up of a modeling domain. The horizontal grid of MIKE 3 is unstructured while the vertical coordinate is structured sigma-coordinate mesh. The simulation period is then specified with a proper time interval controlled by a Courant number. To avoid stability problem, the maximum Courant number must be less than 0.5.

The pollutant can be introduced into MIKE 3 as source or sink term at given locations and depths.

6.2.2 Description of the Method

6.2.2.1 General Considerations

The coupling method used in this study is a passive offline coupling. As defined by Bleninger et al. (2006), a passive coupling assumes that the source-induced flow does not change the flow characteristics of the far field and this is the case for most environmental discharges, such as produced water or sewage outfalls. In a passive coupling approach, only passive flow quantities need to be linked at the location and time that source induced motion are negligible. If the discharge is high enough to affect the ambient flow even in the far field, the passive coupling should not be used because the coupling of flow quantities has to be accomplished as well.

The objective of the present study is to couple a steady state model with a non-steady state time dependent model. The temporal aspects must be considered. In other words, the time intervals for introducing source terms need to be determined. If a very short period (Δt = order of minutes) is used, this may result in an unrealistic change of near field source location. However, if the periods are too long, too much information will be lost and the effects of ambient flow on near field mixing can not be correctly represented. Bleninger et al. (2006) has suggested that the period may be estimated by:

$$\Delta t_c = (1 \text{ to } 3)\max(t_M, t_m) \tag{203}$$

where Δt_c is the coupling time-step, t_M is the jet/plume time scale, t_m is the jet/crossflow time scale.. The Equation (203) gives a time-step of approximately one hour for typical wastewater discharges.

The locations of coupling are determined by the near field model predictions. If the buoyant spreading is not important, the coupling location can be defined at the end of the near filed. If the buoyant spreading is important, the coupling locations are

defined at the end of intermediate mixing. In the latter case, the near field predicted plume traveling time may need to be compared with the coupling time step to verify the assumption of steady state.

To perform the coupling simulation, a minimum far field grid resolution is required to correctly distribute the scalar quantities. More than one grid cell may be required in some cases. Bleninger et al. (2006) has recommended that the size of a domain can be estimated by

$$Size_{NF} = (1 \text{ to } 3)\min(l_M, l_m, L_D) \quad (204)$$

where $Size_{NF}$ is the minimum grid size, l_M is the slot jet/plume transition length scale, l_m is slot crossflow length scale, L_D is the length of diffuser. For a typical produced water discharge, the L_D is excluded from the Equation (204) as no diffuser is used.

6.2.2.2 Procedures

The coupling algorithm used in this study is illustrated in Figure 93.

First, the boundary and initial conditions must be obtained to run the MIKE3 hydrodynamic module (HD) based on any reasonable (Courant number < 0.5) grid resolution. The outputs of MIKE3, for example the velocity field and ambient density profile, together with discharge characteristics are used by PROMISE to determine the minimum grid size and the time step of coupling.

The grid size of MIKE3 is then refined and the HD module is executed again to generate the velocity and density information. The PROMISE is executed to predict the near field concentration and the size of plume. This information is used to create the initial source term for the MIKE 3 Advection-Diffusion module (AD).

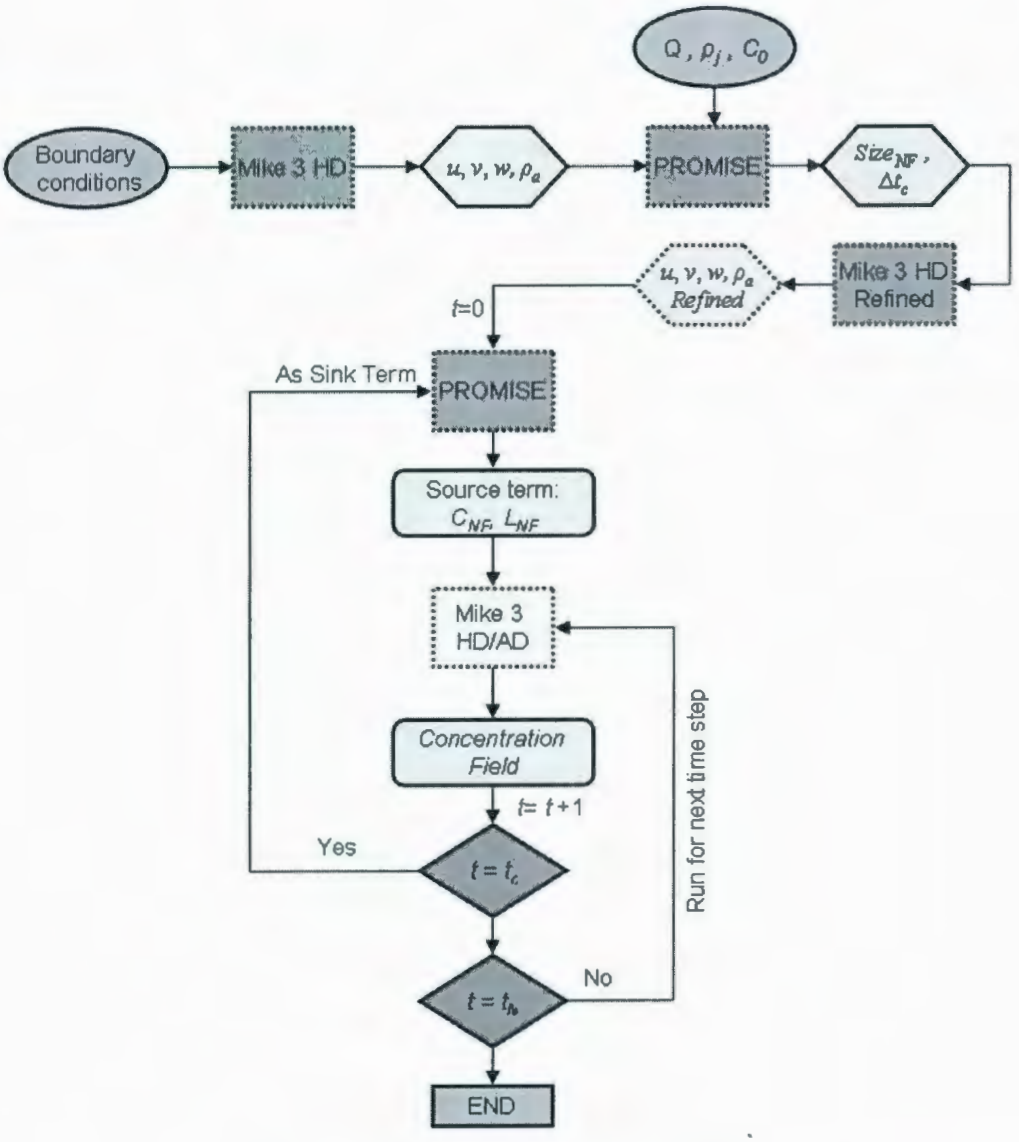

Figure 93. Schematic of the coupling algorithm.

After the concentration field for this time-step is calculated, the MIKE3 model moves forward to the next time step. If the t is less than the t_c, the model will continue running until t_c is reached. At this point, the predicted field will be used by PROMISE as the accumulated background concentration to consider the re-entrainment of far field returned pollutants. To maintain a mass balance, a sink term in the MIKE 3 will

be created to remove the same amount of pollutant re-entrained by PROMISE. This process is repeated several times until the end of simulation ($t=t_N$).

6.3 CASE STUDY

6.3.1 Description of the Hypothetical Cases

To test the coupling algorithm, a hypothetical case study was performed. The most difficult part in running an ocean circulation model, such as MIKE3, is to acquire the boundary and initial conditions. These data in most cases are either unavailable or inadequate. As the objective of this study is to evaluate the coupling algorithm rather than study the hydrodynamic behavior itself, an existing hydrodynamic study was used as the basis and was modified to include the pollutant transport process.

The hypothetical study is to create an outfall in the Oresund, Denmark. The reason for selecting this location is simply because of the availability of data. All required data for this case have been provided with the MIKE3 software. The bathymetry of the study area is shown in Figure 94. It is assumed that an outfall is located at the point (340000, 6150000) at -12.5 m depth. The flow rate of the discharge is assumed to be 0.35 m^3/s via a 0.345 m pipe oriented vertically upward. Three test cases were studied and are described below.

In test case 1, only the far field model MIKE 3 was used. The purpose of this case is to examine the far field model's ability to simulate buoyancy effects. The pollutant with a density of 988 kg/m^3 was introduced at -10 m depth. This discharge density is much smaller than the ambient density (1013 – 1015 kg/m^3) and the plume is expected to rise toward the surface once discharged. In case 1, a coarse grid as shown in Figure

95 was used. The advantage of this coarse grid is that the simulation time can be significantly reduced because a longer time step can be used to give a Courant number less than 0.5. The Courant number for any grid must not exceed 0.5 to ensure the stability of the model. A 24-hour simulation was performed with a time step of 7.2 seconds (this gives a Courant number of 0.385). The computer used for this simulation has a 1.77 GHz CPU and 2 GB memory and the computation time was 1.1 hours.

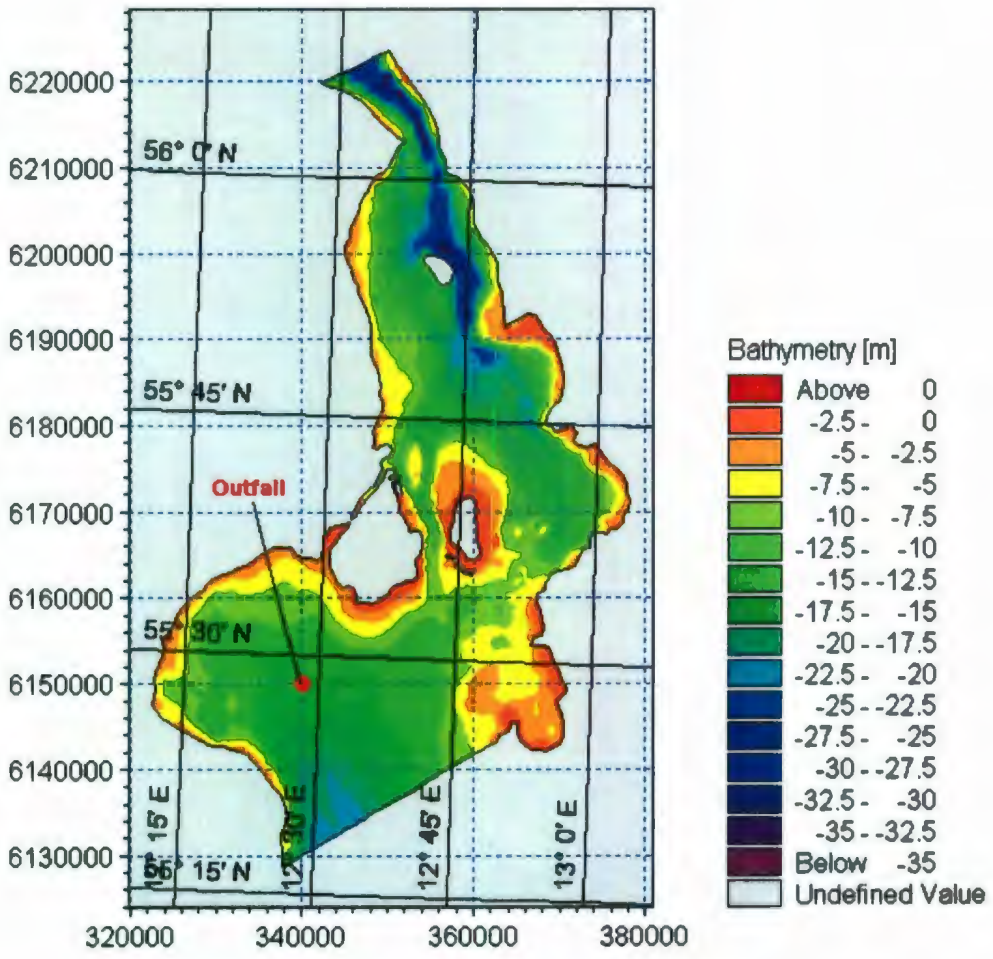

Figure 94. Hypothetical study area with location of outfall.

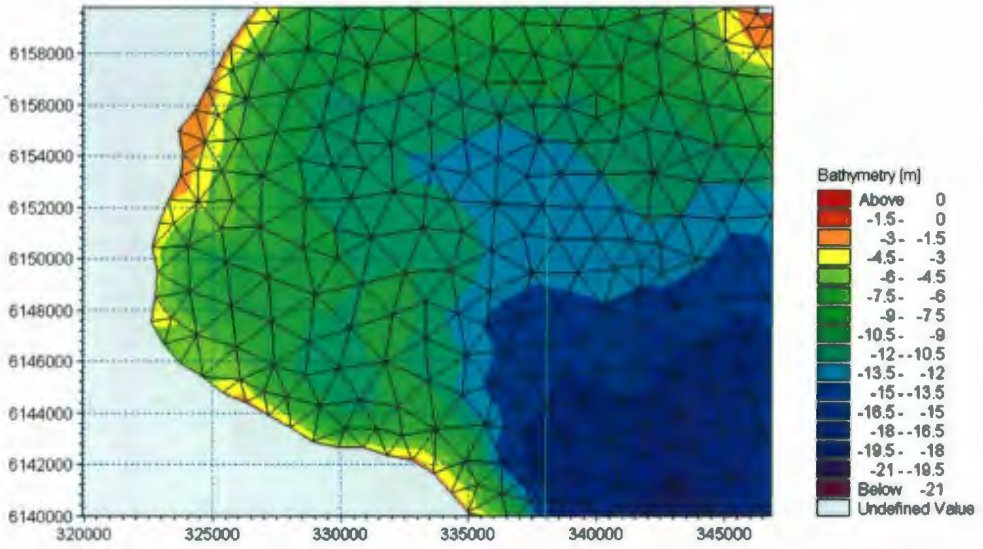

Figure 95. Coarse grid used for the simulation of Case 1 and Case 2.

In test case 2, both PROMISE and the far field model MIKE 3 were used. However, only a simple coupling was used in this case. Before the simulation, the PROMISE was used to calculate the dilution and this concentration was introduced at the terminal level (in this case, the surface). The purpose of this case is to study the effects of coupling under a coarse grid. This case also served as a base case to compare with case 3 to study the effects of grid resolution. The computation time for this case is the same as case 1 because of the same grid resolution.

The purpose of test 3 is to fully evaluate the coupling algorithm described in Figure 93. Different from case 2, the PROMISE was used after each coupling step to calculate the location and concentration for the source term. Further, to correctly introduce the near field term, the computation grid was refined based on the criteria for minimum grid resolution. The grid size at the discharge is only 0.017% that of the coarse grid (as shown in Figure 96). The time step of 0.3 s was used in this case and this gives a Courant number of 0.433 to ensure the stability. Due to the reduced time step, there was a significant increase in computation time. For the same 24 hours

simulation time, the computation time was 33 hours using the same computer excluding the time used in human interaction between each coupling time step (Δt_c = 1 hour). This time is 30 times that of cases 1 and 2.

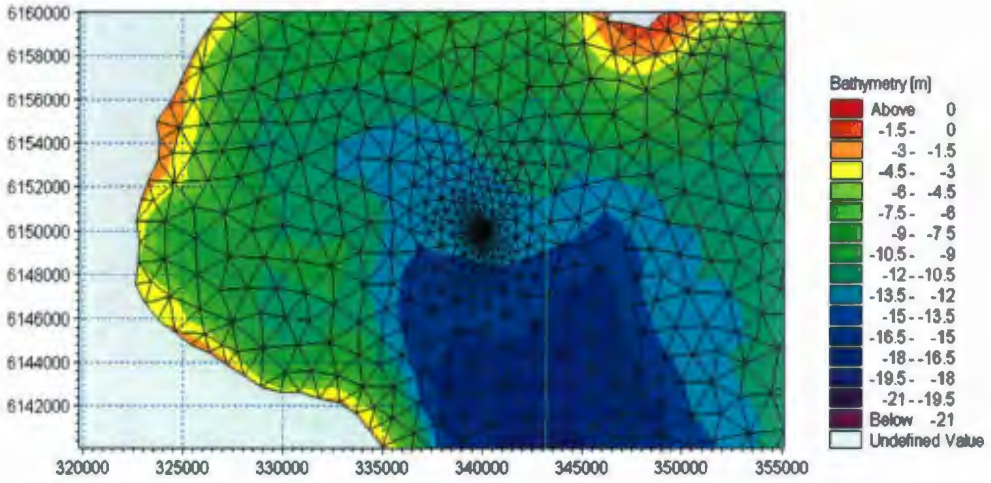

Figure 96. Fine grid used for the simulation of Case 3.

6.3.2 Results and Discussion

The current fields were computed by MIKE3 and outputs were generated after every 1000 time steps. A total number of 120 outputs were generated for the 24 hour simulation period. An example of the current fields is shown in Figures 97 and 98. This current field was used by PROMISE to calculate the near field dilution and coupling locations. It can be seen from the Figures 97 and 98 that the surface current is about 0.27 m/s oriented south and the bottom current is about 0.05 m/s oriented southwest.

The horizontal counter plots for the Case 1 at 3, 6, 12 and 24 hours after discharge are given in Figures 99 to 102. The plume center to edge distance has

increased from about 2400 m (Figure 100) at t= 3 hours to about 8500 m (Figure 102) at t=24 hours. It is shown in Figures 99 to 102 that the plume center concentration is only 0.24 to 0.3, which are much smaller than the expected values. The near field model PROMISE has predicted an initial dilution of about 70. The reason for the low concentration is the coarse grid sizes, which causes the source to be dispersed rapidly over the entire grid and result in a unreasonably high dilution.

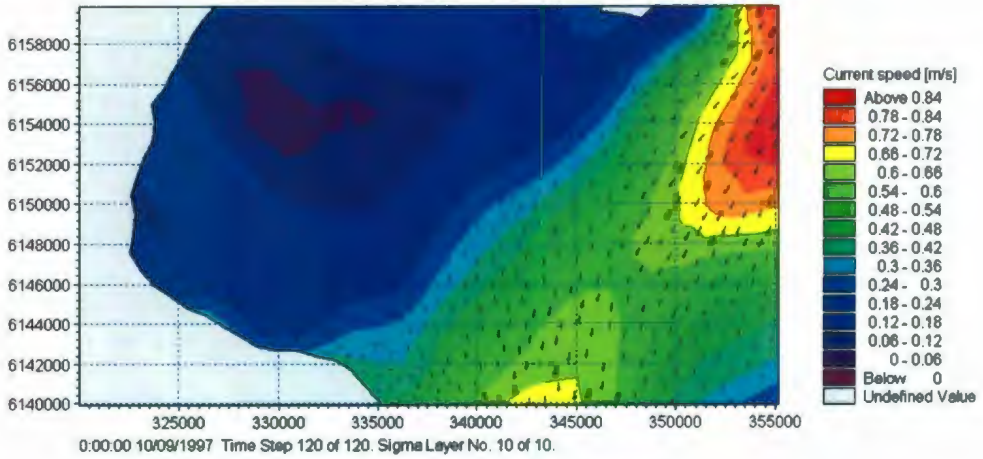

Figure 97. Surface currents, t=24 hours.

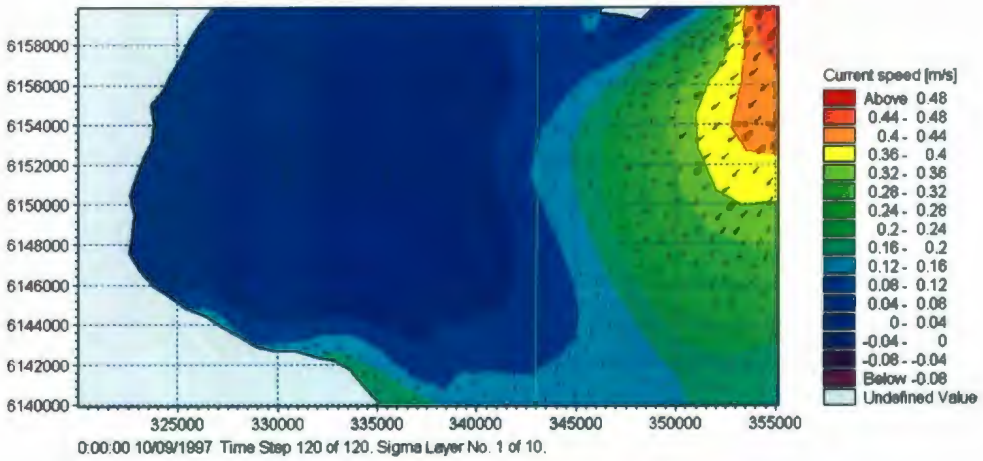

Figure 98. Bottom currents, t=24 hours.

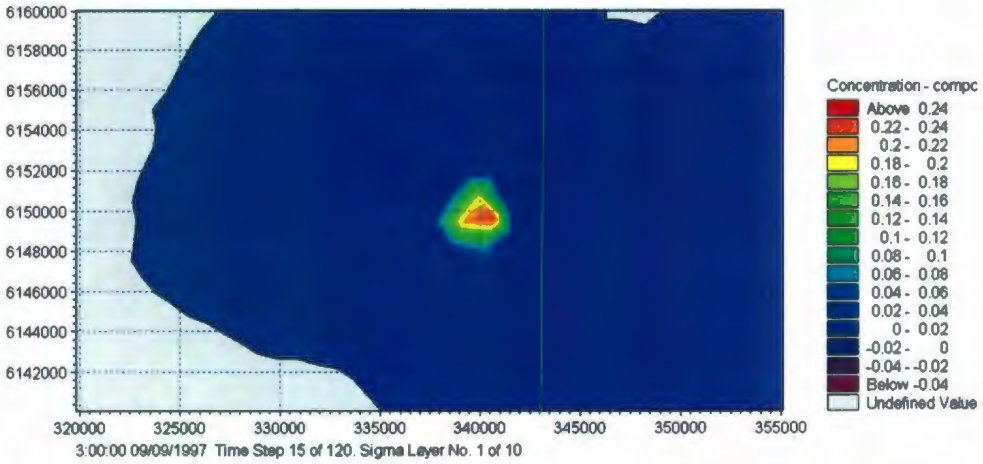

Figure 99. Case 1: Horizontal profile, Time = 3 hours.

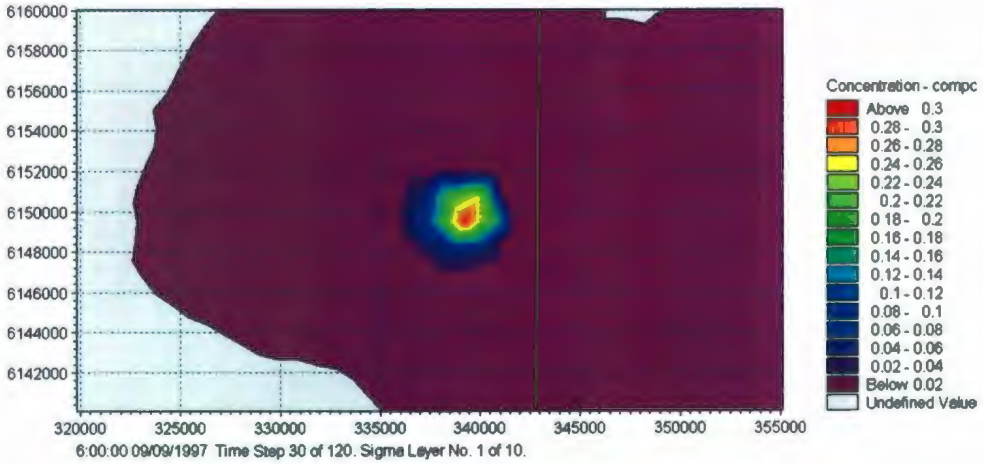

Figure 100. Case 1: Horizontal profile, Time = 6 hours.

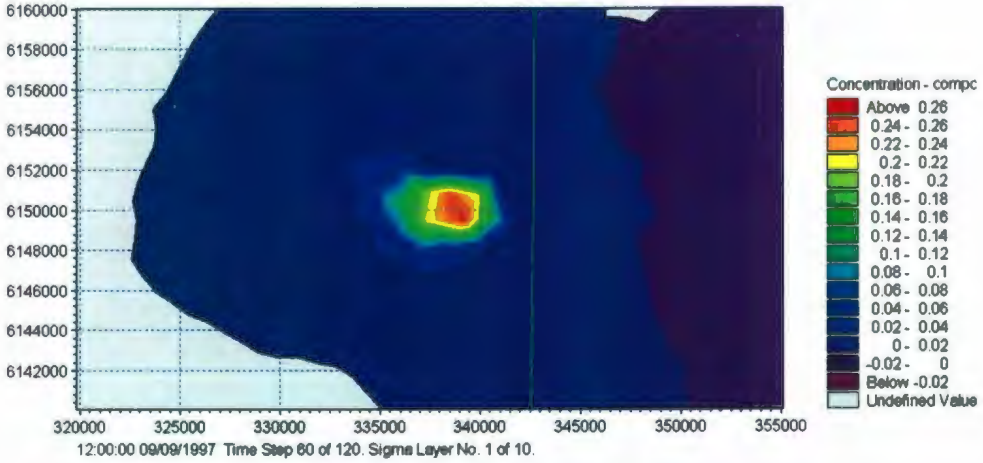

Figure 101. Case 1: Horizontal profile, Time = 12 hours.

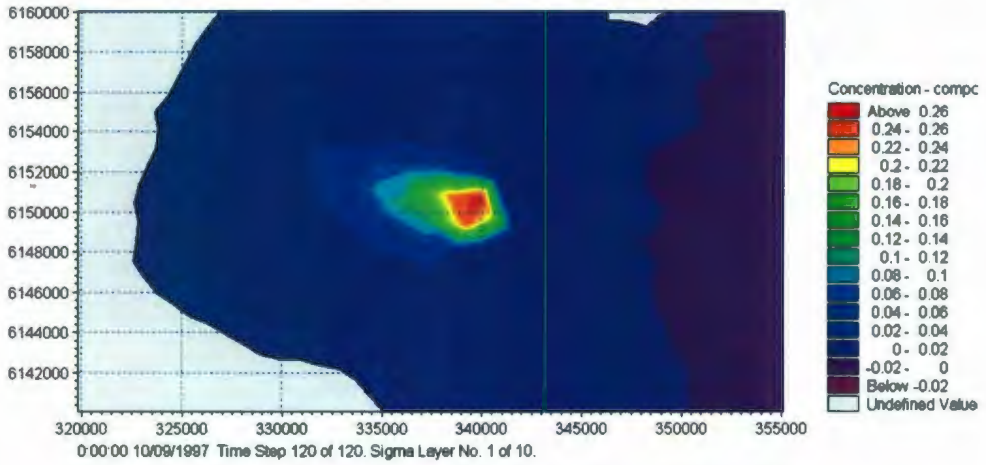

Figure 102. Case 1: Horizontal profile, Time = 24 hours.

To examine the vertical plume profile, a cross-section starting from (326000, 6150000) to (344000, 6150000) was taken and plotted. The location of this cross-section is shown in Figure (103). The vertical profiles for Case 1 at 3, 6, 12, and 24 hours after discharge are presented in Figures (104) to (107). It can be seen that the plume width is about 2400 m at this cross-section at t=3 hours. The maximum height of rise is -9 m. At t=24 hours, the plume width at this cross-section has increased to 6600 m and the maximum rise is about -7 m.

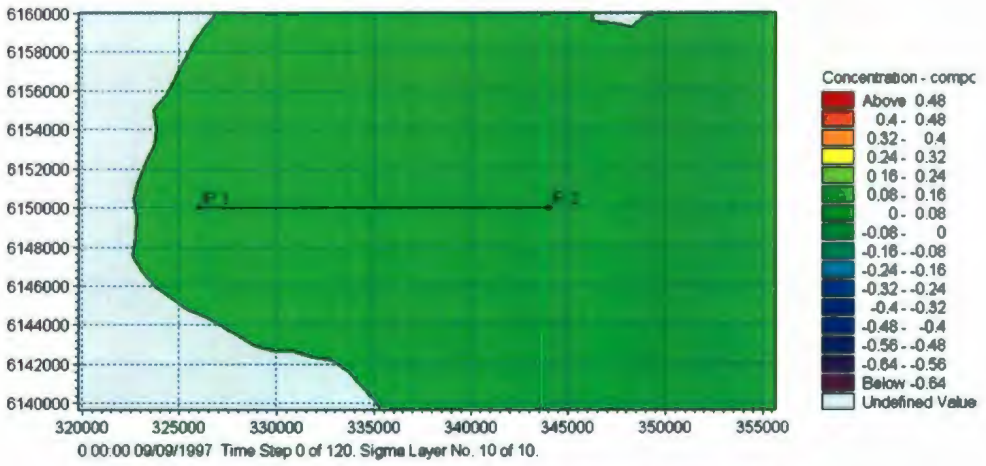

Figure 103. Location of points for vertical profile (Cases 1 and 2).

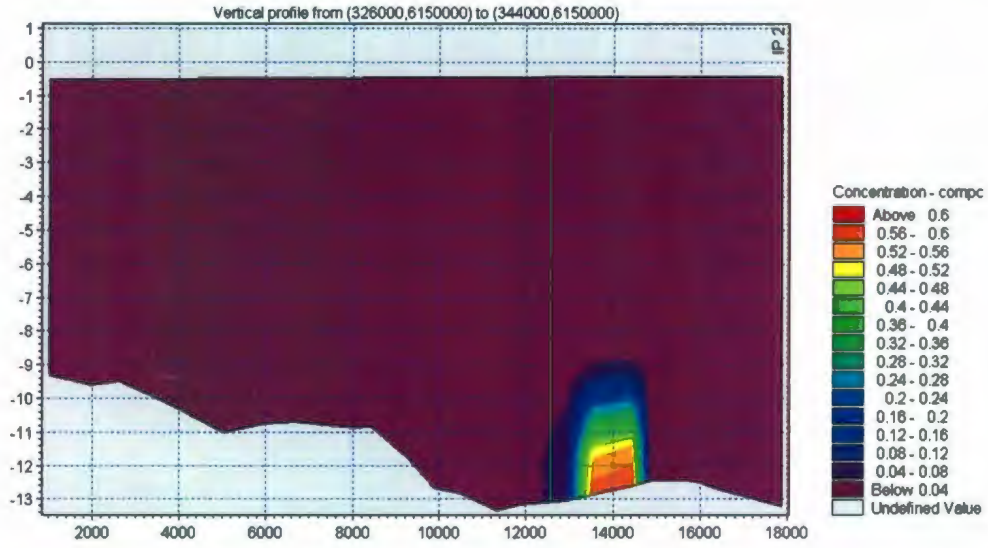

Figure 104. Case 1: Vertical profile, Time = 3 hours.

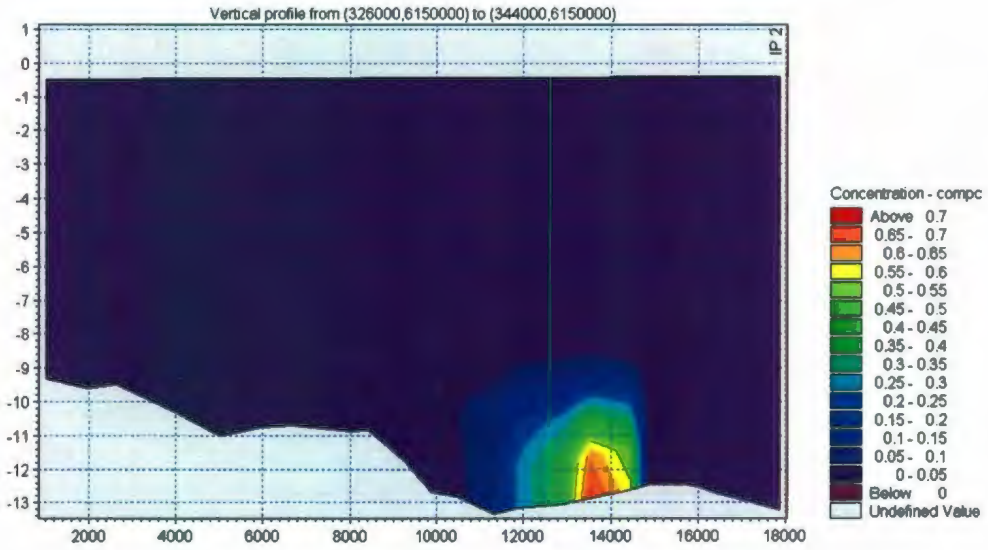

Figure 105. Case 1: Vertical profile, Time = 6 hours.

From the near field prediction, the plume is expected to rise until it impinges the surface. However, the far field model using only a coarse grid failed to reproduce the near field plume dynamic processes, and the plume remains in the bottom layer. To correctly predict the mixing and incorporate the near field dilution, the far field model needs to be coupled with a near field model.

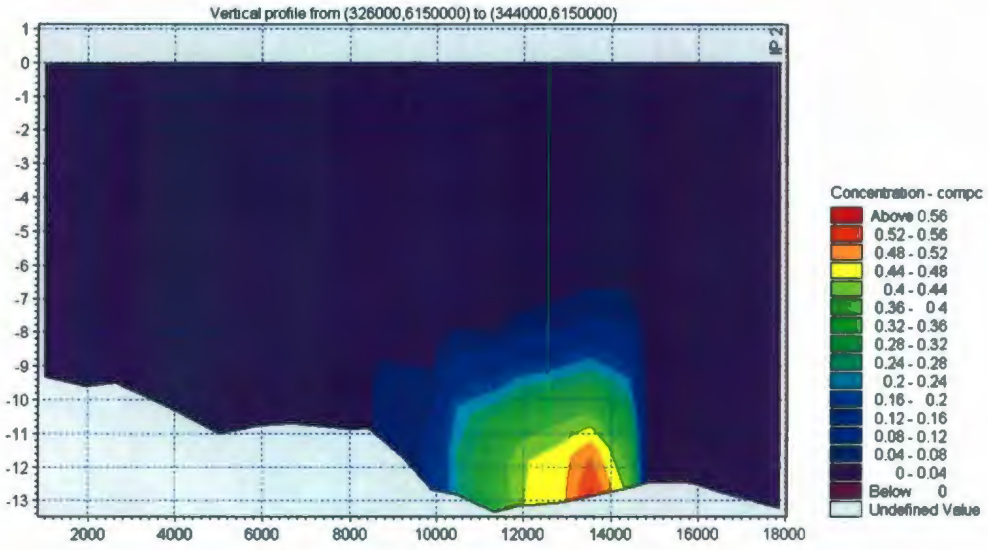

Figure 106. Case 1: Vertical profile, Time = 12 hours.

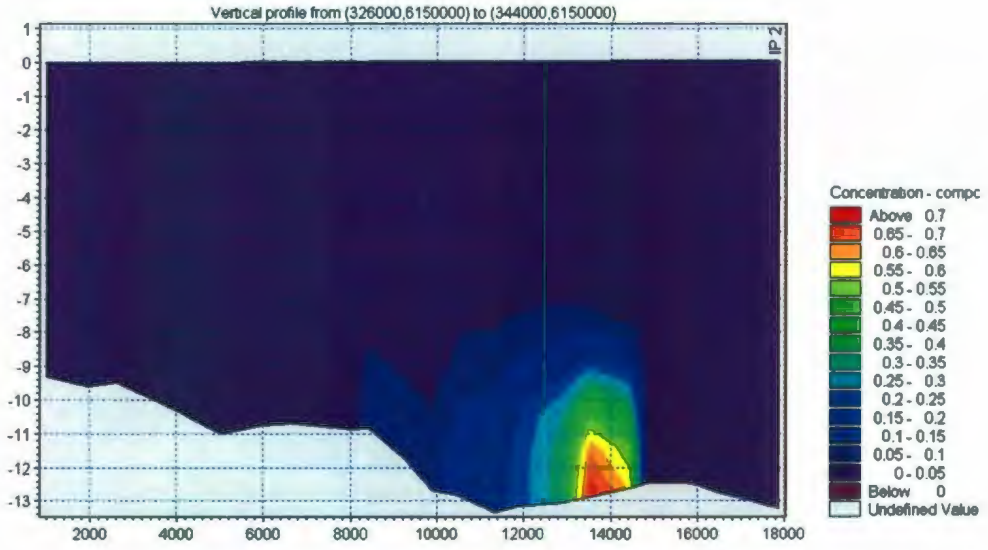

Figure 107. Case 1: Vertical profile, Time = 24 hours.

To account for the near field mixing, the PROMISE was executed and the diluted source was introduced into MIKE 3 at the surface layer in test Case 2. The horizontal profile at t= 3, 6, 12 and 24 hours are shown in Figures 108 to 111. It can be seen that in all 4 time steps the plumes predicted by Case 2 are wider than that by Case 1. Also, the directions of plumes in these two cases are different. The reason for this difference

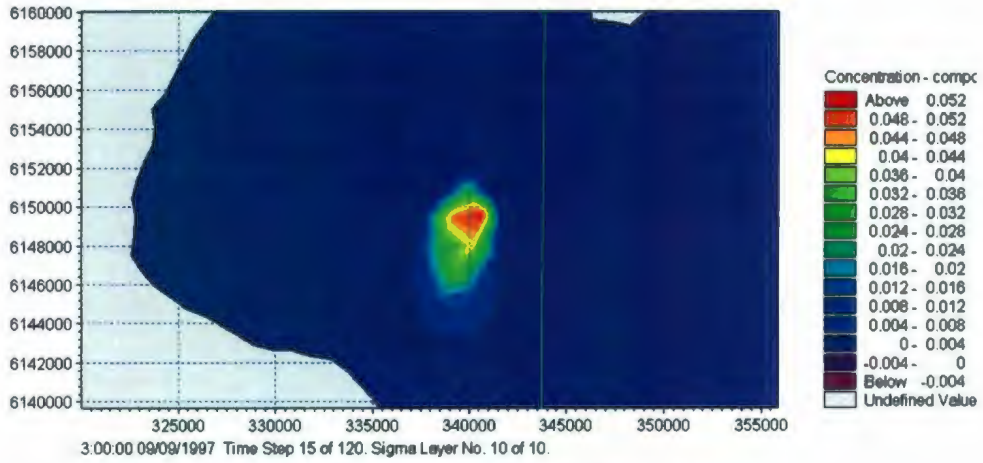

Figure 108. Case 2: Horizontal profile, Time = 3 hours.

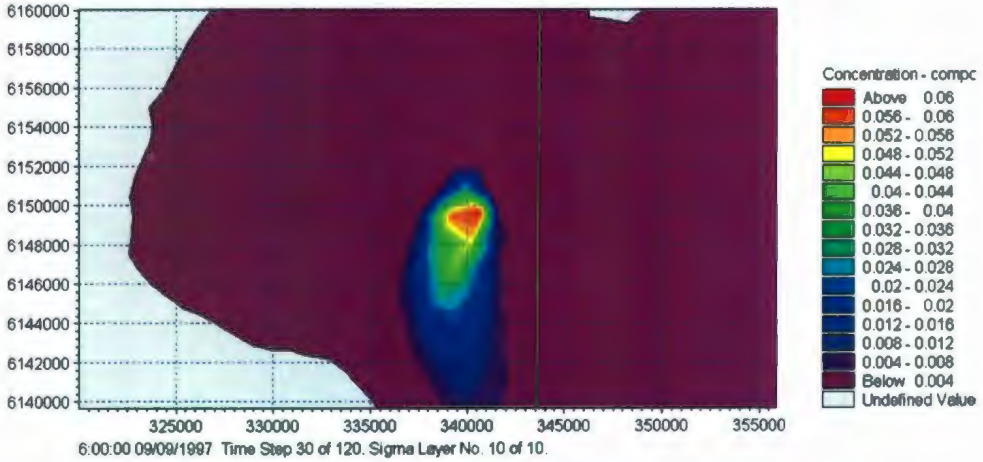

Figure 109. Case 2: Horizontal profile, Time = 6 hours.

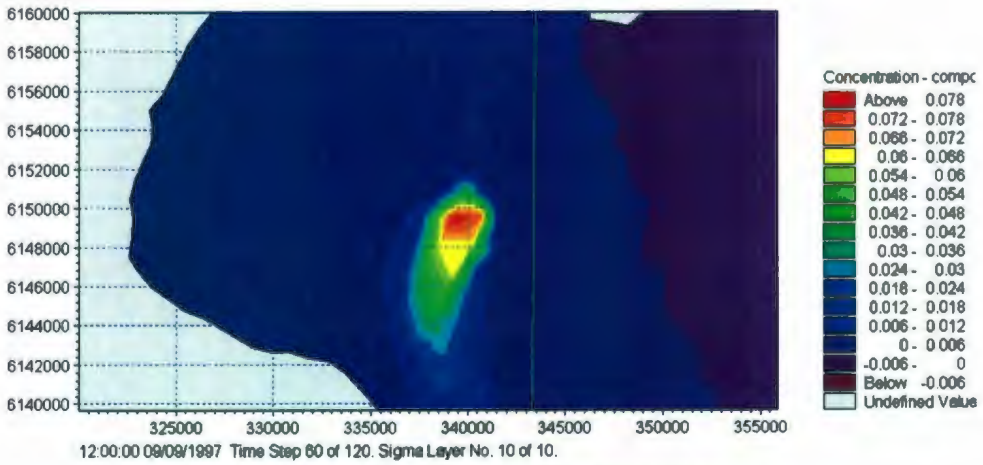

Figure 110. Case 2: Horizontal profile, Time = 12 hours.

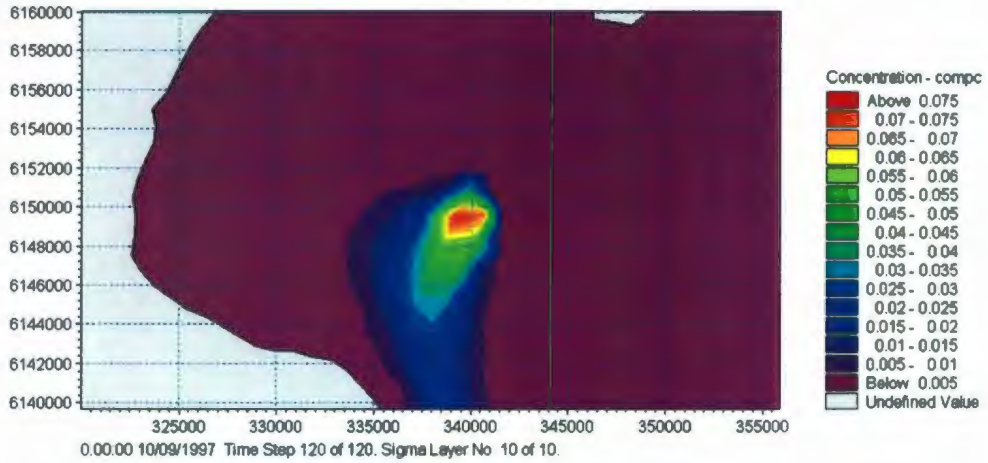

Figure 111. Case 2: Horizontal profile, Time = 24 hours.

is due to the surface current, which is stronger than the bottom currents and the two currents have different directions. In test cases 2, the plume is mainly affected by the surface current while the plume in case 1 is mainly advected by the bottom currents. The vertical profiles for Case 2 at the same cross-section as shown in Figure 103 are given in Figures 112 to 115. It can be seen from these figures that the vertical plume thickness has increased from 7.9 m at t=3 hours to 10.2 m at t=24 hours. The thickness predicted by Case 2 is much higher that of the Case 1. This is most likely due to the higher vertical mixing coefficient at the surface layer. As Case 1, Case 2 also predicted a very low concentration due to the use of a coarse grid.

To correctly predict the concentration, full implementation of the coupling algorithm was conducted in Case 3 and the results are shown in Figures 116 to 125. The horizontal profiles are presented in Figures 116 to 119. It can be seen from the figures that a much smaller plume was predicted in Case 3 than the other two cases. This is the result of a finer grid. As the model did not force the pollutants to disperse over a large grid in this case, the introduced near field concentration can be correctly

incorporated. As a result of this fine grid and the small plume size, the predicted concentrations in this case are much higher than the Cases 1 and 2.

A transition between the two coupling locations is shown in Figure 120. A double-core pattern can be found near the discharge point. The transition is not very smooth due to the fact that the source terms were introduced after each coupling step rather than each modeling step. The coupling step is much longer than the modeling step.

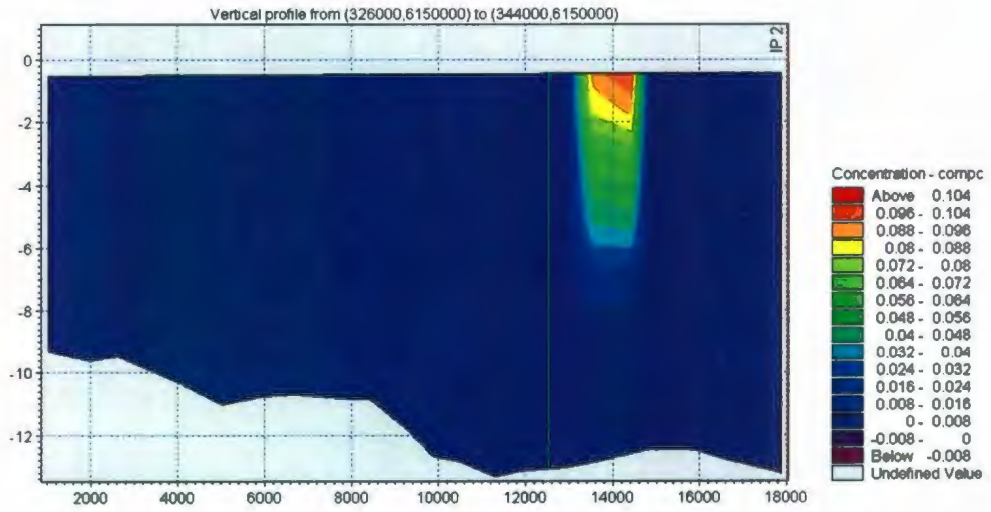

Figure 112. Case 2: Vertical profile, Time = 3 hours.

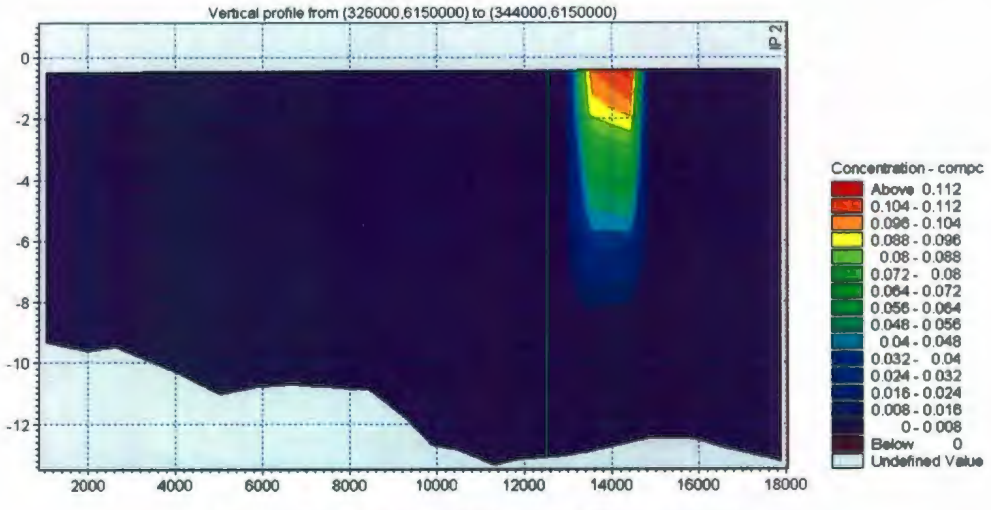

Figure 113. Case 2: Vertical profile, Time = 6 hours.

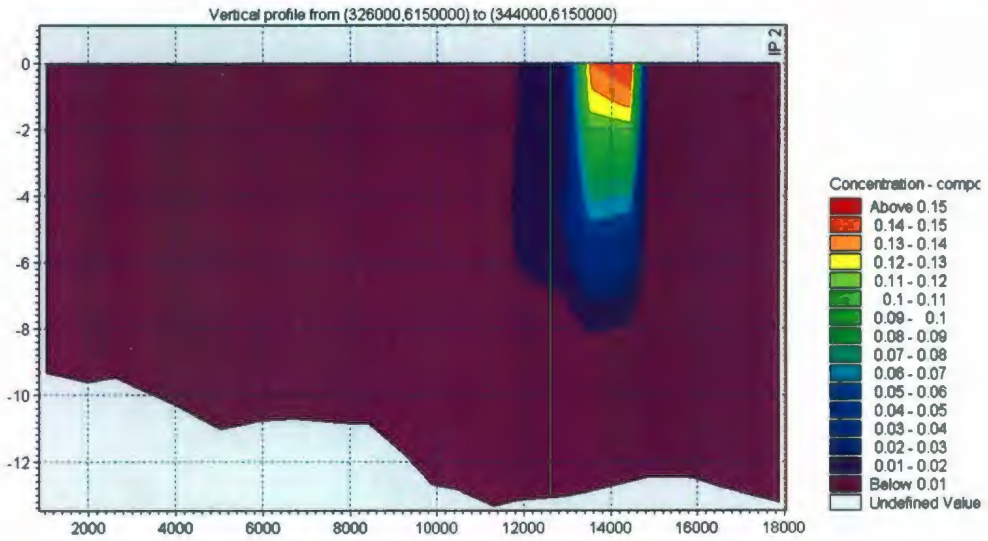

Figure 114. Case 2: Vertical profile, Time = 12 hours.

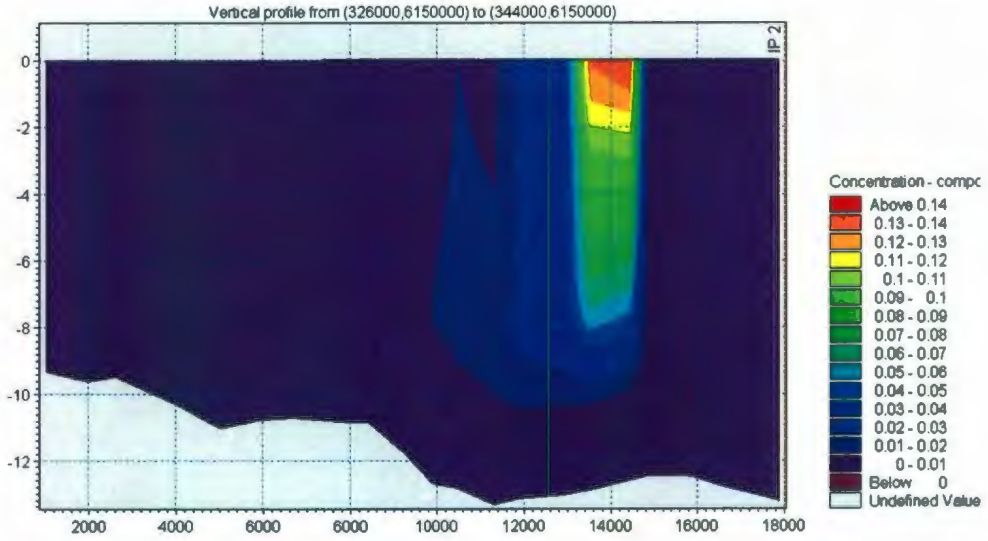

Figure 115. Case 2: Vertical profile, Time = 24 hours.

To examine the vertical profile predicted by Case 3, a cross-section as shown in Figure 121 was plotted at time 3, 6, 12, and 24 hours after discharge. This cross-section is taken from (339600,6150000) to (340400, 6150000) and is smaller than the one used for the previous two cases in order to give a clearer view of the smaller plume. The vertical profiles are shown in Figures 122 to 125.

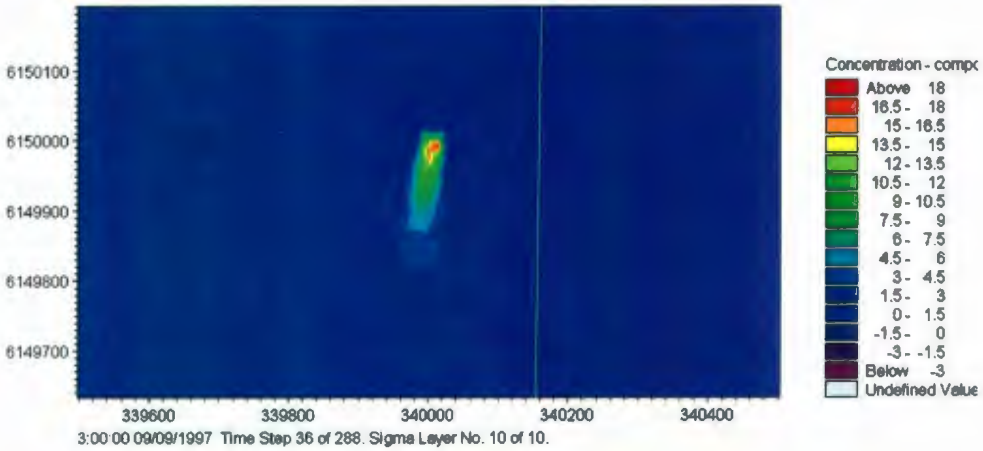

Figure 116. Case 3: Horizontal profile, Time = 3 hours.

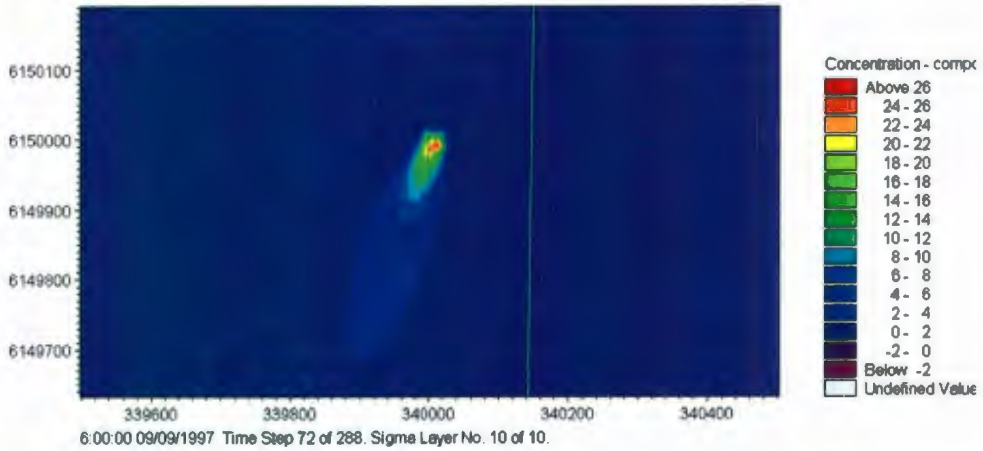

Figure 117. Case 3: Horizontal profile, Time = 6 hours.

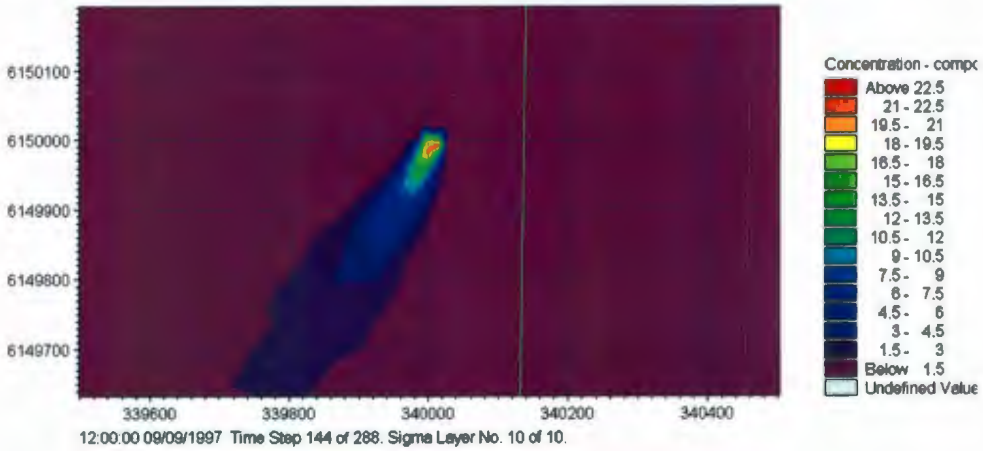

Figure 118. Case 3: Horizontal profile, Time = 12 hours.

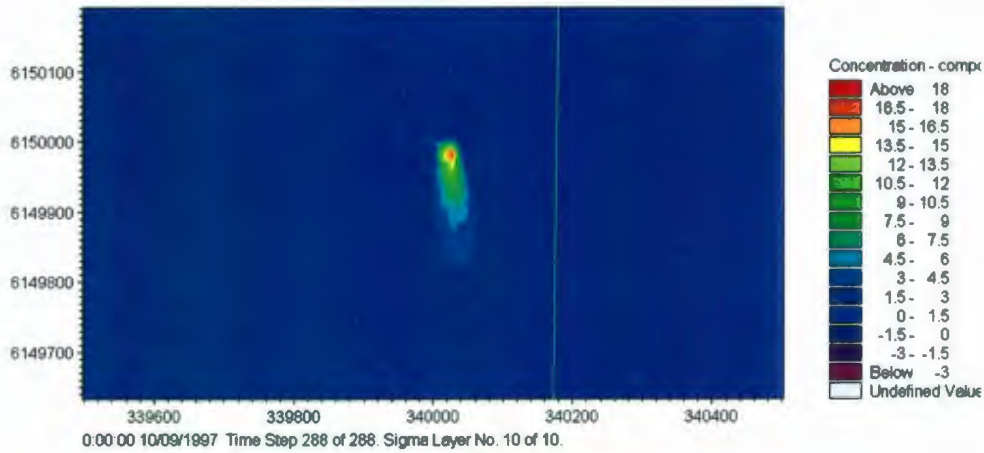

Figure 119. Case 3: Horizontal profile, Time = 24 hours.

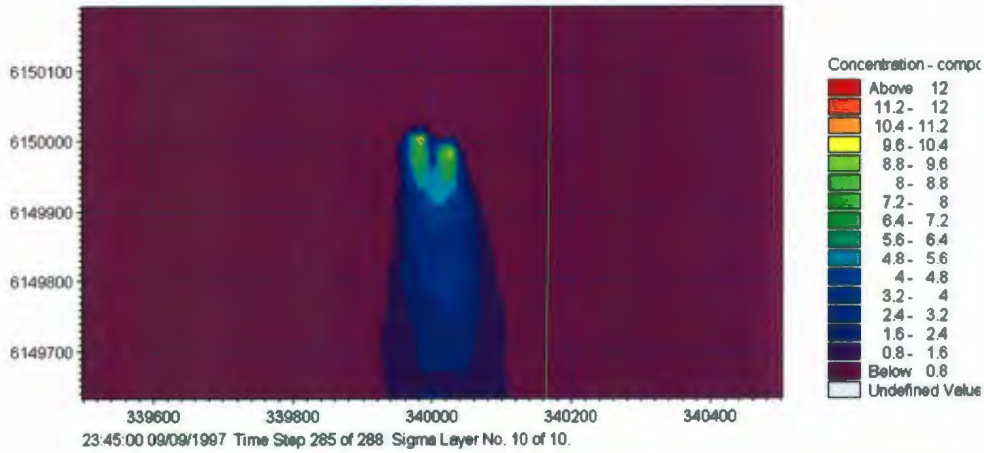

Figure 120. The transition of coupling locations.

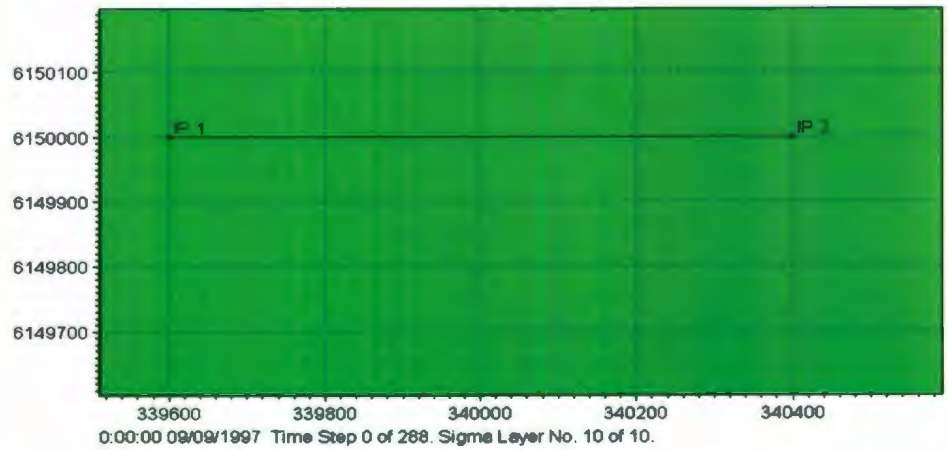

Figure 121. Location of points for vertical profile (Case 3).

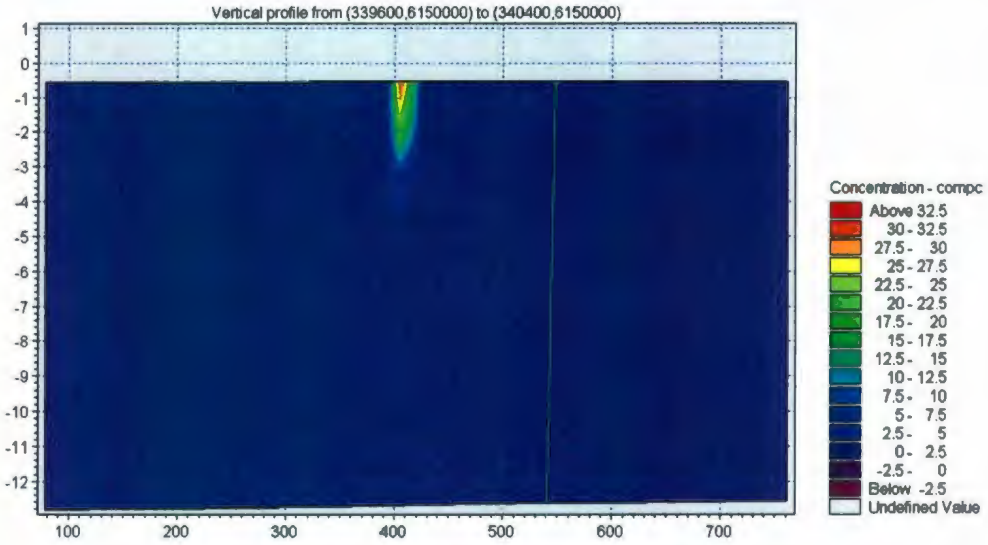

Figure 122. Case 3: Vertical profile, Time = 3 hours.

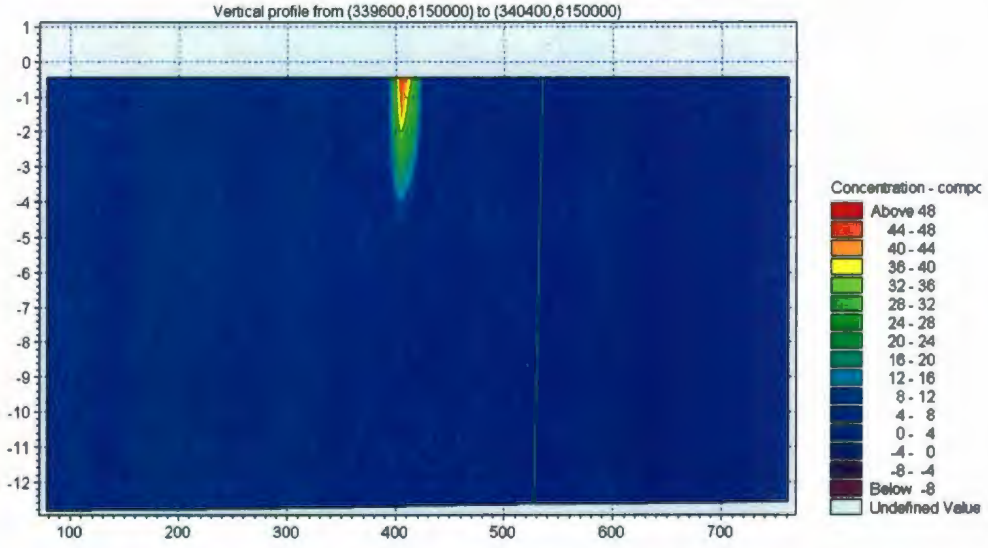

Figure 123. Case 3: Vertical profile, Time = 6 hours.

It can be seen from Figure 122 to 125 that the plume thickness ranges from 3.3 m (t = 24 hours) to 5.0 m (t = 6 hours). The maximum vertical concentration is shown to be 48 (t= 6 hours) and this value is very close to the predicted near field values. Also, the plume remains on the surface layer and this is expected because the discharge is lighter than the ambient. The results imply that the fine grid combined with coupling is effective in predicting the plume behaviors.

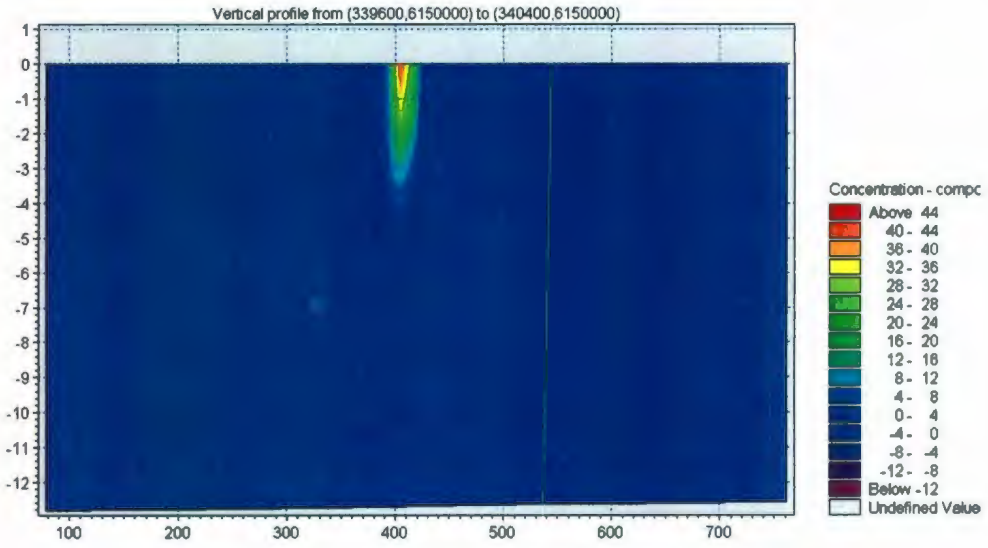

Figure 124. Case 3: Vertical profile, Time = 12 hours.

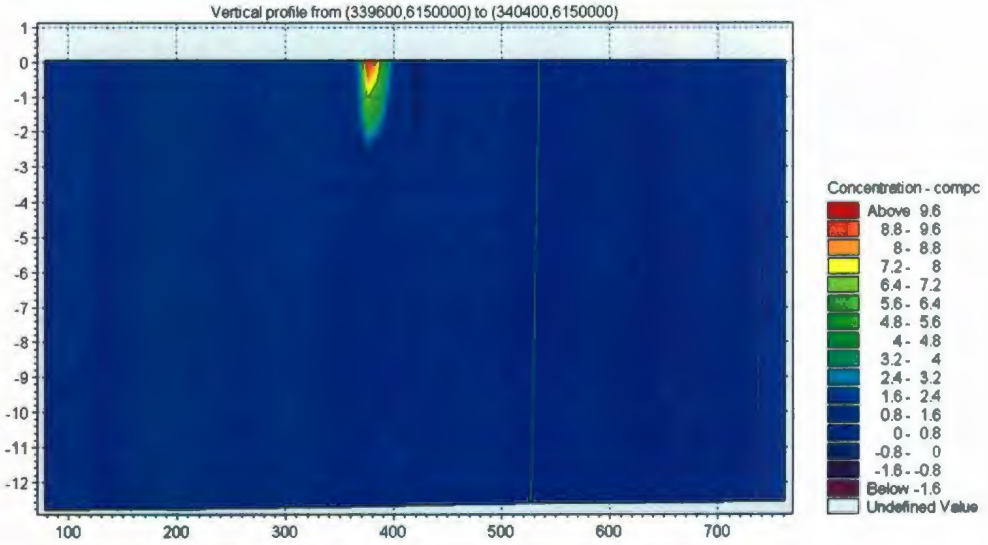

Figure 125. Case 3: Vertical profile, Time = 24 hours.

The vertical profiles presented before only showed the lateral information. To show the vertical plume profile longitudinally, the results for the two coupled cases are presented in Figures 126 to 129. Figure 126 and Figure 128 show the locations where the cross-sections were taken for Case 2 and Case 3 respectively. The vertical profiles for these two cross-sections are presented in Figure 127 and Figure 129.

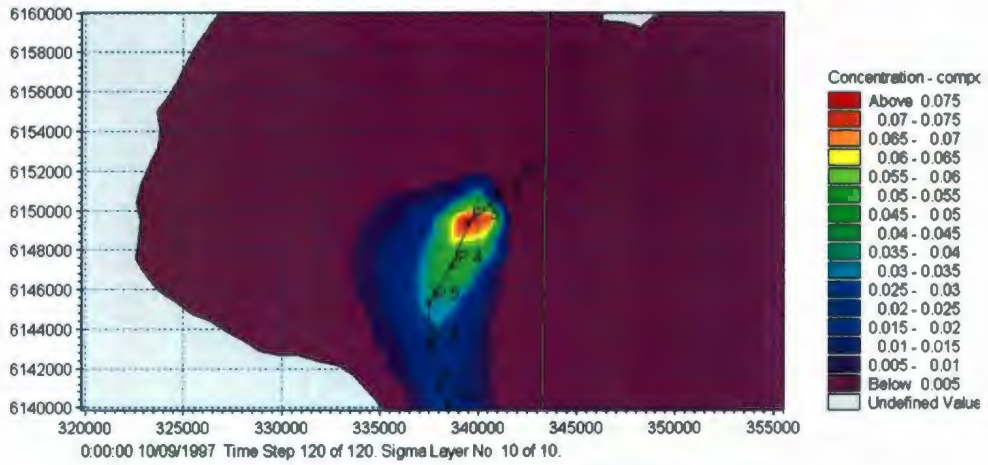

Figure 126. Locations of longitudinal cross-section (Case 2).

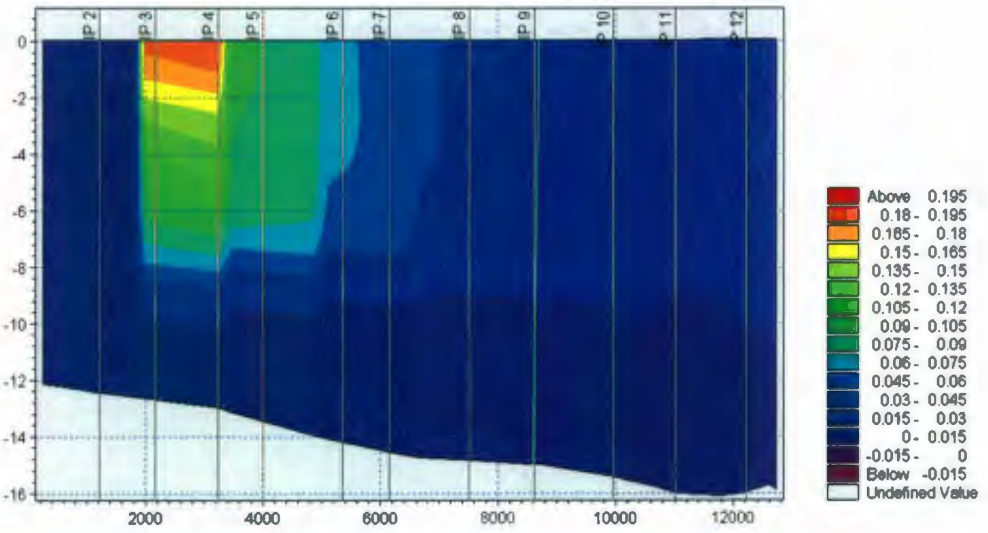

Figure 127. Longitudinal vertical profile after 24 hours (Case 2).

It can be seen from the longitudinal vertical plots, the pattern of plume thickness, plume extent, and dilution are similar to those in the lateral plots. The Case 2 gave a bigger plume dimension and therefore a low concentration due to the coarse grid size. The Case 3 gave a smaller plume dimension and higher concentration due to the fine grid size. The prediction of case 3 is closer to the near field predictions.

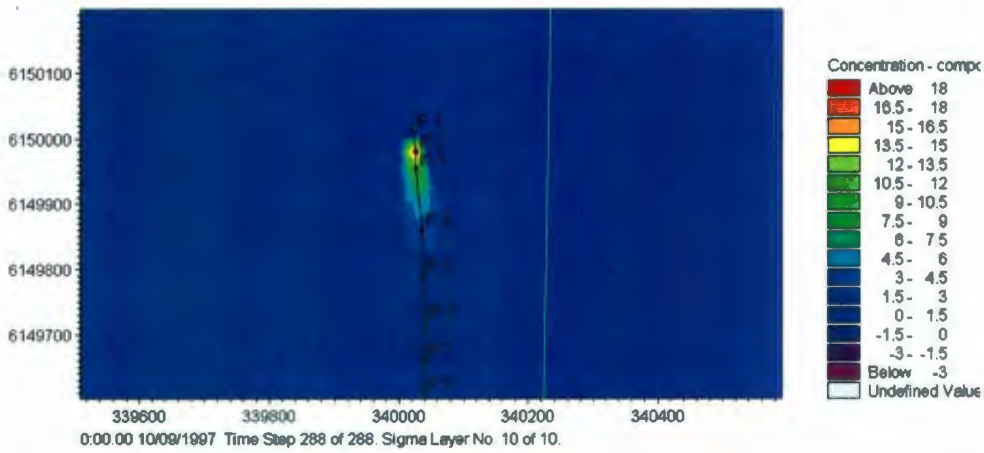

Figure 128. Locations of longitudinal cross-section (Case 3).

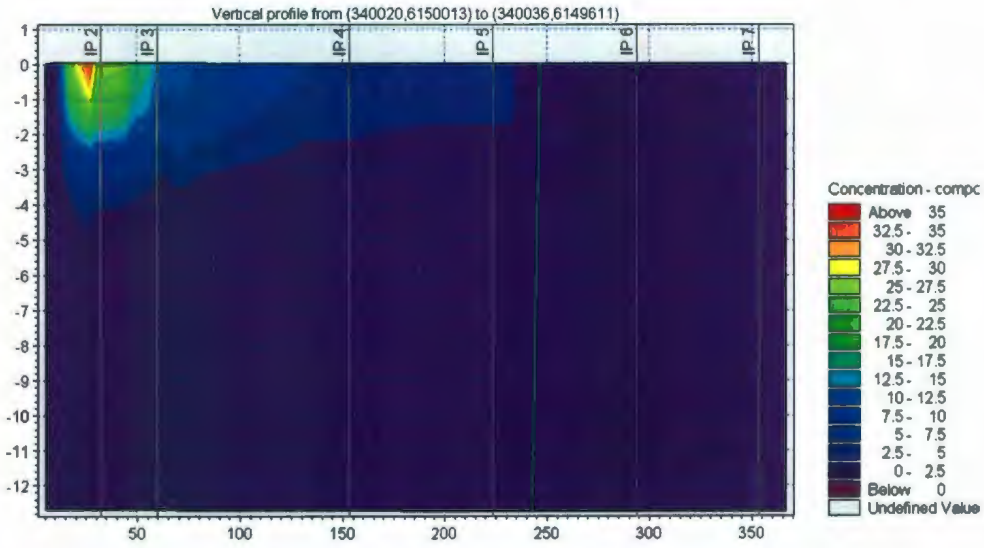

Figure 129. Longitudinal vertical profile after 24 hours (Case 3).

To give a more quantitative description of the predictions, point outputs were generated for the discharge point (340000, 6150000) at two depths, -9m and -1 m. Figure 130 shows the results for all 3 cases at -9 m depth. Because the source was introduced at the bottom in Case 1, highest concentrations were predicted in this case. The sources were introduced at the surface layer in both Case 2 and Case 3, therefore

both cases predicted low bottom concentration. Because of the coarse grid, the predicted concentration in Case 2 is lower than that in Case 3.

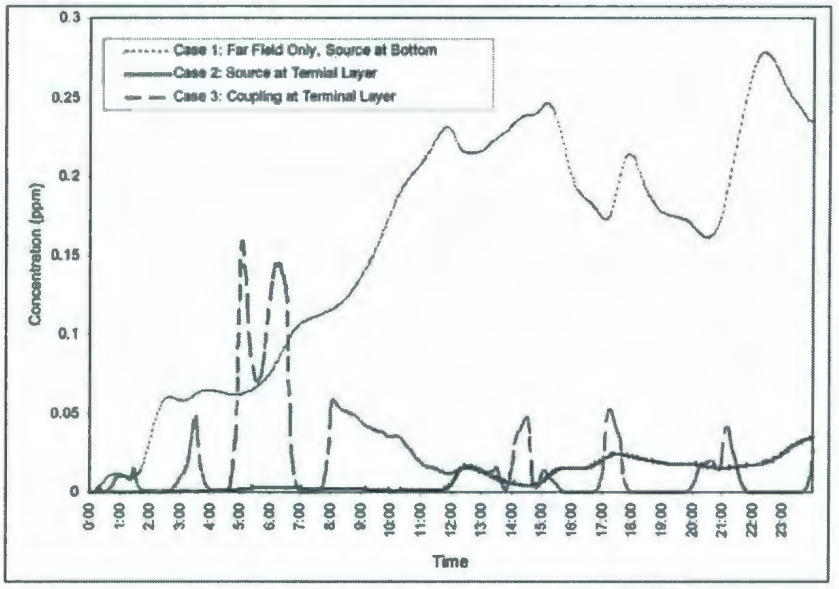

Figure 130. Concentration at the discharge point, depth = -9m.

The results for the -1 m depth are given in Figure 131. Case 1 is not shown in the figure and only the results for case 2 and case 3 are plotted. To check the model performance, the near field prediction is also shown. It can be clearly seen that the Case 2 failed to correctly predict the concentration due to the coarse grid size, which forced higher order of dilution of the source over a large grid cell. On the contrary, Case 3 predicted the concentration reasonably well. The result is very close to the values predicted by the near field model. The small difference between the peak of Case 3 and the near field model prediction is mainly because the near field model prediction is for locations at the end of the intermediate field, but the Case 3 is for locations at the center of the discharge point. There is generally 10 to 40 m distance between these two locations in the current simulation. The near field prediction is the center and has the highest concentration. The concentration decreases as the plume

progresses farther away. Therefore, the predicted lower concentration in Case 3 compared to the near field is expected and reasonable.

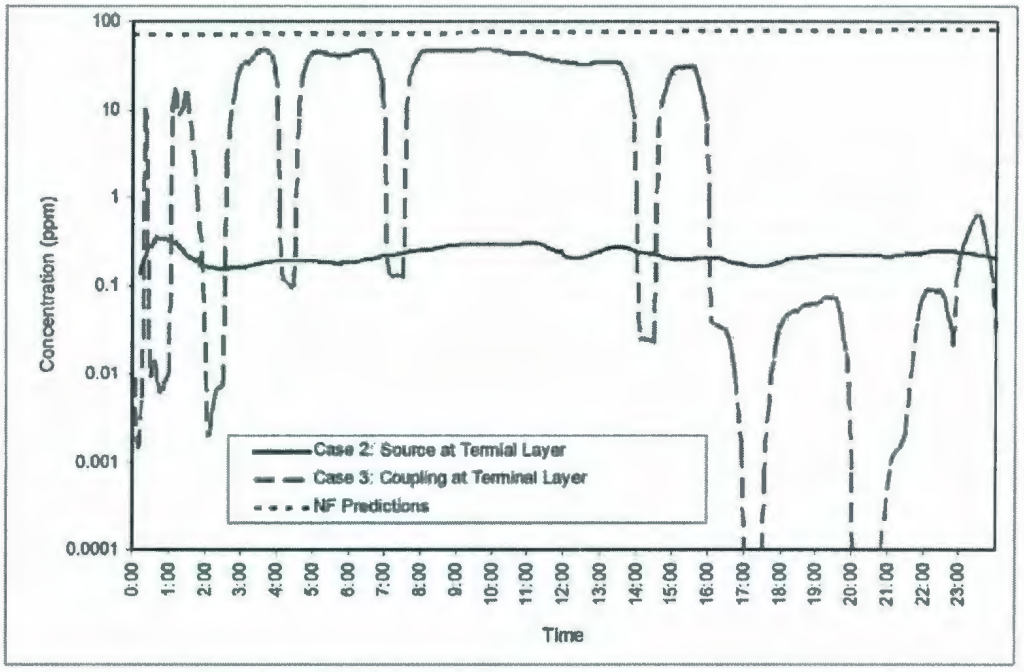

Figure 131. Concentration at the discharge point, depth = -1 m.

6.4 SUMMARY

In this chapter, the steady state model, PROMISE, was coupled with a non-steady state model, MIKE3. The coupling algorithm used was a two way passive offline coupling. Three test cases were studied. Case 1 only used the non-steady state model with a coarse grid. Case 2 used a simple coupling method with a coarse grid. Case 3 used a fine grid and fully adopted the coupling algorithm. A coupling approach is necessary, because the non-steady state model only case fails to resolve the near field dynamics and fails to predict the dilution correctly,. It can be concluded from the study that a minimum grid size must be maintained in order to introduce the source term correctly.

7. MAPPING THE DISPERSION USING AN AUV

Field experiments are important for both the environmental effects monitoring and numerical model validation. Very few field tests for model validation have been reported to date. This is mainly due to the difficulty of collecting data in harsh, remote environments and the high cost associated with these experiments.

This chapter describes a field experiment in mapping an outfall using an Autonomous Underwater Vehicle (AUV). A review of the existing field tests in plume mapping will be presented in section 7.1. A review of AUVs are given in section 7.2. The field experiments using MUN Explorer AUV is described in section 7.3. The comparison of measured data with model predictions is presented in section 7.4.

7.1 REVIEW OF FIELD EXPERIMENTS

The field experiments on mapping produced water are reviewed in this section. Because of the similarity of produced water outfalls and sewage outfalls, field studies on sewage outfalls will also be reviewed here.

7.1.1 Produced Water Outfalls

Smith et al. (1994)

Smith et al. (1994) reported the field tests conducted by the Exxon Company on May 19-22, 1992 for validation of the OOC model. Produced water with a salinity of 85 ppt, a temperature of 32 °C, and a density of 1059 kg/m^3 was discharged from a 15

cm pipe placed 3 m below the sea surface. Effluent samples for measurement of initial tracer concentration were collected just downstream of the static mixer. Samples were collected using both a suction apparatus and manually by a diver.

The suction apparatus consisted of an array of hose bundles deployed at nominal depths of 7.6 and 8.8 m. Each hose bundle contained seven hoses which took samples from ports located at distances of 4, 6, 13, 28, 58, 78, and 103 m from the discharge point. A diver, using a hand-held Van Dorn sampling bottle, collected samples at various distances from the discharge point. The ability of the diver to judge where the plume was located at the instant of sampling ensured that the diver-collected samples were taken from within the plume. The diver also made visual observations of plume depth and direction throughout the study.

The tracer concentrations were analyzed by fluorometry. The concentration from the suction hose array exhibited a high level of variability. The comparison of field test results with model predictions showed that the model predictions and diver-collected samples were in good agreement. The model prediction agreed well with observations in the near field and agreed within a factor of two with observed average concentrations at large distances.

LES (2006)

To study the produced water discharged from the Terra Nova Floating Production and Offloading Vessel (FPSO), Lorax Environmental Services Ltd. has conducted a vessel-based field study that tracked the Rhodamine WT dye added to the produced water discharged on November 18 and 15, 2005 (LES, 2006).

The produced water discharged from the FPSO had a temperature of 60 °C and salinities from 65 to 70 ppt. The density of the discharge was about 1050 kg/m^3. The depth of the discharge may vary from 13-20 m depending on the vessel draught. The depths of discharges were 15.7 m on November 18th and 15.6 m on November 25th.

A 20% Rhodamine WT dye was added to the produced water at the rate of 22 L/h on November 18th and 16.5 L/h on November 25th, and this yielded a projected plume concentration of 50 ppb. A Turner Design SCUFA fluorometer with turbidity channel was connected to a Seabird SEB CTD to measure the fluorescence as well as salinity, temperature and depth every 0.25 seconds and logged the averaged data every 1 second.

Vertical profiles were measured from top to bottom by lowering the CTD/fluorometer over the side of a vessel. These profiles were made along several transects perpendicular to the presumed long-axis of the plume. The distance of the measurements was up to 2.2 km from the FPSO. The surface portion of the plume was studied by continually pumping the seawater from an intake at 5 m below sea surface into a chamber on the deck of the ship and monitored by a fluorometer.

Only the vertical profiles were reported and there is no horizontal profile. This maybe due to the resolution of horizontal sampling points, which were not fine enough to produce a horizontal contour. It was found by this study that there was a disparity between the up- and down-cast. The vertical plots showed the vertical profile was not smooth, but rather patchy. This was more evident for the November 25 tests, where the profiles indicated the plume split into multiple layers.

There are several limitations of the study that severely limits its use in validating a model. First, the Rhodamine dye was added at a constant rate, but the produced

water flowrate varied by a factor of three over the course of the field test. Second, most of the surface portion of the plume is in the upper 1 m, but the sampling location was at 5 m depth. The lengths of some of the transects were too short to capture the entire plume width.

7.1.2 Sewage Outfalls

To study the initial dilution and plume dispersion of four Florida outfalls, dye measurements were made during two cruise periods (10-24 hours), September 18-25, 1991, and February 3-12, 1992 (Proni et al., 1994). A ship equipped with GPS for navigation and sampling station positioning was used. Two or three hours prior to the tests, Rhodamine WT dye was continuously injected into effluent at the treatment plant and the dye concentration was monitored continuously using a fluorometer. The dye concentrations at outfall boils were determined using two sampling methods: 1) a deck mounted sampler whose underway sampler was towed and kept at approximately 2 m below the water surface, taking fluorometer measurement at 1s intervals; and 2) taking samples from the water surface using sampling bottles, from which dye concentrations were later measured using a fluorometer. In addition to dye measurement, currents were measured with mooring systems deployed in the vicinity of the outfall outlet. A Conductivity/Temperature/Depth (CTD) instrument was used to measure temperature and conductivity profiles, from which density profiles were generated. The data obtained were analyzed using a dimensional analysis method and empirical relationships for initial dilution were derived.

In-situ measurements of the shape and initial dilution of the Sand Island, Hawaii sewage plume were conducted between September 25 and October 1, 1994 using an

instrumented towyo platform (Petrenko et al., 1998). Towyo is a term to describe the process of towing an instrument behind a moving ship while simultaneously lowering and raising it between the surface and some deeper depth. This up-and-down motion resembles the track of a yo-yo; hence the term towyo. The platform carried a CTD, a beam transmissometer, and a fluorometer. Towyo transects were obtained by winching the platform between the surface and the bottom as the vessel moved forward at a speed of 1-1.5 m/s, resulting in a depth-varying sawtooth pattern with a horizontal resolution of approximately 250m at middepth and a vertical resolution of at least 0.5 m. The observed dilutions agree well with model predictions for periods when the water column is stratified and current is weak. For strong currents, the RSB model predicts dilution 2.4 times that observed. The test results showed that the plume structure was considerably more complex than the compact shape of the classical mathematical picture of a buoyant plume. Mathematical models implicitly assume that the plume vary smoothly in space, an assumption that is true only for time-averaged plumes. However, the shape of the observed plume is not smooth, but rather patchy. The patchiness has also been observed in a later field study of Carvalho (2002) and is shown in Figure 133.

The field observations of Ipanema beach, Brazil, outfall were reported by Carvalho et al. (2002). Two boats were used for in-situ tracer detection. The first boat was equipped with a differential global positioning system, and either two or three sample collectors at different depths. Each collector was connected with a centrifugal pump that pumped the seawater through a rubber hose to a portable fluorometer. Data were recorded on a data logger, graphic recorder, and a notebook computer. The second boat collected seawater samples by pumping devices and measured

physicochemical parameters (e.g., temperature, salinity, pH, dissolved oxygen) with a water quality analyzer. The current data were measured by a mooring with four current meters installed at 7, 13, 19, and 24 m depth. The test results were compared with the US EPA PLUMES model and the CORMIX model. It was found that the gross properties of the plume can be reasonably predicted by plume models, but there remain some aspects which cannot be, particularly the patchy nature of the waste field (as shown in Figure 132). The understanding on mixing processes can be improved by continuous sampling.

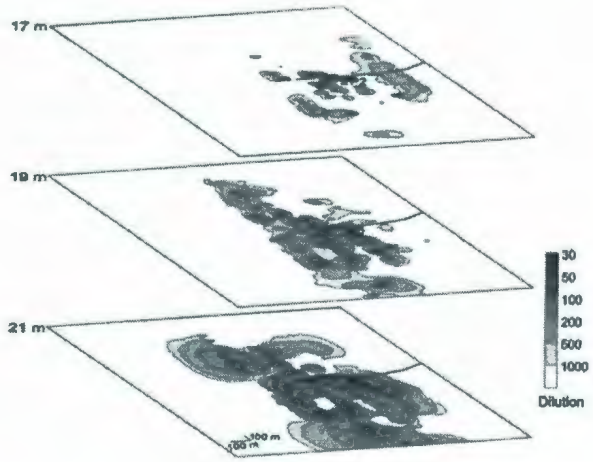

Figure 132. Patchiness of the Ipanema beach outfall (Carvalho et al., 2002).

Conducting field experiments in a harsh marine environment is challenging work and is very time consuming and expensive. The data collected using the traditional towing tests is often incomplete and provide very limited information. For deep water monitoring, the increasing water depth also increases the level of sampling error due to the drift of surface vessel platforms and prolonged sampling times. To map a produced water plume more effectively and accurately, new and innovative means of acquiring data need to be used. One solution is the use of a new generation of

autonomous oceanographic platform -Autonomous Underwater Vehicles (AUVs) - that is capable of tracking water masses, recording chemical/physical/biological properties, and transmitting data without tether to either the seafloor or a vessel. AUVs are able to provide a detailed 4D view of the dynamic ocean.

A detailed review of the capabilities of AUVs will be given in the next section.

7.2 AUTONOMOUS UNDERWATER VEHICLES (AUVs)

7.2.1 Review of AUVs

Autonomous Underwater Vehicles (AUVs) have been under development since the late 1950's (Alt, 2003). To date, more than 66 AUVs have been developed in 12 different countries and AUVs have now reached the beginning of commercial acceptance (Wernli, 2000).

AUVs are self propelled underwater robotic devices, controlled and piloted by onboard computer. Typically, when on the surface, an AUV is normally navigated by a differential-Global Positioning System (DGPS) which gives the AUV highly precise navigation capability. When submerged, the position of an AUV is estimated by measuring its relative speeds over the current or seabed via an Acoustic Doppler Current Profiler (ADCP). For more precise navigation, an inertial navigation unit is used with positioning from a sonar system (long baseline or ultra short baseline). A downward ADCP can also be used to measure the AUV's altitude off the seabed and a forward looking echo sounder can help to prevent collisions.

AUVs are manoeuvrable in three dimensions and this enables them to follow a pre-programmed trajectory precisely. One of the best features of an AUV is the ability

to carry a wide range of payloads or sensors. As AUVs move through the water column, the sensors conduct both spatial and time series measurements.

Compared with traditional ship-based data collection methods, an AUV can obtain much more information in a relatively short time. It has potential to do so cost effectively. An analysis by C&C Technologies showed that the total cost of a deepwater survey could be cut from $770k using a deep-towed system to $291k using an AUV (Wernli, 2000). Unlike Remote Operated Vehicles (ROVs) that require a dedicated ship and human operators at all times, AUVs are self-sufficient, once launched they can return to base autonomously.

Figure 133 shows an AUV in a data collection mission.

Figure 133. MUN Explorer AUV during a mission.

The commercial usage of AUVs has been gaining strength in the areas of seabed mapping and oceanographic measurements due to the AUV's ability to provide high-quality, high-resolution data compared to ship-based collection (Griffiths, 1997; Alt, 2003). The recent development of in-situ environmental sensors and their integration

gives AUVs great potential in performing offshore oil and gas EEM missions; however, very limited work has been conducted in this field.

Not all AUVs are capable of conducting all types of environmental monitoring missions effectively. Many AUVs have been designed for combinations of low-cost, light weight and operations over a confined area (Griffiths, 1997). As a result, these AUVs either have a limited endurance, payload space, depth capability or require continuous communication with a mother control console. Griffiths et al. (1998) have indicated that an AUV must have the following features:

- Have a range capability well in excess of 50 km;
- Be able to carry a sensor payload for the purpose of multi-discipline data gathering;
- Be reliable, robust, and affordable in terms of capital cost and running expenses.

In this section, five different types of AUVs will be described briefly to show the capability of using AUVs to perform environmental monitoring missions.

REMUS

The Remote Environmental Monitoring UnitS (REMUS) is a low cost, light weight vehicle specially designed for coastal water monitoring with a maximum depth of 200 m. The REMUS is 1.5 m long and 20 cm in diameter. Its dry mass is 30kg and its maximum and best energy efficient speeds are 2.05 and 1.02 m/s, respectively. At 1.02 m/s, the REMUS can travel for over 20 hours and over 70 km.

The REMUS AUV has been widely used to detect and map chemical plumes (Fletcher, 2001; Ramos et al., 2002; Farrell et al., 2005). In the Fletcher (2001) study,

the REMUS carried a Rhodamine fluorometer which was used to map Rhodamine plumes at two different sites. The study areas were 400m×100m, and 1000m×800m respectively. Different sampling strategies were used and data were successfully collected at depths as low as 1.5m above the bottom. Ramos et al. (2002) reported an AUV mission for the Averio sea outfall using temperature and salinity as tracers. A survey area of 100m×200m and water depth range from 2 to 12m were studied. The area was divided into six vertical and horizontal sections and surveyed by the AUV. The data obtained were sufficient to plot a 3D contour map of the water column. Unlike the two studies described above in which the AUV followed predefined trajectories, the mission by Farrell et al. (2005) demonstrated that the REMUS is able to find a chemical plume and trace the plume to its source.

ARCS

The ARCS is an AUV developed by International Submarine Engineering Limited (ISE). The ARCS is 6.4m long, 68.6cm in diameter. It has a range of 36km to 235km depending on the type of battery pack used. The maximum depth is 300m. The speed of ARCS is up to 2.8m/s.

The ARCS has been used by Pennell et al. (2003) to measure a chemical (Dimethyl sulphide) plume using a Conductivity Temperature Depth (CTD) sensor and In-Spectr underwater mass spectrometer. The AUV was able to successfully detect the presence of a Dimethyl sulphide plume in an area of about 600m×600m. Although the mission was to detect the Dimethyl sulphide, the ARCS was also able to detect the presence of Toluene in the mission.

AUTOSUB

The AUTOSUB program is operated by Southampton Oceanography Centre in Southampton, U.K. The overall focus of the programs is on using AUVs for marine science. AUTOSUB is a large vehicle, 6.8 m long and 0.9 m in diameter with a payload capability of 100 kg in water. The program has been successful in testing the boundaries of the autonomous nature of the vehicle in that a major focus in recent years has been under ice exploration with missions in near Greenland and the Antarctic. AUTOSUB has conducted an estimated 270 missions with the longest being 292 km or 50 hours. A wide variety of sensors have been integrated into the AUTOSUB since its initial missions in the nineties (Griffiths et al., 2001). These have included physical (CTD and ADCP) and chemical (nitrate and manganese) sensors (Griffiths et al., 2001; Statham et al., 2005). Acoustic measurements have included fisheries echo sounders, side scan sonars and multi-beam sonars which have led to cutting edge research in their given fields (Fernandes et al., 2000; Wadhams et al., 2006).

With this type of range and capability to provide for extensive science missions, AUTOSUB and other vehicles like it are suited to provide unprecedented access to areas otherwise inaccessible using traditional methods.

7.2.2 MUN Explorer AUV

Memorial University of Newfoundland has recently acquired a new Explorer class AUV built by International Submarine Engineering Ltd. The AUV is designed as a 4.5m ocean-going instrumentation platform with a 3,000m depth capability. The

strength of the MUN Explorer AUV is its ability to carry 150kg of scientific payload (instruments), with a power requirement in the hundreds of Watts, on missions of up to 12 hours duration or 100 km. The mission length drops as power requirement increases. The detailed specifications of the MUN Explorer AUV are listed in Table 29.

Table 29. Specifications of the MUN Explorer AUV.

Characteristics	Specifications
Length	4.5 m
Hull Diameter	0.69 m
Dry Weight	700 kg
Displacement	710 kg
Maximum Depth	3000 m
Speed Range	0.5 m to 2.5 m/s
Payload	Without removing trim lead - 150 kg
Turning Radius	10 m
Sensors	MicroCTD, Idronaut dissolved oxygen, Cyclops-7 RWT fluorometer
Navigation	• Watson BA 303 AHRS Sound Ocean System GPS with retractable mast. • RDI Workhorse 300 kHz DVL Paroscientific dept transducer with an accuracy of 0.1% over the 3000m range. • Kongsberg Simrad Mesotech 1007 Digital Altimer
Positioning Systems	LinkQuest MA5000 USBL system
Emergency Equipment	ORE 4336B Transponder locator, NovatechST-AR400 Strobe, RF 700 A1 Radio Beacon

The MUN Explorer is designed such that the whole of the fore end is available for the carriage of different sensor instruments for different types of research missions. Apart from the pressure hull, which houses the batteries, control hardware, and navigation systems, the AUV is freely flooded. The fore section casing consists of a relatively low cost fibreglass shell. For complicated instrumentation outfits, the instruments can be installed in their own dedicated instrumentation section shell piece.

Different users can be provided with an instrumentation section shell piece in order to outfit their instruments, thus making efficient use of the AUV time and availability for missions.

A schematic plot of the MUN Explorer AUV is shown in Figure 134. The Vehicle Control Computer (VCC) is housed inside a pressure hull in the middle of the vehicle. The VCC collects data from all the instruments and controls the execution of missions. This computer can remotely communicate with a Surface Control Console (SCC) while it is on the surface. The SCC transmits pilot commands to the VCC and creates graphical displays to provide information to the operator.

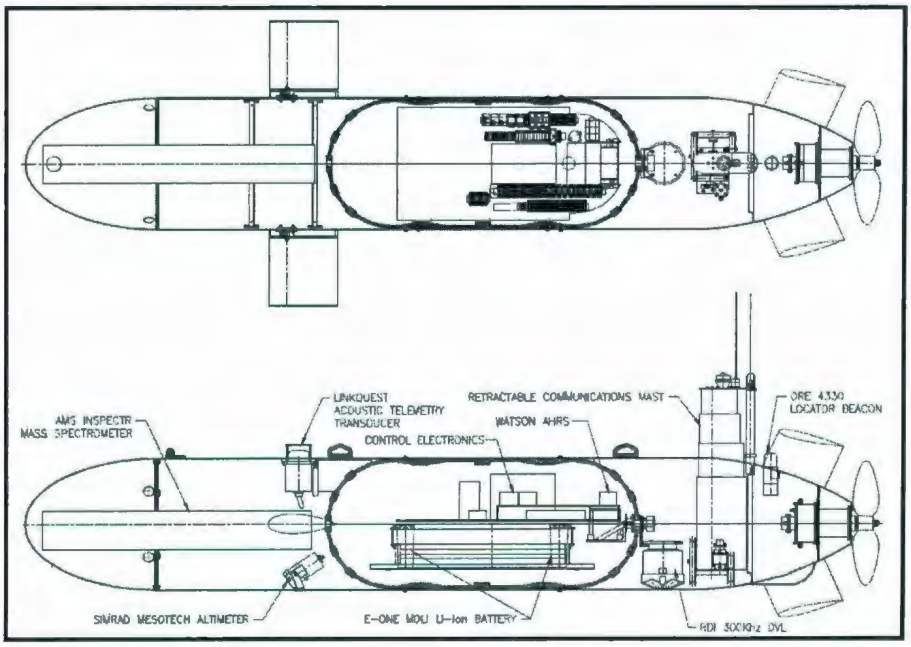

Figure 134. Schematic of the MUN Explorer AUV.

Before the AUV is put in the water, missions are planned on the Mission Planning Workstation using the FleetManager software and uploaded into the VCC. Once in water and the mission is started, the vehicle will follow the pre-planned routes and

depths and collect data. After a mission is completed, the vehicle will return to the pre-programmed location.

7.3 MONITORING OCEAN OUTFALL USING AUV

To study the ability of plume mapping using the MUN Explorer AUV, a field test that tracked the Rhodamine WT dye were conducted on August 31, 2006 and again on September 7, 2006. This section describes the field tests and the results.

7.3.1 Description of Study Site

The field tests were performed in the south arm of Holyrood Bay at the head of Conception Bay. Holyrood Bay is located about 40 km southwest of St. John's, Newfoundland. The location and bathymetry of the study area are shown in Figure 135.

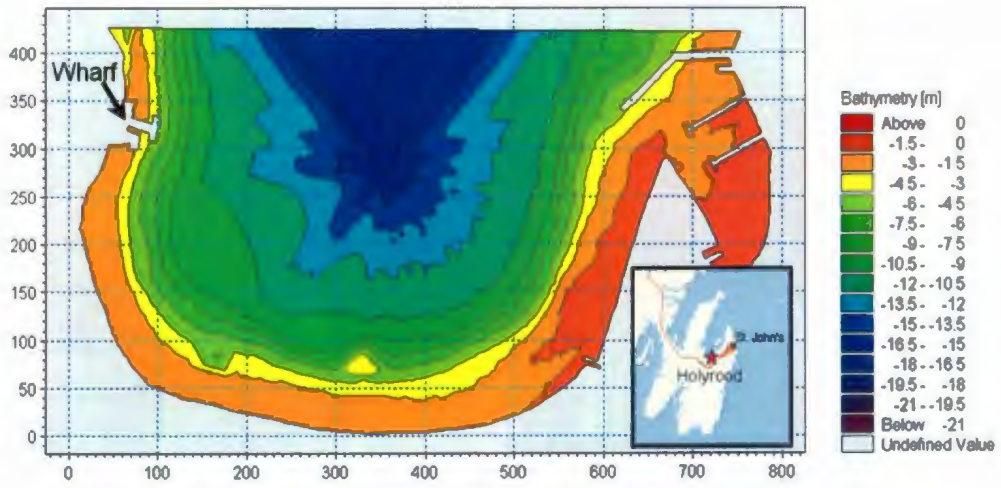

Figure 135. Bathymetry of the study site.

The AUV was launched from the wharf on the west side of the Bay. The water depth at the wharf is about 6 m. Except for the locations close to coastline, the water

depths for most of the study area are deeper than 6 m. The deepest water depth of about 19 m is at the center of the Bay.

7.3.2 Experimental Setup

The objective of this study was to use the MUN Explorer to map a plume similar to produced water outfalls. There is no existing outfall of this type in the study area, therefore a temporary artificial outfall was built on the wharf.

The configuration of the discharge system is illustrated in Figure 136 and pictured in Figure 137. Freshwater was supplied at a rate of about 1.72 L/s and mixed with the concentrated dye pumped from an 800 Liter storage tank to the flow mixer. As the pump has a much higher flowrate than needed, an adjustment tank was used to return most of the dye to the storage tank and only a small amount of dye was sent to the flow mixer by gravity. The flowrate of the dye was controlled to give a mixed water dye concentration of about 11.5 ppm and 22.7 ppm for August 31 and September 7, respectively.

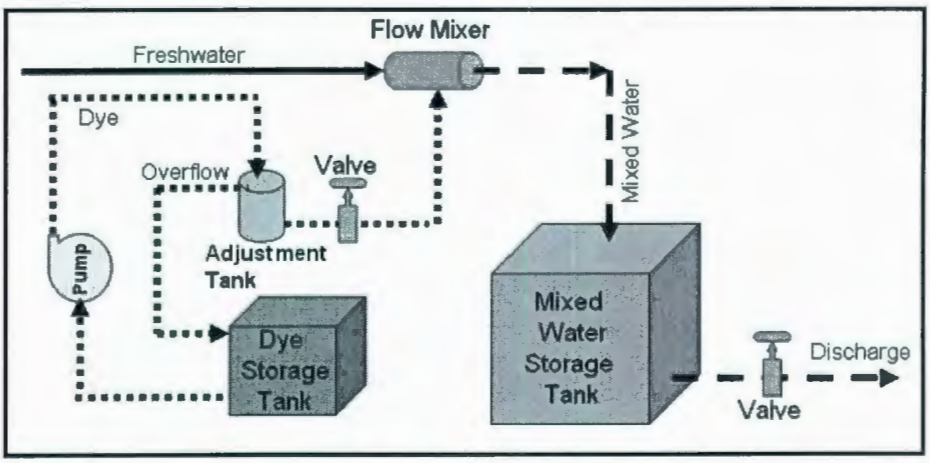

Figure 136. Schematic of the discharge system.

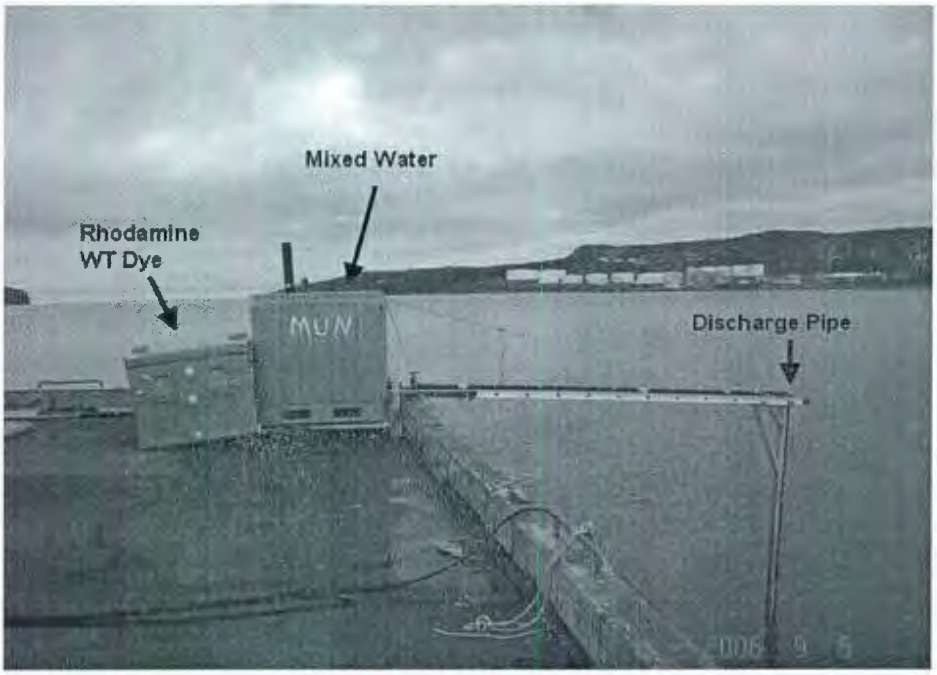

Figure 137. The discharge system setup (photo).

The mixed water was then sent to the mixed water storage tank and discharged into the sea through a 2 inch diameter pipe submerged at about 3m below sea surface. The distance of the discharge pipe to the wharf is about 4 m.

During the experiment, the discharge was started at least two hours earlier than the launch of the AUV to give enough time for the plume to disperse. Taking the example of a mean current speed of 5.86 cm/s, this allows the plume to travel up to 421 m downstream. The vehicle was then launched and the dye concentration was monitored by a Turner design Cylops-7 fluorometer. Salinity and temperature data were also collected by the AUV with a MicroCTD. Figure 138 shows the MUN Explorer AUV with sensors equipped.

For both tests, the vehicle speed was 1.5 m/s. The vehicle data, including the position, heading, and speeds were logged to the vehicle computer at a sampling rate of 0.1 s. The CTD and flurometer have a separate datalogger, which was synchronized

with the vehicle time before mission. The sampling interval of the CTD/fluorometer was 0.2 s (5 data points per second). This setup yields a horizontal resolution of 30 cm along the AUV trajectory.

Figure 138. MUN Explorer AUV with CTD and fluorometer sensors.

7.3.3 Experimental Results

Test No. 1 - August 31, 2006

The mission time for this test was about 2 hours. The vehicle surveyed an area of about 120 m × 240 m. The vehicle trajectories over the course of test are shown in Figure 139. It can be seen from the figure that there is a overlapping of the trajectory and the wharf. There are two possible reasons for this deviation of trajectory: error with the GPS and error with the map. Among these two possible error sources, it is

more likely that this is due to the error of GPS. A GPS for civilian usage generally has an error of about 10 m and this is about the error level observed in Figure 139.

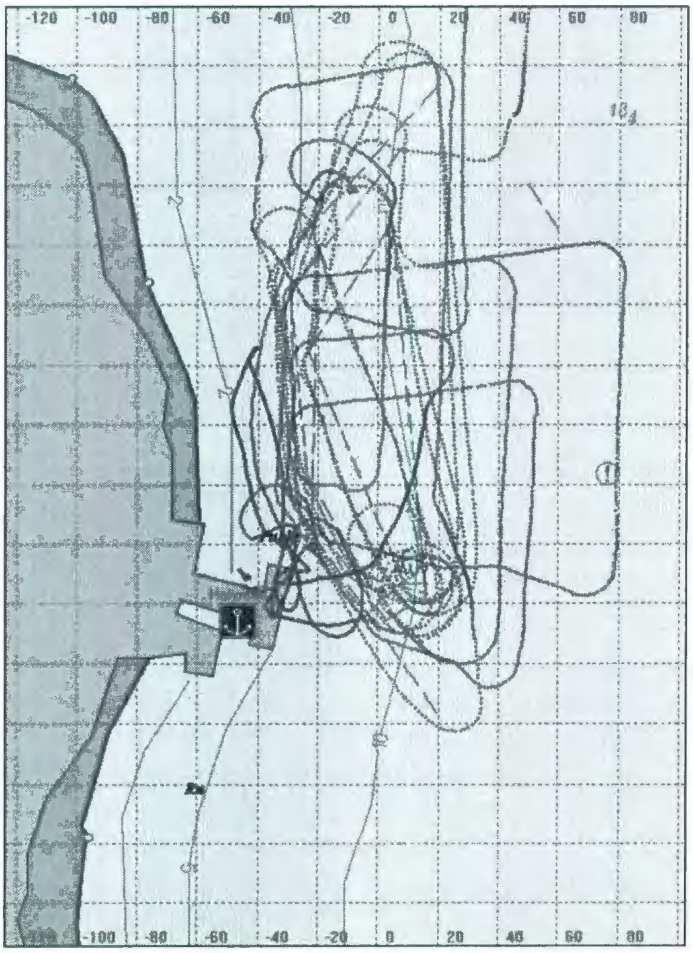

Figure 139. Trajectory of the AUV shown by the *FleetManager* software (August 31, 2006).

The area survey for this test was mainly east and northeast the wharf. This is the projected plume direction based on the observation of drifts of surface floats. This direction was confirmed by the measured currents from a current meter moored about 10 m away from the discharge point. The current data are plotted in Figure 140. It can be seen from the plot that the dominant direction is north east. The current speed range was from 2.21 cm/s to 12.61 cm/s. The mean speed was 5.86 cm/s and the median speed was 5.38 cm/s.

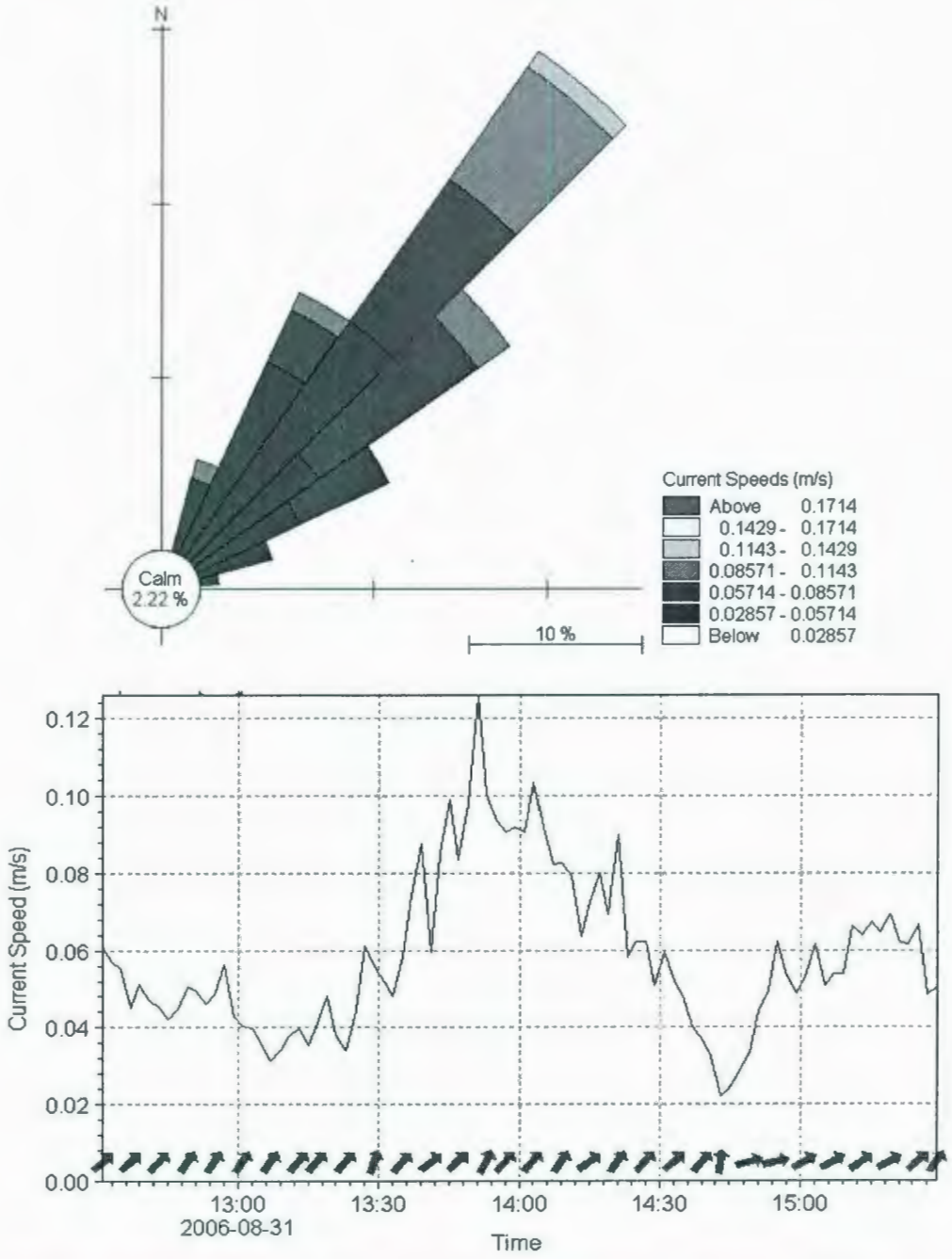

Figure 140. Measured currents on August 31, 2006: Rose plot (top), time series plot (bottom).

The depths of the AUV over time are shown in Figure 141. While most of the time the AUV stays in the upper 1.2 m, the 3 m depth was also surveyed for about 10 minutes.

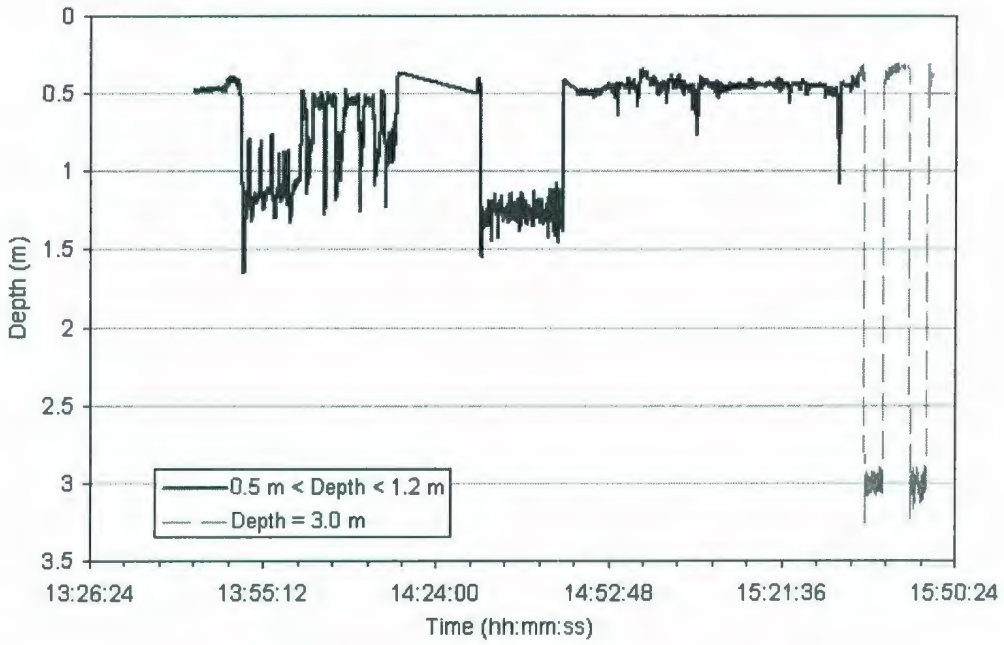

Figure 141. Time series plot of the AUV depth (August 31, 2006).

The measured concentrations over the course of test are plotted in Figure 142. It can be seen that the measured concentration for the study area ranges from 0 to about 273 ppb. By matching the times of Figure 141 and 142, the highest concentration was observed at around 15:12:40 at about 0.47 m depth. This can be confirmed by plotting the concentration versus depth of the AUV (Figure 143). It can be seen from Figure 143 that the majority of the data is in the 0.5 m layer. For the 3 m layer surveyed (as shown in Figure 144), the concentrations range from 0 to about 80 ppb.

As only limited data were collected for other layers, only the data at the 0.5 m layer were used to construct the contour plots (Figures 145 and 146). Figure 145 gives a whole picture of the measured plume while Figure 146 shows more details near the discharge point.

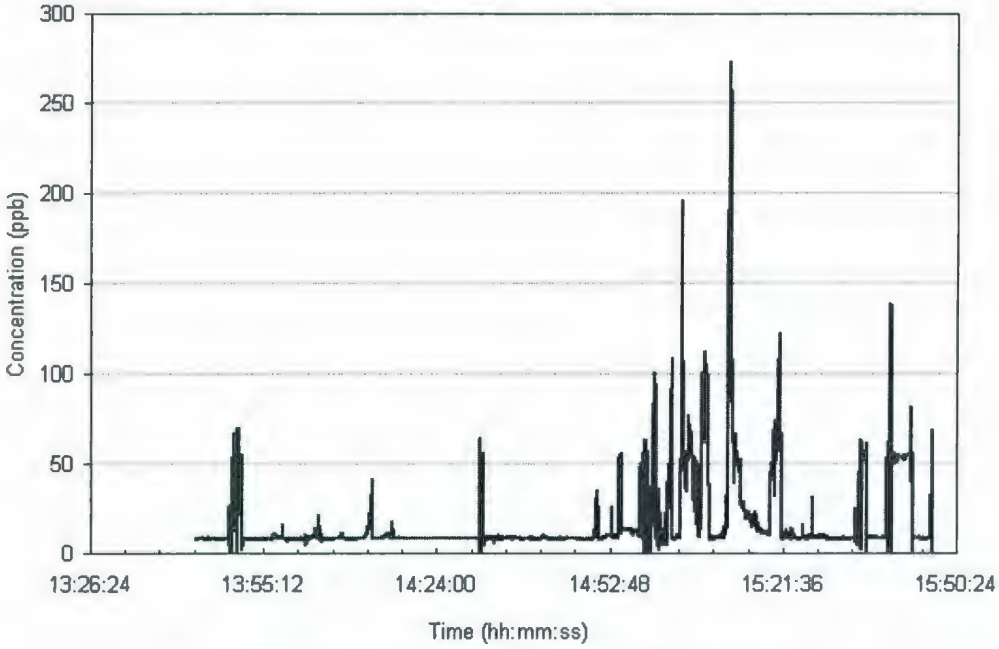

Figure 142. Time series plot of the Rhodamine WT concentration.

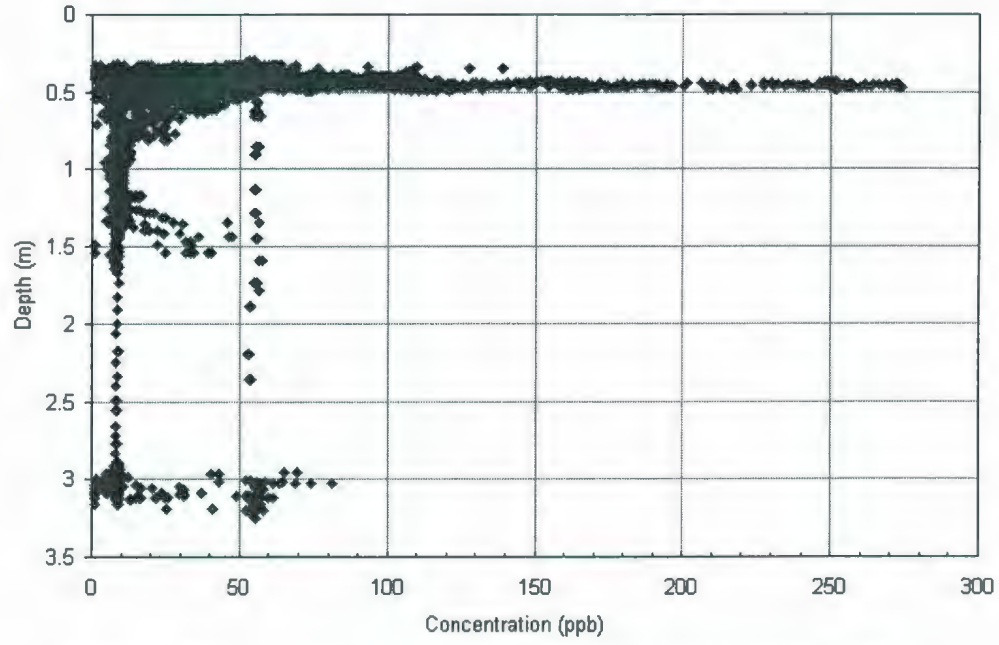

Figure 143. Rhodamine WT concentration versus AUV depth (August 31, 2006).

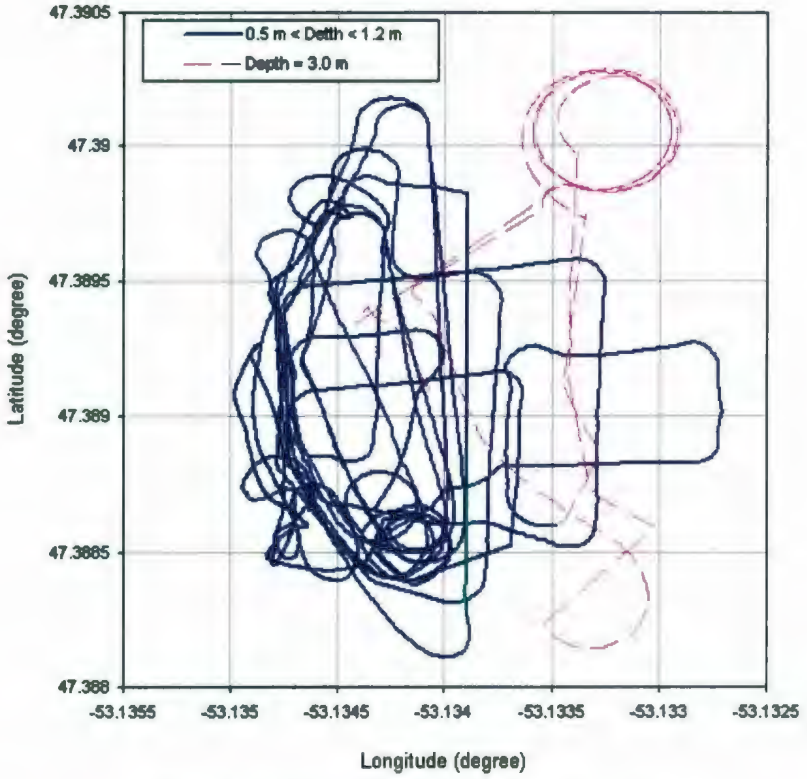

Figure 144. Trajectory of the AUV at different depth.

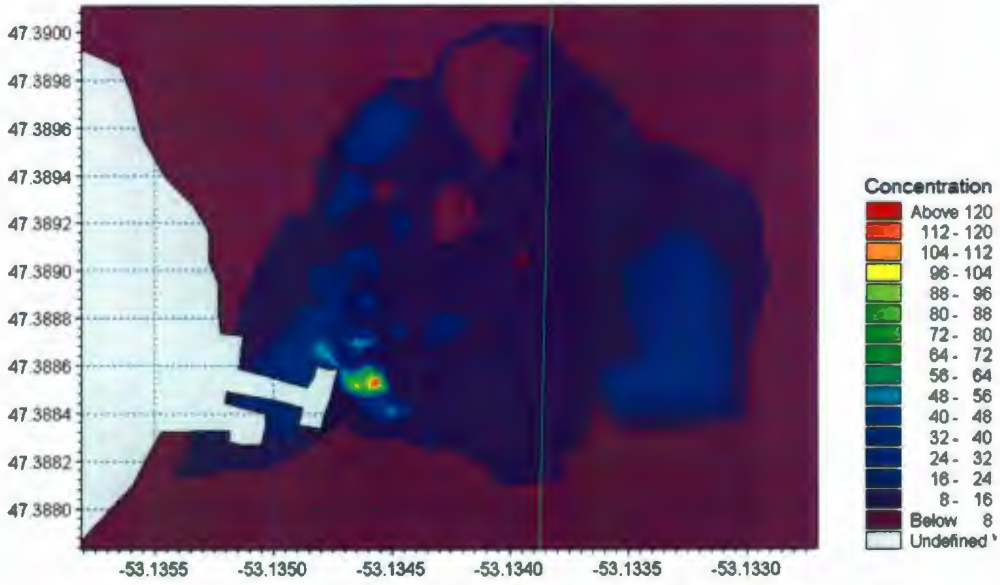

Figure 145. The measured concentration field (large scale)

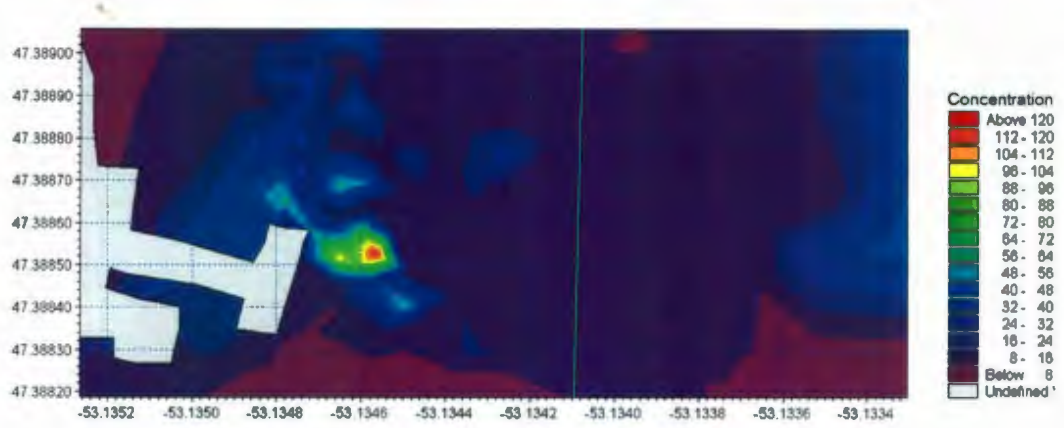

Figure 146. The measured concentration field (small scale).

It can be seen from the contour plots that the AUV was able to map the overall picture of the plume. The plume spread toward the mean current direction - northeast. The highest concentration was measured at the discharge point and decreased toward the plume edge. Similar to the previously described plume mapping tests using a traditional towing method, the plume mapped by the AUV is also not smooth and patchiness was shown. For example, two patches were shown on the north and east edges of the plume.

Test No. 2 - September 7, 2006

The mission time for the second test was about 1 hour and 10 minutes. The area surveyed was about 170 m × 240 m. The vehicle trajectories over the course of the test are shown in Figure 147. As in the August 31 test, an overlapping of the trajectory and the wharf is also present in this case.

The area survey for this test covers both the northeast and southeast of the wharf based on the observation of drifts of surface floats. As in the previous case, a current meter was moored about 10 m away from the discharge point to measure the current information. The current data are plotted in Figure 148. It can be seen from the plot

that the dominant direction is southwest. However, this data is not reliable and may only be used as a reference. The reason is that the current meter was not properly moored and there is an observed drift of the current meter from the initial mooring location.

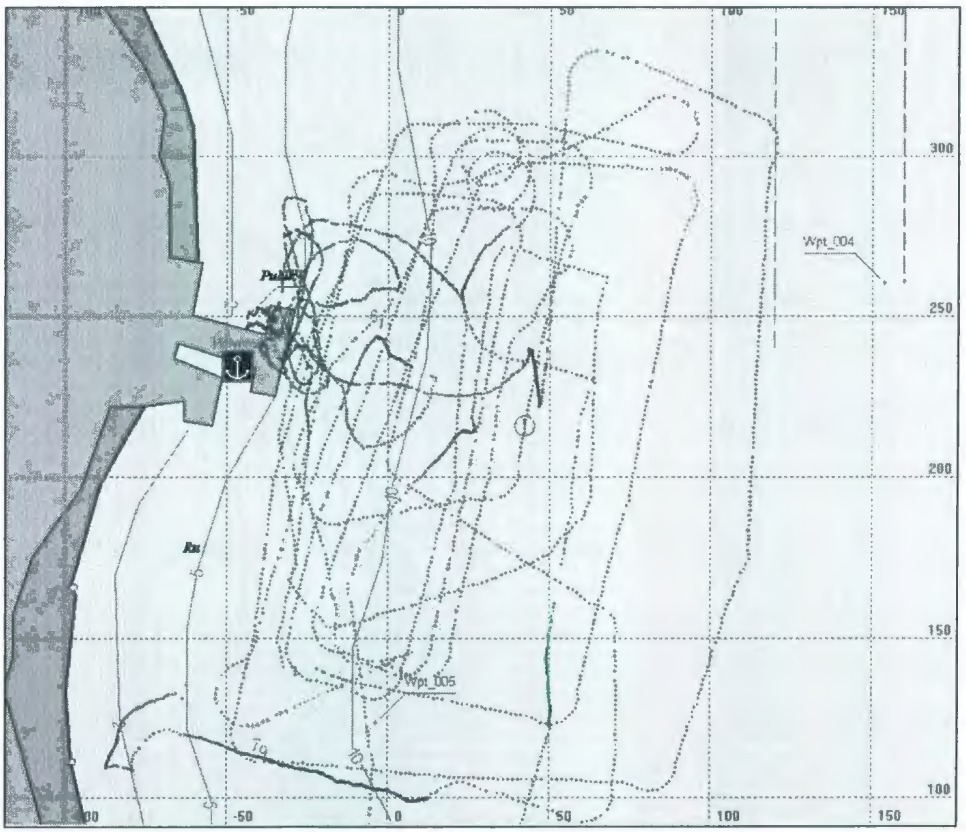

Figure 147. Trajectory of the AUV shown by the *FleetManager* Software (September 7, 2006).

The depths of the AUV over time are shown in Figure 149. The depths of the measurements range from 0.4 m to 1.45 with the majority of the measurements at 0.55 to 0.6 m depth.

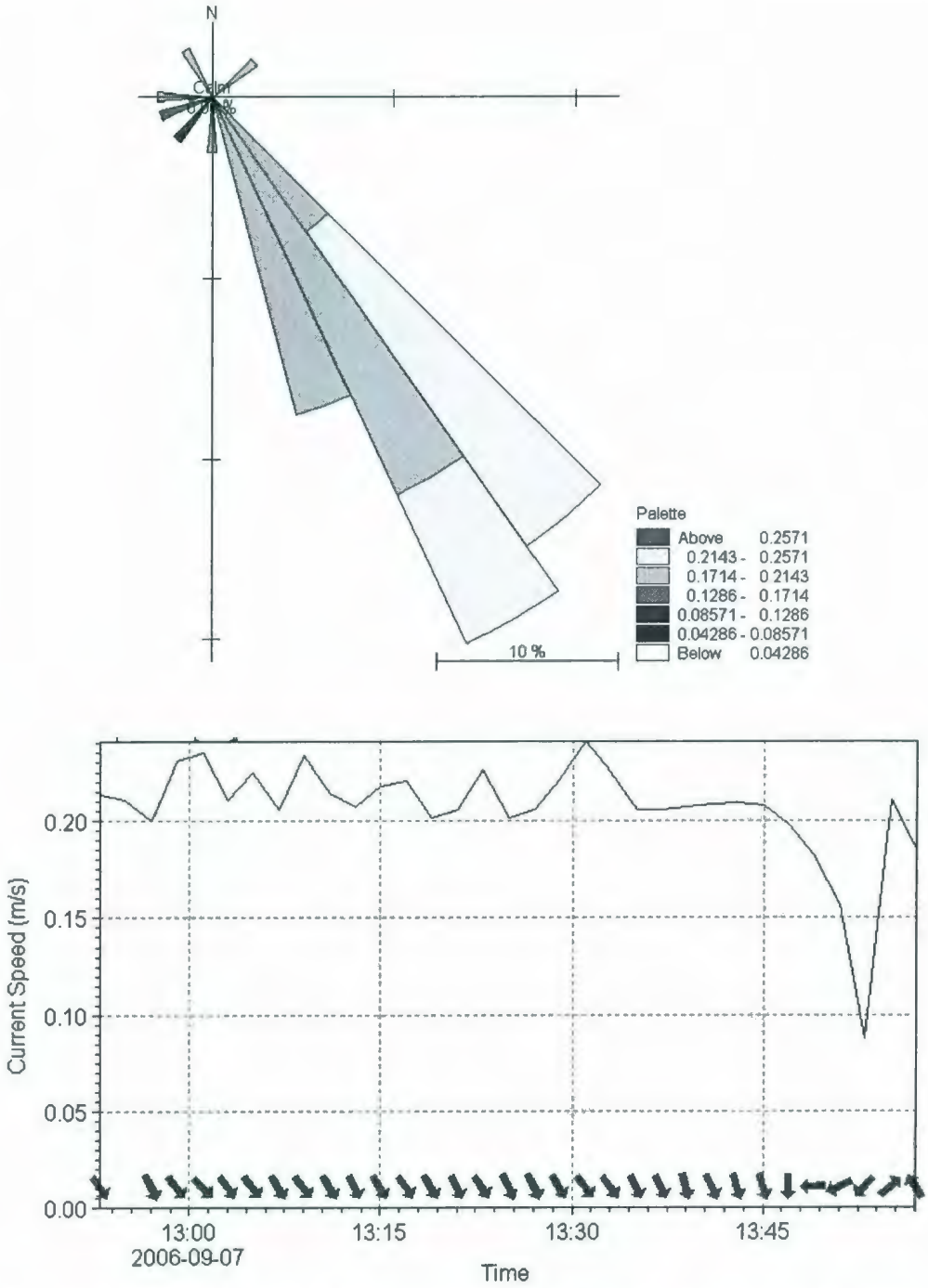

Figure 148. Measured currents on September 7, 2006: Rose plot (top), time series plot (bottom).

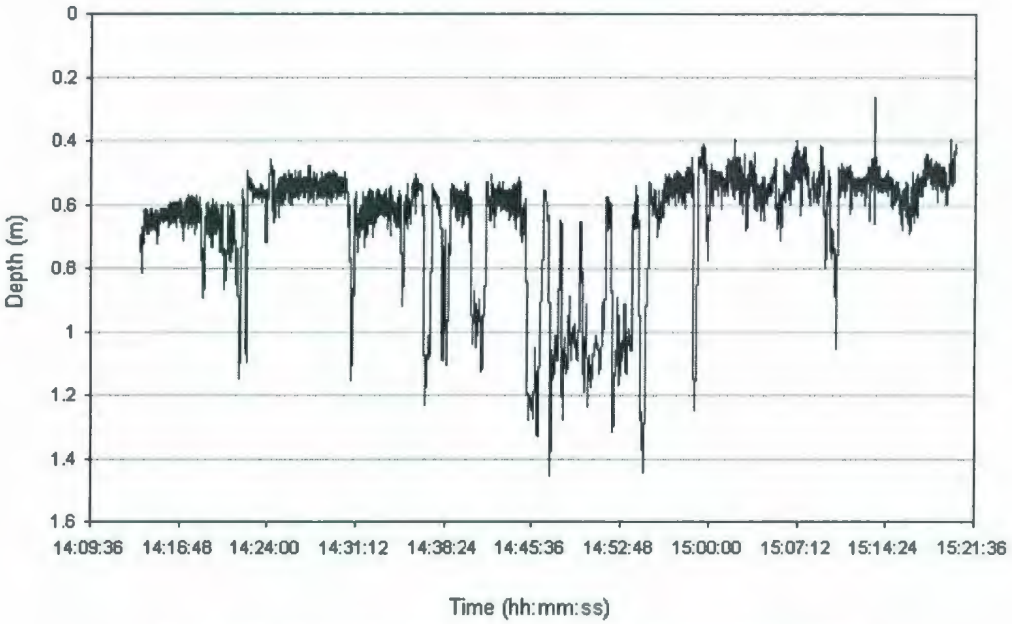

Figure 149. Time series plot of the AUV depth (September 7, 2006).

The measured concentrations over the course of the test are plotted in Figure 150. It can be seen that the measured concentration for the study area ranges from 0 to about 190 ppb. By matching the times of Figure 149 and 150, the highest concentration was observed at around 15:09:00 at about 0.54 m depth. This can be confirmed by plotting the concentration versus depth of the AUV (Figure 151). It can be seen from Figure 151 that the majority of the data is in the 0.5 - 0.6 m layer.

Unlike the August 31 test, the data collected from this test were confined in a 25 cm layer (0.4 - 0.65 m). Therefore, all the data rather than part of the data were used to construct the contour plots (Figures 152 and 153). Figure 152 gives a whole picture of the measured plume while Figure 153 shows more details near the discharge point.

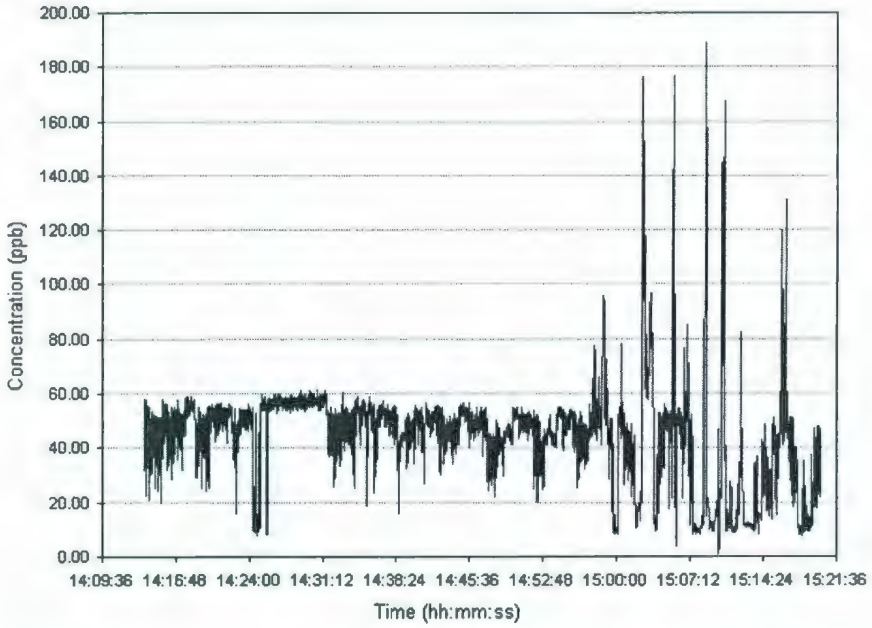

Figure 150. Measured Rhodamine WT concentration with time (September 7, 2006)

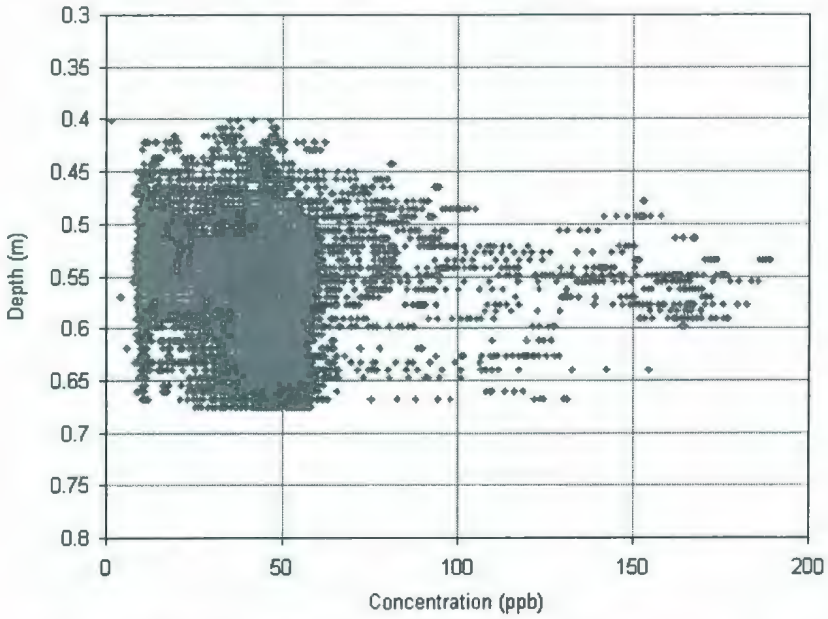

Figure 151. Rhodamine WT concentration versus AUV depth (August 31, 2006).

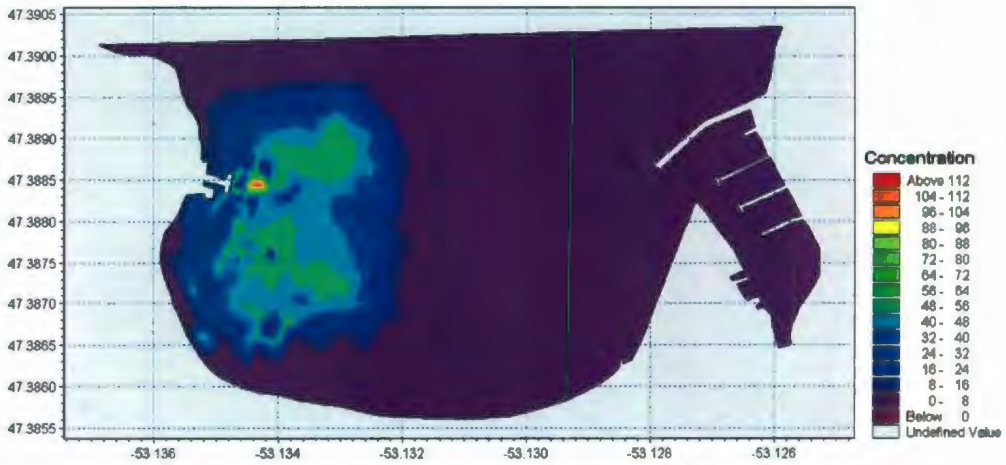

Figure 152. Contour plot of the Rhodamine WT distribution over the study area.

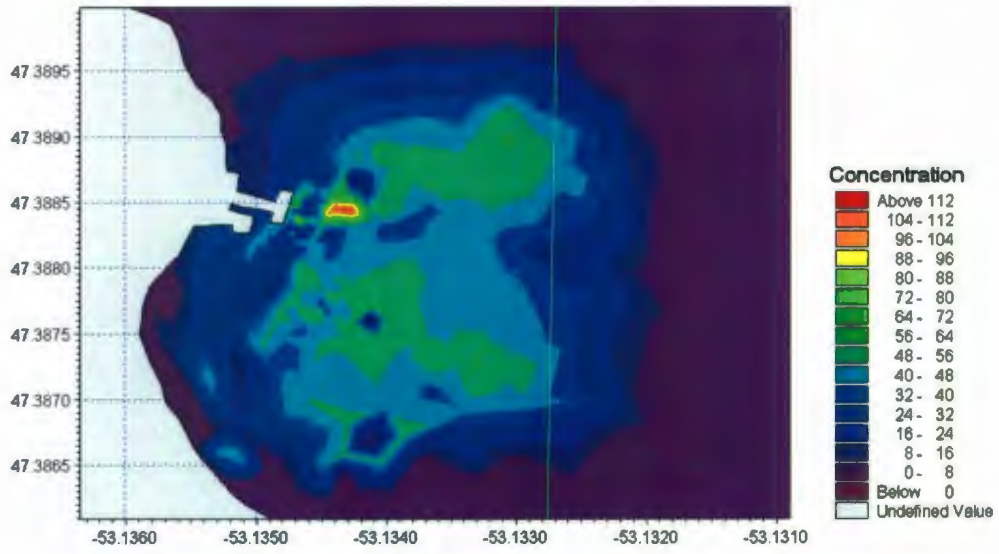

Figure 153. Contour plot of the Rhodamine WT distribution (detailed view)

As in the August 31 test, the contour plots showed that the AUV was able to map the overall picture of the plume. In this second test, the plume spread toward the east. The highest concentration was measured at the discharge point and decreased toward the plume edge. The plume mapped by the AUV for this case is relatively smooth and but still shows patchiness. An interesting pattern shown by the contour is that the plume separated into two centers downstream.

7.3.4 Experience from the Tests

In this study, the MUN Explorer has been used to map a freshwater plume in Holyrood Bay. As this is the first plume mapping mission using this type of AUV, only simple missions were performed. In order to map the plume more effectively and improve the quality of experiments in the future, the following methods are suggested:

- The area survey should be large enough to capture the plume edge. If the farthest points have values greater than zero, the contour beyond these points will be difficult to construct. This is the problem encountered in the present study and an arbitrary edge far away from the plume was assumed.
- The sensors are suggested to be mounted on the bottom of the AUV instead of the side. The reason is that during some surface missions, especially in extreme weather conditions, the sensor may be out of water when the vehicle is trying to maintain position. In these cases, zero values will be collected and this becomes a noise that affects the data quality.
- For the same reason, the AUV depth must be at least 0.7 m if the sensor mounting remains unchanged.
- The present study only mapped one horizontal layer and the advantages of the AUV were not fully used. A longer mission that continually surveys multi-layers is suggested in order to obtain the 3D plume information.
- Due to separated data logging systems, the post-processing was extremely time consuming. The sensor must be integrated to the vehicle and log the data in the same file. This has already been completed after the experiments.

7.4 COMPARISON WITH MODEL PREDICTION

Besides the environmental monitoring, validation of the numerical models is another objective of field studies. However, a detailed validation is often very difficult to perform due to the high degree of uncertainties associated with field measurements. Take the example of most plume mapping studies, where the observed plumes are usually patchy rather than smooth. It is therefore difficult to match the measured concentration with the model prediction, especially the predictions from a steady state model. Although a coupled approach as suggested in chapter 6 may match better with the measurements due to its unsteady nature, this type of modeling approach is generally hard to implement because the available physical oceanography data are often too limited to run the model. Due to this reason, only the measured near field dilution will be compared with the predictions by PROMISE 1 in this study. The comparison described in this section is more qualitative rather quantitative due to many uncertainties.

For the August 31 test, the predicted near field trajectory and dilution are plotted in Figures 154 and 155. The predicted boil point is about 3 m away from the discharge point and the predicted surface dilution is about 83-fold.

As mentioned earlier, the system error of GPS is about 10 m. This error level has been used to offset the measured data to construct the contour. However, the predicted boil point is only 3 m away from the discharge point and this distance is even smaller the system error, therefore the measured boil point has high degree of error and is not reliable. Only the surface dilutions are compared.

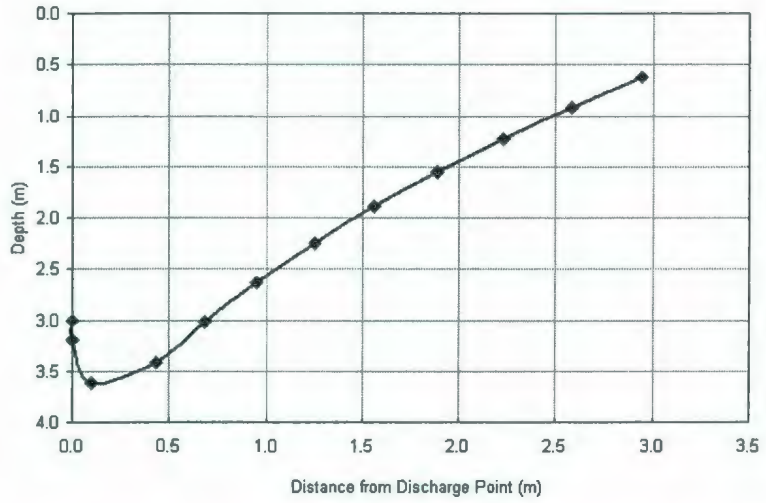

Figure 154. Predicted near field plume trajectory (August 31, 2006).

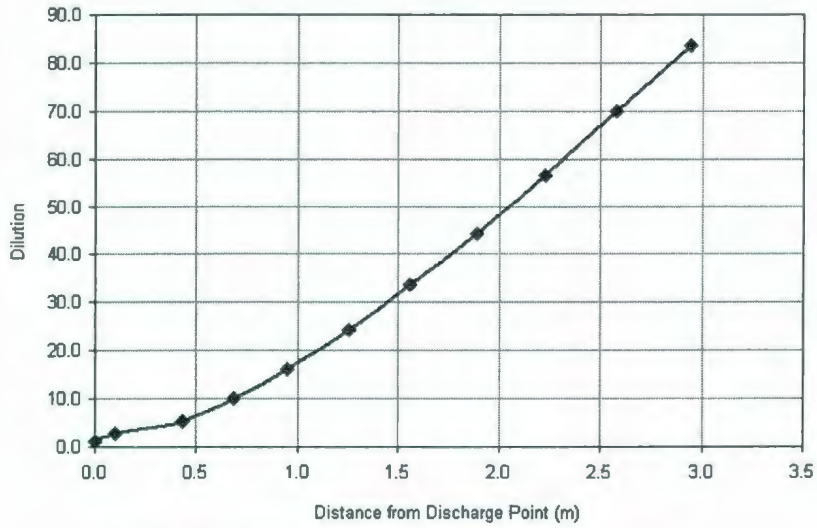

Figure 155. Predicted near field dilution (August 31, 2006).

It was shown by Figures 142 and 143 that the maximum measured concentration is about 273 ppb and this gives a surface dilution of 42. Due to the turbulent nature of the plume, the concentrations are always instantaneous. It is therefore necessary to use the averaged data to give a more representative concentration. The average of 20 highest data at the plume center gives a concentration of 269 ppb and a dilution of 42. This measured dilution of 42 is much smaller than the predicted dilution of 83. There

are a number of reasons that may contribute to this disparity. The main reason may be due to the impacts of wharf. The discharge pipe is close to the wharf and this prevented the plume to continually entrain fresh marine water. The dye may be re-entrained into the plume. Another effect of the wharf is that the currents around it were re-directed and the magnitudes were damped. In both cases, a lower dilution may result.

For the September 7 test, the predicted near field trajectory and dilution are plotted in Figures 156 and 157. The predicted boil point is about 18 m away from the discharge point and the predicted surface dilution is about 333-fold. The dilution predicted is much higher than the August 31 case due to the higher current speed.

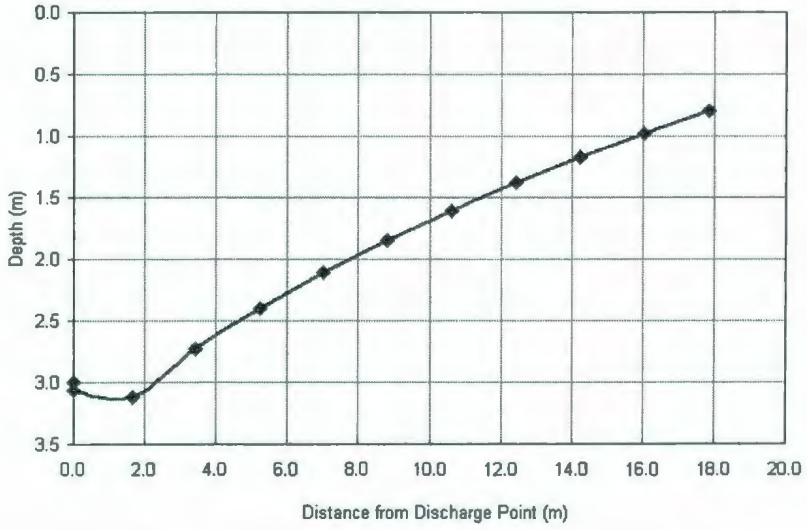

Figure 156. Predicted near field plume trajectory (September 7, 2006).

The measured boil center for this case is about 23 meters from the wharf. Because the discharge pipe is about 4 m away from the wharf and this indicates the measured boil point is about 19 m from the discharge point, which is very close to the predicted

distance of 18 m. Although the two distances agree well, it should be noted there is some error related to the GPS system.

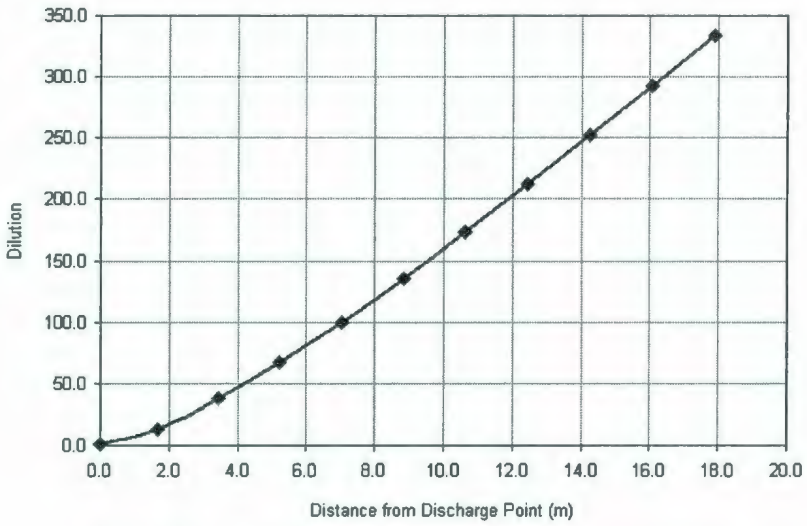

Figure 157. Predicted near field dilution (September 7, 2006).

It was shown by Figures 150 and 151 that the maximum measured concentration is about 192 ppb and this give a surface dilution of 118. As in the previous case, the averaged of 20 highest data were used to give a more representative concentration. The average gives a concentration of 175 ppb and a dilution of 130. This measured dilution of 130 is much smaller than the predicted dilution of 333. Besides the reason described for the previous case that prohibited the dilution, another factor that contributed to this disparity is the current data. A current speed of 0.2 m/s was used in model prediction based on the current meter measurements, however, as mentioned earlier, the current meter data for September 7 was not accurate due to the poor mooring. Due to the high current speed, the dilution has been over-predicted. If a smaller value 0.08 m/s is used, the predicted dilution value of 143 is close to the measured value of 130. A comparison is also give in Table 30.

Table 30. Comparison of Predicted and Measured Data.

Experiment	Parameters	Predicated	Measured
August 31, 2006	Boil	3 m	N/A
	Dilution	83	42
September 7, 2006	Boil	18 m	19 m
	Dilution (u_a=0.2 m/s)	333	130
	Dilution (u_a=0.08 m/s)	143	130

7.5 SUMMARY

In this chapter, several field studies on mapping the produced water and sewage outfalls were first reviewed. Because of the limitations of traditional methods and their high cost, using alternative experiment methods for plume mapping become important. The AUV has been shown as a promising tool for this type of study. The field missions using the MUN Explorer AUV were presented and it can be seen from the results that the horizontal plume profile has been successfully mapped, but this needs to be improved in the future to take the advantage of the AUV and give more detailed information. A full comparison of the model prediction with the measured data was not possible due to the limited information available to run the model. A comparison of the near field prediction with measured data showed that the measured concentrations are higher than predictions. The reasons may be due to the re-entrainment of dye into the plume and also due to the inaccurate input data such as current speeds.

8. CONCLUSIONS

8.1 SUMMARY

In this section, summaries are presented in the context of the scope and purpose of the research, in which the general objective was to develop a methodology for prediction of the dispersion of offshore discharges of produced water in the marine environment. The study has two major components: mathematic modeling and experimental study. The study consisted of four major parts: (1) developing an steady state model which can be used in both deterministic and probabilistic forms; (2) conducting laboratory experiments to validate the near field model and refine the model coefficient; (3) developing a methodology to couple the steady state near field model and non-steady state ocean circulation model to study the large scale and long term dispersion of produced water; (4) conducting field experiments and mapping the outfall using Autonomous Underwater Vehicle.

After a review of the physical basis and state-of-art of presently used models, a steady state model, PROMISE, was proposed in Chapter 3. The model has five sub-models: (1) a near field model which simulates the initial mixing behavior before boundary interaction occurs; (2) a wave effect model which accounts for the effects of both internal and surface waves; (3) a boundary interaction model which may include an upstream intrusion and a downstream control model depending on the impinging angle; 4) a far field dispersion model which models the buoyant spreading and turbulent diffusion process; and (5) a multimedia fate model which simulates the steady state pollutant concentration in multimedia environment. Except the multimedia fate model, which is a direct adoption of an existing model, all other four

sub-models have advantages over other available models. The major advantages of PROMISE are: 1) PROMISE considers the effects of waves on initial dilution, includeing both the effects of surface wave and internal wave; 2) PROMISE uses a unified turbulent diffusion/buoyant spreading model that is more accurate than other models in which separated models are used; 3) PROMISE uses a sea-state dependent vertical mixing formulation while other models either use a constant vertical mixing coefficient or have no vertical effects included; 4) PROMISE can be used for probabilistic based analysis while most other models do not have this capability.

To validate the PROMISE model, extensive experimental data have been collected and compared with the model predictions. It has been found that PROMISE agrees with the experimental data well especially for the dilutions. Compared with other models, PROMISE has better prediction on dilution than on the trajectory. A set of laboratory experiments were performed to further calibrate the PROMISE model and refine the model coefficient. By comparison with the CORMIX model, the measured data are shown to be of good quality. The calibrated PROMISE model predicted the dilution reasonably well with a difference up to 17%.

A hypothetical case study using the PROMISE model was presented in Chapter 5. Two scenarios were evaluated in the study: one with the effect of waves and the other case without the waves. It has been shown by the study that the waves have significant impacts on the dilution. The accumulation of Phenol in fish was also simulated.

To study the long term and far field dispersion, it is important to use a non-steady state model. As the non-steady state model generally cannot resolve the details of near field motion, the coupling of near field model with non-steady state model becomes important. The coupling study of PROMISE with a non-steady state model, MIKE3

was described in chapter 6. The coupling algorithm used was a two way passive offline coupling. It was shown by the three test cases that a minimum grid size must be maintained in order to introduce the source term correctly.

The review of existing field studies showed that a traditional plume mapping can only provide limited information and using alternative experiment methods for plume mapping are needed. The AUV has been shown as a promising tool for this type of study. A field mission using the MUN Explorer AUV for plume mapping has been conducted and the results are presented in Chapter 7. The results show that the horizontal plume profile can be successfully mapped by an AUV. Because only a simple mission was performed in this study, the vertical profile was not mapped and this is suggested for future studies.

8.2 RESEARCH CONTRIBUTIONS

This research has the following contributions:

1. A new steady state model has been developed to model the dispersion of produced water in the marine environment. Different from other existing models, a new entrainment formulation based on extensive experimental data has been used. The new formulation has been proved to give satisfactory prediction of initial dilution.
2. The model is the only model to date that integrated the wave effects on dilution. This included the effects of both internal waves and ocean surface waves. Although it still needs to be improved by take consideration of the wave-current interaction, it provided a preliminary analysis of the wave effects on dilution.

3. A new unified buoyant spreading-turbulent diffusion model has been developed and used in the model system. This is an expansion of a similar model for uniform ambient to more generalized stratified environment. This unified model can give more accurate intermediate field predictions.
4. The proposed model can be used in both deterministic and probabilistic forms. The probabilistic forms consider the uncertainty measures with the model formulation. The approach of providing uncertainty measures to empirical models is not new. However, the present model is a much more comprehensive probabilistic based model and can be used in many more discharge and ambient conditions. The previous models can only be applied to very limited discharge conditions.
5. To validate the model, a laboratory experiment has been performed. Although the concept of the experiment is not new and many similar experiments have been conducted before, the present work was performed in a relatively large scale and the flowrates used in this work were much higher than previous investigations. This is closer to the real field conditions.
6. The PROMISE model has been coupled with a non-steady state MIKE 3 model. A new coupling approach has been used. Different from most of the previous approaches, this approach is a two-way coupling. Although two-way coupling has been used before, the buoyant spreading was not considered before. The present approach is the only two-way coupling method that integrated the buoyant spreading process.
7. In this study, a new generation of oceanography instrument, the MUN Explorer AUV, has been successfully used to map an outfall. This is the first

study that used this type of instrument (vehicle/sensors) for plume mapping in Canada.

8.3 RECOMMENDATIONS

The following recommendations may be useful for future research:

1. Like all other existing models, PROMISE only considered a single water phase. In some platforms, the produced water may mix with significant amounts of air and the effluent becomes two phase flow. Take the example of the produced water discharged from Terra Nova FPSO off the east coast of Canada, where the reported produced water density is 1050 kg/m^3. As the produced water density is higher than the ambient seawater, the produced water discharged vertically downward at 13-20 m depth should descend to the sea bottom. However, the produced water plume is routinely observed at the ocean surface. This is because the sufficient air added prior to discharge provids additional buoyancy that transports a portion of the produced water to the surface (LES, 2006). It is obvious that inaccurate dilution will be predicted by the single phase models in such circumstances. A two phase flow model is needed to handle this type of discharge. Laboratory experiments on saline discharges with different air fractions are recommended.
2. In this study, the PROMISE has been coupled with a three-dimensional hydrodynamic model, MIKE3. The coupling method was a weakly two-way offline coupling. The dynamic interaction between these two models was accounted only after each coupling time-step rather than at each simulation step. This may cause an abrupt change of coupling location and a loss of

accuracy. In order to have better prediction accuracy, an online two-way coupling is needed. However, this method requires a high degree of model integration and this can hardly be implemented with a commercial package, such as MIKE 3. It is recommended that the PROMISE be coupled with a public domain model such as EFDC using an online method. Similar study has been performed by Choi and Lee (2004) but their work needs to be improved by using a near field model such as CORMIX or PROMISE that considers the buoyant spreading process. This coupling process is expected to be extremely difficult.

3. The advantage of PROMISE over other models is its ability to incorporate imprecise information into the model using a probabilistic based approach. The probabilistic based approach considers all uncertainties to be random by assigning a probability distribution to the model parameters. However, not all uncertainties are random and can be objectively quantified (Dou et al., 1997). For example, some uncertainties are due to imprecision and incomplete data, and some are subjective. In this case, the using of fuzzy set theory has proved to be effective. The improvement of PROMISE model with Fuzzy set theory is suggested.
4. The multimedia model used with PROMISE is a simple food chain model. This is a direct adoption of existing model. The model has limited components and does not consider the effects of sediments. Many produced waters have density higher than ambient seawater, and it is likely that those produced water may settle to the bottom and come into contact with the sediments. To evaluate

the impacts of produced water, a multimedia model, for example, a fugacity model, with sediment component will be useful in this case.

5. The PROMISE model need to be further validated, especially for PROMISE2, PROMISE3, and PROMISE4. This can be achieved by conducting field experiments using the MUN Explorer AUV.

REFERENCES

Abraham, G. 1970. "The Flow of Round Jets Issuing Vertically into Ambient Fluid Flowing in a Horizontal Direction," Proceedings of the 5th International Water Pollution Research Conference, San Francisco, July-August, 1970, pp. III 15/1-III 15/7.

Anderson, J. L., Parker, F.L., and Benedict, B. A. 1973. *Negatively Buoyant Jets in a Cross Flow*. EPA-660/2-73-012, U.S. EPA, Washington D.C., October 1973.

Akar, J. P. and Jirka, G.H. 1994. "Buoyant Spreading Processes in Pollutant Transport and Mixing, Part 2: Upstream Spreading in Weak Ambient Current," *Journal of Hydraulic Research*, 33(1):87-100.

ALT, C. V. 2003. "Autonomous Underwater Vehicles," in: *ALPS: Autonomous and Lagrangian Platforms and Sensors Workshop,* La Jolla, California, U.S, 31 March- 2 April, 2003.

Ayoub, G.M. 1971. *Dispersion of Buoyant Jets in a Flowing Ambient Fluid.* Ph.D. Thesis. University of London, London, U.K.

Baumgartner, D.J., W.E. Frick, P.J.W. Roberts, 1994. *Dilution Models for Effluent Discharges*, 3rd Edition, U.S. Environmental Protection Agency, EPA/600/R-94/086, June 1994.

Baumgardner, J. Malone, C., Walker, L. F., and Shanks, R. F. 1993. "Use of Monte Carlo Techniques to Assess POTW Compliance with EPA Water Quality Criteria for Heavy Metals," *Water Environment Research*, 65(5):674-678.

Barilla, P. A. 1968. *Dependance of Entrainment Coefficients Upon Orifice Conditions in Model Studies of a Smoke Plume in a Laminar Cross Wind.* M.S. Thesis. Massachusetts Institute of Technology, Cambridge, MA, U.S.A.

Benjamin, T. B. 1967. "Gravity Currents and Related Phenomena," *Journal of Fluid Mechanics*, Vol. 31, Part 2.

Berry, J.A., and Wells, P.G. 2005. "Environmental Modeling of Produced Water Dispersion with Implications for Environmental Effects Monitoring Design," in: *Offshore Oil and Gas Environmental Effects Monitoring: Approaches and Technologies*, Armsworthy, S. et al. (Eds), Battelle Press, pp. 111-130.

Bleninger, T. and Jirka, G. "Coupling Hydrodynamic Models for Multi-port Diffusers: Design and Control Techniques for Submarine Outfalls," in: *Proceedings of the MWWD-IEMES 2006 Conference*, Antalya, Turkey, November 6-10, 2006.

Brandsma, M.G., Davis, L., Ayers R., and Sauer, T. 1980. "A Computer Model to Predict the Short Term Fate of Drilling Discharges in the Marine Environment," In: *Proceedings of Symposium on Environmental Fate and Effects of Drilling Fluids and Cuttings*. Jan 21-24, 1980, Lake Buewna vista, FL, U.S.A.

Brandsma, M.G., Davis, L., Ayers R., and Sauer, T. 1992. "Modeling Offshore Discharges of Produced Water," In: *Produced Water*, Ray, J.R. and Engelhart, F.R. (Eds), Plenum Press, NY, U.S.A.

Brandsma, M.G., and Smith, J.P., 1996. "Dispersion Modeling Perspectives on the Environmental Fate of Produced Water," In: *Produced Water 2: Environmental Issues and Mitigation Technologies* (Edited by M. Reed and S. Johnsen), Plenum Press, New York, pp. 215-224.

Britter, R. E., and Simpson, J. E. 1978. "Experiments on the Dynamics of a Gravity Current Head," *Journal of Fluid Mechanics*, 88:209-248.

Brown, I. 1984. *Preliminary Investigations of the performance of an Ocean Outfall Diffuser in a Crossflow*. Report 84-5, University of Canterbury, Christchurch, New Zealand.

Cavola, R.G. 1982. *An Experimental/Analytical Investigation of Negtively Buoyant Jets Discharged Vertically Upward into a Crossflow Current*. M.S. Thesis, Oregon State University, Corvallis, OR, U.S.A.

Carvalho, J. L. B., Roberts, P.J.W., and Roldao, J. 2002. "Field Observations of Ipanema Beach Outfall," *Journal of Hydraulic Engineering*, ASCE, 128(2):151-160.

Cheung, V. 1991. *Mixing of a round buoyant jet in a current*. Ph.D. Theis, University of Hong Kong.

Chin, D. A. 1987. "Influence of surface Waves on Outfall Dilution," *Journal of Hydraulic Engineering*, 113(8):1006-1018.

Chin, D. A. 1988. "Model of Buoyant-Jet-Surface-Wave Interaction," *Journal of Waterway, Port, Coastal, and Ocean Engineering*, 114(3): 331-345.

Choi, K.W, Lee, J. H. W. 2005. "A New Approach to Effluent Plume Modelling in the Intermediate Field," in: *Proceedings of the 31st IAHR Congress*, Seoul, Korea, September 11-16, 2005, Pages 4303-4311.

Chu, V.H., and Goldberge, M.B. 1974. "Buoyant Forces Plumes in Cross Flow," *Journal of the Hydraulics Division*, ASCE, 100(HY9):1203-1214.

Chu, V. H. 1975. "Turbulent Dense Plumes in a Laminar Cross Flow," *Journal of Hydraulic Research*, 13(3):263-279.

Chyan, J.M., and Hwung, H.H. 1993. "On the Interaction of a Turbulent Jet with Waves," *Journal of Hydraulic Research*, 31(6):791-810.

Chyan, J.M., Hwung, H.H., Chang, C.Y., and Chen, I.P. 2002. "Effects of Discharge Angles on Dilution of Buoyant Jet in Wave Motions," In: *Porceedings of the 5th International Conference on Hydrodynamics*, Oct 31-Nov2, 2002, Tainan, Taiwan, 485-490.

CORMIX. 2007. http://www.cormix.info

Csandy, G. T. 1973. *Turbulent Diffusion in the Environment*. D. Reidel Publishing Company.

Davidson. 1989. *The Behaviour of Single and Multiple, Horizontally Discharged, Buoyant flows in a Non-Turbulent Crossflowing Ambient Fluid*. Ph.D. Thesis. University of Canterbury, Christchurch, New Zealand.

Doneker, R.L., and G.H. Jirka, 1990. *Expert System for Hydrodynamic Mixing Zone Analysis of Conventional And Toxic Submerged Single Port Discharges (CORMIX1)*, U.S. Environmental Protection Agency, EPA/600/3-90/012, February 1990.

Donigian, A., and Waggy, W. H. 1974. "Simulation-A Tool for Water Resource Management," *Water Resource Bulletin*, 10(2):229-244.

Dou, C. Woldt, W., Bogardi, I., and Dahab, M. 1997. "Numerical Solute Transport Simulation Using Fuzzy Sets Approach," *Journal of Contaminant Hydrology*, 27(1):107-126.

Dunn, W. E., Leylak, J. A., Chittenden, R. M. 1982. "A Laboratory Study of Buoyant Jets in Crossflow," in: *International Association of Hydraulic Research Cooling Tower Workshop*, Budapest, Hungary, October, 1982.

Fan, L-N. 1967. *Turbulent Buoyant Jets into Stratified or Flowing Ambient Fluids*. Report No. KH-R-15, California Institute of Technology, Pasadena, CA, U.S.

Fan, L-N, and Brooks, N.H. 1969. *Numerical Solutions of Turbulent Buoyant Jet Problems*. Report KH-R-18, California Institute of Technology, Pasadena, CA, U.S.A.

Farrell, J. A., Pang, S., and Li, W. 2005. "Chemical Plume Tracing Via an Autonomous Underwater Vehicle," *IEEE Journal of Oceanic Engineering,* Vol. 30, No. 2, pp.428-442, 2005.

Fennel, W. and T. Neumann (2001). "Coupling Biology and Oceanography in Models," *Ambio*, 30(4-5): 232-236.

Fletcher, B. 2001. "Chemical Plume Mapping with an Autonomous Underwater Vehicle," In: *Proceedings of the MTS/IEEE Oceans 2001 Conference,* Honolulu, U.S., 5-8 November, 2001.

Ferrier, A., Funk, D., and Roberts, P.J.W. 1993. "Applications of Optical Techniques to the Study of Plumes in Stratified Fluids." *Dynamics of Atmospheres and Oceans*, 20:155-183.

Fernandes, P.G., Brierley, A. S., Simminos, E. J., Millard, N. W., McPhail, S.D., Armstrong, F., Stevenson, P., and Squires, M. 2000. "Fish Do Not Avoid Survey Vessels," *Nature*, Vol. 404, pp.35-36, 2000.

Gaskin, S. 1995. *Single Buoyant Jets in a Crossflow and the Advected Line Thermal.* Ph.D. Thesis. University of Canterbury, Christchurch, New Zealand.

Ger, A. M. 1979. "Wave Effects on Submerged Buoyant Jets," in: *Proceedings of the 18th IAHR Congress*, September 10-14, 1979, Cagliari, Italy, 295-300.

Golubeva, V. N. 1963. "The Formation of the Temperature Field in a Stratified Sea," *Bulletin of the Academy of Science of the USSR, Geophysical Series* (Translated by Goodspeed, F.) No. 5, 4670-4671.

Griffiths, G. 1997. "Ocean Science Applications for Autonomous Underwater Vehicles – the Workplan for AUTOSUB-1 for 1997-2000 and Beyond," *Unmanned Underwater Vehicle Showcase,* Southampton, U.K., September 1997.

Griffiths, G., Millard, N.W., McPhail, S.D., Stevenson, P., Perret, J.R., Pebody, M., Webb, A.T., and Meldrum, D. T. 1998. "Towards Environmental Monitoring with the

AUTOSUB Autonomous Underwater Vehicle," in: *Proceedings of the IEEE Underwater Technology '98 Conference,* Tokyo, Japan, April, 1998.

Griffiths, G., Millard, N.W., McPhail, S.D., Stevenson,, P., Brierley, A. S., Fernandes, P G, Smeed, D. A., Stansfield, K., Thorpe, S. A., Osborn, T., Farmer, D. M., Statham, P. J., Connelly D. P., German, C.R., Cunningham, A., and Burkill, P. 2001. "Standard and Special: Sensors used During the Autosub Science Missions Programme," in: *Symposium on Sensors and Autonomous Underwater Vehicles,* Miami Beach, Florida, U.S., 4 April, 2001.

Hillebrand, G. 2003. *Coupling of Near- and Far-Field Models for Prediction of Treated Sewage Effluent Discharges into the Coastal Ocean.* Diploma Thesis. Universität Karlsruhe, Germany.

Hodgins, D. O. 1993. *Hibernia Effluent Fate and Effects Modeling.* Report prepared for Hibernia Management and Development Company Ltd. By Seaconsult Marine Research Ltd. Nov 1993.

Hodgins, D.O. and Hodgins, S.L.M. 2000. *Modelled Predictions of Well Cuttings Deposition and Produced water Dispersion for the Proposed White Rose Development.* Seaconsult Marine Research Ltd. June 2000.

Holly, F.M. and Grace, J.L. 1972. "Model Study of Dense Jet In Flowing Fluid," *Journal of the Hydraulics Division,* ASCE, 98(HY11):1921-1933.

Holley, E. R., and Jirka, G. H. 1985. *Mixing and Solute Transport in Rivers.* Report E-85, U.S. Army Engineer Waterways Experiment Station, Vicksburg, U.S.

Hoult, D.P., and Weil, J.C., (1972). "Turbulent Plume in a Laminar Cross Flow," *Atmospheric Environment,* 6:513-531.

Huang, H., and Fergen, R.E. 1996. "OZMA-A Computer Model for Deterministic and Probabilistic Outfall Mixing Zone Analysis," In: *Proceedings of WEFTEC'96 :69th annual Conference & Exposition,* Oct 5-9, 1996, Dallas, TX, pages 305-316.

Huang, H, Fergen, R. E., Proni, J. R., and tsai, J. J. 1996. "Probabilistic Analysis of Ocean Outfall Mixing Zones," *Journal of Environmental Engineering,* ASCE, 122(5):359-366.

Huang, H. and Fergen R. E. 1997. "A Model for Surface Plume Dispersion in an Ocean Current," *Proceedings of the 27th Congress of the International Association for Hydraulics Research, Water Resources Engineering Division,* August 10-15, 1997, San Francisco, CA, U.S.

Hwang, R.R., Yang, W.C., and Chiang, T.P. 1996. "Effect of Surface Waves on a Buoyant Jet," *Journal of Marine Environmental Engineering,* 3:63-84.

Hwung, H.H, Chyan, J.M., Chang, C.Y., and Chen, Y.F. 1994. "The Dilution Processes of Alternative Horizontal Buoyant Jets in Wave Motion," In: *Proceedings of the 24th International Coastal Engineering Conference,* Oct 23-28, 1994, Kobe, Japan, pages 3045-3059.

Jirka, H. H., Abraham, G., and Harleman, D. R. F. 1975. *An Assessment of Techniques for Hydrothermal prediction,* Massachusetts Institute of Technology for U.S. Nuclear Regulatory Commission.

Jirka, G. H., and Akar, P. J. 1991. "Hydrodynamic Classification of Submerged Multiport-Diffuser Discharges," *Journal of Hydraulic Engineering*, ASCE, 117(9):1095-1112.

Jirka, G. H., and Arita, M. 1987. "Density Currents on Density Wedges: Boundary-layer Influence and Control Methods," *Journal of Fluid Mechanics*, 177:187-206.

Jirka, G. H., 2004. "Integral Model for Turbulent Buoyant Jets in Unbounded Stratified Flows, Part I: Single Round Jet," *Environmental Fluid Mechanics*, 4(1): 1-56.

Jones, J. M., Jirka, G. H., and Caughey, D. A. 1983. *Numerical techniques for Steady Two-Dimensional Transcritical Stratified Flow Problems, with an Application to the Intermediate Field Dynamics of Ocean Thermal Energy Conservation Plants*, Technical Report, School of Civil and Environmental Engineering, Cornell University, Ithaca, New York, U.S.

Kim, Y. D., Seo, I. W., Kang, S. W. Oh, B. C. 2002. "Jet Integral-Particle Tracking Hybrid Model for Single Buoyant Jets," *Journal of Hydraulic Engineering*, ASCE, 128(1): 753-760.

Knudson, M. 1988. *Buoyant Horizontal Jets in an Ambient Flow*. Ph.D. Thesis. University of Canterbury, Christchurch, New Zealand.

Koole, R., and Swan, C. 1994. "Dispersion of pollution in a wave environment," in: *Proceedings of the 24th International Coastal Engineering Conference*, Oct 23-28, 1994, Kobe, Japan, 3071-3085.

Kotsovinos, N. E. 1978. Dilution in a Vertical round Buoyant Jet, *Journal of Hydraulic Division*, ASCE, 104(HY5):795-798.

Lee, J. H. W., and Cheung, V. 1990. "Generalized Lagranfian Model for Buoyant jets in Currents," *Journal of Environmental Engineering*, ASCE, 116(6): 1085-1106.

Lee, J.H.W., and Cheung, V. 1991. "Mixing of Buoyant Dominated Jets in Weak Current," in: *Proceedings of the Institute of Civil Engineers*, Part 2, 91:113-129.

Lee, J. H. W., and Chu, V. H., 2003. *Turbulent Jets and Plumes: A Lagrangian Approach*, Kluwer Academic Publishers.

Lee, J. H. W., and Neville-Jones, P. 1987. "Initial Dilution of Horizontal Jet in Crossflow," *Journal of Hydraulic Engineering*, ASCE, 113(5):615-629.

Lee, J. H.W. 1989. "Note on Ayoub's Data of Horizontal Round Buoyant Jet in Current," *Journal of Hydraulic Engineering*, ASCE, 115(7):969-975.

Li, S., and Hodgins, D. O. 2004. "A Dynamically Coupled Putfall Plume-Circulation Model for Effluent Dispersion in Barrard Inlet, BC," *Journal of Environmental Engineering Science*, 433-449.

Lorax Environmental Service, Ltd (LES). 2006. A Rhodamine Dye Study of the Dispersion of Produced water Discharge from the Terra Nova FPSO. Lorax Environmental service Ltd, Vancouver, BC, Canada.

Luketina, D. A. and Imberger, J. 1987. "Characteristics of a Surface Buoyant Jet," *Journal of Geophysical Research*, 92(C5):5435-5447.

Mukhtasor. 2001. *Hydrodynamic Modeling and Ecological Risk-Based Design of Produced Water Discharge from an Offshore Platform.* Ph.D. Thesis, Memorial University of Newfoundland, St.John's, NL, Canada.

Nedwed, T.J., Smith., J.P., Brandsma, M.G. 2001. "Validation of the OOC Mud and Produced Water Discharge Model Using Lab-scale Plume Behavior Experiments," in: 5th International Marine Environmental Modeling Seminar, Oct 9-11, 2001,New Orleans, Louisiana, U.S., pp. 229-250.

Neff, J. M. 2002. *Bioaccumulation in Marine Organisms: Effect of Contaminants from Oil Well Produced Water.* Elsevier Science Ltd.

Neff, J., Lee, K., and DeBlois, E. M. 2007. "Produced Water: Overview of Composition, Fates, and Effects," in: International Produced Water Conference, Oct 17-18, 2007, St. John's, NL, Canada.

OLF, The Norwegian Oil Industry Association. 2004. *Fact sheet from OLF - Zero discharges*, http://www.olf.no/?24066.pdf, December, 2004. Stavanger, Norway.

Orlob, G. T. 1959. "Eddy Diffusion in Homogeneous Turbulence," *Journal of Hydraulic Division*, ASCE, Vol 85, No.9.

Pantokratoras, A. 1999. "Vertical Penetration of Inclined Heated Water Jets Discharged Downwards," *Journal of Environmental Engineering*, ASCE, 125(4):389-393.

Pantokratoras, A. 2002 "Vertical Penetration of Double-Diffusive Water Plumes Discharged Vertically Downward," *Journal of Hydraulic Engineering*, ASCE, 129(7):541-545.

Papanicolaou, P.N. and List, E.J. 1988. "Investigations of Round Vertical Turbulent Buoyant Jets," *Journal of Fluid Mechanics,* 195:341-391.

Pennell, V., Veitch, B., Hawboldt, K, Husain, T., Bose, N., Eaton, G., Ferguson, J. 2003. "Use of an Autonomous Underwater Vehicle for Environmental Effects Monitoring", in: *13th International Symposium on Unmanned Untethered Submersible Technology*, 24 to 27 August 2003, Durham, New Hampshire.

Petrenko, A.A., Jones, B.H., and Dickey, T.D. 1998. "Shape and Initial Dilution of Sand Island Hawaii Sewage Plume," *Journal of Hydraulic Engineering*, ASCE, 124(6): 565-571.

Pincince, A.B. and List, C.L. 1973. "Disposal of Brine into an Estuary," *Journal of Water Pollution Control Federation*, 45(11)2335-2344.

Proni, J. R., Huang, H., Dammann, W.P. 1994. "Initial Dilution of Southeast Florida Ocean Outfalls," *Journal of Hydraulic Engineering*, ASCE, 120(12):1409-1425.

Ramos, P., Neves, M.V., Pereira, F. L., Quintaneiro, I. 2002. "Mapping the Aveiro Sea Outfall Plume: Sampling Strategy for an Autonomous Underwater Vehicle," in: *2nd International Conference on Marine Wastewater Discharges,* Istanbul, Turkey, 16-20 September, 2002.

Reed, M., S. Johnsen, A. Melbye, and H. Rye, 1996. "PROVANN: A Model System for Assessing Potential Chronic Effects of Produced Water," In: *Produced Water 2: Environmental Issues and Mitigation Technologies* (Edited by M. Reed and S. Johnsen), Plenum Press, New York, pp. 317-330.

Reed, M., Johnsen, S., Karman, C., Giacca, D., Gaudebert, B., Utvik, T. R., and Sanni, S. 2001. "DREAM: A Dose-Related Exposure Assessment Model, Technical Description of Physical-Chemical Fates Components," in: *5th International Marine Environmental Modeling Seminar,* 9-11 October, 2001, New Orleans, U.S.

Riddle, A.M., 1993. *Program Setup and User Manual: TRK Water Quality Model*, Brixham Environmental Laboratory, Manual SW111/U, UK.

Roberts, P. J. W. 1999. "Modeling Mamala Bay Outfall Plumes. II: Far Field," *Journal of Hydraulic Engineering*, ASCE, 125(6):574-583.

Roberts, P. J. W., Ferrier, A., and Daviero, G. (1997). "Mixing in Inclined Dense Jets," *Journal of Hydraulic Engineering, ASCE*, 123(8): 693-699.

Roberts, P. J. W. and G. Toms (1986). "Inclined Dens Jets in Flowing Current," *Journal of Hydraulic Engineering, ASCE*, 113(3): 323-341.

Rodi, W. 1980. *Turbulence Models and Their application in Hydraulics – A State of Art Review*. IAHR-Section on Fundamentals of Division II: Experimental and Mathematical Fluid Dynamics, Rotterdam: International Association for Hydraulic Research.

Sabeur, Z.A., Tyler, A.O., Hockley, M.C. 2000. "Development of Particle Based Modelling Concepts for the Simulation of Jet and Plume Like Discharges," in: *Hydraulic Engineering Software VIII*, Blain, W.R. and Brebbia, C.A. (eds), WIT Press, Pages 337-345.

Sabeur, Z.A., and Tyler, A.O., 2001. "Validation of the PROTEUS Model for the Physical Dispersion, Geochemistry and Biological Impacts of Produced Waters," In *Proceedings of the 5th International Marine Environmental Modeling Seminar*, Oct 9-11, 2001, New Orleans, Louisiana, USA, Pages 209-228.

Shuo, N. and Ti, L. H. 1974. "Wave Effects on Buoyant Plumes," In: *Proceedings of the 14th Coastal Engineering Conference*, June 24-28, 1974, Copenhagen, Denmark, 2199-2208.

Sharp, J.J. 1986. "The Effect of Waves on Buoyant Jets," *Proceedings of the Institute of Civil Engineers*, Part 2, 81:471-475.

Smith, J. P., Mairs, H.L., Brandsma, M.G., Meek, R.P., and Ayers, R.C. 1994. "Field Validation of the Offshore Operators Committee (OOC) Produced Water Discharge Model," in: *SPE Annual Technical Conference*, Sep 25-28, 1994, New Orleans, U.S.,pp. 519-530.

Smith, M.R., Gore, D., Flynn, S.A., Vance, I., and Stagg, R. 1996. "Development and Appaisal of a Particle Tracking Model for the Dispersion of Produced Water Discharged from an Oil Production Platform in the North Sea," in: *Produced Water 2: Environmental Issues and Mitigation Technologies* (Edited by M. Reed and S. Johnsen), Plenum Press, New York, pp. 225-245.

Smith, J. P., M. G. Brandsma, Nedwed, T. J. (2001). "Field validation of the offshore operators committe (OOC) mud and produced water discharge model," In: *The 5th International Marine Environmental Modeling Seminar*, Oct 9-11, 2001 New Orleans, Louisiana, USA, pp173-192.

Statham, P. J., Connelly, D. P., German, C. R., Brand, T., Overnell, J. O., Bulukin, E., Millard, N., McPhail, S., Pebody, M., Perrett, J., Squires, M., Stevenson, P. and Webb, A. 2005. "Spatially Complex Distribution of Dissolved Manganese in a Fjord as Revealed by High-Resolution in Situ Sensing Using the Autonomous Underwater Vehicle Autosub," *Environmental Science and Technology,* 39(24):9440-9445, 2005.

TAMU. 2007. http://stommel.tamu.edu/~baum/ocean_models.html

Tate, P. M. 2002. *The Rise and Dilution of Buoyanct Jets and their Behavior in an Internal Wave Field*, Ph.D. Thesis, School of Mathematics, University of New South Wales, Australia.

Transport Development Centre (TDC). 1991. Wind and Wave Climate Atlas, Vol. 1, The East Coast of Canada, prepared by MacLaren Plansearch Limited for Transport Development Centre, Transport Canada, March 1991.

Terrens, G. W. & Tait, R. D. 1993. *Effects on the Marine Environment of Produced Formation Water Discharges from ESSO/BHPP's Bass Straight Platforms*. ESSO Australia Ltd. Melbourne, Australia. 25 pp.

Tian, X. 2002. *3DLIF and Its Applications to Studies of the Near Field Mixing in Wastewater Discharges*. Ph.D. Thesis. Georgia Institute of Technology, Atlanta, GA, U.S.A.

Tong, S.S., and Stolzenbach, K. D. 1979. *Submerged Discharges of Dense Effluent*. Report No.243, Ralph M. Parsons Laboratory, Massachusetts Institute of Technology, Cambridge, MA, U.S.A.

Tsanis, I. K., and Valeo, C. 1994. *Mixing Zone Models for Submerged Discharges*. Computational Mechanics Publications, Boston.

Ulasir, M. and Wright, S.J. 2003. "Influence of Downstream Control and Limited Depth on Flow Hydrodynamics of Impinging Buoyant Jets," *Environmental Fluid Mechanics*, 3(2):85-107.

U.S. Army Corps of Engineers. 1984. *Shore Protection Manual*, Vol. I., 4th Edition.

Viollet, M. P. L. 1979. *A Study of Jets in Cross-currents and Stratified Media*. Translated by Argonne NationalLaboratory, Argonne, Illinois, from Electricite de France, February, 1979.

Wadhams, P., Wilkson, J. P., and McPhail, S. D., 2006. "A New View of the Underside of Arctic Sea Ice," *Geophysical Research Letters,* Vol. 33, 2006.

Webster, D.R., Roberts, J.P.W., and Raad, L. 2001. "Simultaneous DPTV/PLIF Measurements of a Turbulent Jets," *Experiments in Fluids*, 30(1):65-72.

Weil, J. C. 1968. *Model Experiments of High Stack Plumes*. M.S. Thesis. Massachusetts Institute of Technology, Cambridge, MA, U.S.A.

Wernli, R.L., 2000. "AUV Commercialization – Who's Leading the Pack?," in: *Proceedings of Oceans 2000 MTS/IEEE Conference and Exhibition,* Providence, Rhode Island, Vol. 1, pp. 391-395, September 11-14, 2000.

Wright, S. J. 1977a, "Mean Behaviour of Buoyant Jets in a Crossflow," *Journal of the Hydraulics Division*, ASCE, 103(HY5): 499-513.

Wright, S. J. 1977b, *Ambient Crossflow and Density Stratification on the Characyeristic Behaviour of Round Buoyant Jets*, Report No. KH-R-36, California Institute of Tehnology.

Wright, S. J. 1984. "Buoyant Jets in Density-stratified Crossflow," *Journal of Hydraulic Engineering*, ASCE, 110(5): 643-656.

Wright, S.J., Roberts, P. J. W., Yan, Z., and Bradley, N.E. 1991. "Surface Dilution of Round Submerged Buoyant Jets," *Journal of Hydraulic Research*, 29(1):67-89.

Yuan, L. L. 1997. Large Eddy Simulation of a Jet in Crossflow. Ph.D. Thesis, Department of Mechanical Engineering, Stanford University, U.S.

Zeitoun, M. A. et al. 1970. *Conceptual Designs of Outfall Systems for Sesalination Plants*. Research and Development Progress Report No. 550, Office of Saline Water, U.S. Department of Interior.

Zhang, H., and Baddour, R. E. 1998. "Maximum Penetration of Vertical Round Dense Jets at Small and Large Froude Numbers," *Journal of Hydraulic Engineering*, ASCE, 124(5):550-553.

Zhang, X-Y, and Adams, E. E. 1999. "Prediction of Near Field Plume Characteristics Using Far Field Circulation Model," *Journal of Hydraulic Engineering*, ASCE, 125(3):233-241.